Physical and Numerical Modelling of Marine Renewable Energy Technologies, with Particular Focus on Tidal Stream and Tidal Range Devices

James Robert Brammer

Brammer.James@gmail.com

THIS THESIS IS SUBMITTED IN PARTIAL FULFILMENT OF THE REQUIREMENTS FOR THE DEGREE OF

DOCTOR OF PHILOSOPHY (PhD)

Cardiff School of Engineering

Cardiff, Wales, UK

March 2014

Abstract

The past decade has seen a significant rise in the interest of deploying Marine Renewable Energy technologies. Tidal stream technology is developing rapidly, and developers are favouring horizontal axis turbines (HAT's). However, vertical axis turbines (VAT's) are better suited for shallow waters, and higher efficiencies can potentially be gained by utilising shallow water blockage effects. The Severn Estuary is an ideal deployment area in this context. Additionally, due to a large tidal range the estuary has long been the subject of tidal barrage proposals. The original ebb-only STPG barrage has recently been superseded by a two-way generation scheme, therefore the need exists for renewed research into the hydrodynamic impacts of this proposal. Furthermore, little is known about the interaction between tidal range and tidal stream technologies, and if they could coexist in the Severn Estuary.

This thesis uses physical and numerical modelling techniques to assess a range of MRE technologies, with particular focus on their deployment in the Severn Estuary.

Physical model tests of a number of VAT's were conducted in a recirculating flume. Device performance and the wake characteristics were assessed, and it was demonstrated that VATS's could potentially provide competitive performance values if deployed in shallow waters. The CFD code ANSYS CFX was used to predict the unsteady turbine behaviour at the physical model scale; good agreement was achieved with the laboratory data, particularly in predicting the wake behaviour.

The CFD model TRIVAST was then applied to the Severn Estuary. Comparisons were made of the Severn Barrage schemes, as well as two hypothetical HAT and VAT arrays. The model results confirmed that vertical axis turbines are better suited to the Severn Estuary, provided that the technology is feasible. Finally, whilst the Severn Barrage proposals would eradicate the HAT resource, a lesser impact on the VAT resource was observed.

Acknowledgments

Firstly, I would like to thank my supervisors, Professor Roger Falconer and Dr Alan Kwan. Throughout my entire time at Cardiff University they have provided me with a great deal of support, and inspired me to push myself academically.

The Low Carbon Research Institute funded this research. I am grateful for the financial support, and have enjoyed being a part of the LCRI team over the last three years.

I would particularly like to thank Tom Harries. You have been a great friend, and I wish you the best of luck with the end of your PhD.

The experimental work would not have been possible without the expertise of Paul Leach, and I would like to thank the many others who I have worked with along the way, particularly Thorsten Stoesser, Reza Ahmadian, Chris Ellis, Miles Willis, Frank Moloney, all colleagues at the HRC, and of course to the research office and IT staff.

I would also like to thank my examiners Dr George Aggidis and Dr Michaela Bray for reviewing this work.

I am lucky to have a great group of friends, and now that I can reclaim my social life I hope that we keep in touch. In particular thanks to Geraint, Toby, Tom, Rhodri, Matt, Ieuan and Laura, Lee, Scott, Fei, Jenny, Aki and Thanasis.

To all of my family, many thanks for your love and support. Many thanks to Saša's family as well, and I look forward to you all visiting us in France!

Lastly, and most importantly, thank you Saša. Without you I am not sure if I would have survived the PhD (I certainly would have been hungry!), and I will be eternally grateful for having you in my life.

List of Publications

Conference papers

Brammer, J., Falconer, R.A. and Kwan, A.S.K.. 2013. Physical and Numerical Modelling of the Wake Characteristics of the Savonius Tidal Stream Turbine. In: *Proceedings of 2013 IAHR Congress.* Chengdu, China. 8-13th September

Brammer, J., Falconer, R.A. and Ellis, C.. 2013. Physical and Numerical Modelling of the Severn Barrage. In: *Proceedings of 2013 IAHR Congress.* Chengdu, China. 8-13th September

Harries, T., Brammer, J., Bockelmann-Evans, B. and Kwan, A.S.K.. 2013. Quantification and Visualisation of Blockage Effects for a Savonius Type Turbine using Particle Image Velocimetry. In: *Proceedings of 2013 IAHR Congress.* Chengdu, China. 8-13th September

Journal papers

Brammer, J., Falconer, R.A., Ellis, C. and Ahmadian, R.. Under review. Physical and Numerical Modelling of the Severn Barrage. *Science China Technological Sciences*

Table of Contents

List of Figures

List of Tables

Chapter 1 Introduction

1.1 Overview

1.1.1 Drivers of renewable energy

Climate change is a global issue that presents many challenges to society. It is widely accepted that human activities over the past 100 years are the most significant cause of the increased levels of greenhouse gases in the atmosphere. One result of this changing climate is a rise in global temperature, and it is predicted that a rise of 2°C will have a significant impact on natural ecosystems, which will be unable to adapt to such changes (EU Climate Change Expert Group 2008). Alongside these future concerns climate change can be observed today, an example of which is the increased frequency of extreme weather events. This was epitomised in 2012; in the UK nationwide hosepipe bans were introduced in March due to the lack of rainfall, they were subsequently lifted after fewer than 90 days following the wettest April in 100 years, which resulted in severe flooding. Other examples include the 2010 Pakistan floods, estimated to have affected over 20 million people. In addition to the effects of climate change, energy security is fast becoming a global issue as fears increase over the price of oil in a time of financial constraint. With the world's population expected to grow from 6 to 8 billion by 2030, we are facing the 'Perfect Storm', as demand for food, energy and water is to increase by 50%, 50% and 30% respectively (Falconer 2011).

Due to the above issues it is recognised that we need to change not only how efficiently we manage and consume our energy, but also how it is generated. This has led to the development of renewable energy technologies, which generate electricity from sources that occur naturally and repeatedly (Carbon Trust 2010), whilst ensuring that no net greenhouse gases are emitted into the atmosphere.

1.1.2 Renewable energy targets

To ensure that global CO_2 emission levels are reduced there have been a number of agreements which have committed nations to move towards a low carbon economy. Following the Kyoto Protocol, which expired in 2012, further directives have been introduced that look to further reduce emissions over a longer timeframe. In 2009 the

EU enacted the '20-20-20' targets, with the three key objectives being: (i) to reduce the EU's greenhouse gas emissions by 20%, (ii) to improve the EU's energy efficiency by 20%, and (iii) to increase the proportion of final energy consumption from renewable sources to 20%. The UK's target as part of this directive is 15%, and this is further reinforced by the Climate Change Act, which commits the UK to an 80% reduction in CO_2 emissions by 2050.

The Welsh Government has continually expressed its desire to be a world leader in both renewable energy development and deployment, and to become a low carbon nation. This is reflected in the ambitious targets that were set in 2010; namely that by 2025 as a nation it aims to generate up to twice as much electricity annually, compared to 2010 levels, from renewable sources, and by 2050 to be in a position where all energy needs can be met by low carbon resources (WAG 2010).

1.1.3 Renewable energy technologies

There is a wide range of renewable energy sources available, including - but not limited to, wind (onshore and offshore), marine (wave and tidal), hydro, solar (PV, thermal and biomass) and geothermal. Marine energy encompasses both wave and tidal energy; tidal energy can be broken down further into tidal stream and tidal range energy. Offshore wind can also be included under the bracket of marine, however in this thesis the term marine energy refers only to wave and tidal energy. Wave and tidal stream technologies, in particular, have developed rapidly in recent years, with tidal range considered a proven technology due to successful projects such as the La Rance Barrage, in France.

Whilst wind energy is currently the most established renewable technology in the UK, there remains significant potential for the marine energy market to contribute to the UK's energy mix, and as a result it is now a rapidly growing industry. This potential is due to the predictable nature of the tides and the substantial resource available to the UK and specifically within Wales, as shown in Figure 1.1.

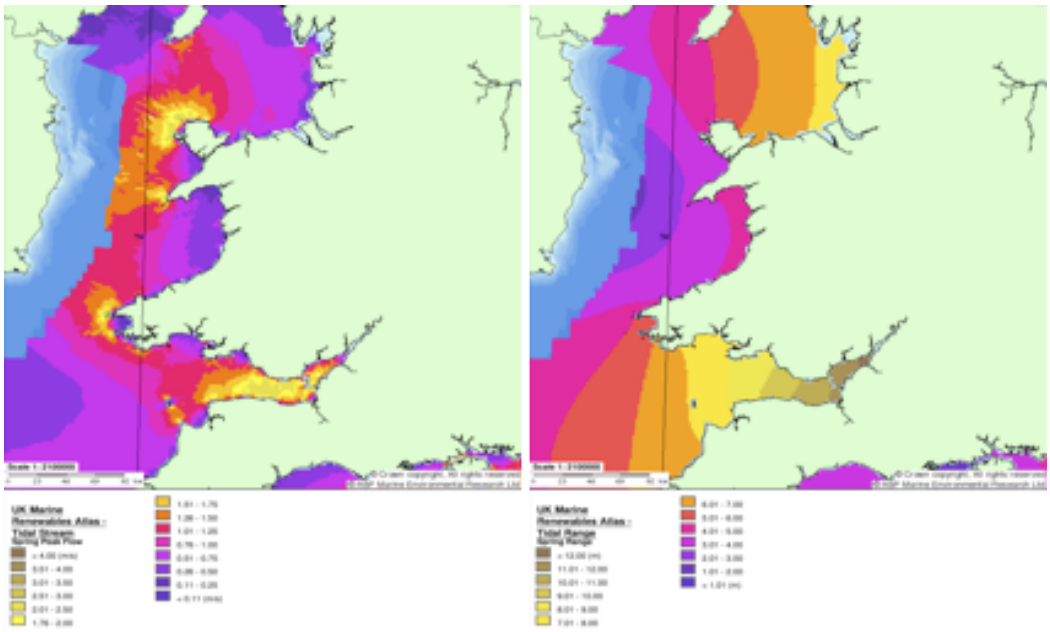

Figure 1.1 Tidal stream (left) and tidal range (right) resource around the Welsh coast. Reproduced from http://www.renewables-atlas.info/ © Crown Copyright

1.1.4 Marine energy from the Severn Estuary

The Severn Estuary has the third largest tidal range in the world, resulting in a unique hydrodynamic regime. In its current state the estuary supports a diverse range of marine habitats, includes a number of major ports and creates phenomena such as the Severn Bore. A balance must be struck between harnessing energy and minimising any negative impact on the estuary, therefore it is unsurprising that the Severn Estuary and Bristol Channel is often at the centre of debate regarding the deployment of marine energy technologies in Wales and the South West of England.

Figure 1.2 shows the regions that define the Severn Estuary and Bristol Channel; it should be noted that for convenience the Severn Estuary and the Inner and Outer Bristol Channel regions are referred to herein as the Severn Estuary, unless stated otherwise.

A wide range of studies has been conducted to assess the potential for marine energy deployment in the Severn Estuary. As part of the Marine Renewable Energy Strategic Framework (MRESF) study, undertaken for the Welsh Assembly Government, it was concluded that up to 0.14 GW of installed capacity could be provided by tidal stream technologies in the Severn Estuary (RPS 2011). Additionally, the Offshore Renewables Resource Assessment and Development (ORRAD) project concluded that up to 0.6 GW could be installed in English territorial waters (PMSS 2010). If combined, this gives a

potential capacity of 0.74 GW, which could be increased to 1.1 GW if the further potential of 0.36 GW available in the Atlantic Approaches is included (Regen SW 2012). It is worth noting at this point that both the MRESF and ORRAD projects used different criteria in their respective assessments, hence there is a large variation in the potential resource. This is discussed further in Chapter 2.

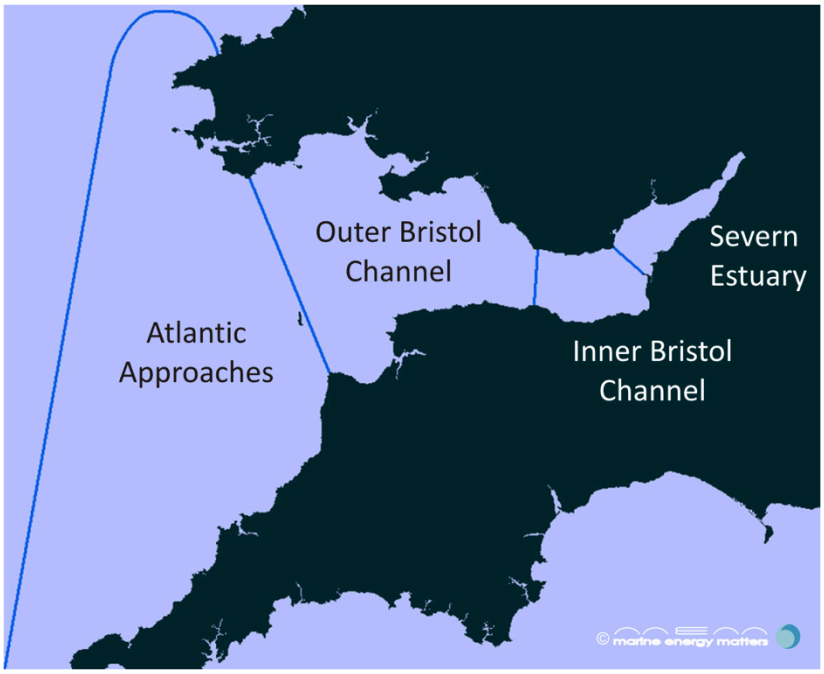

Figure 1.2 Regions of the Severn Estuary and Bristol Channel (Regen SW 2012)

Plans to utilise the large tidal range of the Severn have existed in various forms since the 1920s, however the 1989 Severn Tidal Power Group (STPG) proposal is commonly referred to as the original Severn Barrage (STPG 1993). This scheme had an installed capacity of 8.64 GW and this potential has been confirmed by a number of studies (DECC 2010; Sustainable Development Commision 2007). These plans have since been superseded by a private consortium, namely Hafren Power, who propose a different generation method, with the aim of minimising the environmental impact (Hafren Power 2013). Other smaller schemes for tidal range generation are also being put forward, for example Tidal Lagoon Power propose a 0.24 GW lagoon in Swansea Bay (Tidal Lagoon Power Plc 2012).

Despite having a large potential resource for tidal stream technology, there are currently no significant plans for deployment in the Severn Estuary, with developers opting for sites in Pembrokeshire, Anglesey, and areas around Scotland, amongst others. This is

partly due to the fact that if a Severn Barrage were to be built, tidal currents, and therefore the potential resource in the estuary, could be significantly reduced. However, the issue is more complex. Developers are favouring horizontal axis turbines, which are typically suited to depths between 25 and 40 m, and are rated for flow speeds in excess of 2 ms^{-1}. Whilst vertical axis designs traditionally have lower efficiencies, they hold a number of advantages over horizontal axis designs. They are omnidirectional, but significantly they can be deployed in shallow waters, with their dimensions able to be optimised at specific sites to maximise the area of power take-off.

Table 1.1: Areas of potential deployment of tidal stream devices in the Severn. Data reproduced from http://www.renewables-atlas.info/ © Crown Copyright

Case	*Max distance offshore [km^2]*	*Depth range [m]*	*Mean Spring Peak Current [ms^{-1}]*			
			1.0	*1.5*	*2.0*	*2.5*
A	***-***	***-***	4559	1578	515	32
B	***10***	***25-40***	1186	671	324	0
C	***10***	***10-40***	2109	1257	496	32
D	***5***	***25-40***	612	343	146	0
E	***5***	***10-40***	1325	768	275	32

Note: all areas are in km^2

Table 1.1 highlights the areas of deployment available based on a number of simple constraints. By relaxing the minimum depth constraint from 25 to 10 m, the potential area approximately doubles. Furthermore, reducing the rated velocity from 2 to 1.5 ms^{-1} increases the area by a factor between 2 and 3. Hence the area available for a vertical axis device operable in shallow waters, and at lower flows can be increased five fold compared to a typical horizontal axis device, as shown in Figure 1.3.

Shallow-water devices would be smaller in size and capacity than deep-water technologies. However, the significantly larger area of deployment could provide a feasible solution for energy generation. It is therefore proposed in this thesis that vertical axis turbines are better suited to deployment in the Severn Estuary, and as a result the main aim of this thesis is to investigate and assess the suitability of vertical axis turbine designs for shallow water deployment. This study also focuses on tidal range proposals, namely the Severn Barrage, as a project of this magnitude would affect the tidal stream resource. It is therefore necessary to adopt a holistic approach and consider multiple forms of marine energy in the Severn, and the inter-technology interaction.

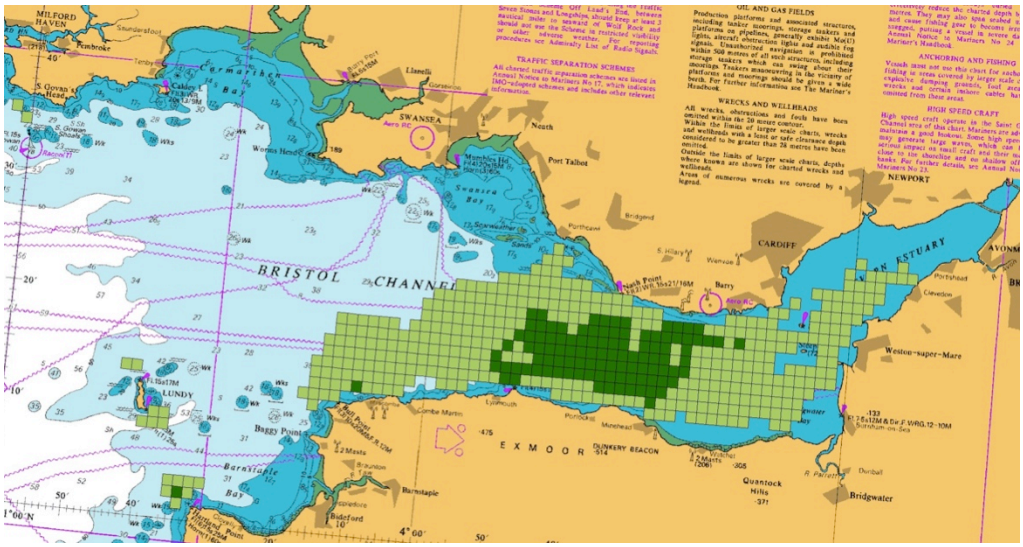

Figure 1.3 Comparison of potential tidal stream resource sites in the Severn Estuary (light green: vertical axis turbine resource, dark green: horizontal axis turbine resource)

1.2 Scope of this study

This study employs both physical and numerical modelling methodologies. As well as offering 'real' data, physical models enable proof of concept tests to be carried out, to quickly assess the viability of different designs. These small-scale tests are considered the principle stage in design development. Numerical modelling, and more specifically Computational Fluid Dynamics (CFD) models can be applied to a wide range of scales and scenarios, some of which cannot be replicated in a laboratory. Validations of these models with reliable data are key in order to have confidence in predictions, hence a joint physical and numerical study is particularly attractive in turbine development. Two main CFD models have been applied and developed in this study, namely the commercial code ANSYS CFX, and the Hydro-environmental Research Centre's own open source hydro-environmental model, namely TRIVAST.

1.2.1 Performance analysis and design of vertical axis tidal stream turbines

The first aim of this study was to conduct laboratory-scale performance tests of a novel vertical axis tidal stream turbine, namely CarBine (Cardiff turBine). Other designs were also tested to serve as a comparison, as well as assessing their suitability for shallow water deployment. Testing was conducted in the recirculating flume at the HRC's hydraulics laboratory, at Cardiff University. Working models of the different turbine designs were established using CFD techniques, and preliminary performance assessments were conducted.

1.2.2 Assessment of the wake characteristics of vertical axis devices

The wake characteristics of a turbine have a significant effect on the design and layout of arrays, and hence how much energy can be extracted per plan area is of considerable significance. As the market leaders favour horizontal axis devices, the majority of research relating to array modelling and device interaction has been focused on such designs. As a result, little is known about the hydrodynamic impact a vertical axis device would have and it was therefore deemed necessary to characterise the wake of the tested turbines in this study. Laboratory measurements were undertaken and used to calibrate the CFD models. This data was extended to the prototype scale to predict the impact that an array of vertical axis turbines would have in the Severn Estuary.

1.2.3 Hydrodynamic impact of the Severn Barrage

To investigate the impact of a barrage in the Severn Estuary, idealised scale models of the ebb-only STPG scheme and the two-way Hafren Power proposal were constructed and testing was carried out using a scaled physical model of the Severn Estuary. Numerical modelling studies were then conducted, at both the physical model and prototype scale. This led to an assessment of both schemes considering their impact on the potential tidal stream resource, and the interaction between the two different technologies.

1.3 Outline of Thesis

A literature review of tidal stream and tidal range technologies, as well as the varying physical and numerical modelling methodologies used to study these technologies, is given in Chapter 2. Chapter 3 provides details of the experimental setup used to investigate the performance and wake characteristics of a number of vertical axis tidal stream turbines. Following this, the results and relevant discussion of these experimental tests are presented in Chapter 4. The governing equations used in CFD models are derived in Chapter 5, with particular attention given to the equations used in the TRIVAST model, as access to the source code was available for this study. Chapters 6 and 7 present the CFD modelling results from the CFX and TRIVAST models, respectively. Finally, the main conclusions from this thesis, and recommendations for future work are made in Chapter 8.

Chapter 2 Literature Review

2.1 Introduction

This chapter provides a literature review of the relevant research previously undertaken in the field of study. Firstly, details of the sources of marine renewable energy are given, and the principles of energy extraction from these sources are outlined. A summary of the main studies relating to resource analysis is then described, with particular emphasis on the available tidal stream and tidal range resources in the Severn Estuary. An overview of the state-of-the-art of both tidal stream and tidal range markets is then presented, highlighting market trends and the direction of technological development. This is followed by a review of prior research in the field, relating to; performance analysis and wake characterisation of tidal stream devices, and tidal range projects. These studies are considered from both a physical and numerical modelling perspective. The chapter concludes with a discussion of the limitations in the current field of knowledge and, as a result, highlights how these issues are addressed in this thesis.

2.2 Tidal Energy

2.2.1 Introduction

It is estimated that 97% of all of the water on the earth is contained within the oceans, which in turn cover 70% of the earth's surface. This enormous body of water is subjected to not only the rotational effects of the earth, but also gravitational forces exerted by both the sun and the moon. This combination of forces results in what we know as the rise and fall of the tides (Pugh 1987). The amplitude of these tides varies depending on a wide range of factors, including the alignment of the sun and the moon, as well as the bathymetry and the presence of continents etc. As a result in deep oceans tidal amplitudes may be of the order of 1m or less, whereas in the Bay of Fundy, Canada, the largest tidal range in the world is observed to have a mean range of 11.7 m (NOAA n.d.). As these bodies of water are transported during a tidal cycle, fast currents can occur in areas of significant depth change, such as headlands or in tidal bays or estuaries (Pugh 1987). It is this rise and fall of the tide, and the fast currents that provide

potential sources for marine renewable energy, in the form of gravitational potential energy (tidal range) and kinetic energy (tidal stream).

Equation 2.1 describes the maximum power of a moving fluid, where ρ and g have their usual meaning, i.e. fluid density and gravity respectively, Q is the discharge in cumecs, and H is the total head of water, in metres.

$$P_{max} = \rho g Q H \qquad 2.1$$

The energy available is therefore dependent on the power, as described in equation 2.1 above, and the length of time over which this power can be generated throughout a tidal cycle. The following sections describe the tidal energy resource in the UK, with particular focus on the Severn Estuary, and further describe the technologies used to extract this energy.

2.2.2 Tidal energy in the Severn Estuary

There have been a number of studies undertaken in the past that have attempted to quantify the available resource of energy in the oceans. Table 2.1 shows the total theoretical marine energy resource in the UK, from a study compiled by the Crown Estate (2012). This report identified the Severn Estuary as having the largest single area of tidal range resource, as well as a strong tidal stream capacity.

Table 2.1 Theoretical marine energy resource in UK waters (Crown Estate 2012)

Type	*Total Energy Yield [TWh/y]*	*Total Power Capacity [GW]*
Wave	69	27
Tidal stream	95	32
Tidal range (Barrage schemes)	96	45
Tidal range (Lagoon schemes)	25	14

Whilst these figures describe the theoretical resource, other studies have estimated the feasible extractable resource. For example, the UK tidal stream energy resource assessment (Black and Veatch 2005) estimated the total tidal stream resource was 110 TWh/y, but with the amount *economically* extractable being reduced to 12 TWh/y; this equates to a much smaller installed capacity in UK waters of about 1-3 GW. This is a

widely cited report (Sinclair Knight Merz 2008; Sustainable Development Commision 2007), and a number of studies concur with this energy yield predictions; Iyer et al. (2013) predicted that 17 TWh/y was feasible, at an installed capacity of 7.8 GW.

Despite this agreement, there is uncertainty in this figure and a number of researchers believe this to be a significant underestimate of the available tidal stream resource. This is due to the way in which the available energy is considered; the common approach for tidal stream resource assessment is to consider the kinetic energy flux through a particular site, with this being the primary source of energy that can be extracted by the turbines. However it has been argued that this approach is flawed, as the kinetic energy flux does not necessarily equate to the power in a tidal wave (MacKay 2007b). Other methods consider the amount of energy dissipated due to bed friction, and consider a turbine doing the work as opposed to the seabed shear. Early work by Taylor (1920) estimated that the total power flux into the Irish sea was 64 GW, three-quarters of which was estimated to be dissipated by bed friction. Furthermore, studies by Salter (2009) estimated that in the Pentland Firth alone, the peak dissipation due to bed friction is 100 GW, of which 40 GW could be extracted by using turbines. In total it is generally accepted that over 200 GW of tidal energy is dissipated on average around the UK coastline (Blunden and Bahaj 2007).

Whilst the debate continues as to the total amount of tidal stream energy available for extraction, the fact remains that there is significant resource, and particularly in the Severn Estuary, of both tidal stream and tidal range energy, as shown in Figure 2.1. Herein the estimated tidal energy resource specifically in the Severn Estuary is discussed in further detail.

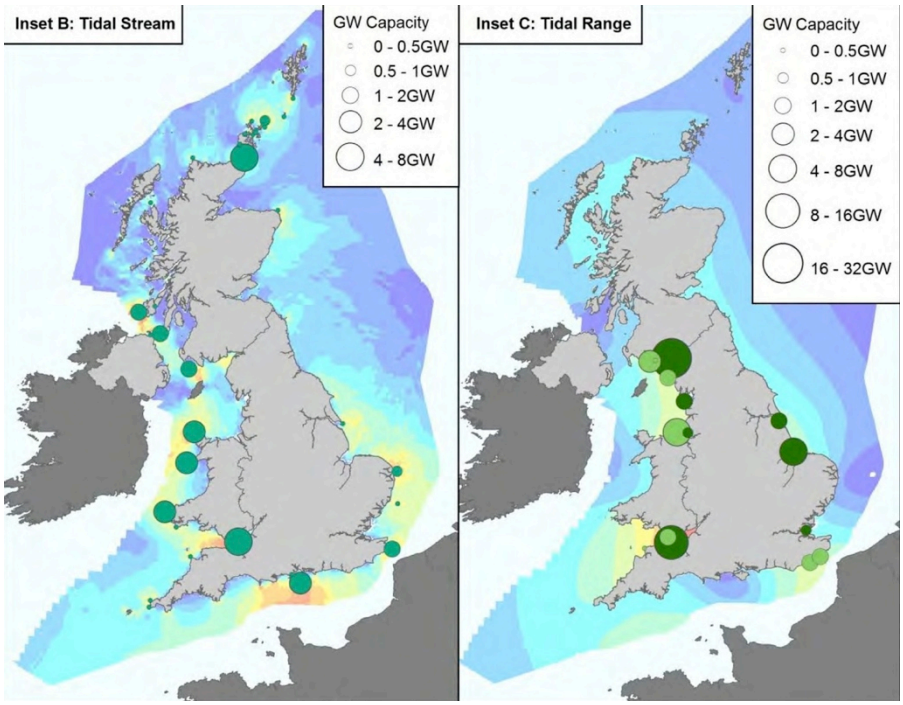

Figure 2.1: Tidal energy resource in UK waters (Crown Estate 2012)

2.2.2.1 Tidal stream resource

Due to the significantly large tidal range resource in the Severn Estuary the majority of studies to-date have focused on tidal range generation, and partly due to the infancy in the industry of tidal stream deployment (DECC 2010). However, two key studies have investigated the potential tidal stream resource, namely: the Marine Renewable Energy Strategic Framework (MRESF) study, conducted on behalf of the Welsh Assembly Government (RPS 2011), which considered marine energy around the Welsh coast, and the Offshore Renewables Resource Assessment and Development (ORRAD) project, which considered the English side of the estuary and the South West coastline. This latter study was commissioned by the South West Regional Development Agency (South West RDA). Both of these studies used the dataset from the UK marine renewable energy resource atlas (referred to herein as the renewables atlas) (ABPmer 2008), which is currently operated by DECC as part of the Offshore Energy Strategic Environmental Assessment (SEA). The Atlas contains GIS data of all types of marine energy, for the entire UK continental shelf. Tidal resource was predicted using the Proudman Oceanographic Laboratory's High Resolution Continental Shelf (HRCS) model, which had a grid resolution at 1.8 km^2, and where necessary the MRESF and ORRAD studies were supplemented with additional datasets and information.

The MRESF study compiled a large GIS database of a wide range of constraints, as well as the renewable atlas data, with the database constraints including: typical device characteristics, bathymetric restrictions, shipping lanes, marine mammal behaviour etc., to name but a few. These were compiled after consultation with representatives of the relevant sectors, and with this database various scenarios were modelled to estimate the available resource.

The main findings from the MRESF study show that the Severn Estuary has a predicted capacity of 0.14 GW. This result was based on the following constraints: a minimum depth of 10 m, a maximum distance offshore of 5 km, and a mean peak spring current (MSPC) of 2 ms^{-1}. This resulted in a resource area of 70 km^2, as demonstrated in Figure 2.2, which also highlights the resource area for a MSPC of 1.5 ms^{-1}, which is much larger at 160 km^2. However, the MRESF did not provide an estimate of the generation capacity using this lower velocity.

Figure 2.2 Tidal stream resource area in Severn Estuary as predicted by MRESF study (RPS 2011)

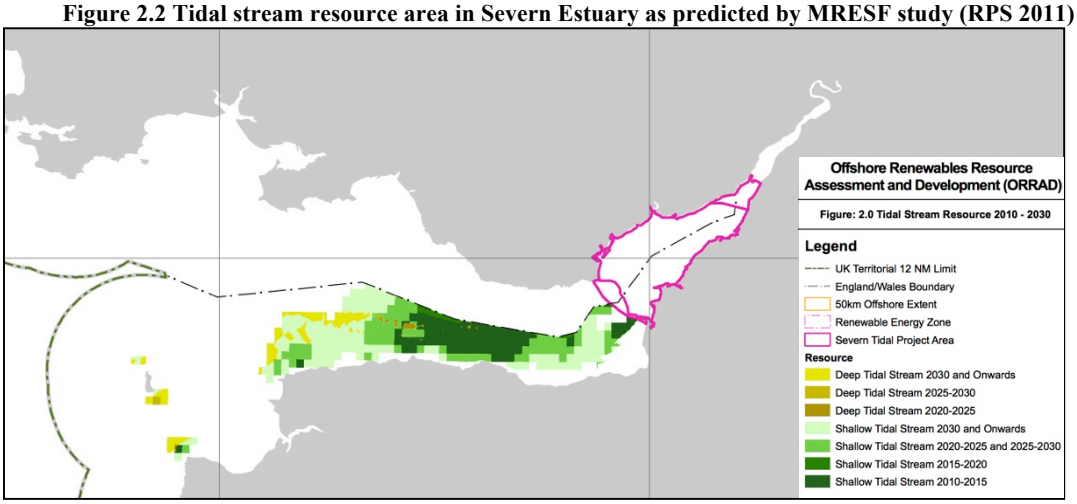

Figure 2.3 Tidal stream resource area in Severn Estuary as predicted by ORRAD study (PMSS 2010)

The resource areas identified by the ORRAD study are shown in Figure 2.3. It is noted that the study excluded the Severn Tidal Project Area in resource calculations, as this area was already the subject of separate tidal range studies. The ORRAD study used various GIS datasets to apply various geospatial constraints, and therefore analyse various scenarios to estimate the feasible resource extractable, principally between the years 2010-2030, and then beyond. In general, the constraints were not as strict as the MRESF study; for example, tidal stream energy was divided into two categories: (i) shallow-water, for depths from 5-35 m, and (ii) deep-water, for depths over 35m. The shallow-water region was restricted to a maximum distance of 10 km offshore, increasing to 20 km by 2030, whereas the deep-water regions were restricted to a maximum distance of 50 km by 2030. This compares to the 5 km limit in the MRESF study, therefore it would be expected based on these assumptions alone that the ORRAD study would identify a larger area of resource. Similar flows were modelled, with a MSPC of 2 ms^{-1} being used, reducing to 1.5 ms^{-1}. This was under the assumption that as the technology of tidal stream turbines developed, then lower currents would become more economical for energy to be efficiently extracted. This study concluded that 0.81 GW could be installed along the English side of the Severn Estuary.

2.2.2.2 Tidal range resource

The energy available from a tidal range scheme is proportional to both the tidal range, and the wetted plan area inside the basin, this is derived in section 2.3.2. Therefore the theoretical maximum resource in the Severn Estuary would utilise the entire plan area of the estuary. This is a clearly an impractical option, and further limited by the fact that the presence of a barrage could reduce the amplitude of the incoming tidal wave, thus reducing the potential energy. Therefore, in order to identify the practical resource available, areas of development must first be located and schemes conceptually designed. Resource analysis therefore tends to occur on a case-by-case basis. Details of the main plans for development in the Severn Estuary that have existed are given below.

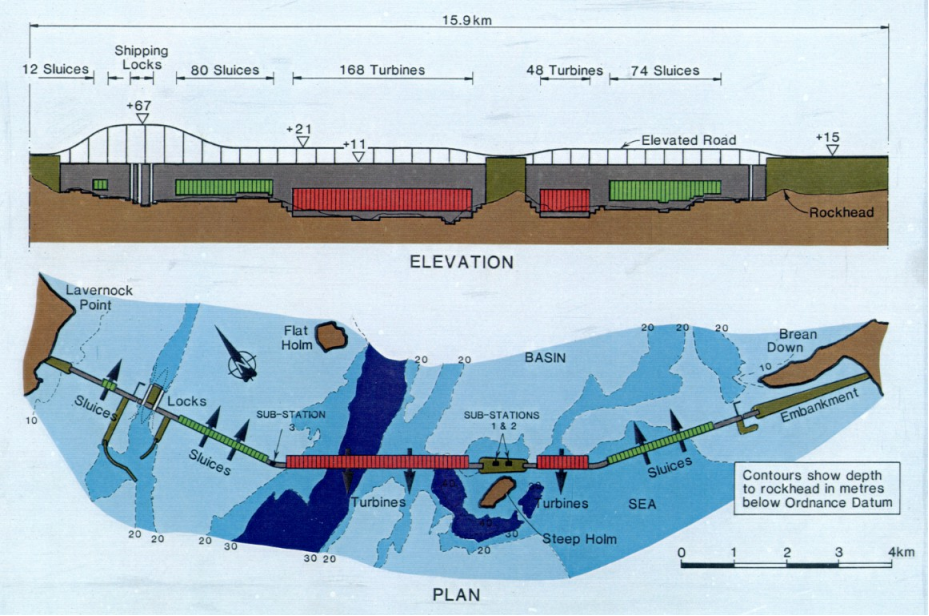

Figure 2.4 Design of STPG barrage (Taylor 2002)

Plans to extract energy using the tidal range in the Severn Estuary have existed in various forms since the 1920s. However the 1979 oil crisis renewed interested in alternative energy technologies, and the Severn Barrage Committee (commonly known as the Bondi Committee) was formed and investigated six different proposals of barrages in the Severn Estuary. The study recommended that a 10-mile barrage be built between Brean Down and Lavernock Point (Severn Barrage Committee 1981). In 1989 the Severn Tidal Power Group (STPG) further developed these plans and investigated a number of different schemes. This resulted in what is commonly referred to as the original Severn Barrage, which was to be located in the same place as recommended by the Severn Barrage Committee, as shown in Figure 2.4. The barrage had an installed capacity of 8,640 MW, provided by 216 bulb turbines, and it could deliver 17 TWh of energy per annum - 6% of the UK's demand. However, due to environmental concerns and at an estimated cost of £8 billion the barrage was deemed unfeasible.

In 2007 the Sustainable Development Commission (SDC) published a report calling for the development of tidal power in the Severn Estuary (Sustainable Development Commision 2007). This report covered a range of barrage and lagoon schemes, as well as tidal stream devices. Following the publication of this report the UK government commissioned the Severn Tidal Power Feasibility Study (STPFS), which aimed to build on the SDC's report, and consider a number of impacts from various schemes including: cost, environmental, social and regional impacts (DECC 2010). After a call for

proposals ten different projects were submitted, which included barrage and lagoon schemes, as well as a tidal fence and reef concept. This included a larger barrage from Minehead to Aberthaw, which would have made maximum use of the potential resource in the estuary, with a generation capacity of 14.8 GW, and annual energy output of 25.3 TWh. The ten proposals, with the locations being shown in Figure 2.5, were reduced to five and the shortlisted schemes studied are shown in Table 2.2.

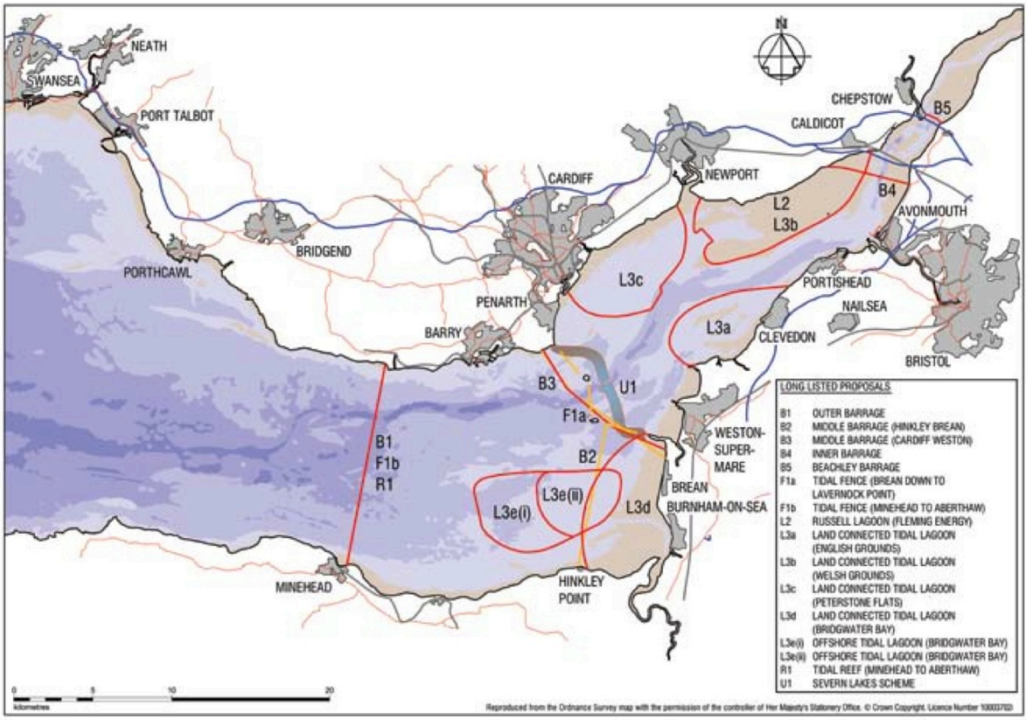

Figure 2.5 Locations of long listed proposals considered in STPFS (DECC 2009)

In the five shortlisted schemes that were chosen, the technology they used was considered proven as it was adopted from the hydropower sector. However the study also wanted to investigate the lesser developed technologies that could still produce energy, but at a lower environmental impact (DECC 2010). Therefore the Severn Embryonic Technologies Scheme (SETS) was established. Three different technologies were investigated under the SETS scheme, including: a Severn Tidal Fence, which used tidal stream turbines, a Spectral Marine Energy Converter, developed by VerdErg which used the Bernoulli principle to create secondary currents from flow through a fence, and finally a tidal bar, which used a new design of very-low head turbines to generate electricity on both tides, with this scheme being developed by Rolls Royce/Atkins (DECC 2010). These proposals ranged in energy production capacity, from 0.9 to 16.8 TWh/y.

Scheme	Installed Capacity (MW)	Annual Energy Generated (TWh/yr)	Levelised Energy Cost (£/MWh), Optimism Bias included		Intertidal Habitat Loss (km2)
			Investor (10% discount rate)	Social (3.5% discount rate[1])	
Cardiff-Weston Barrage	8640	15.6	312	108	160
Shoots Barrage	1050	2.7	335	121	33
Beachley Barrage	625	1.2	419	151	27
Welsh Grounds Lagoon	1000	2.6	515	169	73
Bridgwater Bay Lagoon	3600	6.2	349	126	25

Table 2.2 Scheme summaries from STPFS (DECC 2010)

Once again the Cardiff-Weston scheme was the preferred proposal after this consultation, however, it divided opinion as concerns were raised over its environmental impact. This was primarily due to the mode of operation: ebb-only generation, as this would have raised the minimum water levels significantly upstream of the barrage, resulting in a 160 km^2 loss of intertidal habitat. With an estimated cost in the order of £20bn, and at a time of global financial constraints, the UK government abandoned the proposals in 2010.

A private consortium has since been formed, namely Hafren Power, with the aim of privately financing a barrage. Due to the commercial nature of this new proposal, exact technical details are not publicly known at this stage, however, it is understood that the group have proposed a new design of barrage, whilst producing a similar energy yield. In the scheme a two-way mode of operation is proposed which will use over a 1000 turbines (Hafren Power 2013). The turbines are of a new low head design, as opposed to the traditional bulb turbines that were considered in the STPG scheme. It is envisaged that this scheme will have less environmental impact, with a reduced loss of intertidal zones, and with the tides upstream of the impoundment following much more closely to the natural state.

2.2.3 Design of tidal stream turbines

Due to the nature in which kinetic energy is extracted from tidal streams, much of the technology and knowledge is transferred from the wind industry, and therefore many similarities can be drawn between the two industries. The principle difference between

wind and tidal stream energy is that water is approximately 800 times denser than air, and tidal currents are typically a fifth of wind speeds. As a result a tidal stream device with the same power rating as a wind turbine will be smaller in size, and will rotate at slower speeds (King and Tryfonas 2009). The tidal stream industry is still in relative infancy, with no particular design identified as the optimum (Khan et al. 2009). This is reflected in the European Marine Energy Centre (EMEC), where all of their current berths are full, and with developers testing a number of different design concepts.

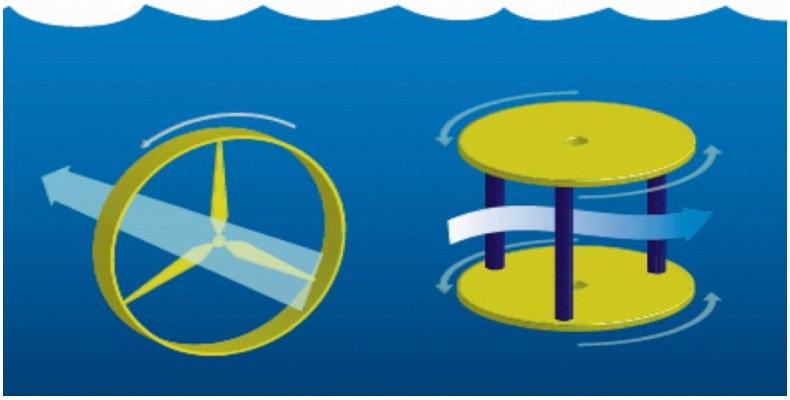

Figure 2.6 Horizontal and vertical axis rotor configurations (Sustainable Development Commision 2007)

Six main types of tidal stream devices have been identified by EMEC, namely: horizontal axis turbines, vertical axis turbines, oscillating hydrofoil, enclosed tips (venturi), Archimedes screw, and the tidal kite (EMEC n.d.). Whilst all types are acknowledged, none have received as much academic and commercial attention as horizontal and vertical axis turbines (Figure 2.6); therefore these two turbine types are the main focus herein.

2.2.3.1 Horizontal axis turbines

Similarly to the wind industry, the horizontal axis turbine is the preferred choice by the majority of turbine developers. This is mainly due to the fact that they traditionally have higher peak efficiencies than their vertical axis counterparts. Typically they are two or three bladed designs, as shown in Figure 2.7, and they may use a yawing system to align the turbine with the incoming flow, with pitch control being implemented to reduce blade loading. It is up to developers to decide how complex to make their systems, and strike a balance between efficiency, cost, and the risk of component failure. For example, Tidal Generation Ltd's 1 MW device implements a thruster system to continually face the incoming flow, and uses blade pitching technology (TGL Ltd n.d.).

(a) **(b)**

Figure 2.7 Horizontal axis turbines; (a) Voith Hydro prototype (Voith n.d.), and (b) artist impression of a SeaGen array (MCT Ltd n.d.)

Conversely, Voith Hydro's design strategy is at the other end of the scale, with their design based on simplicity. No pitching or yawing mechanism is used, with symmetrical blade profiles being used to allow for generation on both the ebb and flood tides (Voith n.d.). Marine Current Turbines Ltd are widely regarded as the world's leader in tidal stream technology; their 1.2 MW bi-directional device has been supplying electricity to the grid in Strangford Lough since 2008, and as of March 2012 has generated over 3 GWh of electricity (RenewableUK 2012).

2.2.3.2 Vertical axis turbines

Vertical axis turbines, whilst having lower peak efficiencies, possess some key advantages over horizontal axis designs. Omni-directionality simplifies the turbine design, and ensures that the device works independently of the incoming flow direction. A vertical axis turbine will also have a larger swept area than an equivalent sized horizontal axis turbine. For example a square area normal to the direction of flow will be 27% larger than a circular area of equivalent diameter. This is particularly advantageous in shallow waters, as both the vertical and lateral dimensions can be optimised to maximise the area of power take-off, whereas the depth of flow would limit dimensions of a horizontal axis turbine. The transverse horizontal axis turbine concept, as shown in Figure 2.8, is akin to a vertical axis turbine. This orientation doesn't allow for complete yawing, however, it is bi-directional and is suited to lateral stretching (McAdam et al. 2013). Both the vertical axis and transverse axis designs can be more generally referred to as cross-flow turbines.

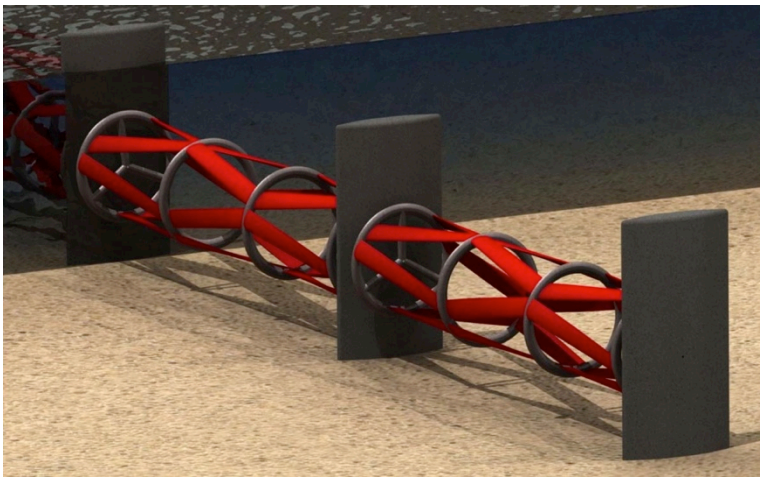

Figure 2.8 The THAWT concept (McAdam 2011)

The majority of cross-flow turbines are based on the Darrieus turbine, which was originally conceived as a wind turbine by French engineer Georges Jean Marie Darrieus (1931). Many variations of this original design exist, as there is a wide range of design parameters that can be changed, including, but not limited to the blade profile, number of blades, straight or helical blades, pitch control etc. The Savonius turbine is a simpler type of vertical axis turbine, consisting of two 'buckets' arranged in an 'S' shape (Savonius 1929). It is widely considered to be a drag force device, driven by the difference in drag on either side of the bucket. However, it has been acknowledged in other studies (Akwa et al. 2012b) that lift forces are also generated throughout certain phases of a revolution. It is generally a low-efficiency device, and has previously been used in applications where reliability is more important than efficiency, e.g. anemometers. The CarBine turbine – one of the designs studied in this thesis, is also a vertical axis drag-type turbine, and further details this design are given in section 2.8.

The tidal stream industry is currently at a pre-commercial demonstrator stage, however, this phase is coming to an end and the market leaders are now looking to deploy arrays to become fully commercial (RenewableUK et al. 2012). To the Author's knowledge, all of the devices currently being tested at a prototype scale are horizontal axis turbines, with the exception of Neptune Renewable Energy's ducted vertical axis concept. However, this company went into administration in February 2013, as it was found that their device was technically flawed (Neptune Renewable Energy 2013).

2.2.4 Tidal barrages and lagoons

The principal of tidal range power is adopted from traditional hydropower whereby a large dam is constructed to retain a body of water, typically based on river flows or run-off from mountains, and the large difference in water levels either side of the dam creates a head difference. Water is then passed through a penstock, or caisson, and in turn drives a number of turbines; hence the gravitational potential energy is converted into electricity. In tidal range energy, instead of permanently retaining water one side of a dam the rise and fall of the tide provides a head difference. Two key types of structures can be built for tidal range schemes, namely barrages and lagoons. Tidal barrages span across the width of a body of water, whether it be a river, bay or estuary, permanently blocking the upstream impounded area. Tidal lagoons on the other hand create impoundments, without blocking the body of water. Lagoons can be either coastally attached, or constructed completely offshore (MacKay 2009).

As the water levels are constantly changing due to the action of the tide there are three main modes of operation that can be implemented, namely: ebb generation, flood generation and two-way generation (Baker 1991). This is shown in Figure 2.9, which also highlights the main operation processes that occur throughout a tidal cycle, including:

- Filling or releasing: sluice gates allow water to pass through the structure, to fill or drain the impoundment accordingly, without power generation;
- Holding: no flow is transferred through the structure, hence the impounded water levels remain constant while the head difference across the structure increases;
- Generating: water flows through turbines, either filling of draining the basin, whilst producing electricity

It is also necessary to define the following terms;

- Starting head: the minimum head required before the generating phase can begin;
- Minimum (or low water) head: the minimum head reached at the end of the generating phase;

It is also noted that additional operating characteristics can be implemented in these schemes, such as pumping, and two basin schemes have been suggested as a way of storing energy, as well as increasing output (MacKay 2007a). Further details of ebb, flood and two-way generation modes are outlined below, and further details can be found in Baker (1991).

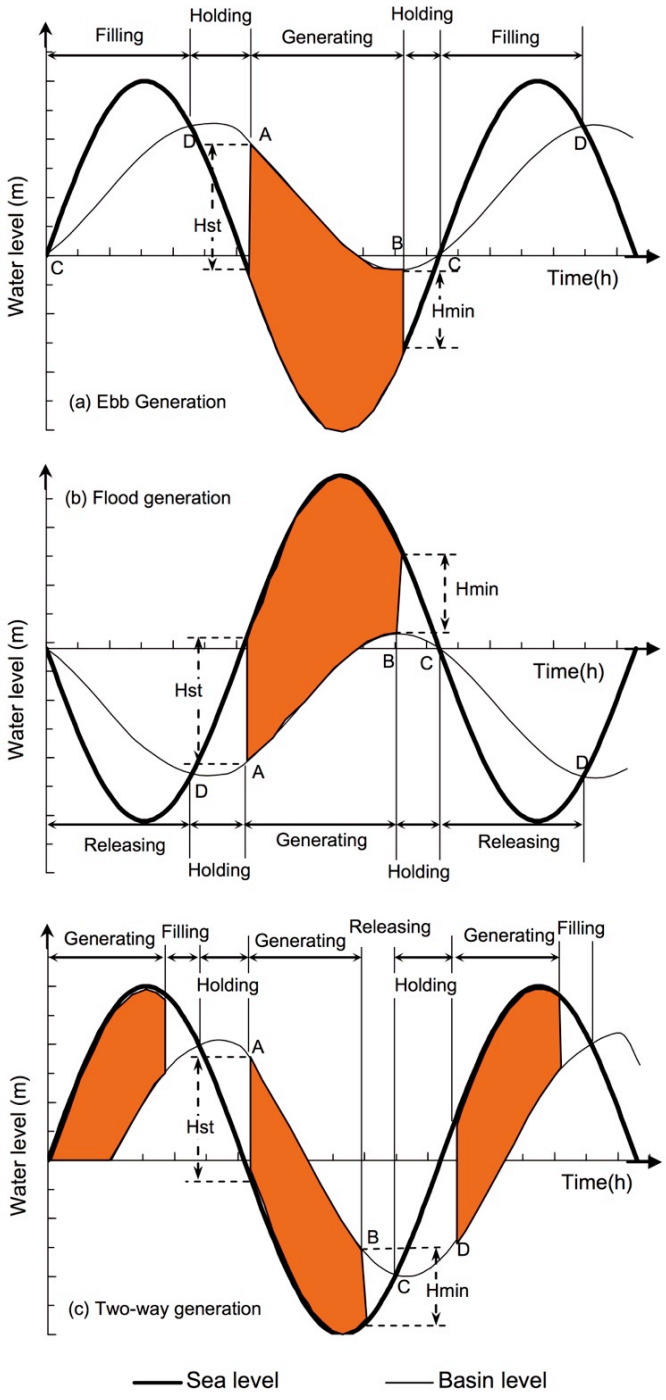

Figure 2.9 Operating modes of a tidal barrage or lagoon (Xia et al. 2010a)

2.2.4.1 Ebb generation

During the flooding phase of the tide the basin is allowed to fill via sluice gates. As the tide turns a holding period is introduced to retain water in the basin. This level is held as the seaward level falls during the ebb tide and the water level difference matches the starting head. The basin is then allowed to drain via a generating phase, until the basin reaches the minimum head level. As the tide turns and begins to flood again, the sluices are opened and the basin is filled again, hence the cycle is repeated.

This is traditionally the favoured mode of barrage operation, as it is generally perceived to produce the most energy per tidal cycle. However, these schemes have proved controversial in the past, as they also result in an increase in the minimum water levels inside the basin, which, depending on the site can result in permanent flooding of areas inside of the basin.

2.2.4.2 Flood generation

This mode of operation follows the same principles as ebb generation, except that the filling and generation phases are reversed, hence electricity generation occurs only on the flood tide. Generally flood generation yields less energy per tidal cycle, as the volume of water in the basin between low water and mid-tide (used in flood generation) will be much less than the volume of water between mid and high tide (used in ebb generation). As a result flood generation is seldom considered as a feasible mode of operation for a barrage.

2.2.4.3 Two-way generation

Two-way generation is a more complex mode of operation, as both ebb and flood generation principles are combined, and electricity is generated on both phases of the tide. Unlike ebb and flood generation the water levels inside the basin follow the natural tide more closely, and as a result this scheme is more popular with environmentalists as it reduces the area of permanent flooding. As the head difference tends to be smaller than one-way schemes the peak power capacity is usually smaller, but similar amounts of energy can be yielded, and as this is distributed in two phases per tidal cycle, it is more advantageous in terms of distribution to the grid. However, the cost of electricity

tends to be higher as traditionally one-way turbines are of a higher efficiency, and a larger number of turbines are needed, as there is less sluicing. Recently there has been renewed interest in implementing two-way schemes, particularly in the Severn Estuary (Hafren Power 2013). Low head and very-low head turbines are currently being investigated and developed (Rolls-Royce Plc and Atkins Ltd 2010), with a view to reducing the high cost of energy associated with two-way generation, whilst maximising the available benefits.

2.3 Energy Concepts

2.3.1 Performance analysis of tidal stream turbines

This section describes the general principles used to describe the performance of tidal stream devices. Referring to equation 2.1 it is necessary to define the total head, *H,* at the region of interest and, assuming a negligible bed slope, the total head can be defined as the sum of the elevation and velocity heads, as given in equation 2.2 (Chow 1959):

$$H = h + \frac{U^2}{2g} \qquad 2.2$$

where h is the depth of flow, U is the mean velocity and g is the acceleration due to gravity. In tidal stream energy it is assumed that only the velocity head provides potential energy, as water level differences across the turbine are deemed negligible and equations 2.1 and 2.2 can therefore be combined to give the maximum potential energy in a free stream:

$$P_\infty = \frac{1}{2}\rho A U^3 \qquad 2.3$$

where A is the swept area of the turbine normal to the flow and ρ is the fluid density. The mean velocity U can be expressed as:

$$U = Q/A \qquad 2.4$$

The power generated by a turbine is a function of the torque, τ, acting about its main axis, and the rotational speed, ω, which is defined as:

$$P_T = \tau\omega \qquad 2.5$$

Therefore, the efficiency of a device, which will be referred to as the power coefficient, $C_{P,}$ is defined as:

$$C_P = \frac{P_T}{P_\infty} \qquad 2.6$$

Another important parameter to define is the tip speed ratio, λ (or *TSR*):

$$\lambda = \frac{r\omega}{U} \qquad 2.7$$

where r is the turbine radius. This dimensionless coefficient relates the angular velocity of the turbine, relative to the incoming flow speed. This is particularly useful in comparing the efficiency of different types and sizes of turbines. Identifying both the power coefficient and the optimum operating condition is a key initial stage in the development of a turbine (Swift 2009).

2.3.1.1 The Lancaster-Betz limit

If a turbine were to extract 100% of the kinetic energy available, it would infer that the fluid stream would come to a standstill; this is not physically possible, as this would imply that there would be no kinetic energy available in the first place. There must therefore be an upper limit to the amount of energy extractable. The Lancaster-Betz limit, referred to herein as the Betz limit, is widely considered to be the upper limit of turbine efficiency (Gorban *et al.* 2001). The law is derived from the principles of one-dimensional conservation of mass and momentum of fluid flow through an unbounded stream tube. An actuator disk represents a turbine and the corresponding energy that it extracts, with further notation described in Figure 2.10.

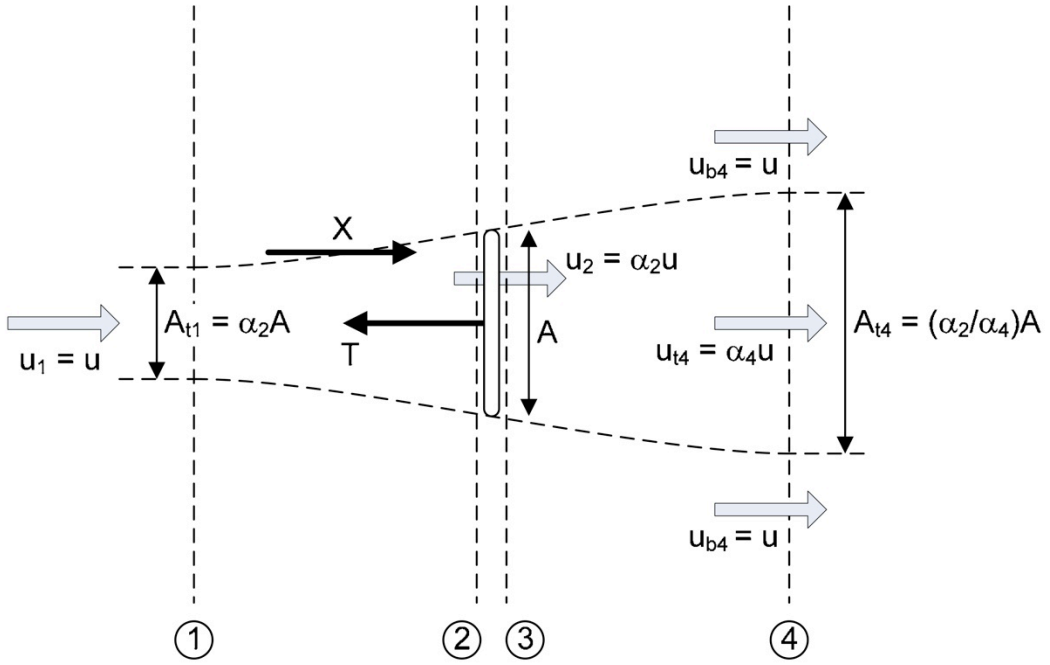

Figure 2.10 One dimensional linear momentum actuator disk theory terminology (Houlsby et al. 2008)

In this analysis energy extraction by the 'turbine' occurs by a reduction in linear momentum, which is represented by the thrust force T that acts on the incoming flow. Through combining the momentum equation, and applying Bernoulli's equation to either side of the actuator disk, expressions for thrust and power can be expressed as:

$$T = \rho A u^2 \alpha_2 \left(1 - \alpha_4\right) = \frac{1}{2}\rho A u^2 C_T \qquad 2.8$$

$$P = \frac{1}{2}\rho A u^3 \frac{\left(1+\alpha_4\right)}{2}\left(1-\alpha_4^2\right) = \frac{1}{2}\rho A u^3 C_P \qquad 2.9$$

Equation 2.9 indicates that the power extractable is a function of α_4, and as a result differentiation to maximise the power yields $\alpha_4 = 1/3$, resulting in a maximum power coefficient of $C_P = 16/27$. Therefore the Betz limit states that up to 59.2% of the available power can be extracted by a turbine. It is also noted that at this maximum point, the thrust coefficient, $C_T = 8/9$.

This theory applies to unbounded flow, and neglects any drag losses due to a hub or rotor blades. As the analysis is one dimensional it assumes that only axial components of velocity are significant, i.e. swirl or radial velocities are ignored (Houlsby et al. 2008). Due to these constraints the theory applies more generally to wind turbines than

tidal stream turbines. The following section describes an adaption by Houlsby et al. (2008) which is better suited to describing the conditions found in open channel flow.

2.3.1.2 Breaking the Betz limit?

The behaviour of a tidal flow in a channel is very different to that of a wind stream. The low density of air allows a stream tube to expand relatively freely when a given flow slows. In contrast the high density of water constrains a tidal flow, as does the free surface (Bryden et al. 2007). Furthermore, the presence of topographic features, such as islands, and the resulting blockage reduces the capacity of expansion. These factors combined make the traditional actuator disk method unsuitable for open channel flows. Figure 2.11 describes an extension to linear momentum actuator disk theory (LMADT) for open channel flows (Houlsby et al. 2008). As well as the flow being bounded by the bed, free surface and blockage, this extension describes the energy losses that occur due to mixing downstream of the turbine, previously neglected by LMADT in an infinite medium, and other extensions (Whelan et al. 2009).

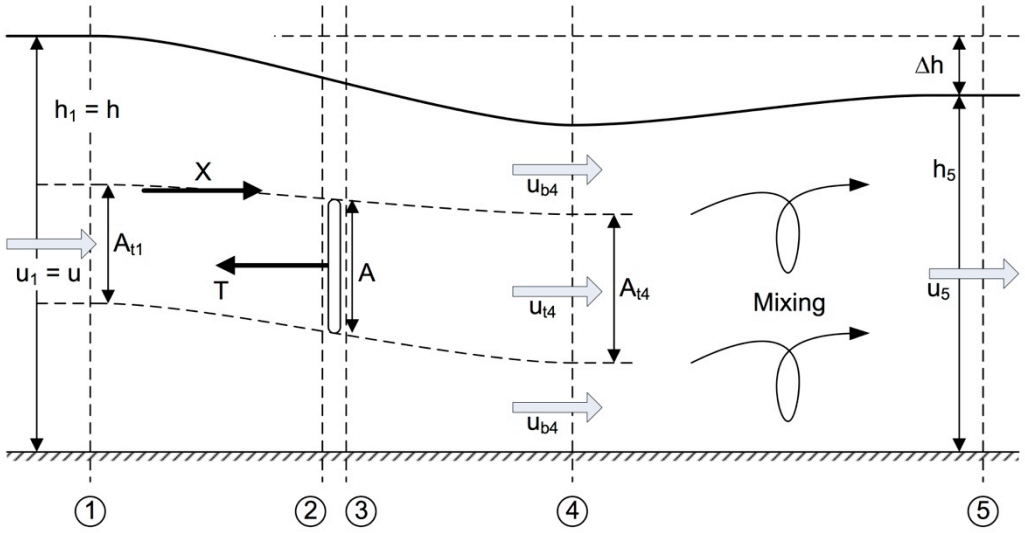

Figure 2.11 One dimensional linear momentum actuator disk theory applied to open channel flow (Houlsby et al. 2008)

In this method the principle difference is that when applying the Bernoulli equation the total head is used, i.e. the terms in equation 2.2. As the flow is constrained an accelerated bypass flow is created around the disk, and these two flows mix and create the downstream conditions. There is an energy loss associated with this mixing, and therefore the wake downstream of a turbine is a significant feature, as minimising the

losses due to mixing would imply that turbine performance would improve. The power of the wake is given as P_W. The resulting efficiency η is given in equation 2.10 and is a function of the Froude number, F_r, and the blockage ratio, as this effects the decrease in water levels downstream of the turbine, denoted as Δh:

$$\eta = \frac{P}{P + P_W} = \frac{P}{\rho g u b h \Delta h}\left(1 - F_r^2 \frac{1 - \Delta h/2h}{\left(1 - \Delta h/h\right)^2}\right)^{-1} \qquad 2.10$$

McAdam (2011) has demonstrated that it is possible to exceed the conventional Betz limit through the application of this theory, through increasing the blockage ratio in a channel. Whilst is has been recognised that it is necessary to consider the total head in energy extraction by these studies, amongst others (MacKay 2007b; Salter 2009), the use of the Betz limit is still widely adopted and used in design.

2.3.2 Energy capture from tidal barrages and lagoons

In the case of a tidal barrage or lagoon the total head, as given in equation 2.2 reduces to $H=h$, as due to the construction of an impoundment the local velocities will decrease to effectively zero, hence the velocity head is assumed to be zero. Therefore the power available is given directly by the difference in water levels either side of a barrage, and is given by equation 2.11:

$$P_{\max} = \rho g Q h \qquad 2.11$$

Integrating the maximum power over the duration of a tidal cycle yields the maximum energy that can be extracted throughout a tide. Integrating the discharge with respect to time gives the total volume of water transferred through the barrage and, as both ρ and g are constant, the energy, E, will therefore be proportional to the plan area of impoundment, A_P, and the square of the head difference:

$$E \propto A_P h^2 \qquad 2.12$$

In practise energy extraction is limited by the tide, and as a result the working head is usually lower than the maximum head. The time to fill and empty the basin also limits energy extraction.

The discharge through the structure depends on the individual design characteristics of the turbines and sluice gates used, as well as the total number installed. These characteristics are represented in the form of a turbine Hill chart, as shown in Figure 2.12. These charts relate the relationship between the specific discharge and unit speed of an individual turbine, through a wide range of operating conditions (Aggidis and Feather 2012; Baker 1991). Turbine efficiency and maximum power achievable are also given, however, due to the commercial nature of turbine design and performance up-to-date Hill charts are rarely available in the public domain.

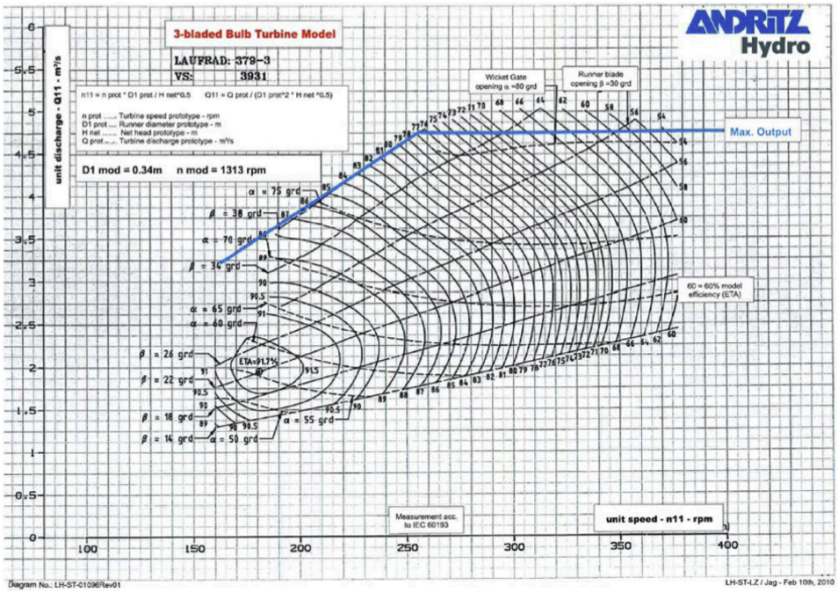

Figure 2.12 A turbine Hill chart (Aggidis and Feather 2012)

The orifice equation can also be used to estimate the maximum discharge achievable based on the head difference, as given in equation 2.13 (Baker 1991):

$$Q = C_d A_T \sqrt{2gh} \qquad 2.13$$

where A_T is the frontal area of a turbine or sluice gate, and C_d is a discharge coefficient that can be specified to represent the characteristics of a turbine or sluice gate. This method has been used in previous numerical modelling studies (Ahmadian et al. 2010; Xia et al. 2010a). Therefore by calculating the discharge using either a Hill chart or equation 2.13, and by calculating the head difference based on the tides, the power from a barrage or lagoon can be represented accordingly:

$$P = \eta \rho g Q h \qquad 2.14$$

where η is the efficiency of the turbines at the operating point.

2.4 Physical modelling of tidal stream turbine performance

Due to the infancy of the industry full-scale devices are still being tested at sites such as those located at EMEC, Scotland, and Strangford Lough, Northern Ireland. EMEC aims to provide standards for developers to conduct full-scale tests (Swift 2009), however, before this can happen much research is conducted at a smaller scale, typically in a hydraulic flume. This research study mainly focuses on investigations at this scale, as with the case of the majority of research studies previously conducted in academia.

2.4.1 Power take-off techniques

As previously discussed in 2.3.1 the power generated by a turbine is the product of the total torque acting about the main axis, and the rotational speed of the turbine. In order to analyse turbine performance and identify the peak operating condition, the relationship between C_P and TSR must be established for a given flow condition. These curves can be repeated for a range of flow conditions. Therefore, a power take-off system must be designed for a set of experiments, which: a) measures the torque and rotational speed, and b) allows these to be varied.

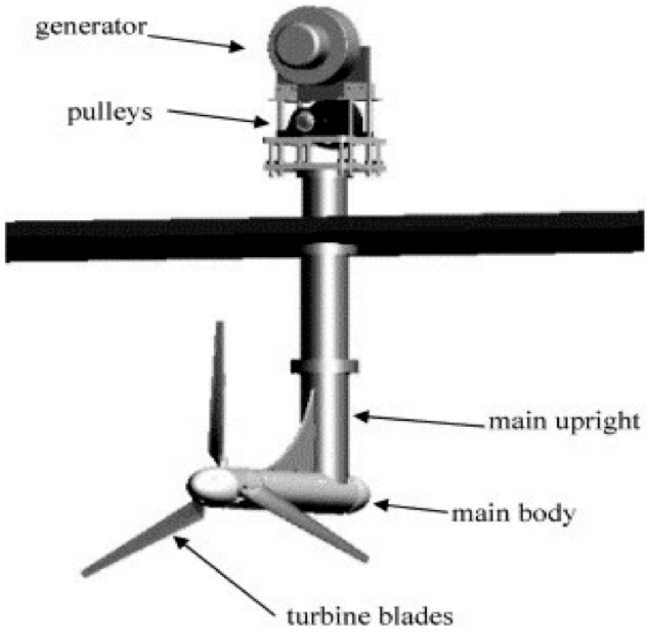

Figure 2.13 Typical electrical generator power take-off system (Bahaj et al. 2007b)

Dynamometers are commonly used to achieve this, and the design of these can vary greatly, depending on the objectives of the tests. These range from using electrical

generators, to directly measuring the mechanical forces. Details of common setups are given below.

The use of an electrical generator to control the torque is an intuitive solution, as the turbine is fulfilling its purpose of producing electricity. The torque applied in the generator is a function of the electrical current, which in turn can be varied by adjusting the resistance. The electrical power is then the product of the electrical current and voltage. This is a common system as highlighted in Figure 2.13 and typically a rheostat is used to vary the resistance (Bahaj et al. 2007b; Kato et al. 2010; Khan et al. 2008a; Kiho et al. 1996; Kyozuka 2008; Myers and Bahaj 2006; Hwang et al. 2009).

A limitation of using a generator system is that the generators tend to require rotational speeds higher than the turbine rotational speed, therefore a gearbox or pulley system is usually required to increase the shaft speed. However, this results in an energy loss. The generators themselves are also not 100% efficient, especially when not operating at their rated speed. This further contributes to energy losses in the power take-off system. Bahaj et al. (2007b), as well as others, employed the use of an in-line strain gauge, in order to measure the torque and thrust acting on the turbine, and before it was subjected to the mechanical losses of a pulley and generator.

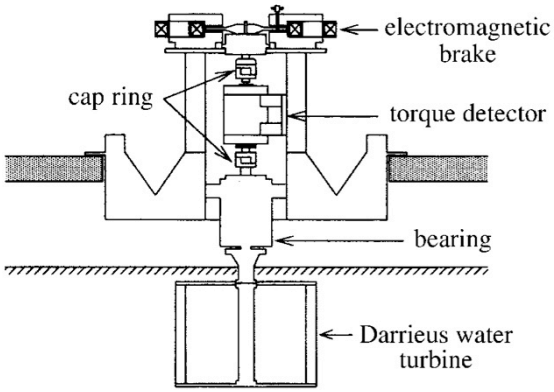

Figure 2.14 Power take-off system using a brake dynamometer and torque detector (Shiono et al. 2000)

A range of mechanical devices has also been used to control the torque on the rotor. A load can be applied via a brake dynamometer, which, can be in the form of a resistive load (Kirke 2011; Khan et al. 2008b; Clarke et al. 2007; Golecha et al. 2011), or an electromagnetic brake (Nakajima et al. 2008; Shiono et al. 2000), as shown in Figure 2.14. Unlike a generator, these systems have the advantage of not requiring gearing,

thereby minimising energy losses. However, other mechanical losses may be present, depending on the system design.

The two methods of power take-off previously discussed are both driven by a turbine, as would be the case at a prototype scale. However, it is possible to drive the turbine in the same way as a pump, and measure the reactive forces on the turbine. This allows for greater control over the speed of the turbine, although this system doesn't reflect exactly how the turbine operates. For example, a turbine that may pulse as it rotates, particularly a vertical axis turbine, may not be accurately modelled if the turbine is being forced to rotate at a constant velocity. AC motors, or servo-motors, can be used to drive the turbines (Mason-Jones et al. 2012; McAdam et al. 2013; Li and Calışal 2010; Fujisawa 1996). Servo-motors have the advantage that as well as driving the turbine, they automatically measure the reaction forces from the turbine, and record the rotational speed of the turbine. If less sophisticated motors are used, additional components will be needed to measure the shaft torque and rotational speed.

To measure the angular velocity of a turbine a range of components exists that has been incorporated into the above-mentioned systems. The average velocity can simply be measured by timing a certain number of revolutions (e.g. Kirke 2011), alternatively devices such as tachometers or encoders enable the velocity to be measured to a high degree of accuracy, with encoders providing an additional advantage by recording the relative angle of rotation, as used by McAdam et al. (2013), and Clarke et al. (2007) etc.

2.4.2 Turbine performance

A summary of the performance of different turbines is given in Table 2.3. This is by no means a definitive list of all performance tests conducted, but aims to highlight some key results that are relevant to this study. Firstly, it can be seen that, as previously discussed in 2.3.1.2, the Betz limit can be exceeded depending on the blockage levels and Froude number. The field tests of a Darrieus turbine by Kiho et al. (1996) show a peak efficiency very close to the Betz limit. This result is much higher than the efficiencies of the other Darrieus tests, in which the power coefficient varied between 0.2-0.4. However, further details of the relative blockage and flow conditions of the test site are not given, which could explain the high value of C_P.

A wide variance in the peak efficiency of the Savonius turbine was also observed in the tests, with the power coefficient varying between 0.05-0.3. This variation of efficiency in both the Darrieus and Savonius turbines can be explained by not only the difference in testing methodologies, but also the difference in the hydraulic conditions of the tests. At different Reynolds numbers the lift and drag characteristics of blades vary, hence different levels of torque contribute to the rotation of the turbine. This is also true for horizontal axis turbines, as acknowledged by Mason-Jones et al. (2012). However, the flow field around a vertical axis turbine is much more complex; the flow is unsteady, and vortex shedding occurs as the turbine rotates with the shedding frequency of the vortices depending upon the size of the turbine. Furthermore, the path of a downstream blade passes through the wake of an upstream blade; therefore the blades are subjected to varying velocities and as a result will generate different forces.

Table 2.3 also shows that for an unblocked flow, and without the use of additional components such as diffusers or flow deflector plates, a horizontal axis turbine has the highest peak efficiency, with a power coefficient between 0.4-0.47. The optimal *TSR* at which these peak values are found varies, however, from 3.5 up to 12. This is much faster than the operating speeds of a vertical axis turbine, which typically has a *TSR* between 1 and 2. A significant point to consider from the tests is that both Bahaj et al. (2007b), and Maganga et al. (2010) noted a significant decrease in the performance of the turbine if it was misaligned to the flow. As tidal flows are generally bi-directional by nature, and in reality are subjected to constant directional changes depending on the site conditions, in order for a horizontal axis turbine to maintain its relatively high efficiency is for a yawing system to be included. In contrast vertical axis turbines do not suffer from this problem since they are omni-directional and hence they have a distinct advantage over their horizontal counterparts. Finally, the tests also show that the use of components, such as diffusers and deflector plates, can significantly increase a turbine performance; the maximum C_P of the Darrieus turbine tested by Kirke et al. (2011) rose from 0.25 to 0.45, and a deflector plate increased the maximum C_P of a Savonius turbine from 0.15 to 0.21, as reported by Golecha et al. (2011).

Table 2.3 Performance values of various tidal stream turbine designs

Reference	*Turbine configuration*	*Turbine Diameter [m]*	*Velocity range [ms^{-1}]*	*C_P (max)*	*TSR (optimal)*	*Notes*
(McAdam et al. 2013)	Transverse Horizontal Axis	0.54	0.3-0.6	1.00	2.5	Recognised blockage effect to increase performance, F_r & R_e dependency
(Kiho et al. 1996)	Darrieus style vertical axis	1.6	1.1	0.56	2.1	Field tests, no details of channel blockage etc.
(Maganga et al. 2010)	3 bladed horizontal axis	0.7	0.8	0.47	12.0	Performance affected by misalignment
(Neary et al. 2012)	3 bladed horizontal axis	0.5	0.4	0.47	5.0	-
(Bahaj et al. 2007b)	3 bladed horizontal axis	0.8	0.8-1.5	0.46	6.0	Multiple configurations tested. Performance effected by yaw
(Kirke 2011)	Darrieus style vertical axis	1.2-2.4	Various	0.45	2.0	Field tests. Multiple straight and helical blades, with diffuser
				0.25	2.0	Without diffuser
(Mason-Jones et al. 2012)	3 bladed horizontal axis	0.5	1.0	0.45	3.5	Reynolds number independency achieved at R_e>10^5
(Kyozuka 2008)	Darrieus-Savonius style vertical axis	0.6	1.0	0.43	2.2	Darrieus only
				0.30	2.2	Darrieus-Savonius combined
(Luznik et al. 2012)	3 bladed horizontal axis	0.8	1.7	0.43	5.5-7.0	-
(Clarke et al. 2007)	3 bladed horizontal axis	0.82	0.8	0.39	7.0	Contra-rotating turbine
(Akwa et al. 2012b)	Savonius	Various	Various	0.30	Unknown	Wind turbine review
(Nakajima et al. 2008)	Savonius	0.14	0.8	0.25	1.1	Transverse axis, 12% blockage
(Blackwell et al. 1977)	Savonius	0.5	7-14	0.24	0.8	Wind turbine tests
(Shiono et al. 2000)	Darrieus style vertical axis	0.3	0.6-1.4	0.23	1.3	Solidity varied
(Golecha et al. 2011)	Savonius	0.25	Unknown	0.21	0.8	With deflector plate
				0.15	0.7	No deflector plate
(Khan et al. 2008a)	Darrieus style vertical axis	0.75-1.0	2.5	0.20	2.0	Number of blades varied
(Yaakob 2013)	Savonius	0.375	0.2	0.16	0.8	Designed for low-flow applications
(Khan et al. 2008b)	Savonius	0.2	1.0	0.05	0.8	Number of stages varied

2.4.3 Wake characterisation of tidal stream turbines

In comparison to the number of performance tests, there has been little investigation into the wake characteristics of tidal stream turbines, with the majority of tests being focused on the studying the wake characteristics of horizontal axis devices. This is due to the infancy of the industry, where early priorities have been focused on device performance and structural integrity. However, as the industry matures the wake behaviour is becoming more recognised as a significant factor, especially in the design of turbine arrays.

To measure the wake of a turbine a range of techniques exist, from using Acoustic Doppler Velocimetry (ADV) probes (referred to as ADVs) for instantaneous point measurements, to capturing a 2D area using Particle Image Velocimetry (PIV) systems (Rose et al. 2011; Good et al. 2011). Acoustic Doppler Current Profilers (ADCPs) are the most common instruments used in measuring velocities at a prototype scale (Fairley et al. 2013). Depending on the sophistication of the equipment used and the data collected, other flow parameters, such as the turbulence intensity or turbulence kinetic energy, can be measured and subsequently analysed. These parameters are important as they can significantly affect the performance and structural integrity of turbine devices (McCann 2007).

The wake of a horizontal axis turbine can generally be regarded as steady and as a result time-averaged velocity profile measurements can give a good indication as to the extent of the wake, and the flow conditions encountered by a downstream turbine. The wake of a vertical axis turbine on the other hand is unsteady, due to the vortex shedding behaviour that occurs as described previously. Therefore time-averaged measurements alone will not reveal the full hydrodynamic behaviour of vertical axis devices. There has been very little experimental measurement of the wake of vertical axis tidal devices, with Shiono et al. (2000) being the only example cited where point measurements were taken downstream of a Darrieus turbine. There have been studies to investigate the flow field of a Savonius rotor using PIV systems (Fujisawa 1996). However, the majority of research in this area relates to vertical axis wind turbines (D'Alessandro et al. 2010; Dobrev and Massouh 2011; Dobrev and Massouh 2012; Ross and Altman 2011).

Actuator disk theory provides a simplified numerical approach to estimating the performance of a turbine, and this theory has been represented in physical models through the use of porous disks in early studies, to simulate the effects of a turbine on a flow field (Sun et al. 2008a; Myers and Bahaj 2010). The porosity of the disks can be varied, and this will impart different levels of thrust on the flow. This porosity variation, in turn, can be used to represent a range of turbine operating conditions. An advantage of using this method is that it can be used as a direct comparison with numerical predictions. However, in terms of accurately representing a turbine the approach is limited. Three-dimensional flow effects cannot be simulated, and as a result features such as swirl from a horizontal axis turbine are not reproduced. This becomes less of an issue if modelling at a very small scale, as scaling issues occur and it becomes impractical to model a turbine. For example, if the 100 mm disks used by Bahaj et al. (2007c) were scale model turbines they would have to rotate at 1500 rpm to rotate at the appropriate *TSR*, which is clearly impractical. The results of tests using porous disks have shown that the spacing of downstream devices will be of the order of 15-20 diameters; Bahaj et al. (2007c) demonstrated that by 20 diameters downstream the wake had only recovered to 90% of the free stream condition, and Myers et al. (2011) demonstrated that the lateral spacing in an array also affected the behaviour of the wake.

In addition to using porous disks, there have been a number of tests undertaken using scale models of turbines (Maganga et al. 2010; Myers and Bahaj 2007; Neary et al. 2013; Tedds et al. 2012). These studies were typically conducted in conjunction with performance tests and as a result use the same turbine model and flume conditions. The conclusions from each study tended to agree with one another, and also with those obtained from porous disk tests. Neary et al. (2013) observed that 80% of the wake recovery occurred after 10 diameters downstream, with no further recovery as the deficit persisted up to 35 diameters downstream. They therefore recommended that the downstream spacing be of the order of 10 to 15 diameters. Tedds et al. (2012) found that 80% recovery occurred after 7 diameters downstream. Maganga et al. (2010) investigated the impact of different turbulence levels in the flume, and found that with 25% turbulence intensity in the flume, 92% of the wake had recovered by 10 diameters, compared to 83% recovery with turbulence intensity levels at 8%, as depicted in Figure 2.15. This is to be expected, as energy from the turbulence contributes to mixing

downstream; this is a significant finding, as tidal stream sites will typically have high levels of turbulence.

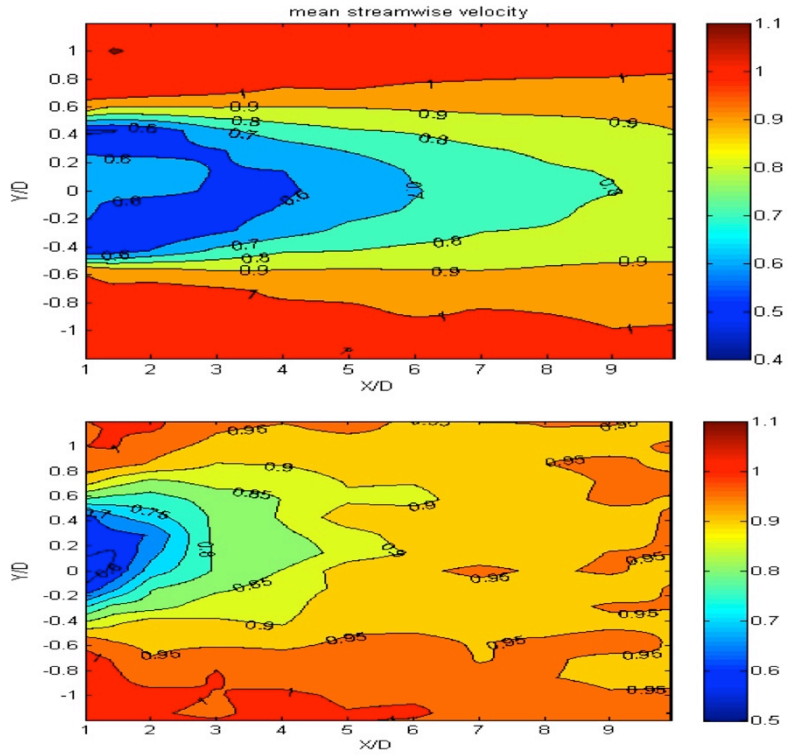

Figure 2.15 Mean streamwise velocities behind a horizontal axis turbine, for varying turbulence intensities (8% at top, 25% at bottom) (Maganga et al. 2010)

2.5 Physical modelling of tidal range schemes

Physical models of river, estuarine and coastal systems can provide a scaled representation of the underlying hydraulic phenomena that occur at a prototype scale. This is achieved through dimensionless scaling relationships of parameters, with flow conditions being considered similar if the model displays similarity in form (geometric similarity), similarity of motion (kinematic similarity) and similarity of forces (dynamic similarity) (Chanson 1999). However, it is not always possible or practical to achieve perfect similitude and hence the criteria are often relaxed. For example, a distorted geometric scale is often used to prevent the model from being too shallow and the Reynolds number being too small, with the horizontal scale often being limited by the size of the laboratory (Novák et al. 2010). Another example that is of particular importance to this study is the relationship between the Reynolds and Froude numbers. These two dimensionless numbers cannot be scaled linearly, and therefore similitude of both of these numbers in a scale model is generally impossible, therefore one must be

prioritised depending on the modelling scenario. For free surface flows gravity effects generally dominate the flow, and therefore it is widely accepted that similitude is best achieved through Froude number consistency (Chanson 1999; Ettema et al. 2000; Novák et al. 2010). As a result the Reynolds numbers in a physical model will generally be lower than for the prototype scale. This is deemed acceptable providing that the Reynolds numbers at the physical model scale are still fully turbulent. This still has implications for the model results however; for example, as previously discussed briefly in 2.4.2 and with particular relevance to this study, the lift and drag forces on a turbine blade are dependent on the magnitude of the Reynolds number.

Whilst the use of numerical models has become fairly routine nowadays, as they are not limited by scaling issues and tend to be less expensive than large bespoke physical models, they are only as reliable as the data driving the model at the boundaries and the data that they can be validated against. Physical models are therefore by no means redundant and continue to play an important role in hydro-environmental impact assessment and are particularly useful for fine flow details.

To the Author's knowledge, there have been no physical modelling studies of the Severn Estuary investigating the hydrodynamic impact of tidal range energy schemes, using scaled bathymetric data for such a specific estuary. However, Jeffcoate et al. (2011) conducted experiments using an idealised barrage structure to investigate the near-field flow regime, and assess the suitability of 2-D and 3-D numerical models. The lack of research in this field is partly due to the bespoke nature of each estuary model. Such models are not transferable and therefore this increases the cost of modelling, combined with the fact that most tidal range schemes are at a concept stage.

For completeness it is noted that in the design of turbines for use in hydropower dams and tidal barrages, physical testing is still widely recommended and adopted (ALSTOM Hydro 2009; Tridon et al. 2010; Vu et al. 2010). This area of modelling does not fall into the scope of this project, however, and is not discussed any further.

2.6 Numerical modelling of tidal stream turbines

The following section describes the numerical modelling techniques available to assess the design and hydrodynamic impact of tidal stream devices and arrays. The level of

sophistication within a model can vary dramatically and, whilst a physical model is limited by the size of the laboratory or the cost of construction, numerical models are usually limited more by the available computer memory and processing power. As a result a balance has to be found to develop a model that will simulate over a reasonable time scale and represent the problem with sufficient accuracy. The main types of numerical model that are typically used in tidal stream applications range from: momentum models, vortex models, cascade models, and computational fluid dynamics (CFD) models. Particular focus is given to CFD modelling herein, as this is the main type of numerical model used in work related to this study. However, where appropriate other modelling techniques are also discussed.

Generally, two scales of modelling are considered in this study, namely: near-field and far-field. The near-field applies to a region surrounding a turbine up to typically 20 diameters in size, therefore the modelling scale can range from the chord length of a single turbine blade, to device interaction in arrays. The far-field encompasses the region beyond the near-field, with the size of which being large enough such that any imposed boundary conditions do not unduly affect the modelling results. This can range from modelling a river, or estuary - such as the Severn, to the entire continental shelf, depending on the study and resources available.

2.6.1 Near-field modelling

As discussed, the near-field region covers a wide range of scales, and as such many different studies have been conducted at the near-field scale. Details are given herein of the numerical modelling tools used to investigate: a) the performance of a device, and b) the wake characteristics of tidal stream devices.

2.6.1.1 Performance analysis

The actuator disk theory in which the Betz limit was defined in 2.3.1.1 also forms one of the simplest momentum models for predicting turbine performance, namely the single stream tube model. There have been a number of extensions to the single stream tube model to address the limitations of actuator disk theory, and this has led to a wider, collective group of momentum models. These include: Blade Element Momentum Theory (BEMT), double or multiple stream tube models, and double-disk models.

BEMT is one of the most widely applied extensions to the actuator disk theory. This model adds rotational momentum to the actuator disk, which is achieved by dividing the stream into annular sections, rotational effects from individual blade sections can then be added, which are calculated depending on the lift and drag characteristics of the blade profile (Ingram 2005; Buckland et al. 2010). This is a common method that has been extensively used in the design of both wind and tidal stream turbines (Whelan et al. 2009; Batten et al. 2008), and models have been demonstrated to show good agreement with laboratory data (Batten et al. 2006; Bahaj et al. 2007a). This theory is being further developed in a number of areas to make it more suitable for a tidal environment and distinguish it from wind turbine analysis. Such refinements include, for example, accounting for blockage effects as discussed in 2.3.1.2 (Whelan et al. 2009), improving the inflow conditions by introducing turbulent flow profiles (Togneri et al. 2011), and adding wave-current interactions (Barltrop et al. 2007), to name but a few examples. BEMT has been also been coupled with CFD models (Batten et al. 2013; Malki et al. 2013; Turnock et al. 2011; Bai et al. 2009). By using a CFD model to resolve the flow field around a turbine, more accurate inflow conditions for the BEMT model can be provided. This enables array modelling and the effect of device interaction on performance to be investigated, as the wake generated by an upstream turbine provides the boundary conditions for corresponding downstream turbines.

Single stream tube BEMT models are typically used to predict the performance of horizontal axis turbines, as a single actuator disk represents the turbine geometry. Other momentum models, such as the multiple stream tube model, can be used to simulate vertical axis behaviour. This provides a better representation of the different lift and drag forces that are induced on each disk, as opposed to the annular representation for horizontal axis turbines. Strickland (1975) developed a model to predict the performance of a Darrieus wind turbine, as more recently have a number of other researchers (Coiro et al. 2005; Islam et al. 2008; Biadgo et al. 2013; Beri 2011). Both Winchester and Quayle (2009), and Dai et al. (2011) have applied these models to Darrieus tidal turbines. The Savonius wind turbine and other vertical axis designs have also been modelled using similar methods (Pope and Naterer 2012; Cooper and Kennedy 2004).

Vortex and cascade models are two other types of model that have been applied to predict the performance and wake characteristics of both wind and tidal stream turbines (Mccombes et al. 2009; Urbina et al. 2010; Wang et al. 2007; Scheurich et al. 2011; Li and Calışal 2010 p.1). They are typically more accurate, but have a higher computational cost (Zanette et al. 2010). However, these models are not as widely used as BEMT and CFD models, and do not fall into the scope of this study. They are therefore not discussed any further in this thesis, but more details can be found in Strickland et al. (1979), Van Dusen (1978) and Islam et al. (2008).

The use of CFD models, with no coupling to simplified models such as BEMT, is the most sophisticated method of numerical modelling available to analyse the behaviour of tidal stream turbines. This comes as little surprise, since this method has the highest demand on computational resources. CFD models generally solve the Reynolds Averaged Navier-Stokes (RANS) equations, which define the fluid flow with respect to both space and time (Bates et al. 2005). They can therefore describe complex dynamic fluid flow problems such a tidal flows, however it is often the case that the computational resources available compromise the sophistication of a CFD model. The main limiting factors are: the number of dimensions (1D, 2D, or 3D simulation), the choice of turbulence closure model, the mesh size, and the time dependency of the model. Further details, including the derivation and implementation of the RANS equations, are given in Chapter 5.

A significant advantage of these models is that they are discretized with respect to space, with a mesh being used to define the modelling domain. Therefore, unlike momentum and vortex models, the entire turbine structure can technically be modelled, including: the rotor blades, the hub and nacelle, the supporting structure and the site bathymetry. In practise, however, many simplifications have to be made to save computational resources. Nonetheless, being able to model the turbine blade geometry means that the forces generated by the blades can be calculated directly, whereas other models require previously acquired lift and drag data. This results in a more accurate prediction of turbine performance, and offers greater flexibility in design as multiple blade geometries and scales can be investigated, and without having prior data of the blades.

Generally when analysing the performance of turbines using CFD, simplified rectangular domains are usually modelled, akin to a hydraulic flume, for validation with experimental data. Site bathymetry is rarely modelled at a near-field scale, and a constant flow profile, which is either uniform or follows a log law, is commonly used instead of a tidal curve.

In modelling horizontal axis turbines a 3D domain is required as the principle flow direction is axially aligned. However, the flow field around a horizontal axis turbine can be considered time independent providing a constant upstream velocity is assumed. Hence, it is common to run a steady or quasi-steady analysis for such turbine studies (Mason-Jones et al. 2012; Wu et al. 2012; O'Doherty et al. 2009; McSherry et al. 2011). Furthermore, as turbines also have rotational phases, single segments of a swept area (i.e. a single blade) can be modelled to reduce the model complexity. This approach uses symmetric and periodic boundary conditions (Lee et al. 2012; Lawson et al. 2011).

Vertical axis turbines have the advantage that they can be modelled in two-dimensions, which dramatically reduces the size of the computational domain. However a steady or quasi-steady analysis is not suitable if the turbine geometry is to be modelled, as this method cannot accurately model the vortex shedding that occurs as the turbine rotates. Therefore an unsteady (or transient) analysis must be performed, and the turbine must be rotated during the simulation. Sliding mesh or re-meshing techniques can be used, and these methods take a considerably longer time to run than a steady analysis. A two-dimensional analysis of Darrieus turbines has been conducted by Gretton el al. (2009), Lain and Osorio (2010), Maître et al. (2012), Khalid et al. (2013a), and Hwang et al. (2009). Akwa et al. (2012a) investigated the performance of a 2D Savonius wind turbine. Three-dimensional models have also been applied by a number of researchers (Marsh et al. 2012; Park et al. 2012; Hyun et al. 2012; Yaakob et al. 2012; Khalid et al. 2013b) and, as expected, the results from such model studies show better agreement with laboratory data when compared to momentum models.

2.6.1.2 Wake modelling

The same modelling techniques described to investigate the performance of a tidal stream turbine can be used to model the wake characteristics of such devices. This

includes coupling actuator disk theory and BEMT, with CFD models, as well as using standalone CFD models. Coupling actuator disk theory with a CFD model provides the simplest and most computationally efficient solution (Sun et al. 2008b; Harrison et al. 2010; MacLeod et al. 2002; Nishino and Willden 2012), and it is akin to physically modelling porous disks, as described in Section 0. Coupling BEMT with a CFD model, as already discussed increases the accuracy compared to coupling simple actuator disk theory as three-dimensional flow effects are introduced. These models have been used not only to consider performance, but have also been used to study the length of wake, and the device interaction of arrays (Batten et al. 2013; Malki et al. 2012; Bai et al. 2013). A similar method has also been implemented by Antheaume et al. (2008) to investigate arrays of Darrieus turbines.

There has been very limited use of transient models to investigate the wake of tidal stream turbines. This is because a steady or quasi-steady analysis has been demonstrated to show good approximation of the flow field of horizontal axis turbines, and vertical axis turbines have received less commercial interest than horizontal axis turbines, so studies of this class of turbines have generally been focused on power generation. However, Gant and Stallard (2008) conducted an unsteady analysis of a horizontal axis turbine, represented by an actuator disk, to investigate the effect of time-dependant turbulence on performance and wake development. Khalid et al. (2013a) briefly commented on the wake structure behind a twin Darrieus turbine system. However, the aim of this study was primarily to investigate only the performance of the turbines. Finally, Dobrev and Massouh (2011) used CFD techniques to investigate the near wake region of a Savonius wind turbine, however, to the Author's knowledge there have been no studies concerning the near-wake of vertical axis tidal stream turbines.

2.6.2 Far-field modelling

As previously discussed, near-field studies tend to focus on a single device, or turbine-turbine interaction, and to date the principle aim of studies has been to investigate performance and energy capture, as well as array design and layout. Far-field modelling investigates the wider impact of marine energy installations and, as such, whole arrays are considered, as opposed to a single device, as these are small in comparison to an estuary or coastal water basin. As a result the principle difference in modelling the near-

field and far-field is the scale. When modelling a turbine blade in a near-field study, such as Mason-Jones et al. (2012), the mesh sizing is of the order of millimetres or less, in order to both represent the geometry and accurately model the flow structure. Conversely, in far-field modelling a mesh size of 100 metres may be considered high resolution, depending on the modelling domain, as shown in Figure 2.16, and for many studies it is not uncommon for the mesh sizing to be of the order of kilometres. The implication of modelling over a much larger scale is the effects of a turbine array are averaged over the plan area of the grid cells that contain the array. This is commonly achieved by the addition of sink terms in both the momentum and continuity equations of the numerical model. These sink terms represent both the thrust imparted on the flow by the turbine, and the drag forces due to the supporting structure etc.

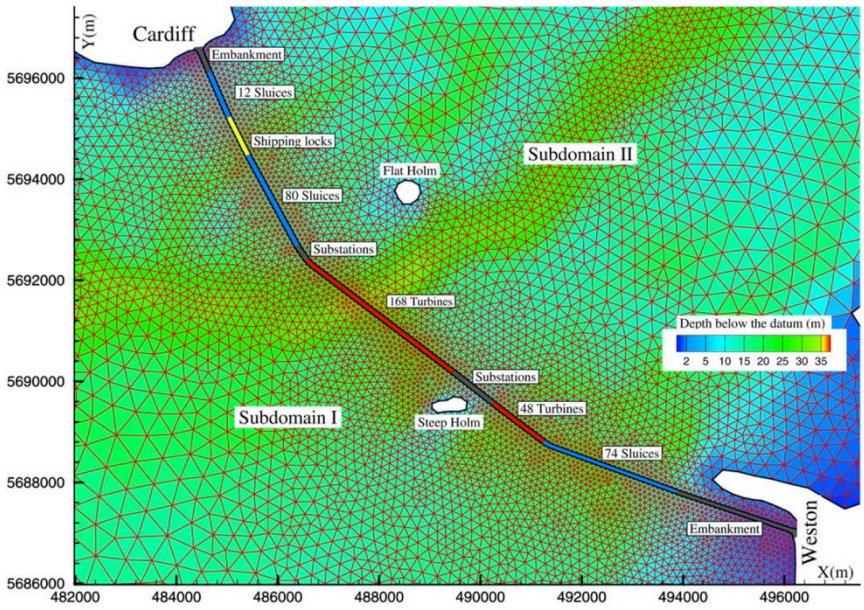

Figure 2.16 Unstructured mesh modelling the Severn Estuary (Xia et al. 2010a)

In far-field modelling, the Reynolds Averaged Navier-Stokes equations can be averaged over the area (1-D), depth (2-D), or vertical layers (3-D) and specifically solve free-surface flows. In tidal waters if the flow is primarily in the horizontal direction then a depth-averaged model can be applied, providing there is no significant vertical velocity or stratification. Depth-averaged models are therefore the most common applied, as they use significantly less computational resources than 3-D models, and have been demonstrated to provide accurate predictions of the tidal current and elevations, providing the body of water is well mixed.

As far-field models solve the governing equations of fluid flow, they can be used in marine energy assessment in a number of ways. Firstly, they can be used to assess the potential tidal stream resource as they provide detailed predictions of the tidal currents and elevations. The UK marine renewable energy resource atlas was compiled using the Proudman Oceanographic Laboratory's High Resolution Continental Shelf (HRCS) model (ABPmer 2008), and studies in academia have also been conducted such as Walkington and Burrows (2009), and Xia et al. (2010c), who investigated the impact of the Severn Barrage on the tidal stream resource. As well as predicting potential resource, the effects of turbine arrays on tidal currents and elevations has been assessed (Chen et al. 2013; Couch and Bryden 2007; Defne et al. 2011; Yates et al. 2013; Plew and Stevens 2013). These observed minimal differences in water levels, however, local velocity fields were affected. As expected, velocities downstream of an array were reduced, however, an increase in the tidal currents adjacent to the arrays were observed, due to the additional flow resistance from the presence of the turbines. If the tidal currents diverge away from the turbines this could have implications to the resource available. Furthermore, changes in the hydrodynamics of the site could lead to morphodynamic changes (Neill et al. 2012; Robins et al. 2012).

This class of numerical model is commonly coupled with a water quality model, and therefore the hydro-environmental changes can be assessed. A wide range of water quality parameter changes can be modelled, including sediment transport, nutrients, dissolved oxygen, and salinity, to name but a few (Kadiri et al. 2012). Both Ahmadian et al. (2012) and Fallon and Nash (2012) modified the numerical model DIVAST (Depth Integrated Velocities And Solute Transport) to investigate the effects of tidal stream arrays in the Severn and Shannon Estuaries, respectively. Ahmadian et al. (2012) found that for a large hypothetical array, distributed over an area of 7.2 km^2, suspended sediment levels were affected significantly within 15 km of the array, with this effect also affecting faecal bacteria levels in the Estuary. In a further study, Ahmadian and Falconer (2012) investigated the shape of an array on the hydro-environmental parameters. Other studies worth noting are: Couch and Bryden (2007), which makes a qualitative assessment of the hydro-environmental impacts, James et al. (2010) which investigates erosion rates around an array as well as other water quality parameters, and Kadiri et al. (2012) conducted a review of the potential water quality impacts of both

tidal stream and tidal range schemes. Finally, Yang et al. (2013) investigated changes in transport processes and flushing characteristics of a tidal channel and bay system.

2.7 Numerical modelling of tidal range schemes

In this section two main types of mathematical modelling are discussed, namely 0-D and CFD modelling which, as described in the previous section, the latter consists of 1-D, 2-D and/or 3-D models that simulate the fluid flow. Tidal range modelling studies are conducted not only to assess barrage design and maximum power output etc., but also to investigate the far-field impacts a barrage or lagoon scheme would have on the hydro-environment.

2.7.1 0-D models

0-D models provide the simplest method of modelling a tidal barrage. They are otherwise known as two-tank or flat-estuary models, and work on the main assumption that volume of water let passed through the barrage raises the basin water level by an amount equal to the volume of water transferred divided by the plan area of the basin (Baker 1991). It is therefore necessary to define a relationship between the plan area of the basin and the depth, which can be achieved from navigational charts or other relevant sources of bathymetric data. A limitation of this model is that it doesn't account for any hydrodynamic processes on either side of the barrage; the downstream water levels are specified by the user as a tidal curve and as a result are unaffected by flows through the barrage. Also, the water levels inside the basin are assumed to rise uniformly, and no tidal currents are predicted.

The flow through the barrage is calculated by using a Hill chart, which is based on an empirical relationship between the head difference, discharge, turbine speed and power generated. With a tidal curve specified, and an appropriate Hill chart selected, depending on the turbine design, the model can be run quickly and a wide range of parameters can be optimised, such as the mode of operation, starting head and the holding period. Other functions can also be modelled, such as pumping, sluicing and two-basin schemes. These models are therefore suitable in the early design stages to compare different designs and operating conditions, however, due to the simplifications

discussed, and depending on the characteristics of the water basin, they can over-predict power output (Baker 1991).

0-D models have been used in a number of research studies (Aggidis and Benzon 2013; Burrows et al. 2009b; Wolf et al. 2009), where these studies have been focused on tidal generation in UK estuaries. Using such a modelling approach Burrows et al. (2009b) identified eight potential sites, including; the Severn, Dee, Mersey, Ribble and Wyre estuaries, Morecambe Bay, the Solway Firth and the Wash.

2.7.2 CFD models

In general, the same coastal models that have previously been discussed to model far-field impacts of tidal stream turbines are also used to model the impacts of a tidal barrage or lagoon on the aquatic environment. The general details of these models are therefore the same, and discussed in 2.6.2. The advantage of using such models is that they address the limitations of 0-D modelling, in that the hydrodynamics is fully resolved. This not only provides a more accurate prediction of power generation, but the near and far-field impacts of a barrage or lagoon can be investigated. This includes, but is not limited to the effects on: water levels, both upstream and downstream of the impoundment, tidal currents, wave propagation, flooding, and water quality indicators - if the model is coupled to an environmental model.

Due to the modelling scale the geometric details of a barrage, turbines and sluices etc. are not usually modelled precisely. Instead a closed boundary condition defines the wall of the barrage, separating the two domains. Source terms are then added to the continuity and momentum equations respectively, to transfer the correct volume of water through the barrage, and ideally momentum is also conserved. Power take-off is then implemented. The power is calculated using equation 2.13, and as referred to in section 2.3.2 the discharge can be calculated using either the orifice equation (equation 2.12), or a more sophisticated method can be adopted, in which a relationship between the head difference, discharge and output power is established, usually through incorporating a Hill chart, or an idealised representation to define the turbine characteristics.

The effects of a tidal barrage in the Severn Estuary have been modelled in a number of studies. Xia et al. (2010b) investigated the hydrodynamic characteristics of three proposed generation schemes, namely: the Severn Barrage, Fleming Lagoon and the Shoots Barrage. As expected the schemes will have a varying impact on the hydro-environment as they differ greatly in size. The Severn Barrage is the largest proposed scheme with a rated capacity of 8.64 GW, and model predictions show a large reduction in the tidal currents for ebb-only generation, and changes in both the maximum and minimum water levels, particularly upstream of the structure. In this study all three barrages were operated for ebb-only generation, however, other studies have considered other operating modes (Xia et al. 2010a) with this having a significant effect on particularly the upstream water levels. Ebb-only generation would result in an increase of between 4-5 m on the minimum water levels upstream of the barrage, permanently flooding large inter-tidal areas, whereas both two-way and flood-generation only partially affect these levels. Ahmadian et al (2010) also studied ebb-only generation for the Severn Barrage, and investigated the hydro-environmental impacts using the 2-D model, DIVAST, and Zhou et al. (2014) investigated the far field impacts using a continental shelf model, as shown in Figure 2.17. Other barrages around the UK have also been modelled, to assess the potential power generation and hydro-environmental impacts (Wolf et al. 2009; Burrows et al. 2009a), and their interaction (Wilson et al. 2012), as well as projects around the world (Bae et al. 2010).

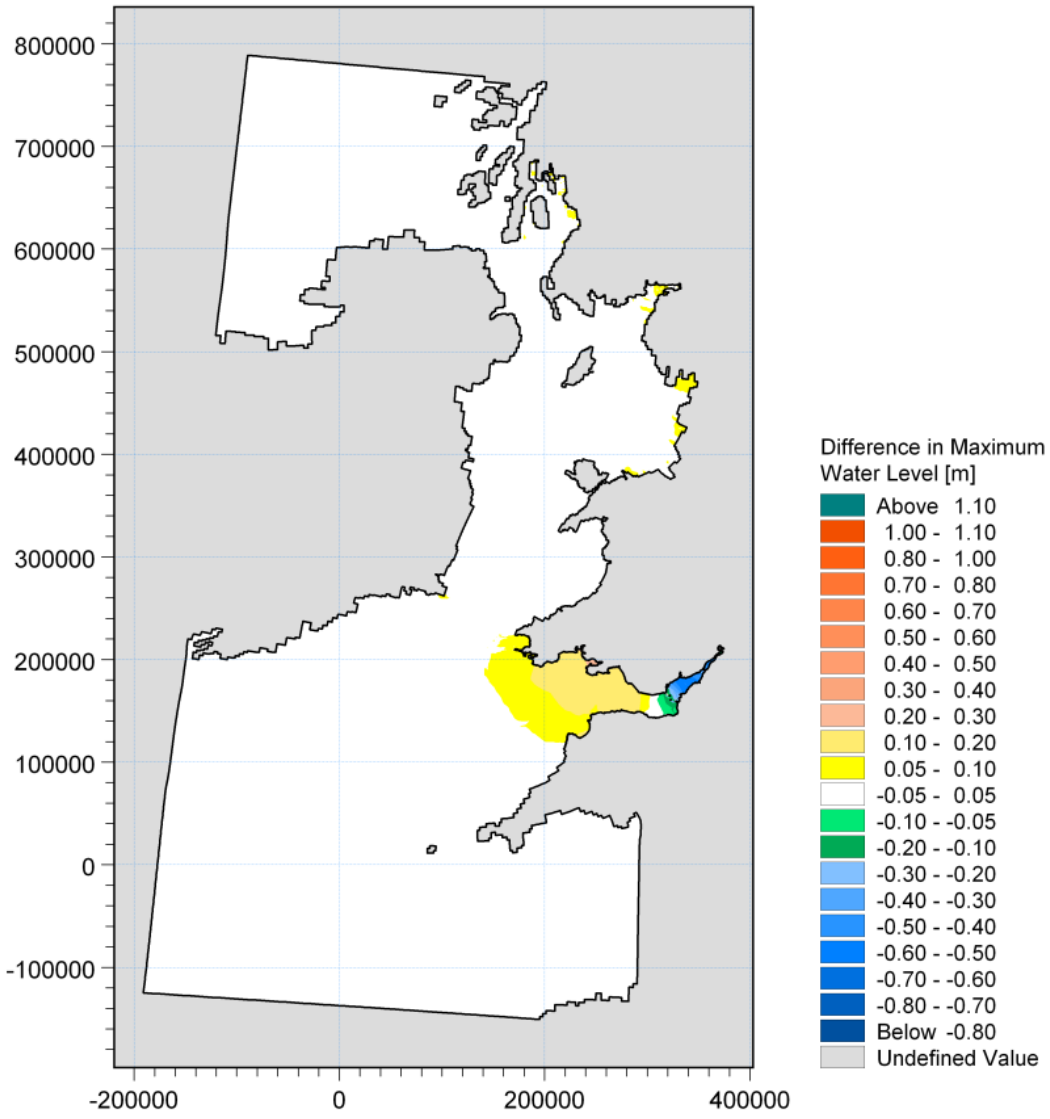

Figure 2.17 Numerical predictions of far-field effects of a Severn Barrage (Zhou et al. 2014)

2.8 The CarBine turbine

The CarBine (Cardiff turBine) concept was founded at Cardiff University, by Dr Alan Kwan. The turbine is a vertical axis design, which is based on the principle of using drag forces to rotate the turbine, unlike most other turbines that rely on lift forces generated by hydrodynamic blade profiles. Without the need of such blade profiles the turbine design is simplified, but the main reason for using drag over lift forces is due to the principle difference between the power in a moving stream of water, and air (i.e. between a tidal stream and a wind stream). Water is approximately 800 times denser than air, and therefore referring to equation 2.3, the power in a stream of water is much more dependant on this fluid density, whereas in a wind stream the power is more

dependant on the wind velocity. Therefore the turbine aims to maximise the increased drag forces that arise due to the higher fluid density. As a vertical axis drag device, the total torque that can be used to drive a generator is the sum of the moments in both the clockwise and anti-clockwise directions. Therefore in order to maximise the efficiency, the turbine is design in such a way that in the desired rotational direction, the drag forces are maximised, and in the alternate direction the 'negative' drag forces are minimised. This principle is shown schematically in Figure 2.18.

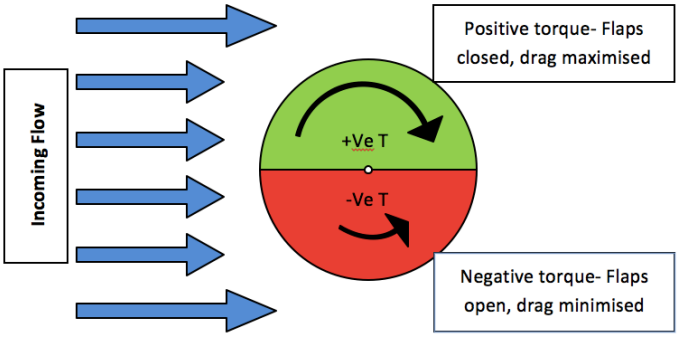

Figure 2.18 Schematic of a vertical axis drag type turbine operation

The CarBine turbine achieves this by using a number of flaps that have restricted degrees of freedom, depending on their local position relative to the turbines angle of rotation. On the 'positive' generating side the flaps are closed, thus maximising the area normal to the flow, and increasing the drag. On the 'negative' side of the turbine the flaps are free to move and align with the oncoming flow, therefore minimising the negative drag. An early design of the CarBine turbine is given in Figure 2.19.

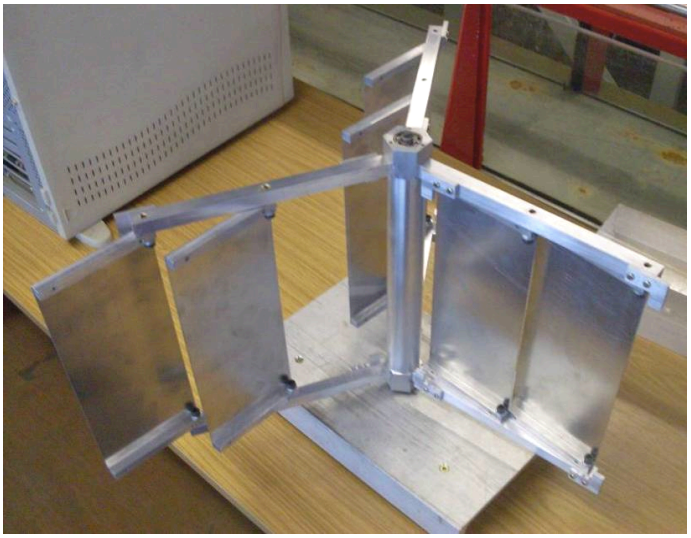

Figure 2.19 An early test model of the CarBine turbine (Challans 2009)

Prior to this thesis, two MSc projects performed an initial assessment of the performance of the CarBine concept, namely Chrysafis (2008), and Challans (2009). The two studies firstly conducted a theoretical analysis to estimate the maximum efficiency of the turbine. This analysis was based on Bernoulli's theory, as detailed in section 2.3.1, and led to a predicted device efficiency of 50.6%. However, both studies made a fundamental error in their calculation of the drag force on the turbine flaps, which is explained below. The drag force acting on a body in a fluid is given as: -

$$D = \frac{1}{2} C_D \rho A v^2 \qquad 2.15$$

where D is the drag force, C_D is the drag coefficient, A is the area normal to the flow, and v is the relative velocity between the fluid and the object (i.e. a function of the tip speed ratio). Therefore if the object is moving at the same speed as the fluid, then the total drag force will be zero. Hence in the case of a vertical axis turbine, at a *TSR* of 1 the total torque will equal zero, and therefore for a drag device it is not possible for the turbine to rotate at higher *TSR*s. Both Chrysafis and Challans took the value of v as the free stream velocity for all turbine speeds, which is only true if the turbine is stationary. This led to a high estimation of the turbine efficiency.

As well as the analytical estimation of performance the MSc studies conducted laboratory tests in the recirculating flume in the Hydro-environmental Research Centre, at Cardiff University. Efforts were made to measure the total torque acting on the turbine, as well the rotational speed in order to calculate the power output of the turbine. As the turbine was a new concept, and given the short time period available to the researchers, relatively crude methods were used to measure the power take-off. This included taking static torque measurements in order to predict the dynamic behaviour of the turbine, as well as measuring the work done by the turbine when lifting a weight using a pulley system. The rotational velocity was measured by counting the number of revolutions over a given time period. A maximum efficiency of 34% was measured by Challans (2009), which, considering the resources available was deemed successful in proving the concept of the CarBine design, and justifies further investigation into the performance of the device.

2.9 Conclusions

The Severn Estuary has the largest single area of tidal range resource in the UK, with estimates in excess of 15 GW, and the largest scheme proposed to extract this energy is the Severn Barrage, which would have a capacity of 8.64 GW and provide 6% of the UK's energy demand. The estuary also has a significant, albeit smaller, tidal stream resource with an estimated 1 GW being available (RPS 2011; PMSS 2010). This capacity is the same order of magnitude of other tidal range schemes with Tidal Lagoon Power's Swansea Bay proposal being 0.24 GW capacity, and the Shoots barrage having a proposed capacity of 1.05 GW.

The tidal stream market is at the early stages of its development. However, designers are favouring horizontal axis turbines, and many standards and conventions are being set based on this type of device. The reason for this is due to the knowledge transfer from the established wind energy market, although it has been argued that vertical axis, or cross-flow turbines are better suited for marine energy (McAdam 2011; Salter and Taylor 2007). It is unsurprising that horizontal axis turbines dominate the wind energy market as they have the highest efficiency in unbounded flows. However, tidal turbines can be subjected to constrained flows, and it has been demonstrated that competitive efficiencies can be achieved through the use of vertical axis turbines; hence there is a need for continued research in this area.

The majority of resource studies estimate the kinetic energy flux, and have not considered this constrained flow approach. Therefore the identified resource and areas suitable for deployment are generally more suited to horizontal axis turbines, however, a number of other sites may exist that are more suited to vertical axis turbines. Furthermore, array spacing, which is key in predicting the energy estimates, is based on requirements of horizontal axis turbines. Vertical axis turbines could be spaced closer together, potentially increasing the output per unit area. Little is known of the wake effects of vertical axis tidal turbines, and therefore this research aims to better understand the wakes of these devices.

The Hafren Power Severn Barrage proposal is for a new two-way barrage design, that uses nearly five times more turbines than the original STPG scheme; thus there is no

sluicing. The hydrodynamic impact will therefore be different to the original barrage and new research is required on the pros and cons of this scheme. Therefore both the STPG and Hafren Power schemes were modelled in this study, to not only assess and compare the initial hydrodynamic impact, but also to study the impact on the available tidal stream resource.

Chapter 3 Physical modelling of tidal stream turbines

This chapter provides details of the experimental setup used to test a number of scale model tidal stream turbines. Firstly, details are given of the recirculating flume used in testing, and the hydraulic parameters used to represent tidal stream flow. Whilst the physical modelling aspect of this research project is built on earlier work from two MSc students, these research projects used relatively crude methods for power take-off, and the existing components and turbine models were deemed unsuitable for testing. Therefore a new power take-off system was designed and implemented. This system is described in section 3.3, and is followed by the testing methods used to characterise the wake of the tested turbines. The design and characteristics of the tested turbines are then given, and the chapter concludes with a summary of the testing schedule. For clarity, the author and another PhD student, who worked on a similar project, designed the power take-off system. Whilst both projects considered the performance of the tested devices, the author then focused on the wake behaviour and far-field aspects of the turbines, whereas the other PhD student focused on near field aspects such as start-up behaviour.

3.1 Recirculating flume

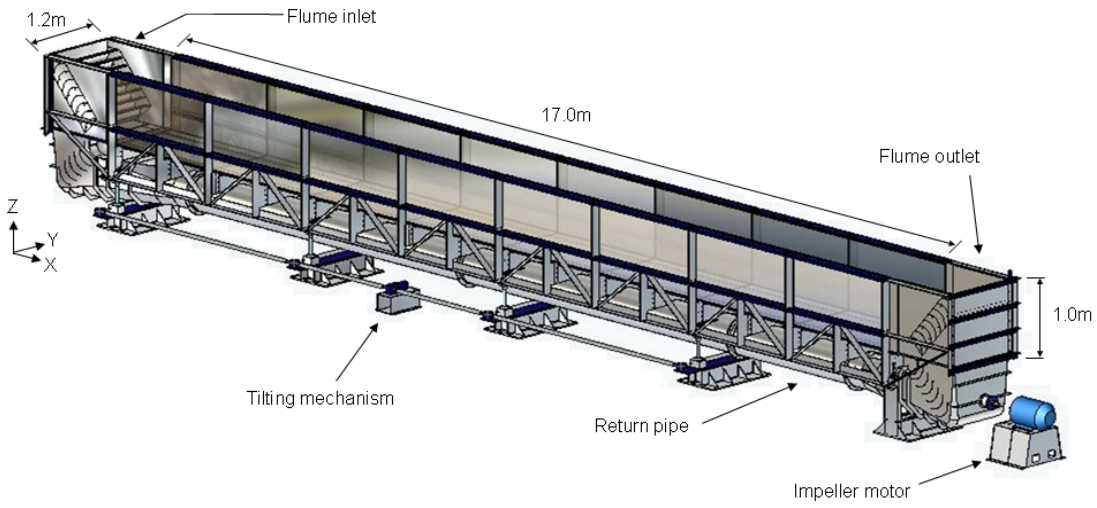

Figure 3.1 Recirculating flume at Cardiff University

All experimental testing was carried out in the recirculating flume in the Hydro-environmental Research Centre, at Cardiff University, as seen in Figure 3.1. This flume has maximum working dimensions of 17 m in length, 1.2 m in width and 1.0 m in depth. A pump regulates the flow in the flume, which is capable of producing flow rates

of up to 1.0 m^3s^{-1}. In addition the flume can be operated bi-directionally, be programmed to run tidal curves if required and has a tilting mechanism to enable a bed slope to be specified. The flume has also been modified to include two instrumentation benches that can traverse the length of the flume, whilst providing access to any relevant equipment. However, these benches do limit the maximum working depth to 0.5 m, and this was the peak depth considered in the study.

3.2Hydraulic parameters

One of the main purposes of the physical modelling tests was to investigate the performance of a new vertical axis turbine design, named CarBine (Cardiff turBine), and draw comparisons with other common designs. As a result the turbine models tested had no definitive scale, per se, and were not intended to represent a full scale device, but rather allow the design concept to be tested and evaluated against existing designs. Therefore, efforts were made to conduct the experiments over a range of realistic Reynolds and Froude numbers, to more generally represent the typical hydraulic conditions that tidal stream turbines are subjected to in the field. The Reynolds (R_e) and Froude (F_r) numbers are defined respectively as:

$$\mathrm{R_e} = \frac{Ul}{\nu} \qquad 3.1$$

$$F_r = \frac{U}{\sqrt{2h}} \qquad 3.2$$

where U is the mean flow velocity, l is a characteristic length, h is the depth of flow and ν is the kinematic viscosity. The choice for the characteristic length depends on the application; in open channel flow it is typically taken as the hydraulic radius, conversely in comparing turbines the blade chord length is generally used.

As identified in the literature review, developers are seeking sites that are typically between 20-40 m in depth, and devices are rated for flow speeds of around 2 ms^{-1}, however, flow speeds can exceed 4 ms^{-1}. This gives a conservative Froude number range of between $0.1 < F_r < 0.3$, with the Reynolds number varying between $10^6 < R_e < 10^8$. Table 3.1 gives the flow conditions used in the recirculating flume, for both the performance and wake characterisation tests. Flow condition [A] provides the closest

representation of a tidal stream device based on a Froude number scaling, however, after preliminary tests it was found that this flow speed was unsuitable for performance testing, as the forces generated by the turbines were too small to provide meaningful data. Therefore this flow condition was used only for the wake characterisation studies. Flow conditions [B]-[E] were therefore established for performance testing, at higher Froude numbers than ideally desired. This was deemed an acceptable compromise in the laboratory, as the main aim of the study was to make relative comparisons between the various turbines tested; therefore the conditions were the same for all models. This also enabled higher Reynolds numbers in the flume, and the velocity range used was comparable with that used in previous studies by other researchers, as discussed in the literature review.

Table 3.1 Hydraulic conditions in recirculating flume

Scale	*Flow condition*	*Flume pump power*	*Depth*	*Mean velocity*	*Froude number*	*Open channel Reynolds number*	*Tests conducted*	
		PP [%]	*h [m]*	*U [ms^{-1}]*	*F_r*	*R_e*	*Performance*	*Wake*
Typical full scale	*n/a*	*n/a*	10	1.5	0.15	1.5x10^7	*n/a*	*n/a*
	n/a	*n/a*	10	3.0	0.30	3.0x10^7	*n/a*	*n/a*
	n/a	*n/a*	25	2.5	0.16	6.3x10^7	*n/a*	*n/a*
	n/a	*n/a*	40	4	0.2	1.6x10^8	*n/a*	*n/a*
Flume	[A]	12.5	0.5	0.37	0.17	1.9x10^5	✗	✓
	[B]	25	0.5	0.78	0.35	3.9x10^5	✓	✗
	[C]	30	0.5	0.84	0.38	4.2x10^5	✓	✗
	[D]	35	0.5	0.98	0.44	4.9x10^5	✓	✗
	[E]	40	0.5	1.09	0.49	5.5x10^5	✓	✗

To measure the water velocity a Nortek Vectrino ADV was used. This samples the 3D water velocity at a single point, at a frequency of 200 Hz. Due to this high sampling frequency turbulence data was also captured. To obtain velocity profiles at different sections along the flume, a point-to-point spacing of 5 cm was used. Each data point was logged for a 120 second period, and processed using the software WinADV. The measured velocities were then averaged using numerical integration to give the mean velocity U (where further subscripts denote direction), and the turbulence intensity, I, was calculated using the following equation:

$$\mathrm{I}\,[\%] = 100 \times \frac{u'}{U} \qquad 3.3$$

where u' is the root-mean-square of the velocity fluctuations, given as:

$$u' = \sqrt{\frac{1}{3}\left(u'^{2}_{x} + u'^{2}_{y} + u'^{2}_{z}\right)} \qquad 3.4$$

Typically hydraulic flumes normally have honeycomb sections installed at the inlet, to be used as a method of controlling the upstream conditions; in particular the honeycomb reduces the level of turbulence by breaking up large eddies. However, due to the high flow rates used in this study it was found that standing waves were created with the honeycomb in place, so it was decided to remove this section. This proved beneficial, as tidal stream sites are highly turbulent by nature and therefore this was also thought to better represent the full-scale conditions, with the measured turbulence intensity levels equalling approximately 10% with the honeycomb in place, compared to 5% without. This technique has previously been adopted by Maganga et al. (2010).

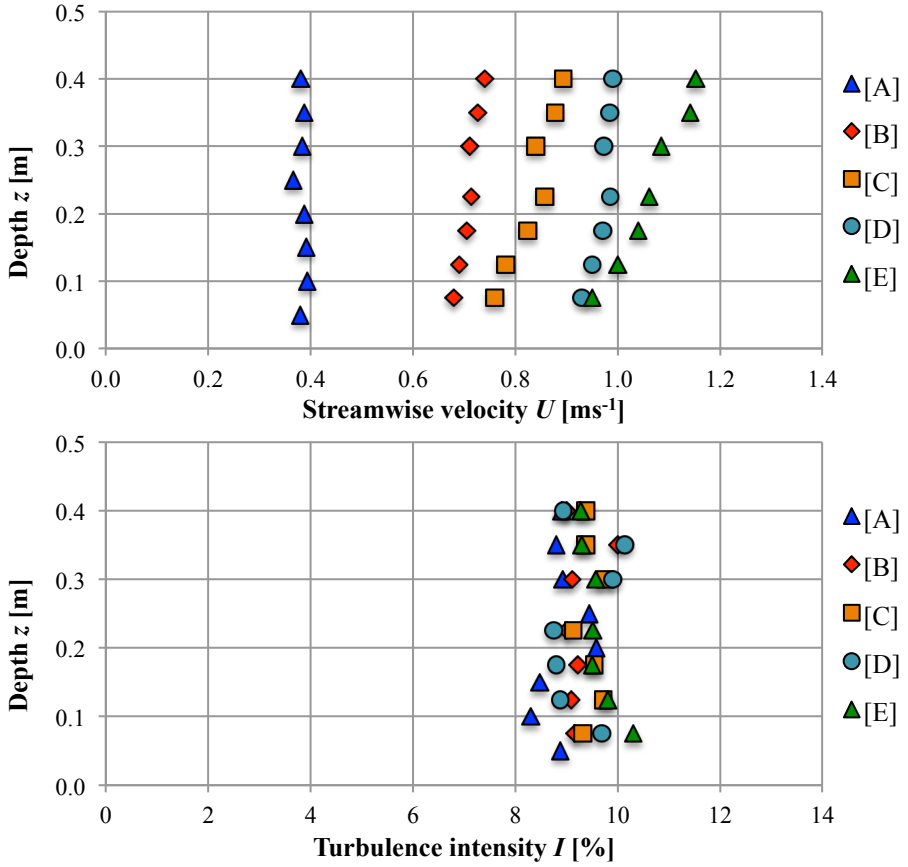

Figure 3.2 Average vertical profiles of: streamwise velocity (Top), and turbulence intensity (Bottom) for flow conditions [A]-[E]

Figure 3.2 shows vertical profiles of the streamwise velocity and turbulence intensity levels in the flume, for flow conditions [A]-[E], and Figure 3.3 shows the corresponding horizontal profiles. The flow conditions follow a logarithmic profile, as expected for turbulent flow in a channel, and as the flow was increased the boundary layer further developed, exaggerating the profile. The horizontal velocity profiles show good symmetry with the centreline of the flume, providing ideal conditions for testing the turbines. However, a slight bias to one side was noted in the turbulence intensity levels, which were between 8-10% throughout the flume; this was attributed to the swirl created by the pump in the delivery pipe. It was decided that this effect was small, and would have a negligible effect on the test results.

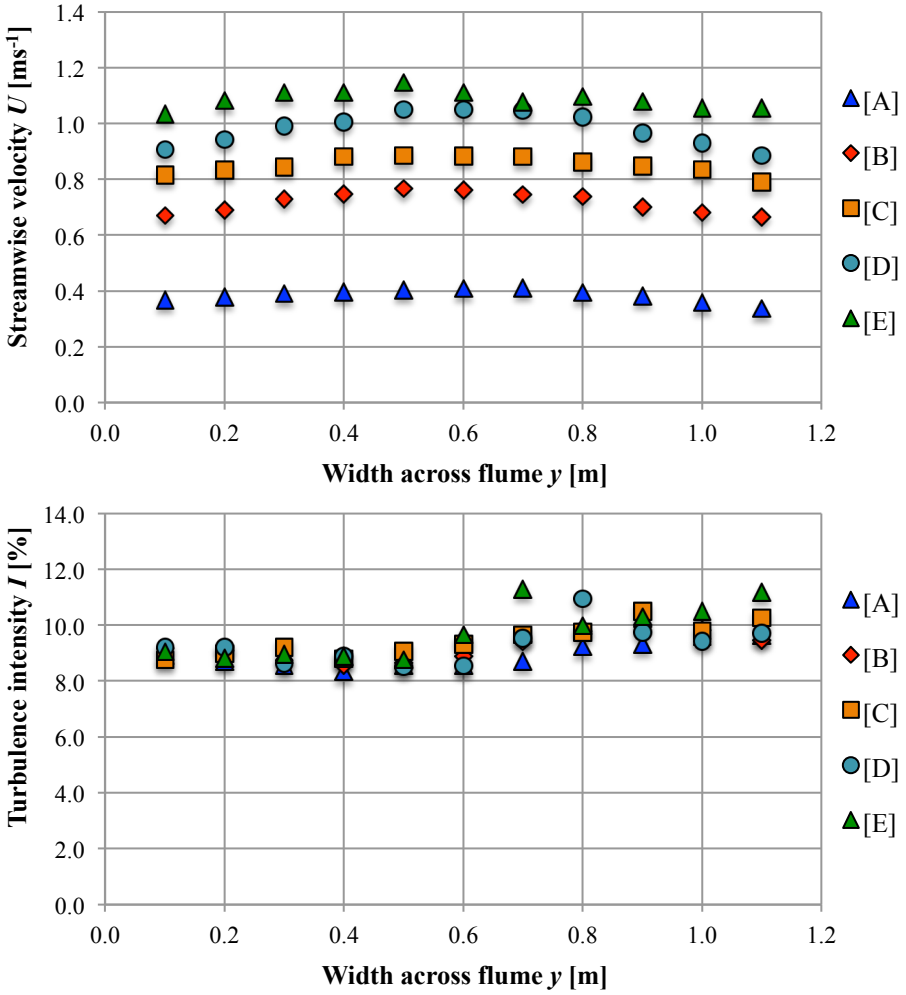

Figure 3.3 Average horizontal profiles of: streamwise velocity (Top), and turbulence intensity (Bottom) for flow conditions [A]-[E]

3.3 Performance testing

The turbine models were located at a distance of 7 m downstream of the flume inlet, allowing the flow to reach a steady condition by the time it reached the turbine, whilst leaving a further 10 m downstream for the wake to fully develop, as shown in Figure 3.4. For the largest turbine tested (i.e. 0.4 m diameter) this equated to a distance of 25 diameters, which was deemed sufficient, as the wake of horizontal axis turbines generally recovers between 10-15 diameters downstream. All of the turbines were located at mid-depth, along the centreline of the flume.

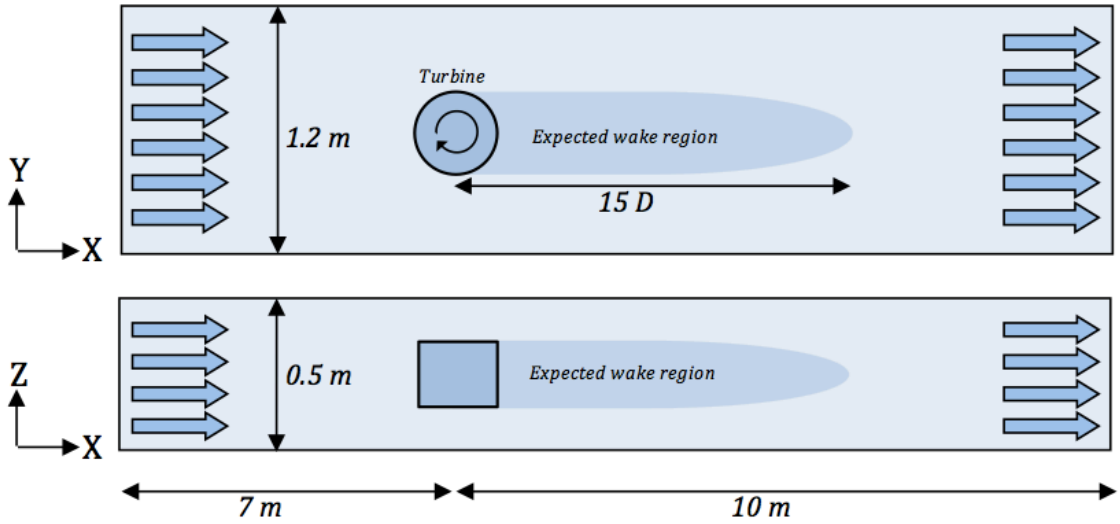

Figure 3.4 Schematic of experimental layout (Top: plan view, Bottom: side view)

3.3.1 Power take-off

Initially, it was proposed to use a generator based power take-off system, to control and measure the output from the turbine. A permanent magnet generator (PMG), manufactured by DVE technologies, was trialled as shown in Figure 3.5, and rheostats were used to vary the generator load. However, the generator had a rated output of 200 V at a speed of 200 rpm, but all of the turbines rotated much slower than this rated speed. Therefore a gearbox would have been necessary, which would have introduced unnecessary mechanical losses. Hence, it was decided to redesign the power take-off system. For completeness, this initial system used a contactless optical tachometer (manufactured by Compact Instruments) to record the angular velocity of the turbine.

The redesigned system made use of a brake dynamometer, as whilst no electricity was generated this allowed for direct measurement of the forces generated. This system is shown in Figure 3.6, and further details of the main components, namely the brake dynamometer [1], a load cell [2], a shaft encoder [3] and the data acquisition system [4], are given below.

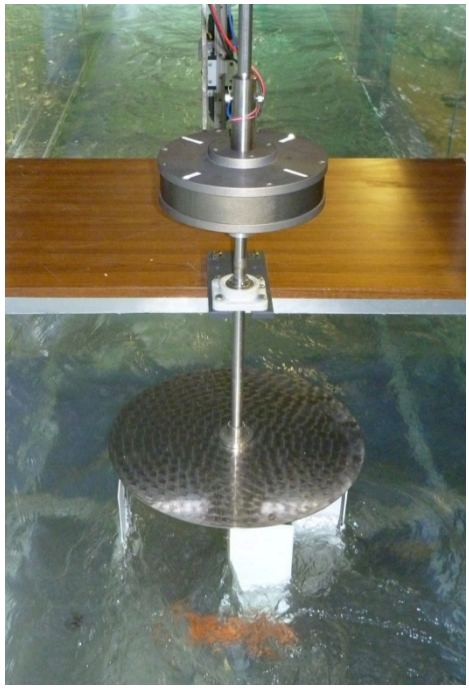

Figure 3.5 Initial power take-off system using PMG

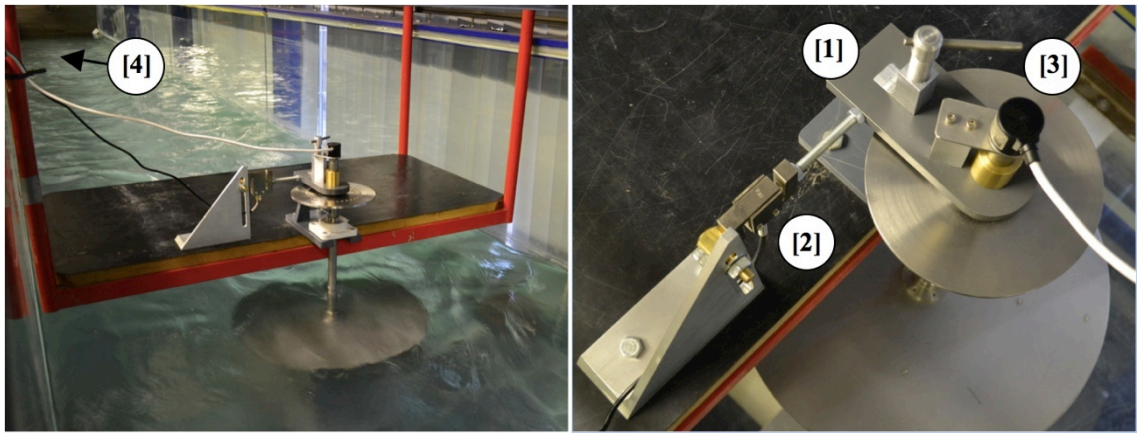

Figure 3.6 Final power take-off system used in experiments

[1] Brake dynamometer

The power take-off point of the turbine was the central shaft, which for the turbines tested protruded above the water surface. This conveniently allowed for a direct connection to the dynamometer, and avoided any unnecessary energy losses. A bespoke

disk brake was designed and manufactured so that a variable amount of friction could be applied, to control the rotational speed of the turbine.

[2] Load cell

The brake dynamometer was connected to the instrumentation bench via a load cell, at a fixed distance from the shaft axis of 10 cm. Hence the corresponding load, depending on the amount of friction applied, could be directly converted into the shaft torque, and logged to a computer. The load cell had a range of up to 500N, and was calibrated before testing to ensure data accuracy.

[3] Shaft encoder

To measure the rotational velocity of the turbines, a shaft encoder was connected directly to the main shaft, and fixed on the same mounting bracket as that connected to the disk brake. A shaft encoder converts the angular position of a shaft into an electrical signal, thereby allowing the angular velocity to be calculated. This was a big advantage compared to using an average value of the angular velocity as it allowed further analysis of the performance, through comparing the 'real time' fluctuations in torque and velocity, relative to the angle of rotation. The encoder had a resolution of 400 counts/rev, i.e. it was accurate to 0.9 degrees.

[4] Data acquisition

The load cell and shaft encoder were connected to a LabJack U6 datalogger, and the live data was streamed to a desktop PC at a frequency of 100Hz, and managed using the Daqfactory software package. This package required the user to build a unique interface to communicate with the components and perform any necessary calibration to the raw data. The data was then logged to separate files, and further analysis could then be completed using normal data processing techniques. Three variables were recorded, namely: the torque, the angular velocity and the angle of rotation, which was recorded relative to a known datum. The Labjack and component connections, and a screenshot of the Daqfactory interface design are shown in Figure 3.7.

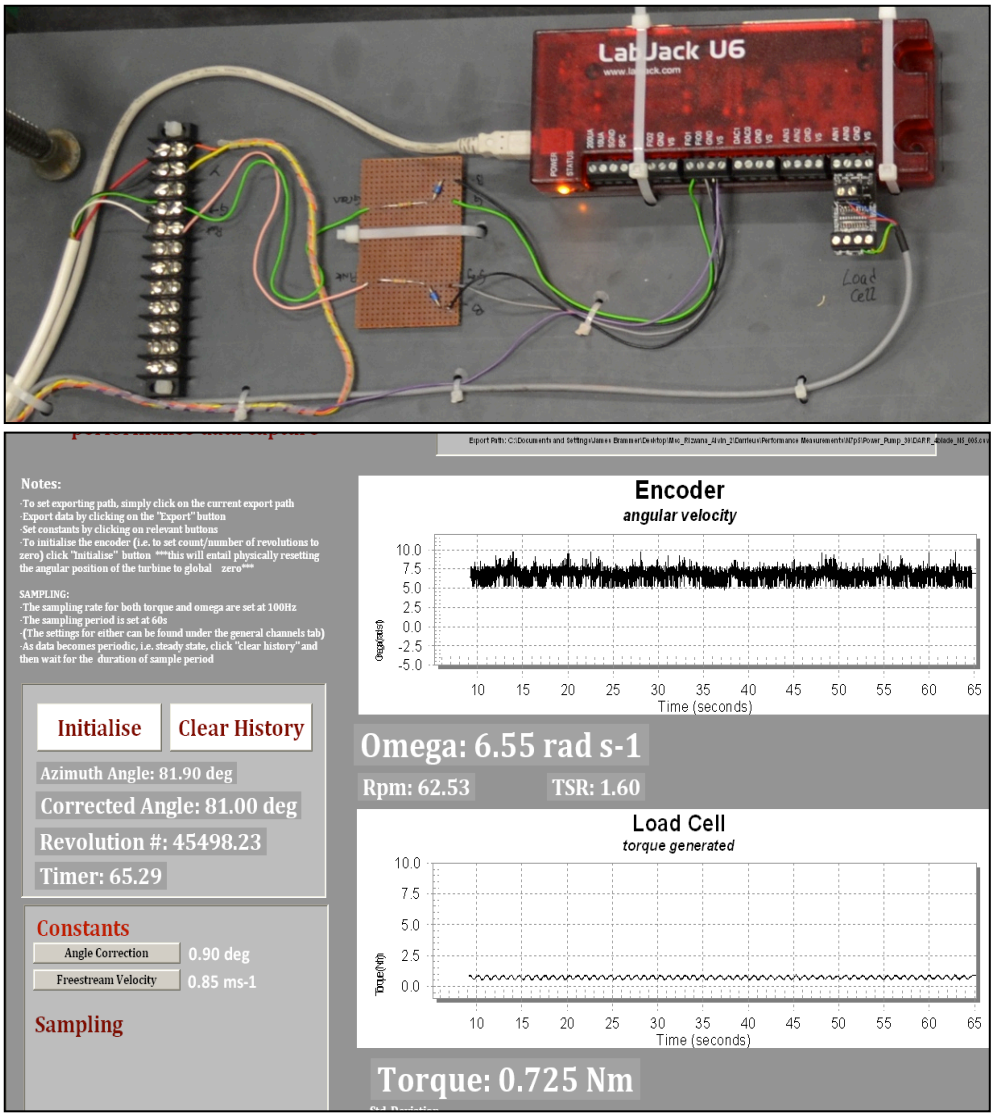

Figure 3.7 (Top) Labjack datalogger with connected components, and (Bottom) Custom Daqfactory interface used for data acquisition

3.3.2 Testing procedure

Figure 3.8 shows a flow chart of the procedure carried out to capture the required data to analyse the performance of any particular turbine. Typically ten points were taken for a given upstream velocity, to ensure that the peak of the power curve was identified. This process was then repeated for each flow condition (i.e. B-E from Table 3.1). The recorded data could then be post-processed using the necessary equations to calculate the *TSR*, power, device efficiency, and any other parameters.

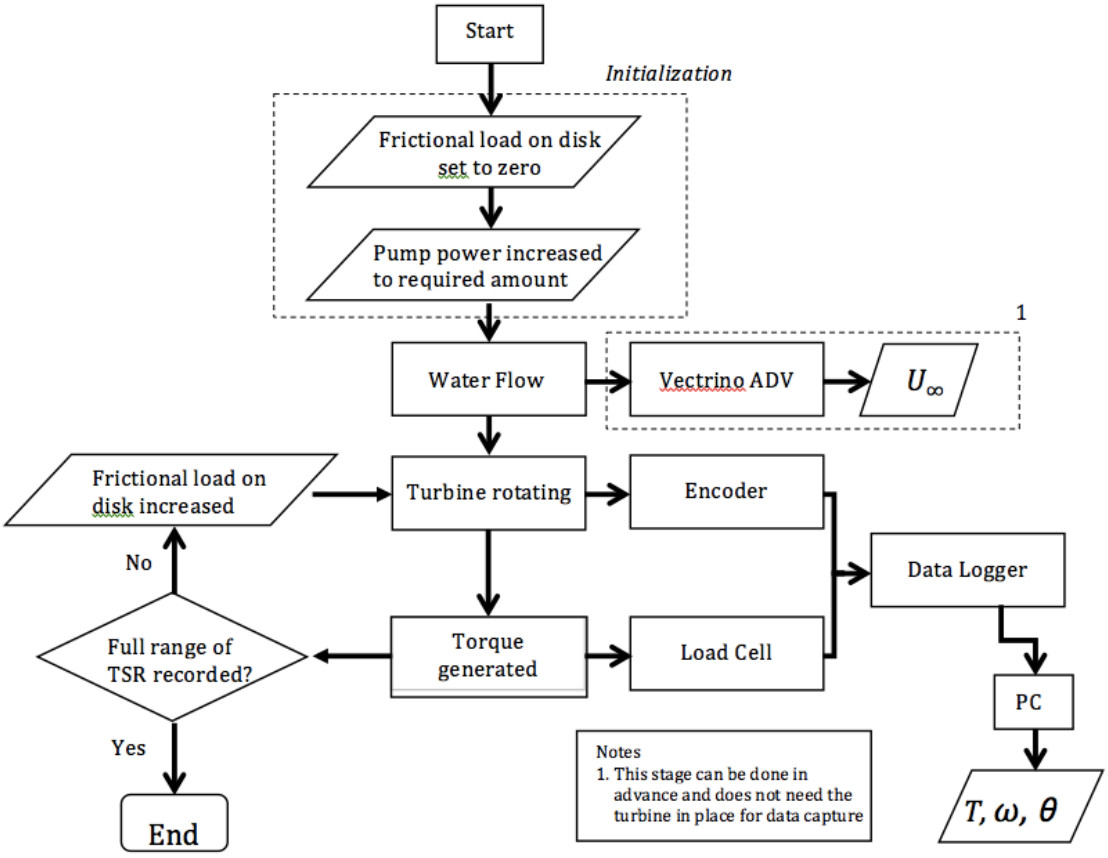

Figure 3.8 Flow chart of performance testing procedure for a single turbine

3.4 Wake characterisation

To characterise the wake of each turbine a number of velocity profiles were measured throughout the flume. For all of the tests the turbine was run at its optimum *TSR*, as identified by the previously undertaken performance tests. For each profile the spacing was 0.05 m and the velocity was recorded for 120s, after sensitivity tests concluded that this was a sufficient length of time. As it was not possible to synchronise this large number of data points using a single Vectrino, the velocity was averaged over time. However, the unsteady behaviour was also examined at specific point locations.

3.4.1 Profile locations

As different turbine sizes were investigated in the wake study, the location of the velocity profiles was normalised by dividing the distance by the relative turbine diameter. For clarity this meant that for a turbine of 0.4 m diameter, a downstream distance of x/D=8 corresponded to a distance downstream of 3.2 m from the turbines axis. This convention only applied to the locations of the profiles and not the spacing

between measurement points, as these were extended to the width and depth of the flume at all times.

Horizontal profiles were recorded at mid depth, at distances of x/D= -3, 0, 1, 2, 4, 8 and 16. At x/D= -3, 1, 4 and 16 three vertical profiles were measured, one along the centreline of the flume (i.e. y/D=0), and two in line with the edges of the turbine (i.e. y/D=±0.5).

Figure 3.9 shows these locations, where each red transect represents a velocity profile in the horizontal or vertical direction. The unsteady velocities were analysed at the points of intersection between the horizontal and vertical transects, i.e. at mid-depth at the same lateral locations of the vertical profiles. In total 245 individual point measurements were taken for each turbine model.

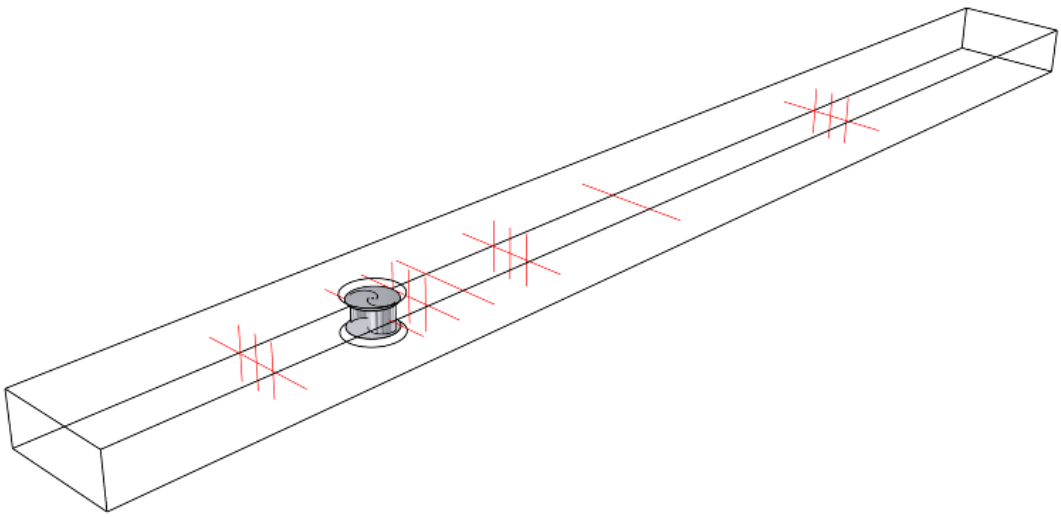

Figure 3.9 Velocity profile locations in recirculating flume

3.5 Turbine design

Three main turbine designs were tested in this study, namely: CarBine, the Savonius turbine and the Darrieus turbine. As the purpose of the research was to make relative comparisons between each design and vary certain geometric parameters, it was decided to design and manufacture the turbines, and all components, in such a way that the turbine configuration could be quickly and easily changed. This led to a 'kit style' design. The basis of this was a central shaft that extended above the water surface for connection to the power take-off system, and two large disks that could be fixed to the

shaft via two removable bosses. A number of holes were drilled into the disks, allowing turbine blades to be fixed at multiple locations. For consistency the diameter and height of all the turbines was the same, with $D = 0.4$ and $H = 0.25$, respectively, but with one exception in that a smaller Savonius rotor was created for the wake characterisation tests to compare a smaller blockage ratio. The standard and small Savonius turbines had a blockage ratio, which is defined as the swept area over the area of flow, of 17% and 4% respectively. All wet components were manufactured from stainless steel. The shaft was connected to the bottom of the flume via a bearing, which was fixed to a support beam that ran across the width of the flume. A second bearing was fixed to the instrumentation bench, restricting the turbine to one degree of freedom, i.e. rotation only.

3.5.1 CarBine

The CarBine models tested by Chrysafis (2008) and Challans (2009) were both of a 3-arm double flap configuration, and the turbine had a diameter of 0.4 m and a height of 0.25 m. These dimensions were kept consistent with the new model, which had the flexibility of being able to test a number of flap configurations. Each flap was 0.1 m in width, and 0.25 m in height. To test single flap configurations, i.e. one flap on each arm, plastic stoppers were manufactured, whereas in double flap configurations the flaps overlapped to ensure that they closed. In the models by Chrysafis (2008) and Challans (2009) the movement of the flaps was restricted to 90 and 180 degrees respectively, whereas in this study no restriction was applied, as the flaps were free to rotate about the connecting shaft between either disk. Figure 3.10 shows a 4-arm double flap CarBine turbine installed in the flume, with further details of the configurations tested and key dimensions being given in section 3.6.

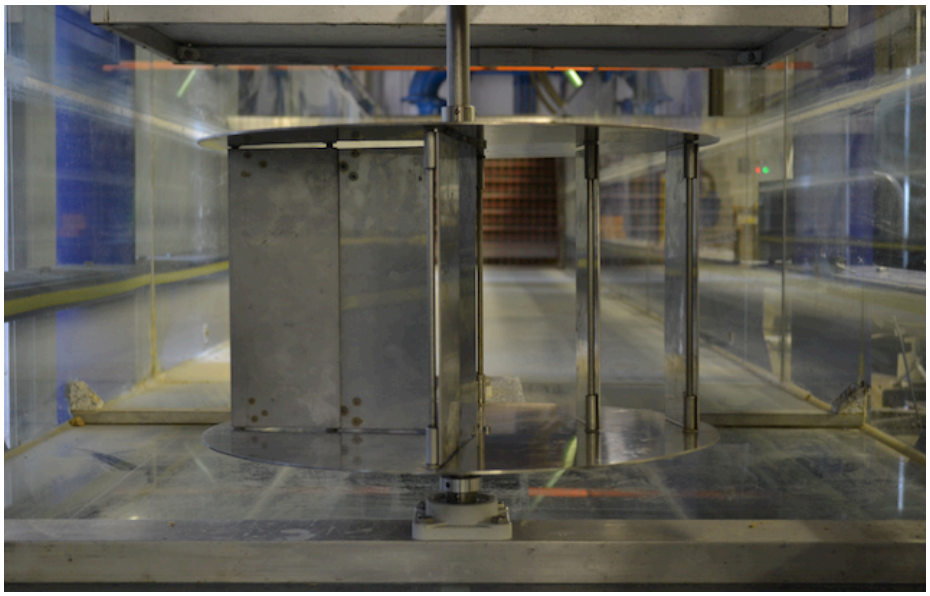

Figure 3.10 CarBine turbine installation

3.5.2 Savonius turbine

The Savonius turbine in its simplest form consists of two buckets arranged about a central axis, as shown in Figure 3.11. However, with this turbine a wide range of parameters can be varied, such as: the number of buckets, the number of stages (or helical design), the overlap ratio, the aspect ratio, the bucket thickness etc. In this study where possible the design has been based on recommendations from previous research (Akwa et al. 2012b), but the aspect ratio was constrained by the dimensions of the flume. Two sizes of the Savonius type turbine were tested in this study; with the values used being summarised in section 3.6.

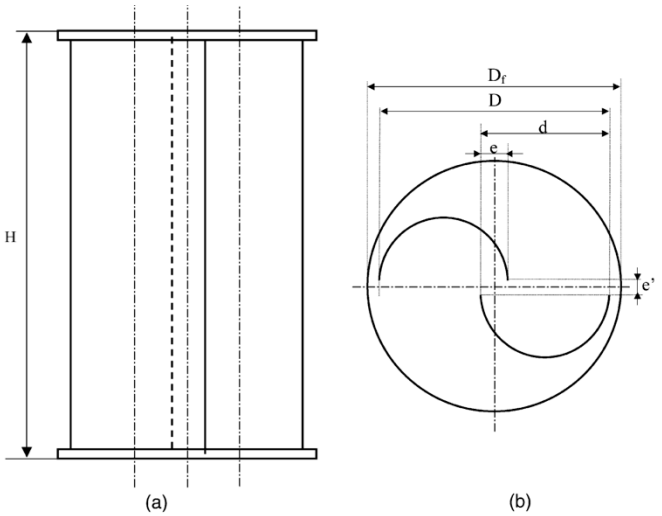

Figure 3.11 Design parameters on the Savonius turbine (a: side view b: plan view) (Menet 2004)

3.5.3 Darrieus turbine

The Darrieus turbine was also studied in the latter stages of this project, and is subject to on-going tests by other researchers at Cardiff University. As for the Savonius turbine, a range of design parameters could be varied for each design. A wide variety of blade profiles could also be used, with the blades being straight, curved (known as an 'egg-beater' Darrieus), or helical. The number of blades could also be varied, as well as the pitch angle. The Darrieus turbine tested in this study used straight blades, cut from PVC using a multiple-axis CNC machine. This model also used new disks, cut from clear Perspex. Due to the presence of the disks this configuration is often referred to as a 'squirrel-cage' Darrieus (Dai et al. 2011), as shown in Figure 3.12. A variety of configurations were tested, with further details being summarized in section 3.6.

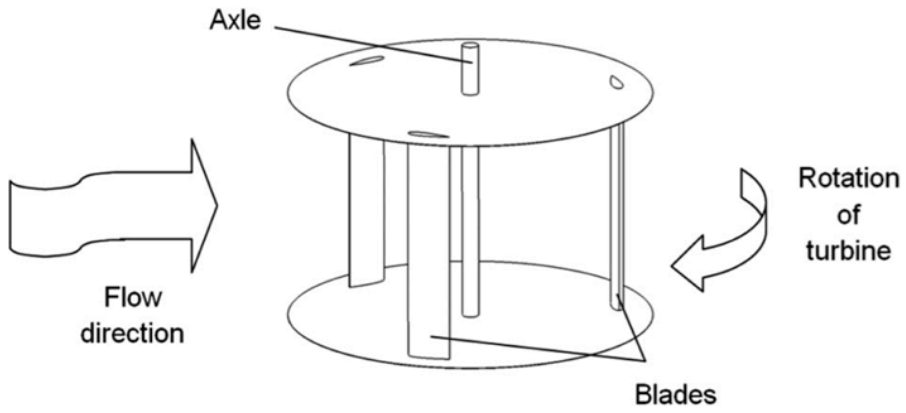

Figure 3.12 A squirrel-cage Darrieus turbine (Dai et al. 2011)

3.6 Testing schedule

A summary of the tested turbine configurations is given below in Table 3.2. In total over 40 separate tests were conducted in the recirculating flume.

Table 3.2 A summary of a turbine tests conducted in recirculating flume

Reference	*Turbine*	*Configuration*	*Tests conducted*		*Flow conditions ran*				
			Performance	*Wake*	*A*	*B*	*C*	*D*	*E*
CB_3S	CarBine	3-arm; single flap	✓	✗	✗	✓	✗	✗	✗
CB_4S	CarBine	4-arm; single flap	✓	✓	✓	✓	✗	✗	✗
CB_5S	CarBine	5-arm; single flap	✓	✗	✗	✓	✗	✗	✗
CB_6S	CarBine	6-arm; single flap	✓	✗	✗	✓	✗	✗	✗
CB_3D	CarBine	3-arm; double flap	✓	✗	✗	✓	✓	✓	✓
CB_4D	CarBine	4-arm; double flap	✓	✓	✓	✓	✓	✓	✓
CB_5D	CarBine	5-arm; double flap	✓	✗	✗	✓	✓	✓	✓
CB_SAVa	CarBine-Savonius	Savonius buckets, two curved flaps mid bucket, flaps closed	✓	✗	✗	✓	✓	✓	✓
CB_SAVb	CarBine-Savonius	Savonius buckets, two curved flaps mid bucket, flaps fully open	✓	✗	✗	✓	✗	✗	✗
CB_SAVc	CarBine-Savonius	Savonius buckets, two curved flaps mid bucket, 10deg flap restriction	✓	✗	✗	✓	✗	✗	✗
SAV_SML	Savonius	H=0.125 m; D=0.2 m; overlap ratio= 15%; 0.01 m shaft	✓	✓	✓	✗	✗	✗	✗
SAV_LRG	Savonius	H=0.25 m; D=0.4 m; overlap ratio= 15%; 0.02 m shaft	✓	✓	✓	✓	✓	✓	✓
DAR_4b_0.0p	Darrieus	NACA 8416 profile; 4-arm; 0 deg pitch	✓	✗	✗	✓	✓	✓	✓
DAR_4b_2.5p	Darrieus	NACA 8416 profile; 4-arm; 2.5 deg pitch	✓	✗	✗	✓	✓	✓	✓
DAR_4b_5.0p	Darrieus	NACA 8416 profile; 4-arm; 5.0 deg pitch	✓	✗	✗	✓	✓	✓	✓
DAR_4b_7.5p	Darrieus	NACA 8416 profile; 4-arm; 7.5 deg pitch	✓	✗	✗	✓	✓	✓	✓
DAR_4b_10.0p	Darrieus	NACA 8416 profile; 4-arm; 10.0 deg pitch	✓	✗	✗	✓	✓	✓	✓

Chapter 4 Recirculating flume tests and results

This chapter provides a summation of the results from the recirculating flume tests, and draws comparisons between the different types of turbines considered where necessary. For full datasets of the tests refer to Appendix A. The Reader is also reminded of the main variables and equations used for processing the data, which are given below:

Free-stream velocity [ms^{-1}]	U_∞	4.1
Turbine radius [m]	r	4.2
Turbine height [m]	H	4.3
Turbine swept area [m^2]	$A_T = 2rH$	4.4
Torque [Nm]	T	4.5
Thrust [N]	F_T	4.6
Angular velocity [rads^{-1}]	ω	4.7
Revolutions per minute [min^{-1}]	$RPM = \frac{2\pi\omega}{60}$	4.8
Power [W]	$P = T\omega$	4.9
Tip Speed Ratio	$TSR = \frac{r\omega}{U_\infty}$	4.10
Power coefficient	$C_P = \frac{2T\omega}{\rho A_T {U_\infty}^3}$	4.11
Torque coefficient	$C_T = \frac{2T}{\rho A_T r {U_\infty}^2}$	4.12
Thrust coefficient	$C_{F_T} = \frac{2F_T}{\rho A_T {U_\infty}^2}$	4.13
Turbulence Intensity	$I = \frac{u'}{U_{avg}}$	4.14

4.1 Performance tests

The following tests assess each of the turbine configurations in their respective ability to convert the kinetic energy of the fluid stream into useful mechanical energy. As described in Chapter 3, the power take-off system used measured this mechanical energy as the product of the total torque acting on the turbine due to the forces on the turbine blades, and the corresponding angular velocity. In practise this mechanical energy would be used to drive a generator, and therefore produce electricity. The reader is reminded of Table 3.1, which describes the hydraulic flow conditions used in the recirculating flume, and Table 3.2, which gives an explanation of the different turbine designs tested.

4.1.1 CarBine

Figure 4.1 shows the maximum power coefficients obtained for each CarBine configuration tested, for flow conditions [B]-[E]. The results show that the CB_4D configuration (i.e. four arms, with two flaps on each arm) yielded the highest efficiency at 19% for flow condition [E], however, its average efficiency was 16%, and the CB_3D and CB_3D+3 configurations produced similar performances. Whilst the lift and drag coefficients of a flat plate are independent of the Reynolds number, both the CB_4D and CB_5D configurations show an increase in respective performance as the flow increased in the flume, whereas the other turbine configurations exhibited independency to the flow condition. This shows that flap interaction occurs, affecting the performance of the turbines. Furthermore, a clear decrease in performance can be seen between the CB_4D and CB_5D turbines, highlighting that an upper limit to the number of flaps exists. Interestingly the CB_6S and CB_3D+3 configurations performed better than the CB_5D, which suggests that it is the inner flaps that result in the detrimental flap interaction.

It is important to not only consider the efficiency of each configuration, but also the individual characteristics that contribute to the efficiency. Figure 4.2 and Figure 4.3 show the average turbine torque and angular velocity respectively, for each turbine configuration at the operating point that yielded the maximum power coefficient.

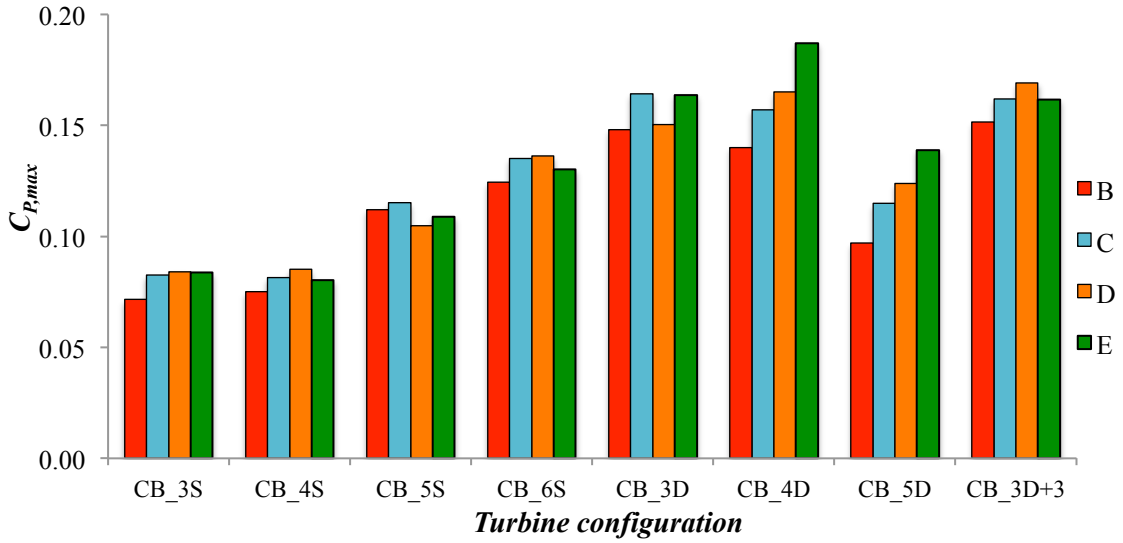

Figure 4.1 Maximum power coefficients obtained for CarBine configurations, for flow conditions [B]-[E]

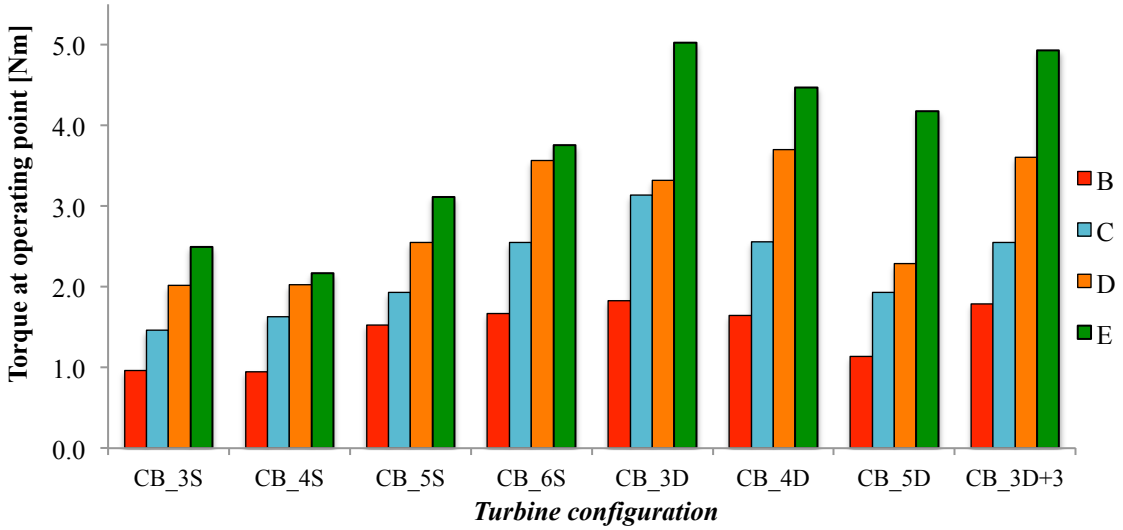

Figure 4.2 Average torque generated at operating condition, for flow conditions [B]-[E]

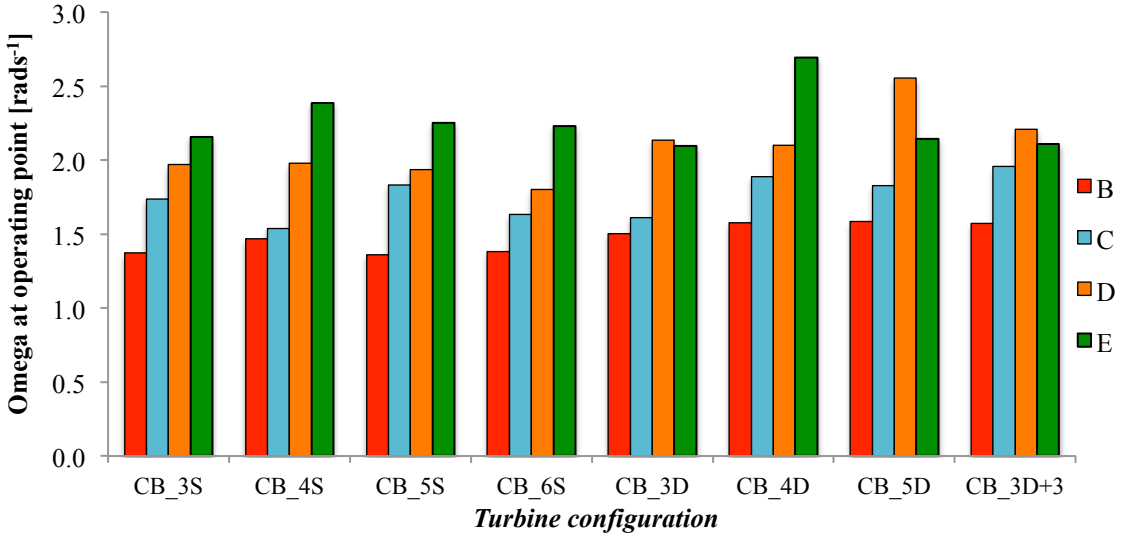

Figure 4.3 Average omega at turbine operating condition, for flow conditions [B]-[E]

The results show a wide variation in the torque and, as expected, the double flap configurations generate larger torque than the single flap configurations, as the flap area is doubled. The effect of flap interaction can also be seen, as increasing the number of arms from three to five results in a reduction of torque for the double flap turbines. The operating speed of the turbines is fairly constant across all the configurations tested; however, small changes in velocity can affect the performance significantly. For example, whilst the CB_4D turbine does not produce the highest torque, the extra arm results in a faster angular velocity than the CB_3D turbine, which leads to an increase in the power output. It is therefore emphasised that the performance of a turbine is a function of both the torque and angular velocity.

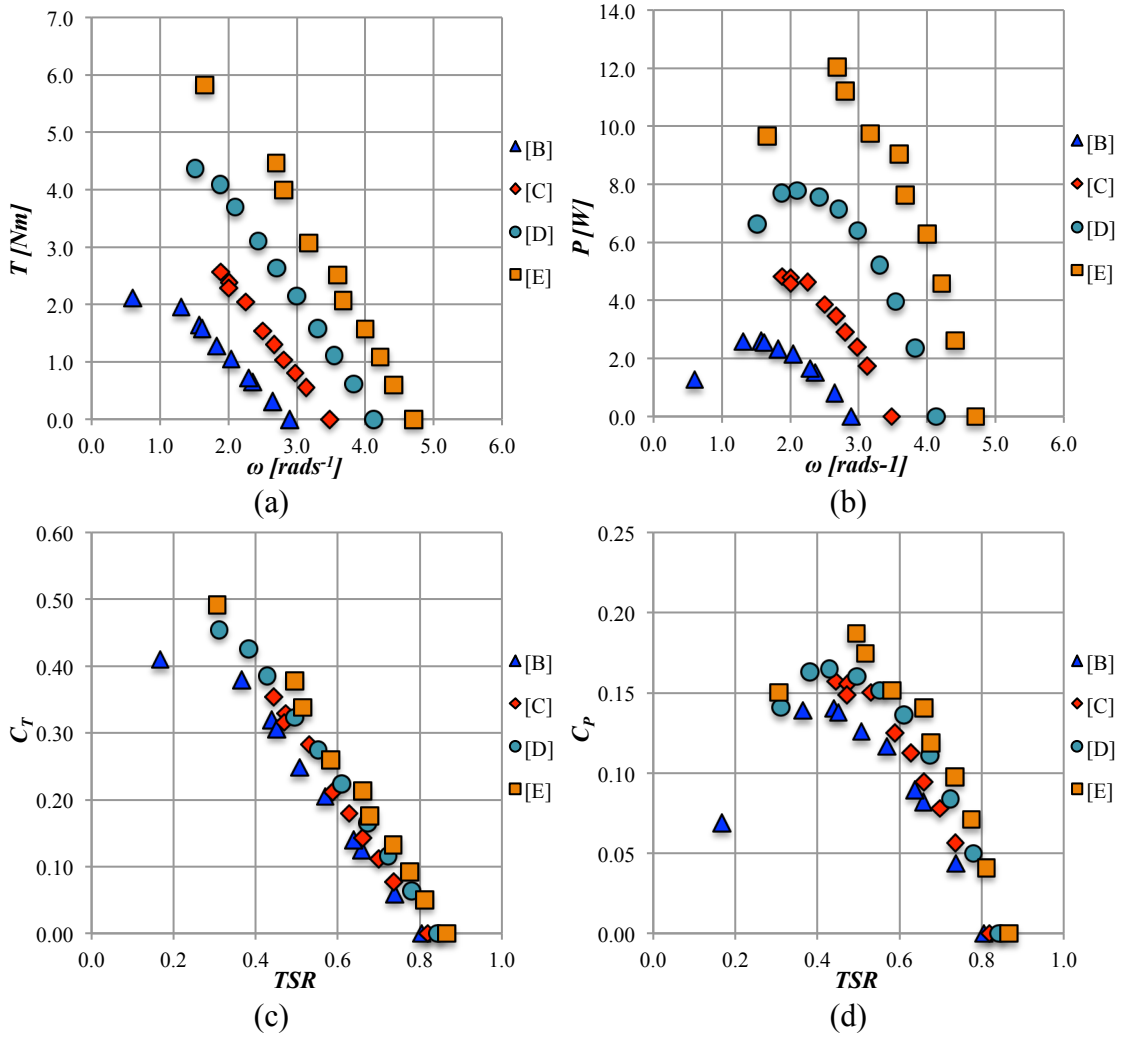

Figure 4.4 Time-averaged performance data for CB_4D turbine configuration, for flow conditions [B]-[E]: (a) Torque versus omega, (b) Power versus omega, (c) C_T versus TSR, and (d) C_P versus TSR

Figure 4.4 shows the time-averaged performance values for the optimum CarBine configuration (CB_4D). Figure 4.4(a) and (b) show the measured values of torque and

power, respectively, against angular velocity. The freewheeling speed (i.e. the maximum angular velocity of the turbine, with no load applied) varied between 3 and 5 $rads^{-1}$, depending on the flow condition. Subsequently, as the load on the turbine increased, the torque increased linearly until the turbine stalled. The corresponding stall torque was between 2 and 6 Nm. For each curve there is a clear peak in output power, with flow condition [E] generating a peak output of 12 W for an operating speed of 2.7 $rads^{-1}$. The data was normalised and represented in Figure 4.4(c) and (d). The freewheeling tip speed ratio varies from 0.8 to 0.9, and for each flow condition the peak coefficient of power was measured between tip speed ratios of 0.4 and 0.5. The dependency of the performance on the flow condition can be seen in these figures, through the range of values of freewheeling speed, and peak performance, especially when compared to a configuration that demonstrated independency to the flow condition, with CB_6S being a good example of this dependency, as shown in Figure 4.5.

The results discussed so far have been time-averaged to give overall performance values, however, it is also necessary to consider the dynamic behaviour of the turbines. Figure 4.6 shows the measured dynamic torque and angular velocity, relative to the angle of rotation, where 0 degrees is in line with the x-axis of the flume (i.e. the streamwise direction). Results are given for the CB_3D, CB_4D and CB_5D configurations respectively. For the three and four arm turbines in particular, large variations in both torque and omega are observed. These variations are in phase with the number of arms, and the peak torque for both turbines occurs at 75 degrees. With five arms these variations are less pronounced, with a near constant torque generated throughout a revolution. These variations result in the turbine pulsing as it rotates, and the dynamic power was clearly subject to variations. This behaviour is undesirable in a turbine, as it causes issues from a power generation perspective, and is a common problem associated with vertical axis turbines. This issue can be alleviated, however, through offsetting a number of stages or, where appropriate, through the use of helical blades.

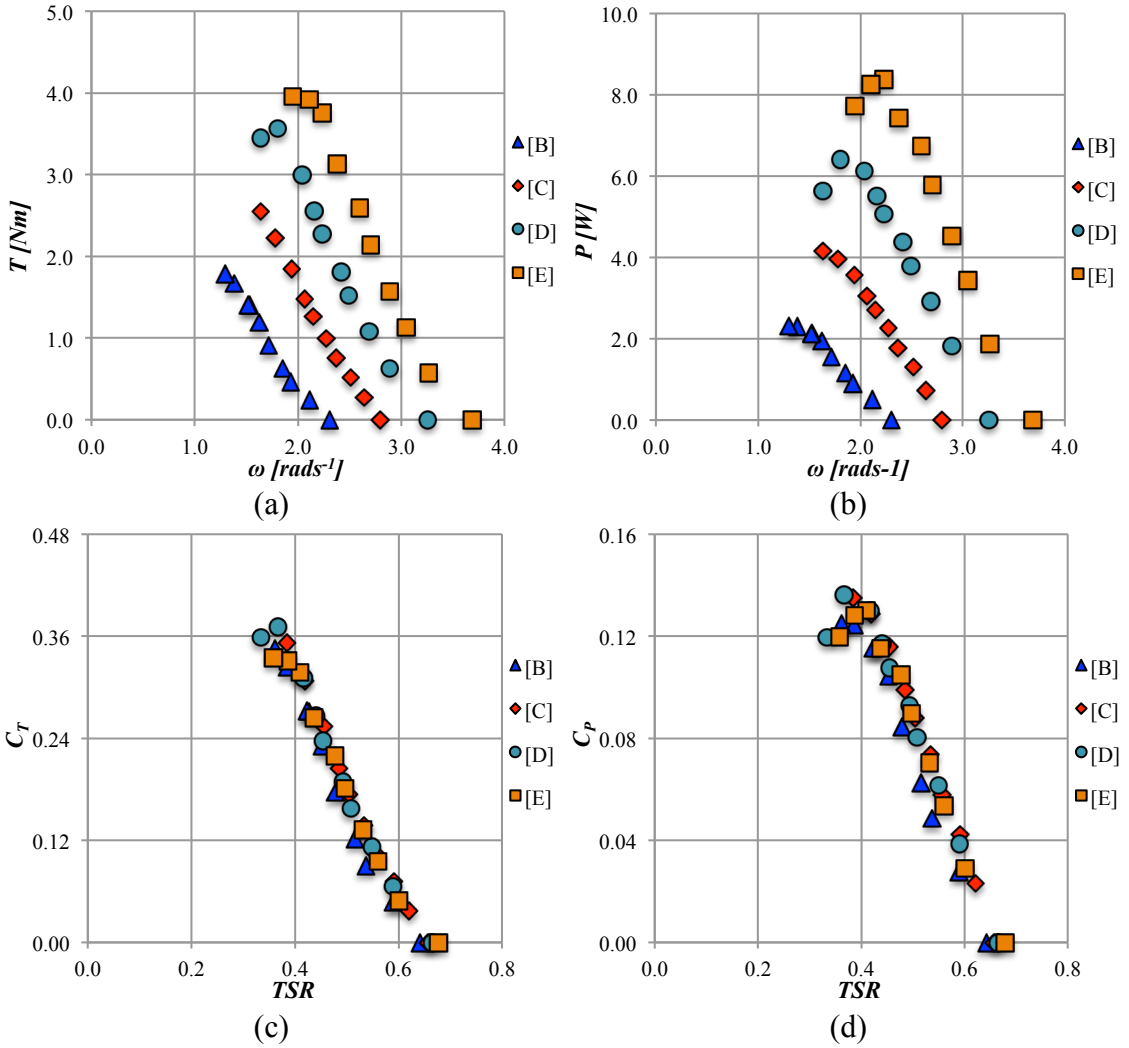

Figure 4.5 Time-averaged performance data for CB_6S turbine configuration, for flow conditions [B]-[E]: (a) Torque versus omega, (b) Power versus omega, (c) C_T versus TSR, and (d) C_P versus TSR

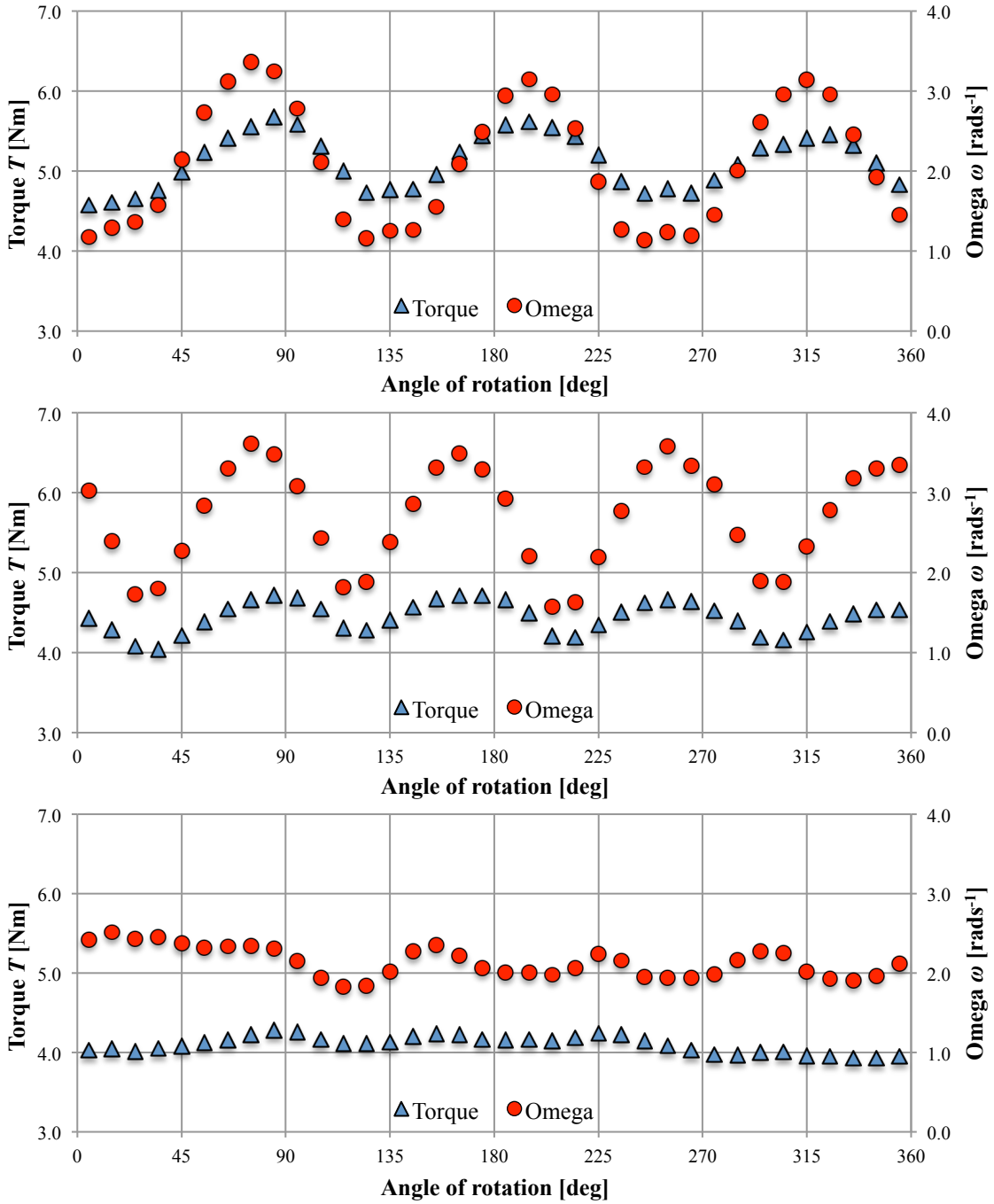

Figure 4.6 Dynamic performance behaviour of various CarBine configurations, for flow condition [E] (Top: CB_3D, middle: CB_4D, bottom: CB_5D)

4.1.2 Savonius

Figure 4.7 shows the relationship between the rotational velocity of the turbine and: (a) the torque applied, and (b) the power generated of the SAV_LRG configuration, for flow conditions [B]-[E]. From freewheeling, of which the speed of the turbine varies between 6.4 and 10.6 rads^{-1}, the torque applied linearly increases until the turbine stalls, in a similar way to the CarBine models tested. The stall velocities varied between 2.6 and 4.1 rads^{-1}, for which the corresponding stall torque was 1.8 and 5 Nm respectively. A peak output of 24 W was generated at an operating speed of 6.4 rads^{-1}.

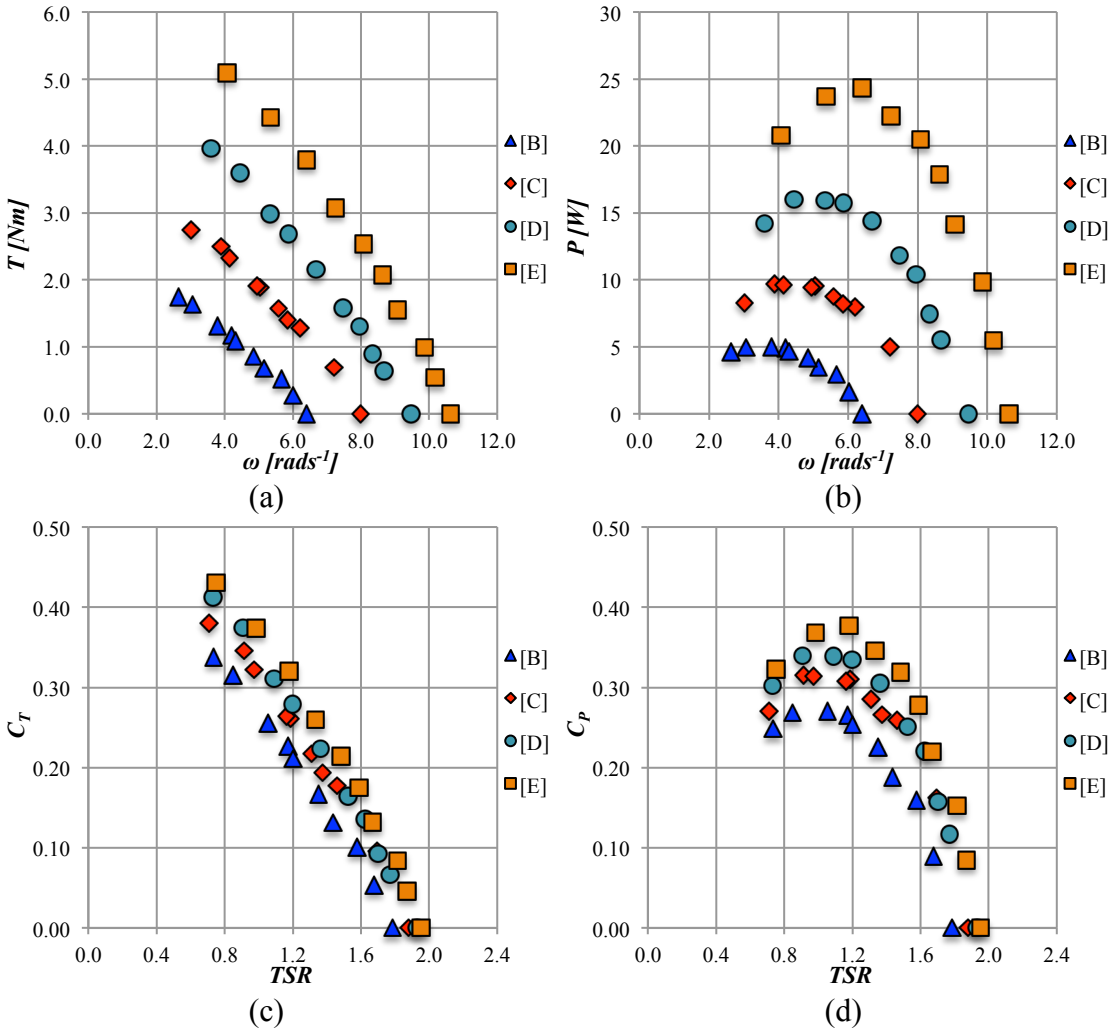

Figure 4.7 Time-averaged performance data for SAV_LRG turbine configuration, for flow conditions [B]-[E]: (a) Torque versus omega, (b) Power versus omega, (c) C_T versus TSR, and (d) C_P versus TSR

Considering the normalised coefficients, the freewheeling tip speed ratio varied between 1.8 and 2.0, and for each flow condition the turbine stalled at a tip speed ratio of 0.7. The peak power coefficient of the turbine varied depending on the flow condition, from

0.26 to 0.37, and at tip speed ratios of between 1.0 and 1.2. These performance were higher than those reported in the previous studies of Savonius turbines, and are due to a combination of factors, including: a high blockage ratio in the flume, at 17%, and increasing Reynolds and Froude numbers. Minimal free-surface effects were observed for flow conditions [B] and [C], but were noticeable for higher Froude numbers. This would have increased the total head available for energy extraction. Furthermore, it is anticipated that the lift and drag coefficients of the Savonius buckets would be sensitive to the Reynolds number. A significant point to make is that it is a common misconception that the Savonius turbine is only a drag device, that is to say that the torque generated is a result of the drag forces alone. For this to be true the turbine would not be able to rotate above a *TSR* of 1, as the turbine would be rotating faster than the free stream flow velocity. Therefore these results show that lift forces contribute to the torque of the Savonius turbine.

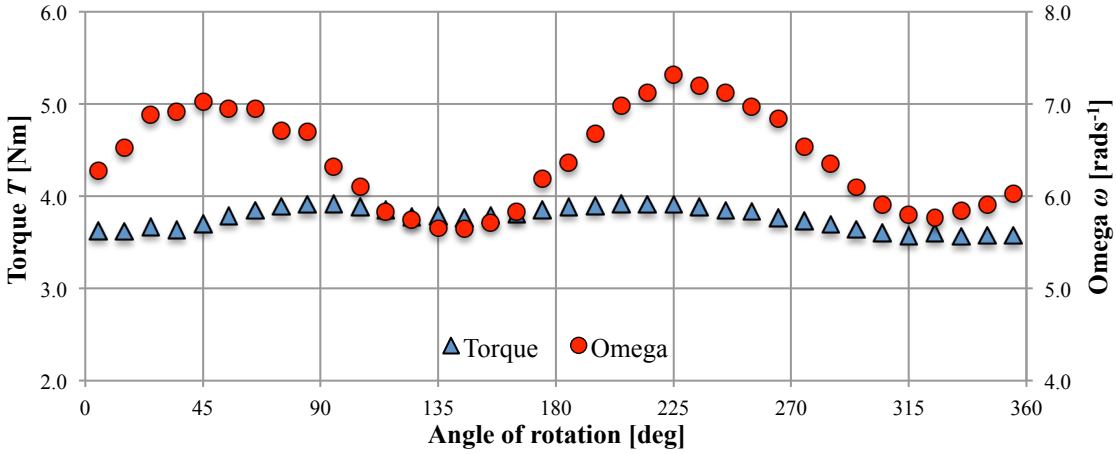

Figure 4.8 Dynamic performance data of SAV_LRG turbine configuration, for flow condition [E]

The dynamic data for the SAV_LRG turbine, at flow condition [E], is given in Figure 4.8. Like the CarBine turbines, this also experienced a pulsing velocity, and a variation in the torque as the turbine completed each revolution. As expected the frequency of the variations is in phase with the two buckets of the turbine. The data shows that compared to the CB_4D configuration, at the peak operating condition the torque of the Savonius is less, however, the turbine rotates over two times faster, and it is this high angular velocity that attributes to the superior performance. This is primarily due to the difference in drag forces: A bucket that is open to the flow will have a much higher drag than a flat plate, additionally, whilst the flaps of the CarBine models open to reduce

negative drag, the curved surface of the Savonius buckets has been demonstrated to generate lift forces, thus contributing to the total torque, rather than reducing it.

4.1.3 CarBine-Savonius

Flat plates were chosen as the original flaps for the CarBine turbines, not only to build on the prototypes inherited from the previous work undertaken by the MSc projects, but also because their design simplicity made their manufacture fast and cost effective, and thereby enabling a larger number of configurations to be tested. This in turn provided a reliable baseline dataset, which could then be built on in future research. Based on the encouraging performance results from the Savonius turbine tests, it was proposed that through combining the Savonius buckets with the flap principal of CarBine, the negative drag could be further reduced; this led to the CB_SAV configuration. Figure 4.9 shows the design of this configuration, and due to time constraints only three variations of this design were tested: a) where the flaps were locked shut, in which the turbine was effectively the original SAV_LRG model, b) where the flaps were allowed to open freely, and c) where the flaps were restricted to a movement of 10 degrees.

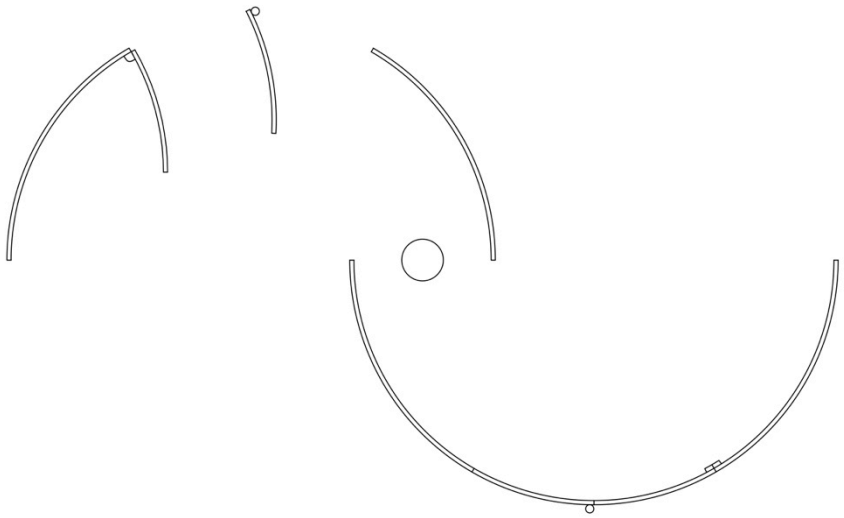

Figure 4.9 Design of CB_SAV configuration

Unfortunately this particular test was unsuccessful in improving the performance of the turbines. Figure 4.10 compares the non-dimensionalised performance of the original SAV_LRG turbine (left), and the CB_SAVa configuration (right). The reader is reminded that as the flaps were locked shut in the CB_SAVa configuration, the same

performance results should be observed. However, it can clearly be seen that the second turbine does not perform as well as the original Savonius model, with the freewheeling *TSR* reducing from 1.9 to 1.7, and the peak power coefficient reducing from a range of 0.25-0.4, to 0.18-0.25.

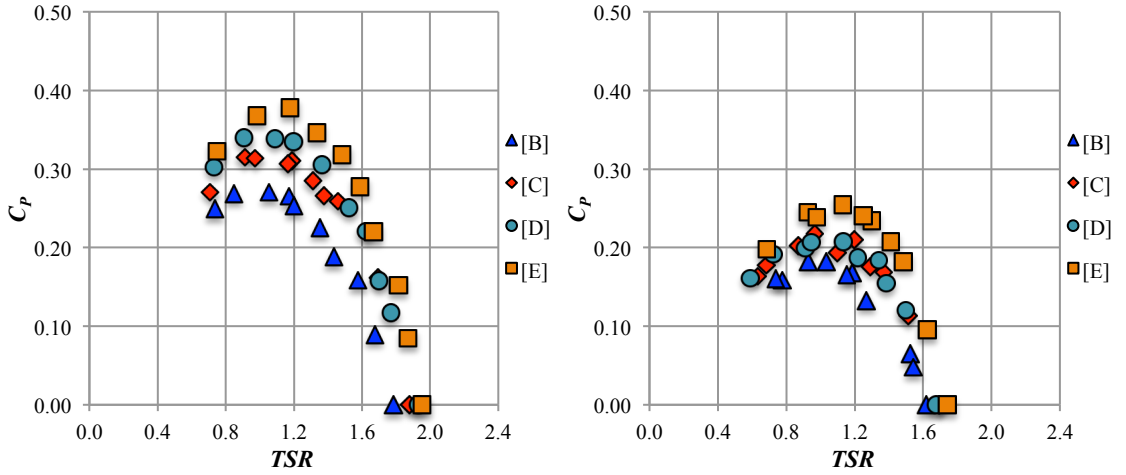

Figure 4.10 Comparison of power coefficients for SAV_LRG (left) and CB_SAVa (right) configurations, for flow conditions [B]-[E]

As the flaps were locked shut in this configuration the only geometric differences between these turbines was the supporting bars that allowed the flaps to pivot. One of these bars was on the outside edge of the buckets, which therefore disrupted the flow field as the bucket was rotating against the flow. The separation induced by the bar would have increased the negative drag force, and reduced the generated lift forces, resulting in slower rotational speeds and reduced turbine performance. Due to time constraints in the laboratory it was not possible to attempt to rectify this issue, and hence only two further configurations were tested. Figure 4.11 shows the performance curves of all three CB_SAV configurations, as well as the CB_4D and SAV_LRG turbines, for flow condition [B]. It can be seen that the location of the flaps (i.e. the central third of each bucket) further reduced the turbine's performance. It was observed in testing that the buckets closed at approximately 45 degrees into a revolution, therefore dramatically reducing the available torque. Furthermore, the flaps 'slammed' shut during rotation, and this action was deemed to be detrimental to the performance and have implications for the structural integrity of the device.

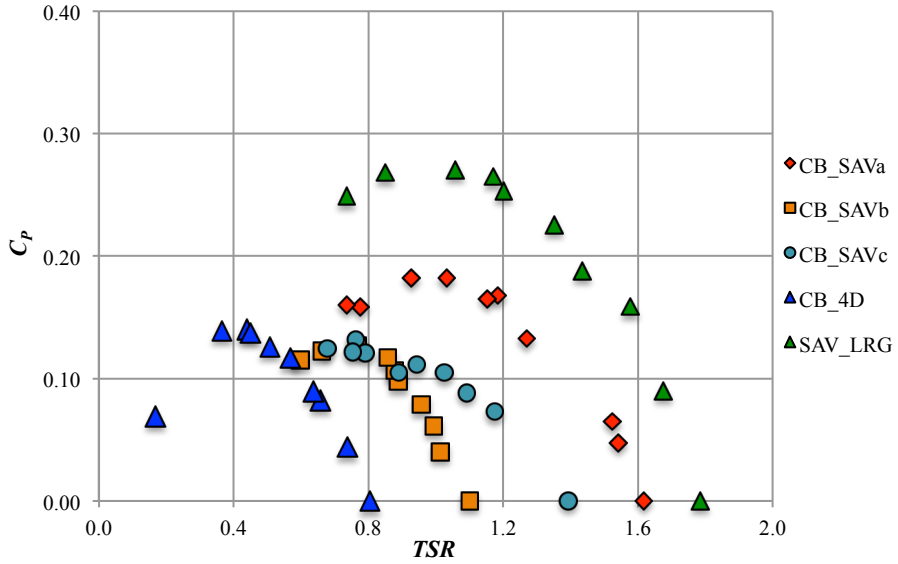

Figure 4.11 Performance curves of modified CarBine and Savonius turbines, for flow condition [B]

Whilst this test can be considered unsuccessful, the concept of merging the CarBine and Savonius designs together still shows potential, and further refinement to the design of such a concept is needed in future studies to investigate whether or not a viable solution exists, and if performance can be improved further. In particular the operating speeds of the CB_SAV configurations are significantly quicker than the CarBine turbines, and as the *TSR* was above 1.0 at a number of operating points, lift forces were still generated throughout a revolution, albeit not as effectively as for the original Savonius turbine. Therefore, it is possible to introduce flaps as a mechanism to reduce drag, whilst still generating lift forces.

4.1.4 Darrieus

As previously discussed the Darrieus turbine is the subject of on-going testing at Cardiff University by a number of researchers, and in the current study only one turbine design has been tested, to provide a baseline dataset for future research. The turbine was a straight-bladed four-arm configuration, using a NACA 8416 airfoil, and the blades were tested for a number of pitch angles. Figure 4.12 shows the relationship between the maximum efficiency obtained and the respective pitch angle, and it can be seen from the data that a pitch angle of 5 degrees proved to be the optimum angle.

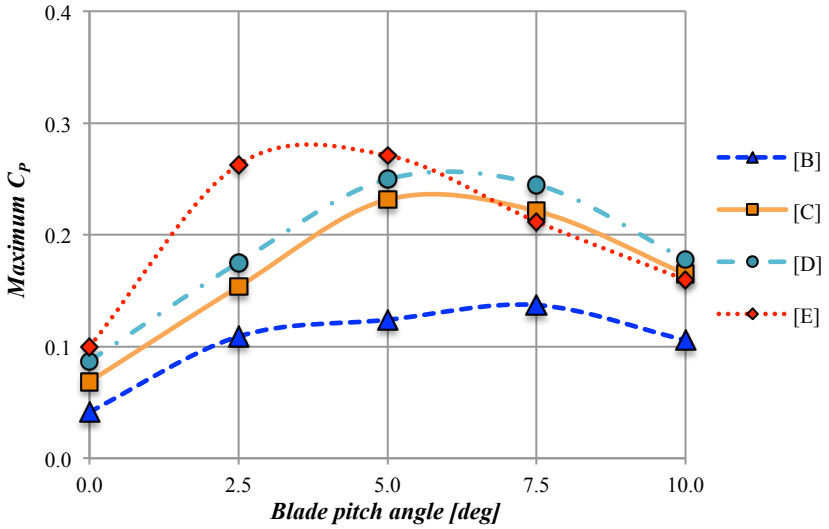

Figure 4.12 Maximum power coefficient versus pitch angle for Darrieus turbine

From Figure 4.12 and following further examination of the performance data collected the results indicate that at a pitch angle of 5 degrees the turbine stalled very close to the peak operating condition, which is obviously undesirable in the operation of a turbine. However, with a 2.5 degree pitch angle a clear peak in the performance was defined before the turbine stalled; this behaviour is shown in Figure 4.13. For the pitch angles tested the turbines freewheeled at a *TSR* of approximately 2.0, and the peak efficiency was obtained between *TSR*s of 1.3-1.6. A peak power of 17 W was measured at the highest flow condition. As well as the pitch angle, the performance data shows a high dependency to the flow conditions, with the lift and drag characteristics being shown to be sensitive to the Reynolds number.

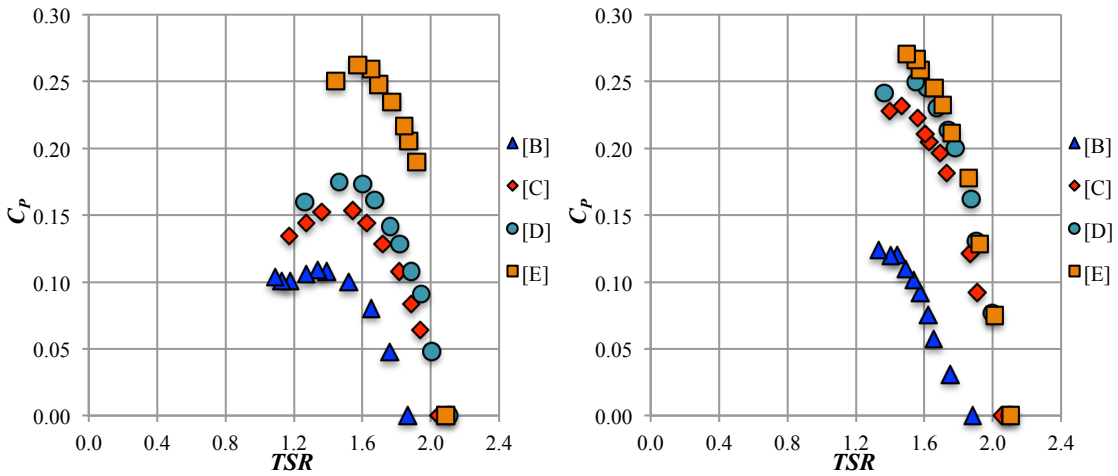

Figure 4.13 Performance curves of tested Darrieus turbine for: (left) 2.5 deg pitch angle (right) 5.0 deg pitch angle

Furthermore, as the Darrieus turbine operates at high speeds, and lower torques, the turbine was likely to be more sensitive to frictional losses in the power take-off system, compared to the higher torque CarBine and Savonius turbines. The dynamic torque and angular velocity of the Darrieus turbine with a 5-degree pitch angle is given in Figure 4.14. From these results it can be seen that both the torque and omega are relatively constant, as the four arms provide a much smoother rotation than for the other turbines tested. Overall the performance data bears similarity with experiments of a Darrieus turbine of a similar solidity, conducted by Shiono et al. (2000), in that the freewheeling *TSR* was 2.0, with peak efficiencies of the order of 25%.

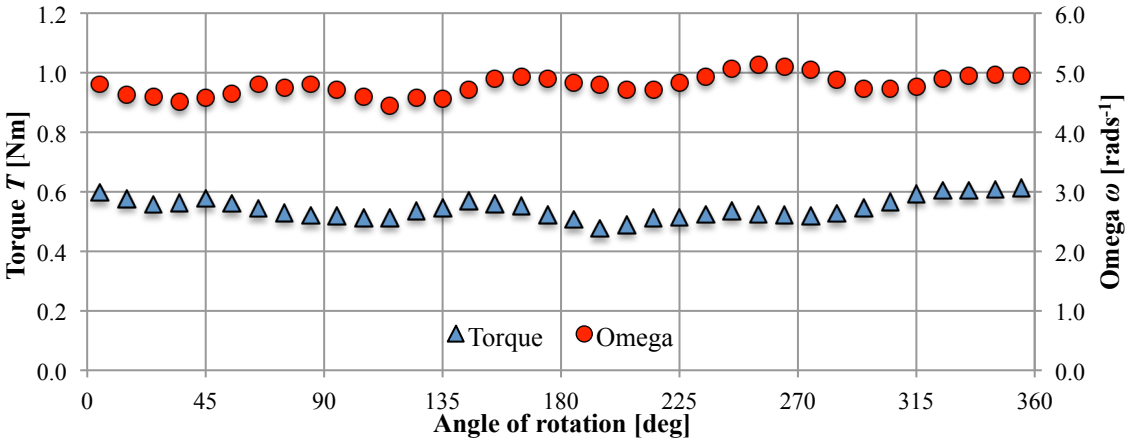

Figure 4.14 Dynamic performance data of DAR_4b_5.0p turbine for flow condition [B]

4.1.5 Summary of performance tests

A summary of the time-averaged performance data for all of the turbine configurations tested is given in Table 4.1, and for two of the four flow conditions used for testing, namely [B] and [E]. The Savonius turbine was the best performing turbine, with a peak power coefficient of 0.38 measured at a tip speed ratio of 1.2.

Table 4.1 Summary of performance tests (Bold indicates best performing configuration)

Turbine	*Configuration*	*Flow con.*	*ω [rads^{-1}]*	*T_{ave} [Nm]*	*P [W]*	*TSR*	*C_P*	*C_T*
CarBine	CB_3S	[B]	1.37	0.97	1.3	0.38	0.07	0.19
		[E]	2.16	2.50	5.4	0.40	0.08	0.21
	CB_4S	[B]	1.47	0.95	1.4	0.41	0.08	0.18
		[E]	2.39	2.17	5.2	0.44	0.08	0.18
	CB_5S	[B]	1.36	1.52	2.1	0.38	0.11	0.30
		[E]	2.25	3.12	7.0	0.41	0.11	0.26
	CB_6S	[B]	1.38	1.67	2.3	0.39	0.12	0.32
		[E]	2.23	3.76	8.4	0.41	0.13	0.32
	CB_3D	[B]	1.50	1.82	2.7	0.42	0.15	0.35
		[E]	2.10	5.03	10.5	0.39	0.16	0.42
	CB_4D	**[B]**	**1.58**	**1.64**	**2.6**	**0.44**	**0.14**	**0.32**
		[E]	**2.69**	**4.47**	**12.0**	**0.49**	**0.19**	**0.38**
	CB_5D	[B]	1.58	1.13	1.8	0.44	0.10	0.22
		[E]	2.14	4.17	8.9	0.39	0.14	0.35
	CB_3D+3	[B]	1.57	1.78	2.8	0.44	0.15	0.35
		[E]	2.11	4.93	10.4	0.39	0.16	0.42
Savonius	**SAV_LRG**	**[B]**	**3.79**	**1.32**	**5.0**	**1.06**	**0.27**	**0.26**
		[E]	**6.41**	**3.79**	**24.3**	**1.18**	**0.38**	**0.32**
CarBine-Savonius	**CB_SAVa**	**[B]**	**3.33**	**1.01**	**3.4**	**0.93**	**0.18**	**0.20**
		[E]	**6.14**	**2.67**	**16.4**	**1.13**	**0.25**	**0.23**
	CB_SAVb	[B]	2.75	0.85	2.3	0.77	0.13	0.16
		[E]	*Data not collected*					
	CB_SAVc	[B]	2.74	0.89	2.4	0.76	0.13	0.17
		[E]	*Data not collected*					
Darrieus	DAR_4b_0.0p	[B]	3.67	0.21	0.8	1.02	0.04	0.04
		[E]	8.56	0.75	6.4	1.57	0.10	0.06
	DAR_4b_2.5p	[B]	4.81	0.42	2.0	1.34	0.11	0.08
		[E]	8.54	1.98	16.9	1.57	0.26	0.17
	DAR_4b_5.0p	**[B]**	**4.78**	**0.48**	**2.3**	**1.33**	**0.12**	**0.09**
		[E]	**8.15**	**2.14**	**17.4**	**1.50**	**0.27**	**0.18**
	DAR_4b_7.5p	[B]	4.70	0.54	2.5	1.31	0.14	0.10
		[E]	7.75	1.76	13.6	1.42	0.21	0.15
	DAR_4b_10.0p	[B]	5.15	0.38	2.0	1.43	0.11	0.07
		[E]	8.03	1.28	10.3	1.48	0.16	0.11

The turbines tested were all subjected to blockage effects from the flume walls, however, corrections to the data to quantify for this effect have not been made mainly for two reasons. Firstly, the blockage effect depends on not only the blockage ratio, which is defined as the ratio of the swept area of the turbine to the cross-sectional area of flow, but also a number of design characteristics such as: the number of arms, the number of blades, the turbine solidity, etc. Therefore a Savonius turbine, which has a high solidity due to the overlapping buckets, will block the flow significantly more than a CarBine turbine, in which the flaps opened to provide less resistance to the flow,

despite both turbines having an equivalent swept area. The common methods that currently exist for blockage corrections are derived from actuator disc theory and, as such, are more appropriate for horizontal axis turbines. Comparatively there has been little research to quantify the effects for vertical axis devices (Ross and Altman 2011), and it was therefore deemed appropriate not to apply any corrections. Secondly, as identified in the literature review, blockage effects could be used advantageously to enhance performance, particularly in shallow waters. The blockage ratio used in testing was 0.17, and this can be considered modest compared to the study by McAdam et al. (2013), in which the blockage ratios were as high as 0.63. Based on this review it can be assumed that higher efficiencies could be obtained when blockage effects are considered, however further research is required in this area.

A surprising outcome from the tests is that the Savonius turbine outperformed the Darrieus, by a significant margin. The solidity of the Savonius was higher than the Darrieus (0.59 compared to 0.32) and therefore would benefit more from blockage effects. However, these turbines were both considered to have high solidities, and therefore the lower performance of the Darrieus was attributed to the fact that: a) the configuration tested was an initial base-case model, and therefore was not optimised for performance, and b) the Darrieus was more susceptible to frictional losses as it is typically operated as a high-speed-low-torque rotor. Another key point to consider is that the Froude number range in testing was higher than would be expected, therefore a greater proportion of the total head was available as kinetic energy, although the efficiency was represented as the proportion of velocity head extracted only, to be consistent with the majority of studies previously conducted. Finally, the Reynolds numbers in the flume were lower than those expected in field conditions, therefore one would expect improved performance from the Savonius and Darrieus turbines, as the resistive drag forces would reduce with an increase in the Reynolds number.

4.2 Wake characterisation

The section provides the key data from wake characterisation tests of the following turbine configurations: CB_4S, CB_4D, SAV_SML and SAV_LRG. For each of the configurations tested the turbines were operated at their respective optimum tip speed ratios, as identified from the performance tests. For the CarBine turbines this was 0.5,

and for the two Savonius turbines this was 1.0. As with the performance data obtained, full datasets for each test can be found in Appendix A.

4.2.1 CB_4S

The time series data of the CB_4S configuration is given in Figure 4.15. The top two graphs give an indication of the unsteady and asymmetrical behaviour of the flow, as these point measurements were located 1 diameter downstream of the turbine, and behind the tip of the advancing and returning arms respectively ($y/D = \pm 0.5$). As the closed flap opens the flow separates, and a clear period (at $y/D = 0.5$) is visible. This occurs every 1.65s, which corresponds to a quarter of a revolution. Behind the open flaps (at $y/D = -0.5$) there is little disturbance to the flow field as it is the intention of the flap to align with the flow, to minimise drag. As expected, the streamwise velocities (x-direction) dominate the flow, with significant transverse components of velocity measured in the vicinity of the opening flaps. Peak velocities in the flume were approximately 0.4 ms^{-1}, indicating little flow acceleration. Further downstream, at x/D = 4 and 16, the flow returns to a fairly steady state, with turbulence levels decreasing as the wake continues to mix.

Figure 4.16 shows the time-averaged vertical profiles of velocity magnitude (top), and turbulence intensity (bottom) respectively, at increasing distances downstream of the turbine. The results further highlight the asymmetrical nature of the wake, and as one would expect, a larger reduction in the average velocities was observed behind the closed flap (at y/D = 0.5). Furthermore, a peak turbulence intensity of 40% was measured at this location. The centreline profiles also showed a reduction in velocity, as the movement of the flap, together with the shaft and base, influenced the flow. By 4 diameters downstream the flow profiles had mostly recovered to the upstream conditions, and the turbulence intensity levels were below 10%.

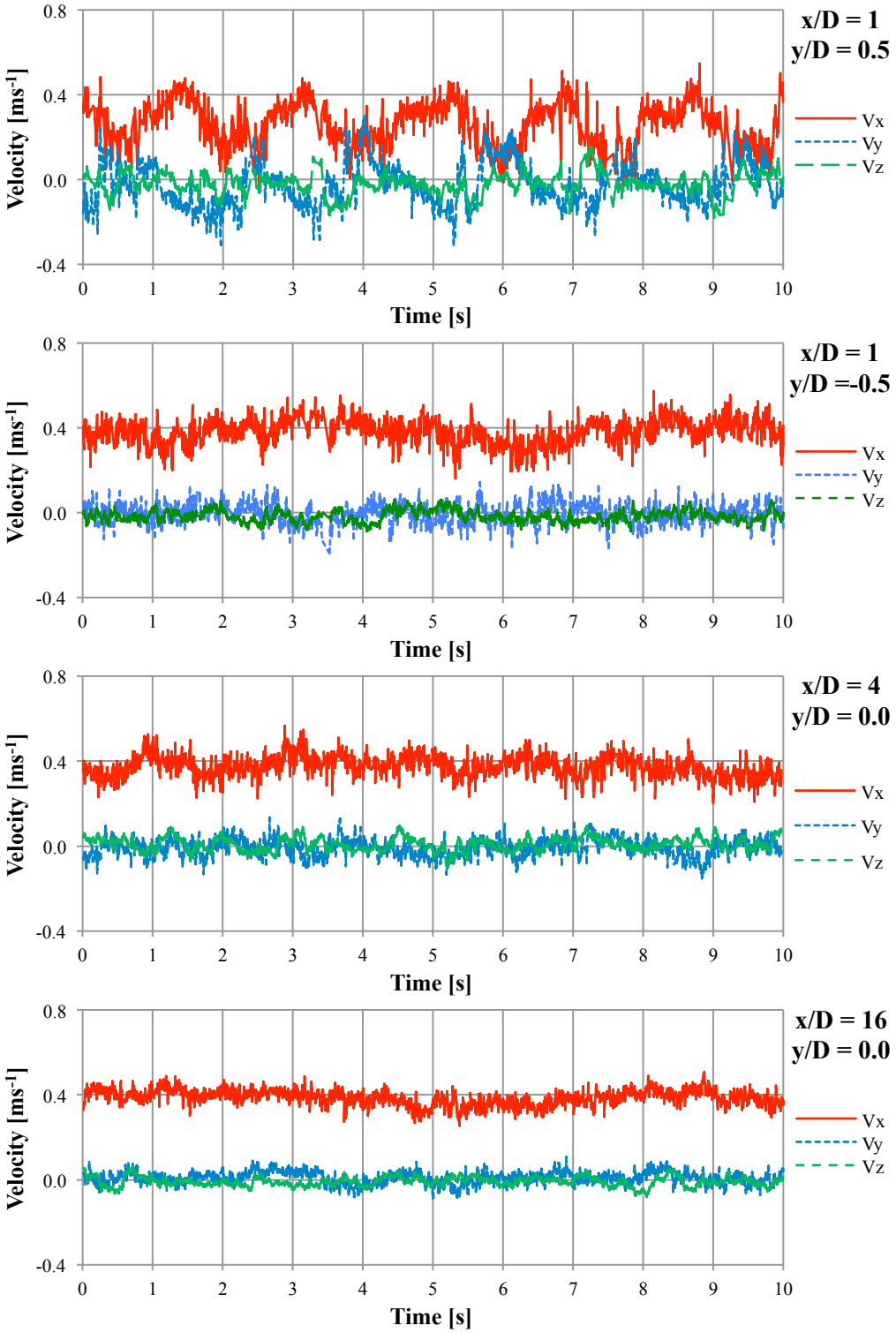

Figure 4.15 Time-series velocity measurements downstream of CB_4S turbine

The time-averaged horizontal profiles of velocity and turbulence intensity are given in Figure 4.17 and Figure 4.18 respectively. Due to the vertical axis configuration of these turbines the horizontal directions (x and y) are the dominant vectors, and hence these profiles give a better indication of the time-averaged effects downstream of a device. In

particular, the asymmetrical nature of the wake is clearly visible, with the difference between the open and closed flaps providing varying drag forces across the turbine section. In line with the turbine (at x/D = 0) flow acceleration was observed close to the tips of the turbine, and this acceleration was greater between $0.8<y<1.2$, which corresponds to the closed arm, and with this fluid acceleration propagating in the flow direction. The secondary currents created by this acceleration were still evident downstream in the far wake region, as mini peaks in velocity were seen at distances of y = 0.25 and 1.0 m. However, the wake can be considered as recovered when the velocities were within 90% of the upstream condition, and turbulence intensity levels had reduced to 10% or less.

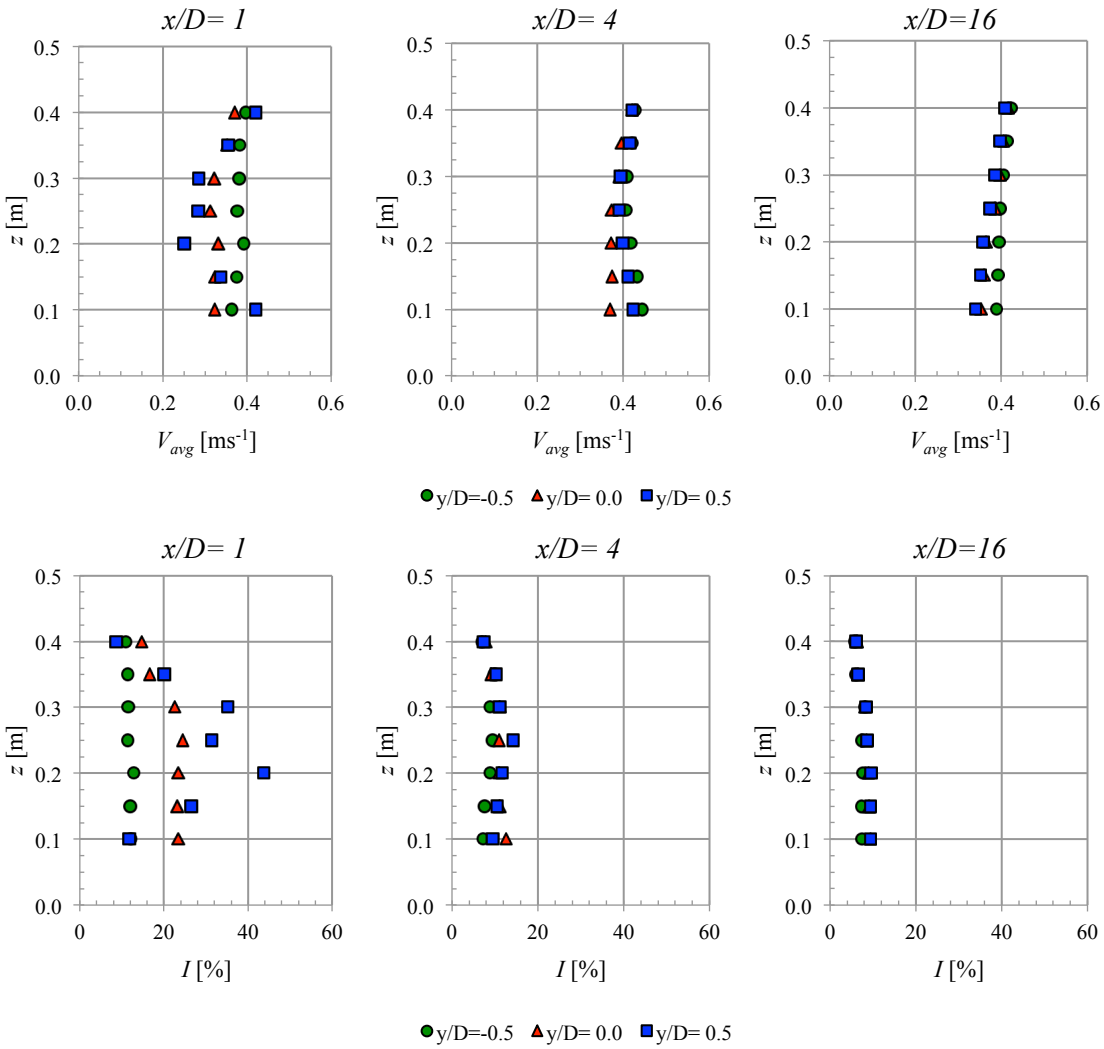

Figure 4.16 Time-averaged vertical profiles downstream of CB_4S turbine (Top: velocity magnitude, Bottom: turbulence intensity)

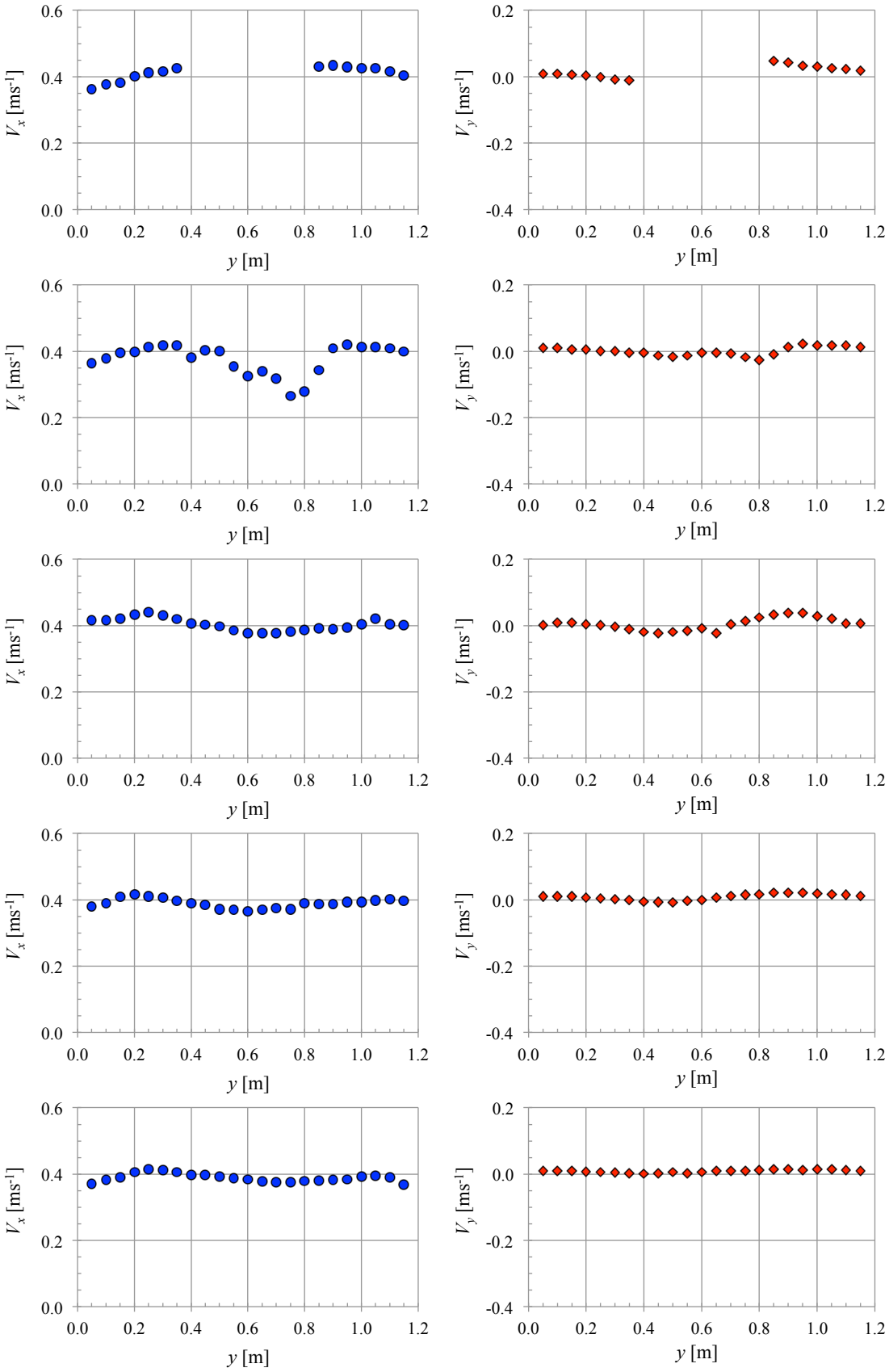

Figure 4.17 Time-averaged horizontal profiles downstream of CB_4S turbine (Left: V_x, Right: V_y)

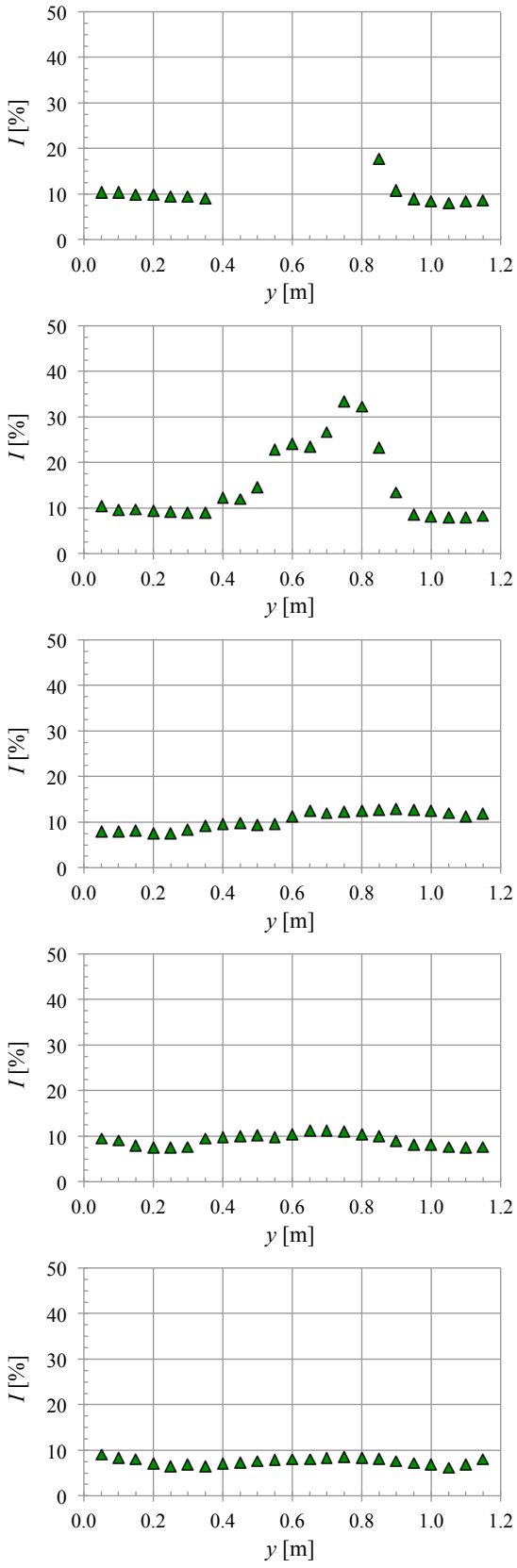

Figure 4.18 Time-averaged horizontal profiles of turbulence intensity, downstream of the CB_4S turbine

4.2.2 CB_4D

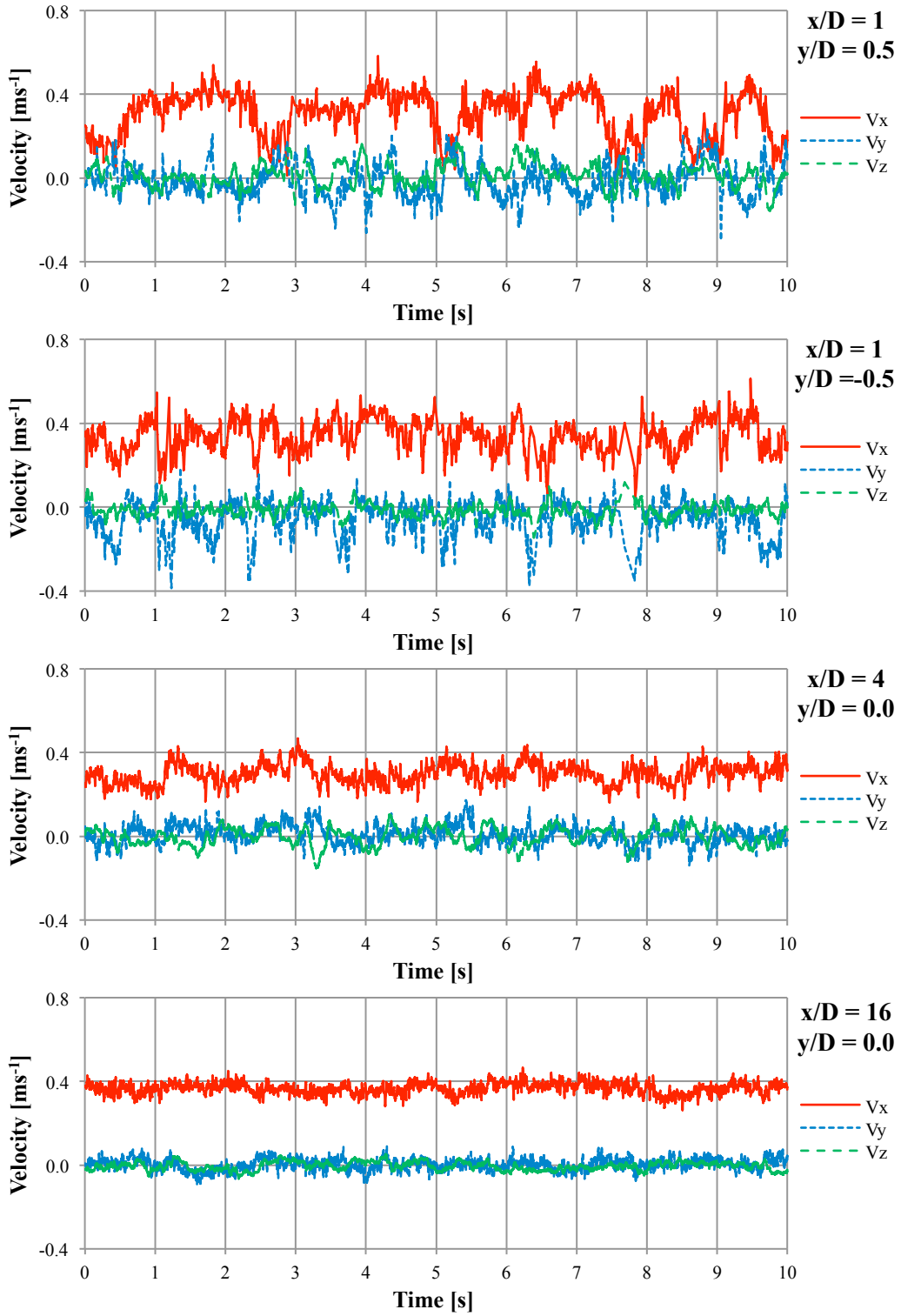

Figure 4.19 Time-series velocity measurements downstream of the CB_4D turbine

The time-series data for the CB_4D configuration are given in Figure 4.19. For the single flap configuration a clear separation behaviour was visible, whilst for the double

flap configuration the behaviour of the wake was less apparent as the additional flaps created a more complex flow field. This is because for the double flap configuration, the inner and outer flaps opened at different angles of a revolution and therefore the separated flows interact with each other as they are shed from each flap.

Behind the open flaps the velocities are closer to the upstream levels. However, the additional inner flaps generate more drag, and therefore the flow was more turbulent. Similarly for the CB_4S configuration, the wake recovered relatively quickly downstream, with velocities returning to a more uniform condition by 4 diameters downstream and with the turbulence levels decreasing as the wake re-energised.

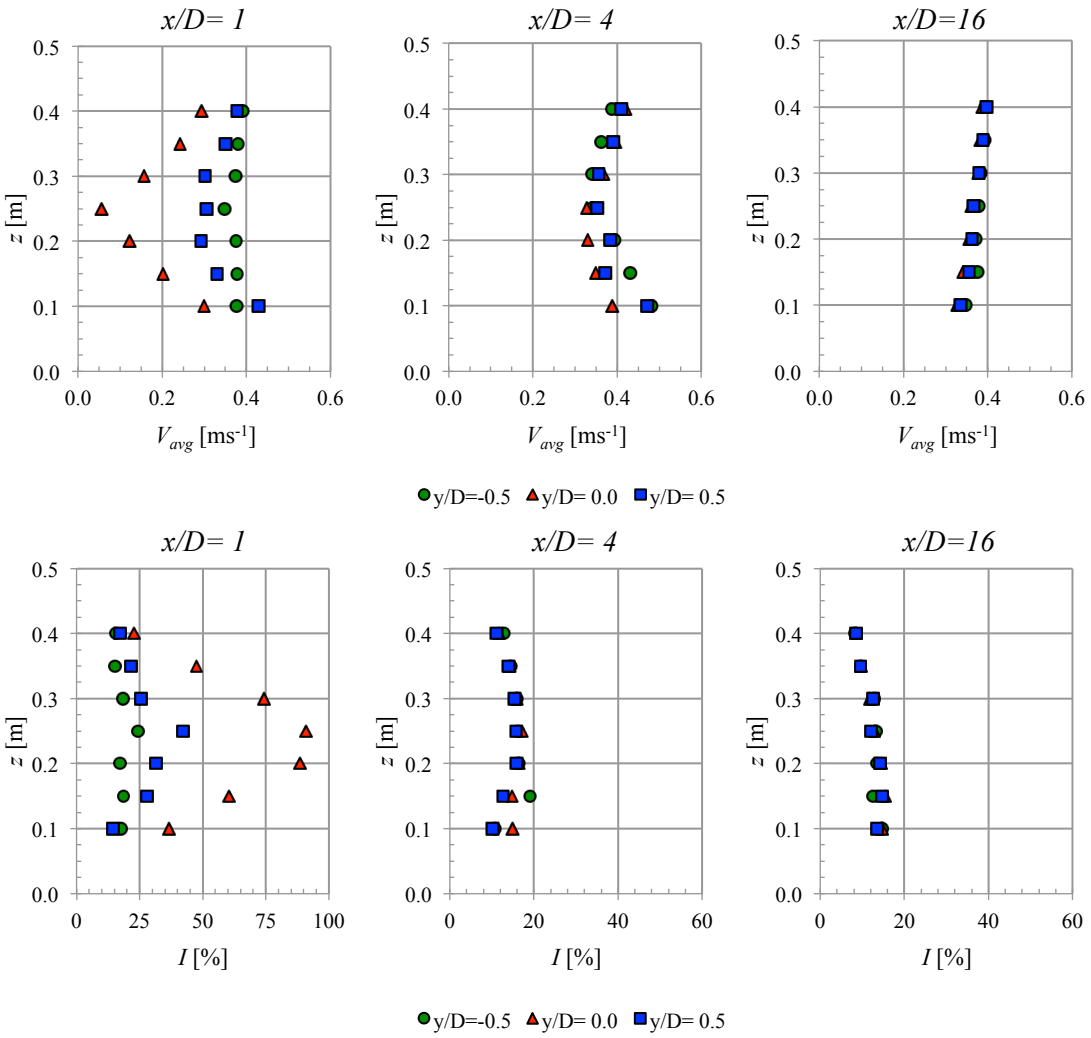

Figure 4.20 Time-averaged vertical profiles downstream of CB_4D turbine (Top: velocity magnitude, Bottom: turbulence intensity)

The time-averaged vertical profiles of velocity magnitude and turbulence intensity for the CB_4D configuration are given in Figure 4.20. Unlike the CB_4S configuration, the

largest change in the average velocities was at y/D = 0, i.e. behind the centre of the turbine, as opposed to behind the tip. This is a result of the increased drag from not only the additional closed flap, but also the extra open flap, as well as the influence of the shaft and base. Whilst the increase in drag resulted in a greater reduction in velocities, and increased turbulence intensity levels in the region of the turbine, similar recovery patterns to that of the CB_4S configuration were observed, with the flow profiles recovering to upstream conditions by 16 diameters downstream.

The horizontal profiles of velocity and turbulence intensity, for the CB_4D configuration are given in Figure 4.21 and Figure 4.22, respectively. At x/D = 1, the velocity profiles show that the maximum deficit is behind the closed flaps, towards the central axis, for the reasons previously discussed. The minimum velocity measured at this location was 0.1 ms^{-1}, representing a 75% reduction in the upstream condition. Further downstream at x/D = 8, whilst a deficit was still visible the velocities were within 90% of the upstream values, so the wake could be considered to have recovered at this location.

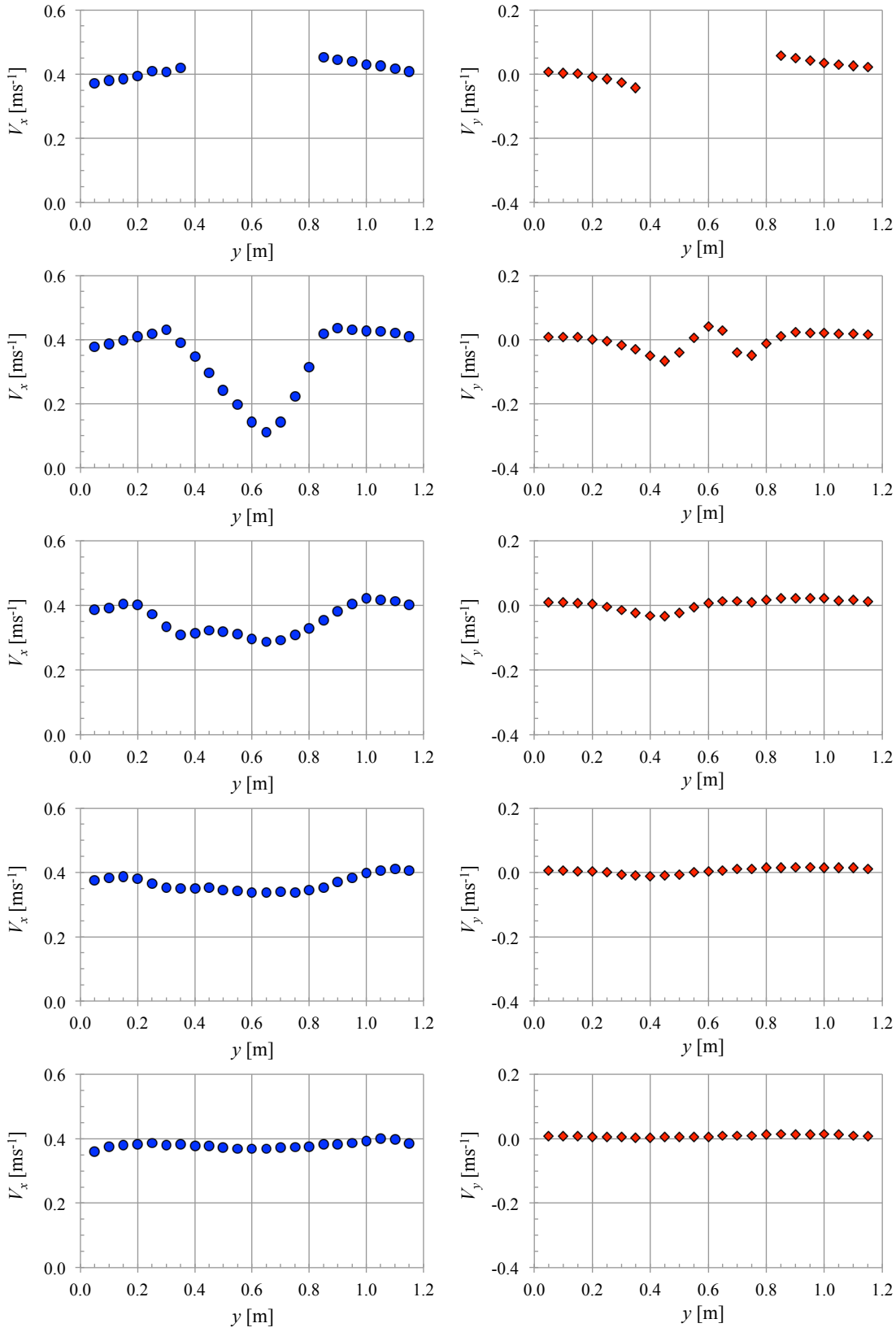

Figure 4.21 Time-averaged horizontal profiles downstream of CB_4D turbine (Left: V_x, Right: V_y)

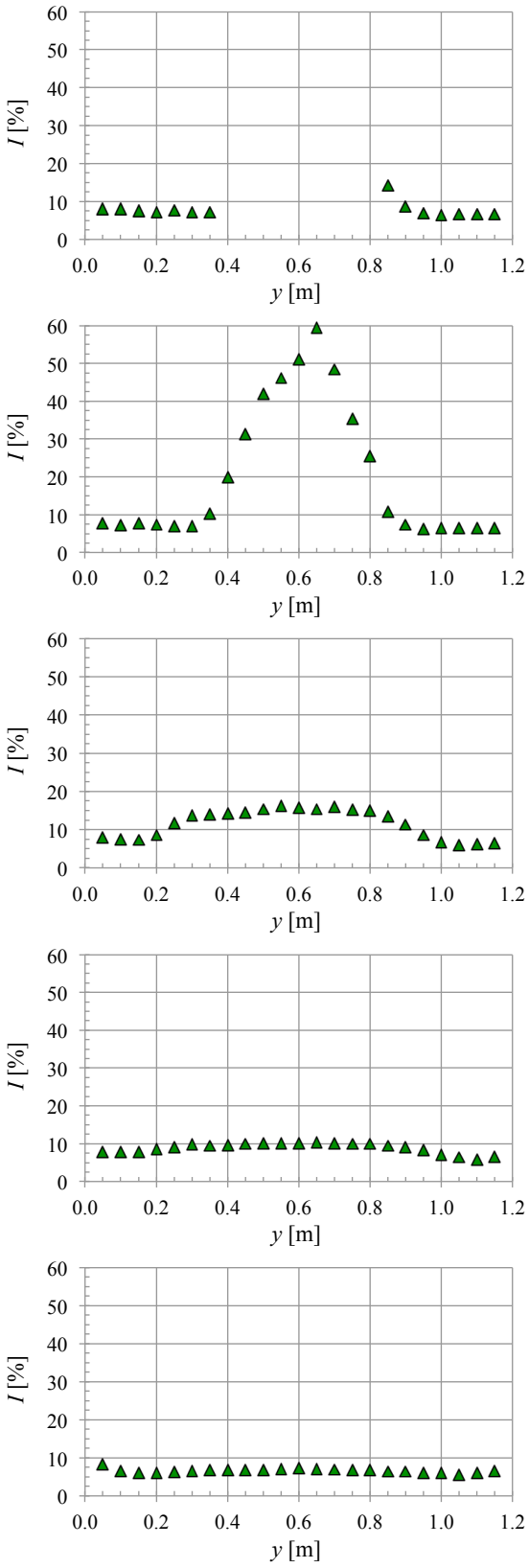

Figure 4.22 Time-averaged horizontal profiles of turbulence intensity, downstream of CB_4D turbine

4.2.3 SAV_SML

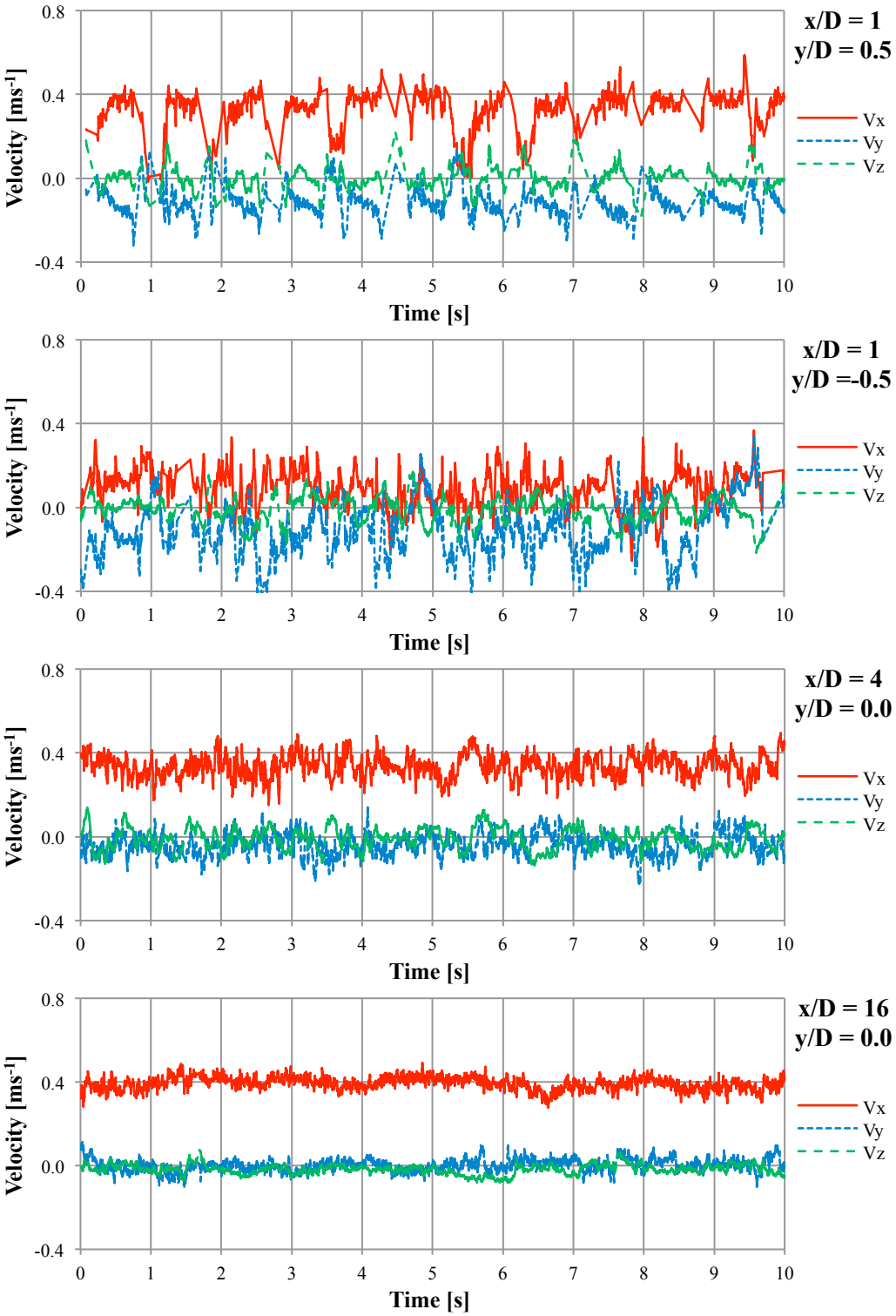

Figure 4.23 Time-series velocity measurements downstream of SAV_SML turbine

The significant difference between this configuration and the others tested is that, as the name suggests, it is smaller in size, with both the diameter and height of the turbine being half that of the other configurations. Therefore, in order to maintain an equivalent

tip speed ratio, the angular velocity of the turbine was doubled. This is reflected in Figure 4.23, which shows the time series data for this configuration. At a *TSR* of 1.0 a single revolution took 1.7s, the velocities in the top graph (i.e. y/D = 0.5) show the vortex shedding behaviour that occurs twice in this time period, representing the two buckets of the Savonius. In between the vortex shedding, the velocity behind the advancing bucket (i.e. at y/D = 0.5) remained relatively undisturbed, with an average value of approximately 0.4 ms^{-1} measured, whilst behind the returning bucket (at y/D =-0.5) the velocity was highly turbulent and was much lower at 0.1 ms^{-1}. This is due to the relative velocity between the flow and the tip of the bucket, as the drag and lift forces are proportional to the square of the velocity. As the advancing bucket moved in the same direction as the flow at a *TSR* of 1.0 (i.e. the same speed), the relative velocity, and the drag force were both zero. On the other hand, the relative velocity between the flow, and the returning bucket was twice as fast as the free-stream flow speed. This resulted in a higher drag force, hence the large reduction in velocities and the high levels of turbulence downstream of the turbine. Significant velocities in the transverse (y-axis) direction were measured, as the curved shape of the buckets deflected the flow as they rotated. As with the other turbines modelled in this study the far wake characteristics were similar, with turbulence levels decreasing as the distance downstream increased, and as the flow returned to a quasi-steady state.

Figure 4.24 shows the time-averaged vertical profiles for the SAV_SML turbine, and the significance of the height difference between this turbine and the others tested can be seen. As expected, there was less impact on the velocities close to the bed and the free surface as there was significantly less blockage in these regions. As with the time-series data, the largest changes in velocity occurred behind the returning bucket, and the minimum velocity was recorded at mid-depth, with the turbulence intensity levels exceeding 70%. At a distance of 4 diameters downstream the time-averaged flow behind the advancing bucket had recovered, whereas behind the returning bucket the velocities had recovered by approximately 75%. By 16 diameters downstream all three profiles had recovered to the corresponding upstream levels.

The horizontal profiles of the time-averaged velocities and the turbulence intensity are given in Figure 4.25 and 4.26. In line with the turbine (at x/D = 0), despite the low

blockage ratio of 0.04, flow acceleration was still observed, with this effect being more prominent on the side of the advancing bucket.

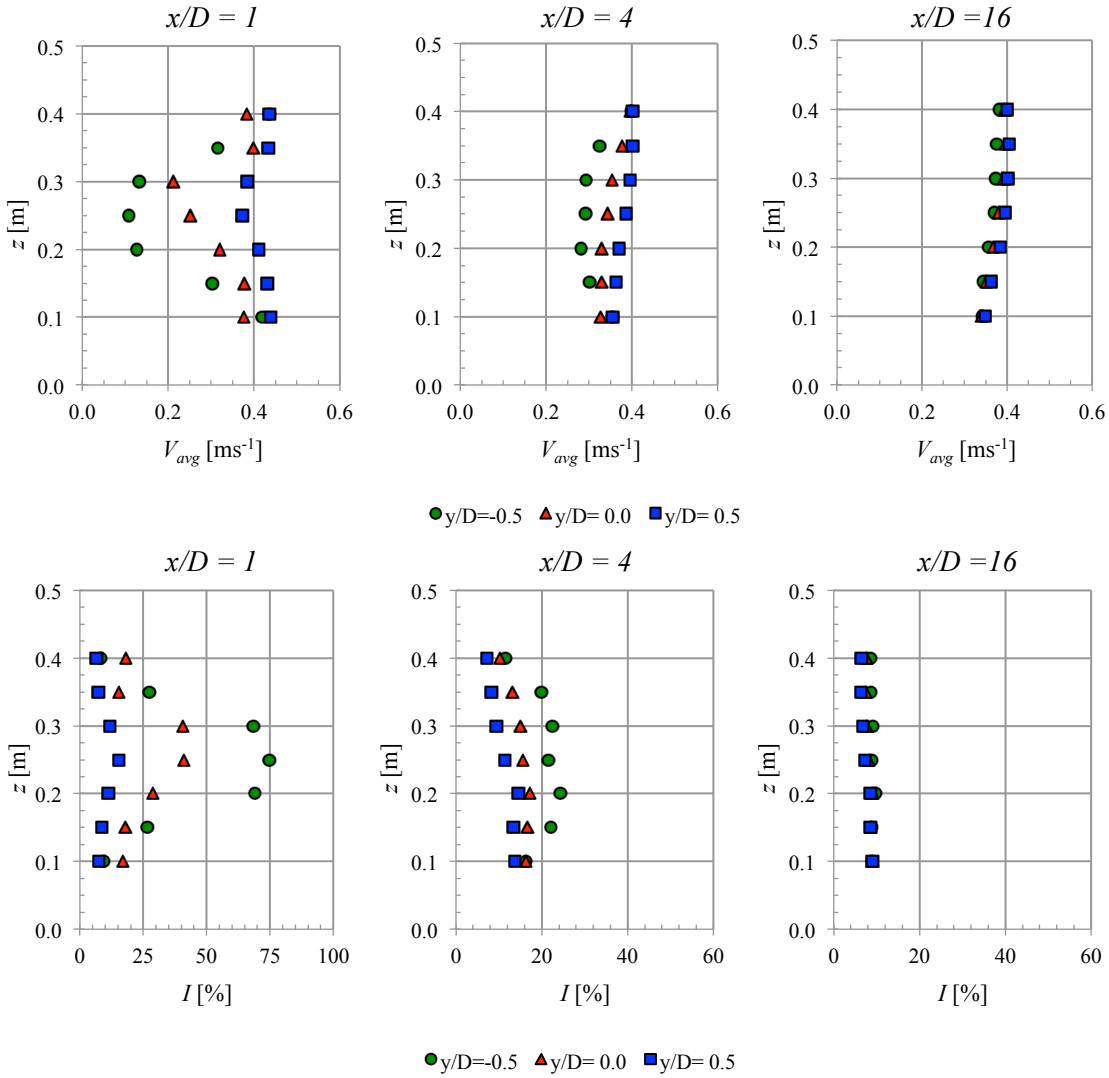

Figure 4.24 Time-averaged vertical profiles downstream of SAV_SML turbine (Top: velocity magnitude, Bottom: turbulence intensity)

At one diameter downstream of the turbine a large velocity deficit occurs behind the tip of the returning bucket (measured at y = 0.5 m) at a minimum velocity of 0.1 ms^{-1}. A large transverse component can be seen, and this 'pushes' the wake to one side of the turbine as it continues to mix downstream, this effect stabilised at a distance of y = 0.4m, i.e. one diameter to the side relative to the turbines axis. The minimum velocities and peaks in the turbulence intensity can be seen at this distance. As with the other turbines, at 16 diameters downstream the velocities and turbulence intensities were within 90% of the upstream conditions and the lateral flow distribution can therefore be considered to be fully recovered at this location, however the wake is still visible.

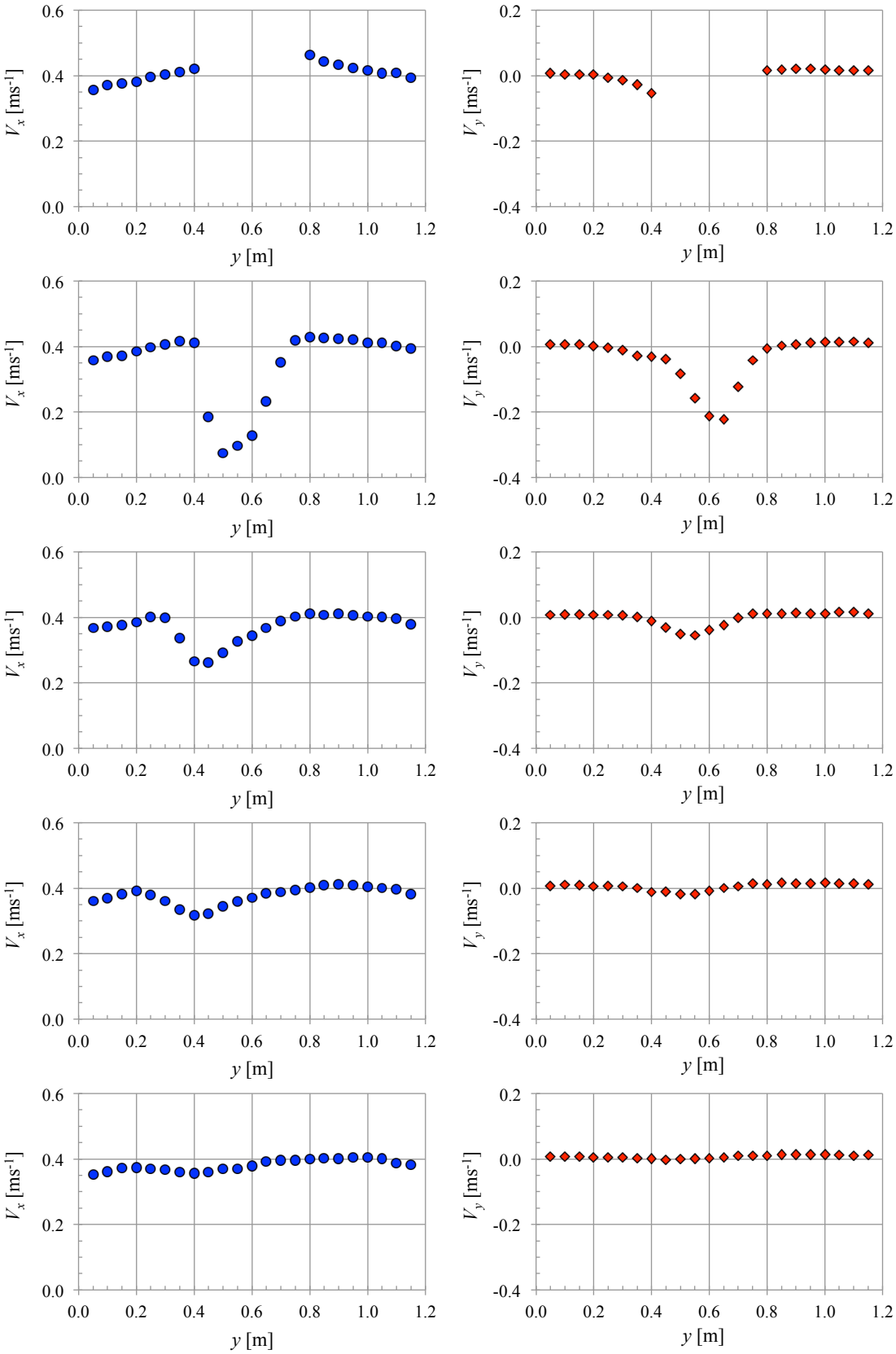

Figure 4.25 Time-averaged horizontal profiles downstream of SAV_SML turbine (Left: V_x, Right: V_y)

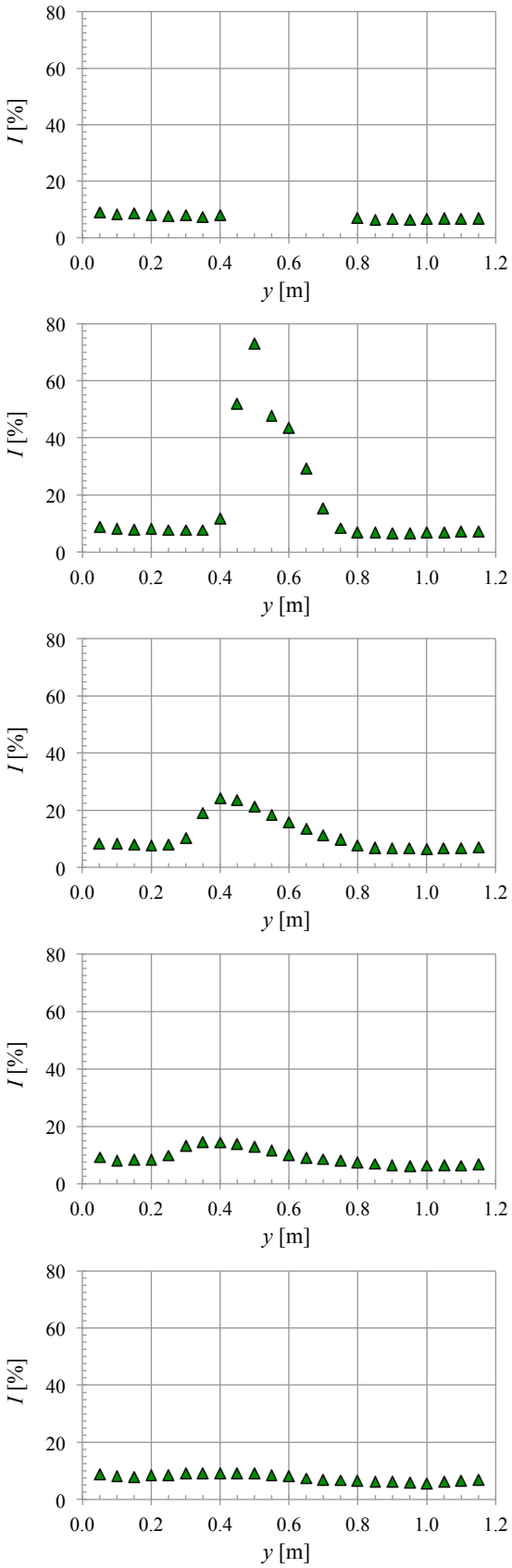

Figure 4.26 Time-averaged horizontal profiles of turbulence intensity, downstream of SAV_SML turbine

4.2.4 SAV_LRG

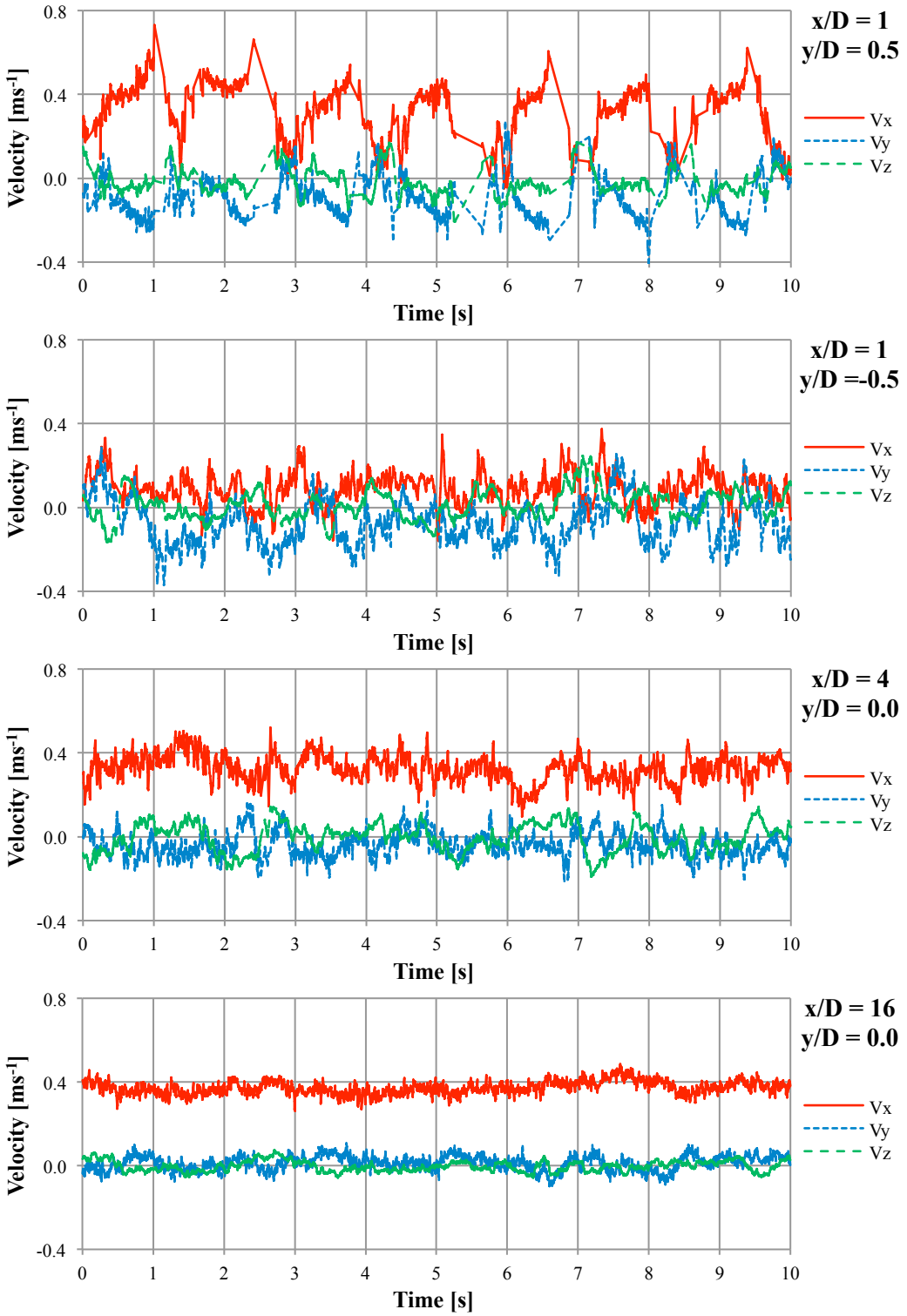

Figure 4.27 Time-series velocity measurements downstream of SAV_LRG turbine

As expected the hydrodynamic characteristics of the SAV_LRG turbine were similar to those for the smaller model previously tested. When the diameter reverted back to the standard 0.4 m, as used for the other turbines, the time taken to complete a revolution

compared to the SAV_SML model doubled, as the angular velocity was halved to maintain a *TSR* of 1.0. This is reflected in Figure 4.27, in which the separation behaviour occurred every 1.7s. As well as a slower turbine velocity, the blockage in the flume corresponded to the highest value tested due to the high solidity of the turbine. This resulted in greater flow acceleration around the device, and hence higher velocity peaks were observed. Despite this high blockage and the larger secondary currents created as a result, the wake damped down sufficiently such that by 16 diameters downstream the flow had reached a steady and uniform structure.

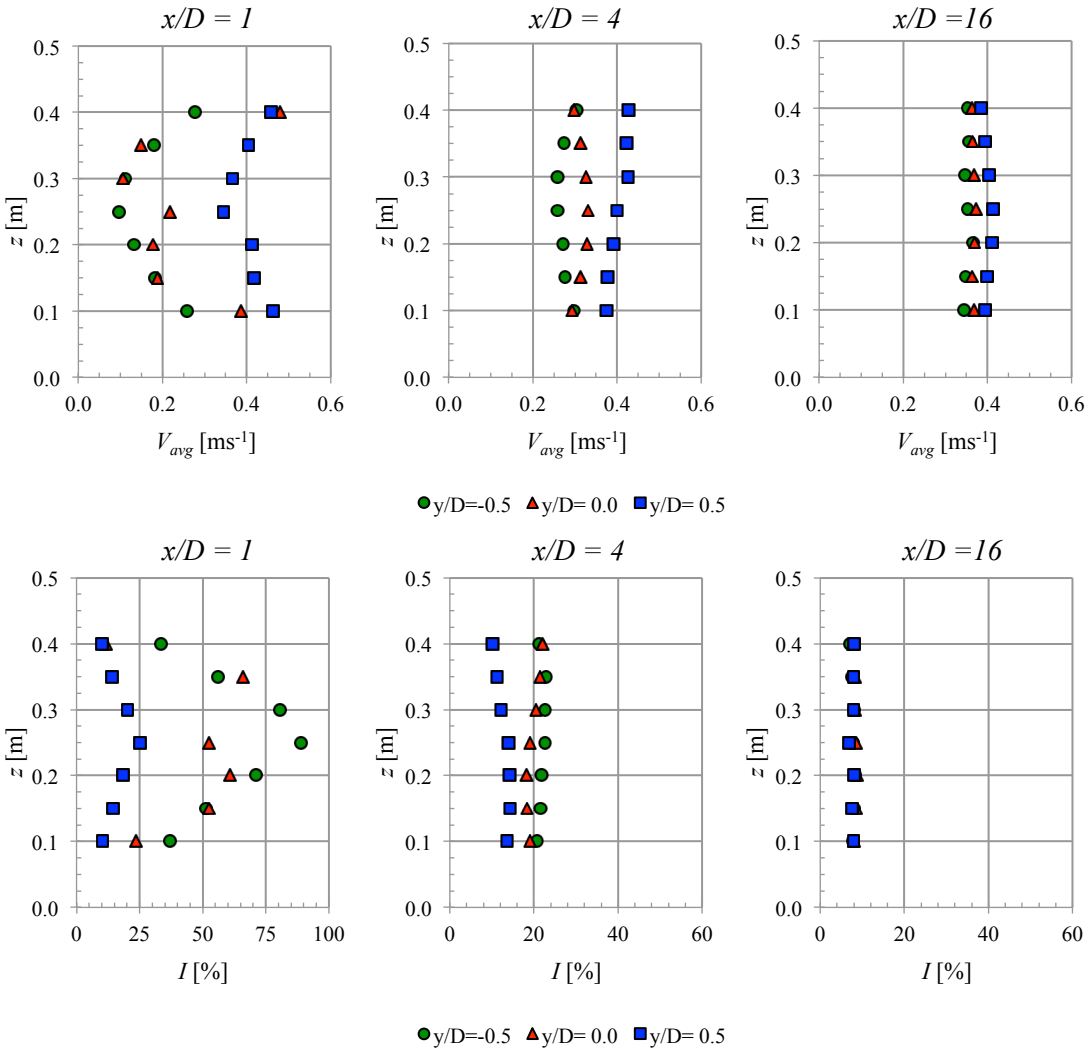

Figure 4.28 Time-averaged vertical profiles downstream of SAV_LRG turbine (Top: velocity magnitude, Bottom: turbulence intensity)

The vertical profiles, as given in Figure 4.28, show that the largest reductions in the velocity occurred at mid-depth behind the returning bucket. A minimum velocity of 0.1 ms^{-1} was measured at this point, which was the same magnitude as for the SAV_SML

turbine. However, the turbulence levels were higher, with a peak turbulence intensity of 90% measured, and with levels on average being 50% at one diameter beyond the turbine. Increases in the velocity close to the bed and free surface were again visible, as the height constrained the flow. At x/D = 4 the turbulence intensity levels were on average 20%, and the differences between the velocity profiles were still visible. By x/D = 16 the flow condition had largely recovered, with turbulence intensity levels being below 10%. However, the flow profile at y/D = 0.5 was still greater than the upstream conditions.

The horizontal flow profiles, as given in Figure 4.29 and Figure 4.30 highlight the significant flow acceleration due to the large blockage of the turbine. In line with the turbine at x/D = 0, a peak average velocity of 0.53 ms^{-1} was measured, representing a 40% increase compared to the average velocity. However, it is noted that for the unblocked SAV_SML turbine, a 20% increase in the peak velocity was measured around the turbine.

The secondary currents created due to the blockage persisted for the length of the flume, and at 16 diameters downstream approximately for half of the profile (i.e. y = 0.6 m and greater) the flow velocities were in excess of 0.4 ms^{-1}. However, whilst the maximum velocities were greater compared to the smaller Savonius model, the minimum velocities were the same for both turbine models. Furthermore, in the far wake region the minimum velocity points in the horizontal planes were also located at y = 0.4m, with it being assumed that the flume walls and the strong secondary currents constrained this expansion and stopped the wake moving further to one side. This was based on the results for the SAV_SML turbine, where it was expected that the wake would align at a distance of 1 diameter to the side of the turbine axis. However, due to the good agreement of the minimum velocities for both turbine sizes, the wake behaviour was shown to be scalable for both turbine sizes, despite these blockage effects.

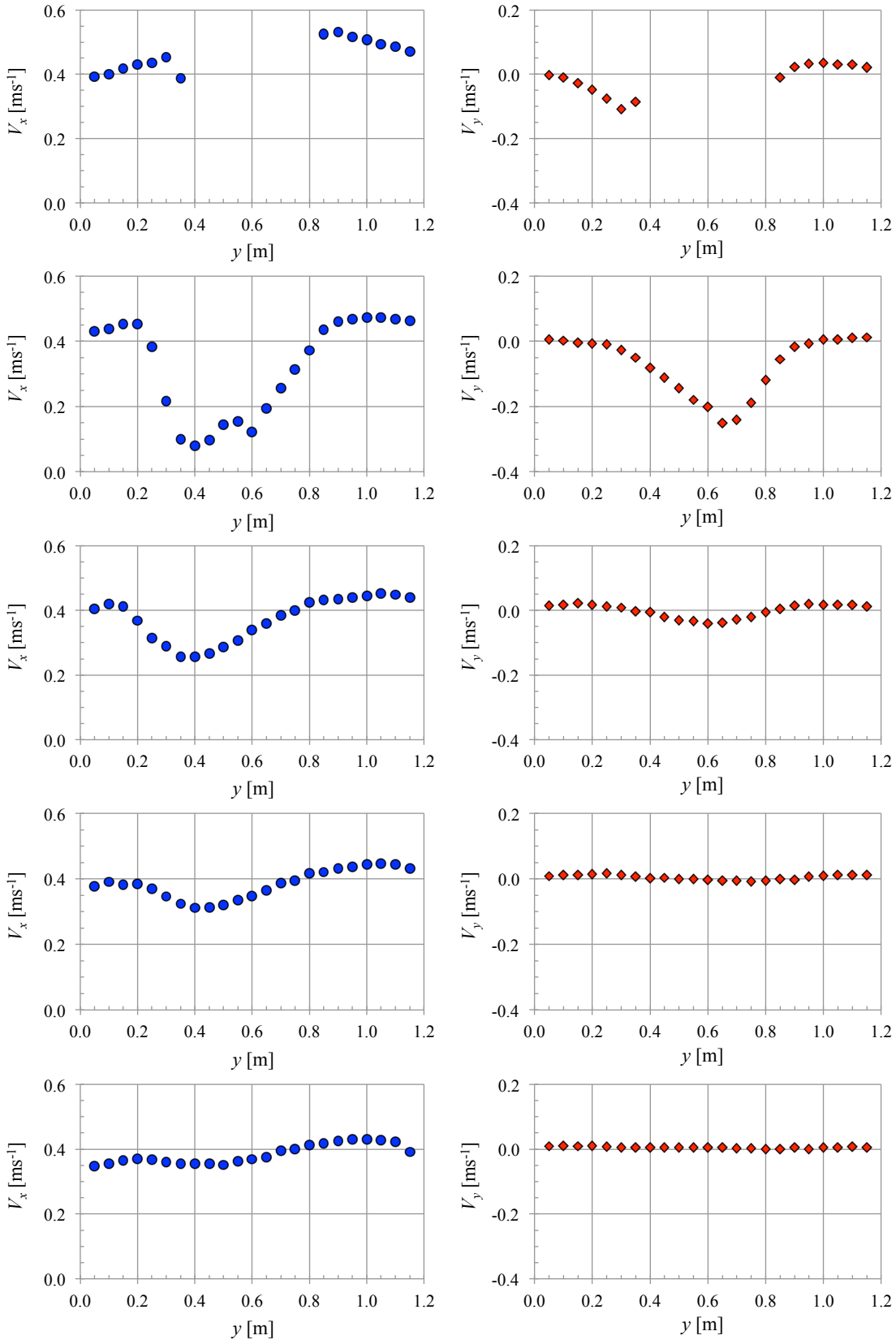

Figure 4.29 Time-averaged horizontal profiles downstream of SAV_LRG turbine (Left: V_x, Right: V_y)

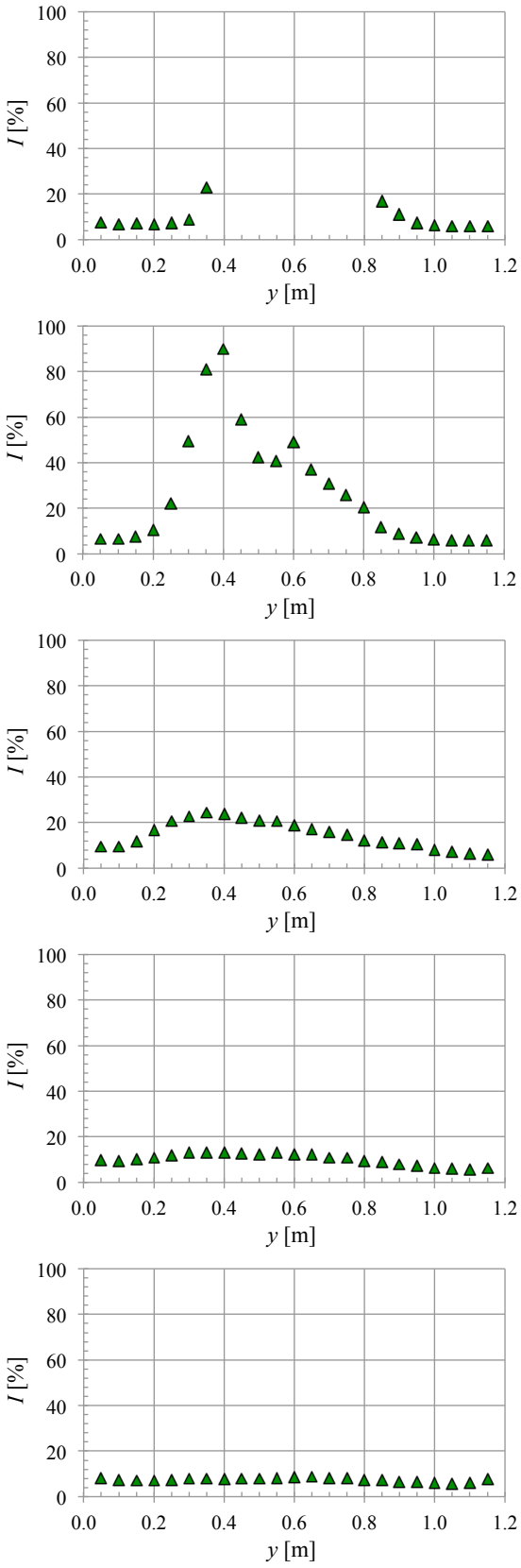

Figure 4.30 Time-averaged horizontal profiles of turbulence intensity, downstream of SAV_LRG turbine

4.3 Conclusions

In this chapter the results are presented and discussed from a series of tests conducted in the Hydro-environmental Research Centre's large recirculating flume. Two main types of test were conducted, namely performance testing of the turbine and the corresponding wake characterisation. A number of vertical axis turbine designs were considered, and comparisons have been drawn between the various designs.

Firstly, whilst efforts were made in the experimental design to minimise energy losses and measure parameters at high sampling frequencies, no formal quantification of the experimental error has been conducted. Such an error analysis is recommended as a future improvement to the experimental setup, and therefore at the present time this has to be taken into account when analysing the data, and in particular when comparing it with the CFD results in Chapter 6.

The tests of the CarBine configurations firstly showed that the MSc research, undertaken previously, was optimistic in the prediction of the power, which was thought to be due to the relatively crude methods used. The power take-off system designed and implemented in these tests was shown to produce reliable and repeatable readings, and significantly provided dynamic data as well as average values. The best performing CarBine turbine was the CB_4D configuration, in which the maximum C_P value varied between 0.14 and 0.2, depending on the flow conditions. This is not a very competitive performance value, however, the turbines tested were not intended to represent final designs, but rather to provide a reliable baseline dataset for comparison in future studies. The CarBine turbines used drag forces only, but further studies could include varying the flap shape to reduce the negative drag and generate lift forces to increase the rotational speed of the turbine. One of these advancements in design was attempted in this study by merging CarBine with a Savonius turbine. However, this test proved unsuccessful in increasing the turbine performance.

The Savonius turbine responded very well to the hydraulic conditions in the flume and was the best performing turbine in the tests, with the peak efficiency ranging from 27% to 38%. These levels of efficiency are competitive with other turbines, particularly given the simplistic nature of the turbine design and operation. Therefore, provided that

the turbine behaviour could be transposed to a larger scale, the Savonius turbine could prove to be a feasible design solution for energy generation.

The Darrieus turbine tested did not perform as well as expected, with the peak efficiency varying between 12 and 27%. However, the turbine tested was the first in an on-going series of tests and was not expected to have a particularly high performance. For example, the camber of the blades did not align with the circumference of the turbine. Furthermore, as the Darrieus turbines are typically high-speed-low-torque, the turbine was more susceptible to friction losses in the power take-off system.

Whilst the Froude numbers in the flume were higher than for typical field conditions, the Reynolds numbers were typically two orders of magnitude lower. It is expected that at higher Reynolds numbers the negative drag of the Savonius and Darrieus blades would reduce, and hence the results from these tests can be considered conservative. However, further research is required to confirm this hypothesis and particularly for the Savonius turbine. In addition, the disks used to mount the turbine blades would have provided a source of negative drag, although how much effect this had on the turbine performance was not quantified in the tests. These losses could be minimised in final designs.

Overall the tests have demonstrated that utilising a blockage effect can enhance turbine performance. The blockage used in testing was relatively modest, at 17%, which suggests that even higher outputs could be achieved. Without a high blockage ratio (i.e. in deeper waters) it is unlikely that the turbines tested could produce an efficiency that is competitive with horizontal axis designs. However, in shallow waters, such as the Severn Estuary, these vertical axis designs could be better suited to energy generation, as they can be stretched laterally to maximise the area of power take-off and induce higher blockage ratios.

As well as conducting performance tests, it was important to investigate the hydrodynamic impact the turbines had on the aquatic environment, as the wake characteristics have implications on downstream devices and the spacing between the turbines. Previous research has focused on the wake characteristics of horizontal axis devices, and little is known about the wake of vertical axis devices, especially those that

specifically use a high blockage ratio to enhance performance. Similar characteristics were observed for the turbines, which can be generally summarised as follows:

- Asymmetry, in that as one half of the turbine rotates with the flow, the other half rotates against it. Hence the thrust force imparted on the flow varies across the width of the turbine.
- Unsteady, vortex shedding occurs as the turbine rotates, and with the frequency of shedding depending on the size, and therefore the rotational velocity of the turbine, as the optimum *TSR* is maintained.
- Shorter than horizontal axis turbine wakes, in that despite the unsteady nature of the flow in the near wake region, by 16 diameters downstream the flow had recovered to a uniform and steady state velocity profile, for all of the turbines tested. Furthermore, due to the asymmetrical nature of the wake, some parts of the wake recovered as close as 4 diameters downstream.
- Secondary currents were created, with the magnitude of the currents depending on the blockage and solidity of the turbine. The free stream currents mixed with the wake downstream, but in some cases could still be visible at a distance of 16 diameters downstream.

Based on these observations the spacing requirements for vertical axis turbines would be very different to that of horizontal axis turbines. Not only could turbines be spaced closer together, which would increase the array output power per unit area, but the output could be further increased by exploiting turbine to turbine interactions and the secondary currents created. Further research is required in this field to confirm these conclusions, however, as not only does the unsteady flow in the near wake region potentially affect the turbine performance in a negative way as well as a positive one, but it could also have structural implications to any downstream turbine devices.

Chapter 5 Computational Fluid Dynamic modelling

5.1 Introduction

In this chapter details are given of the theoretical background and solution procedures of the numerical models used in this research study. Two Computational Fluid Dynamics (CFD) models were used, namely the commercial code ANSYS CFX (referred to herein as CFX), and the HRC's own numerical model, TRIVAST. It should be noted that TRIVAST is the 3-D version of the more commonly known DIVAST model, and reduced to DIVAST when the number of layers is reduced to unity. CFX was used to model the near-field aspects of the vertical axis turbines tested, with particularly interest in the wake behaviour, although initial performance assessments have also been made. Comparisons have been made with the laboratory data obtained in Chapter 4, to validate the model predictions. TRIVAST is more suitable to model far-field applications, and as such the model was set up to predict the hydrodynamics of a mean spring tide in the Severn Estuary. Developments were then made to the code to include the effects of energy extraction from tidal stream turbine arrays and, based on spacing recommendations obtained from both the reviewed literature and the experimental tests conducted in Chapter 4, hypothetical horizontal and vertical axis turbine arrays were then modelled.

The TRIVAST model was also modified to include the effects of the two main proposed Severn Barrage schemes, firstly at a physical model scale. This work was conducted in conjunction with an MSc project that focused on laboratory experiments using the HRC's scaled physical model of the Severn Estuary, with the corresponding data obtained from these studies being used for model calibration. Finally, the model was then extended to the prototype scale, to assess the far-field impacts of the two Severn Barrage schemes, as well as the interaction between a tidal barrage and tidal stream arrays.

5.2 Governing equations

In general terms CFD models solve the Navier-Stokes equations for fluid flow and are based on the principles of continuity of mass and conservation of momentum within the

modelled body of fluid. The exact form of these equations depends on the application and the sophistication of the model used to solve them, however, the most common sets of equations for hydrodynamic applications are the Reynolds-Averaged Navier-Stokes (RANS) equations, for incompressible flows. Herein the governing equations are derived, based on the equations and notation used in the TRIVAST model, as access and modifications to the source code were available for this code. In contrast CFX is a commercial software tool, and access to the source code was not available. For full details of the governing equations used in CFX the reader is referred to the relevant manual (ANSYS, Inc. 2010b), and further details of the TRIVAST and DIVAST models can be found by Lin and Falconer (1997), and Falconer and Lin (2002b; 2002a), respectively.

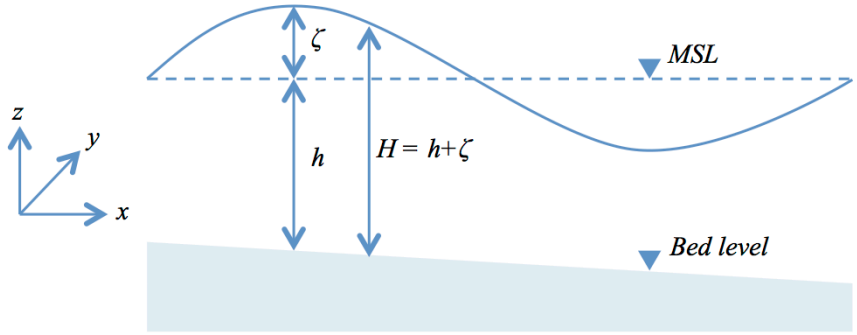

Figure 5.1 A typical estuarine water body

The three-dimensional RANS equations, for incompressible and unsteady turbulent flows, are given in their conservative form as follows;

Continuity equation:-

$$\frac{\partial u}{\partial x}+\frac{\partial v}{\partial y}+\frac{\partial w}{\partial z}=0 \qquad 5.1$$

Momentum equations:-

$$\frac{\partial u}{\partial t}+u\frac{\partial u}{\partial x}+v\frac{\partial u}{\partial y}+w\frac{\partial u}{\partial z}=fv-\frac{1}{\rho}\frac{\partial p}{\partial x}+\frac{1}{\rho}\left[\frac{\partial \tau_{xx}}{\partial x}+\frac{\partial \tau_{xy}}{\partial y}+\frac{\partial \tau_{xz}}{\partial z}\right] \qquad 5.2$$

$$\frac{\partial v}{\partial t}+u\frac{\partial v}{\partial x}+v\frac{\partial v}{\partial y}+w\frac{\partial v}{\partial z}=-fu-\frac{1}{\rho}\frac{\partial p}{\partial y}+\frac{1}{\rho}\left[\frac{\partial \tau_{yx}}{\partial x}+\frac{\partial \tau_{yy}}{\partial y}+\frac{\partial \tau_{yz}}{\partial z}\right] \qquad 5.3$$

$$\frac{\partial w}{\partial t}+u\frac{\partial w}{\partial x}+v\frac{\partial w}{\partial y}+w\frac{\partial w}{\partial z}=-g-\frac{1}{\rho}\frac{\partial p}{\partial z}+\frac{1}{\rho}\left[\frac{\partial \tau_{zx}}{\partial x}+\frac{\partial \tau_{zy}}{\partial y}+\frac{\partial \tau_{zz}}{\partial z}\right] \qquad 5.4$$

where t = time, u, v, w = mean velocity in the x, y, z directions respectively, f = Coriolis parameter, p = pressure, ρ = density, τ = components of stress tensor (where the subscripts denote planar direction), and g = acceleration due to gravity.

5.2.1 Three-dimensional layer-integrated equations

The principal assumption in layer integrating equations 5.1-5.4 is that the pressure distribution is hydrostatic, i.e. the gravitational acceleration is much larger in the z-direction momentum equation than the other components of acceleration. Equation 5.4 therefore reduces to:-

$$\frac{\partial p}{\partial z}+\rho g=0 \qquad 5.5$$

The TRIVAST model solves these governing equations of motion using a finite difference scheme on a regular square mesh in the horizontal plane, and an irregular mesh in the vertical. Three types of layer exist: top, middle and bottom. The top layer thickness must be larger than the tidal range of the body of water, to cover all flooding and drying problems, the middle layer is of uniform thickness, and the bottom layer thickness also varies in order to represent the local bathymetry. A sketch of this layer description is given in Figure 5.2.

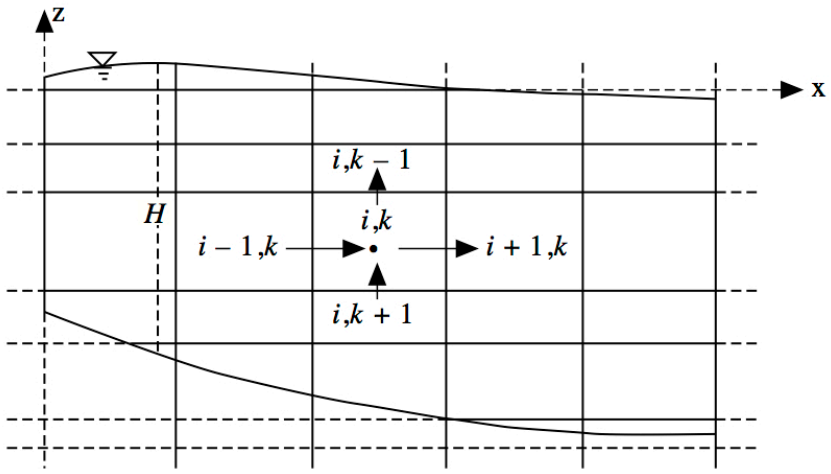

Figure 5.2 Vertical grid notation in the *x*-*z* plane, as used in TRIVAST (Lin and Falconer 1997)

Using this notation the governing equations are integrated over the *k*th layer, where k = 1, 2, 3, …, *NL*. Letting:

$$\langle \circ \rangle_k = \int_{k+\frac{1}{2}}^{k-\frac{1}{2}} (\circ) dz \qquad 5.6$$

where $k \pm ½$ refers to the interface between the layer k and $k \pm 1$.

Integrating the continuity equation over the layer k yields:-

$$\int_{k+\frac{1}{2}}^{k-\frac{1}{2}} \left(\frac{\partial u}{\partial x} + \frac{\partial v}{\partial y} + \frac{\partial w}{\partial z} \right) dz = 0 \qquad 5.7$$

which therefore gives

$$w_{k-\frac{1}{2}} - w_{k+\frac{1}{2}} + \int_{k+\frac{1}{2}}^{k-\frac{1}{2}} \left(\frac{\partial u}{\partial x} + \frac{\partial v}{\partial y} \right) dz = 0 \qquad 5.8$$

Using Leibnitz rule, interchanging the differential operators $\partial/\partial x$ and $\partial/\partial y$ with the integral, and accounting for the limits of integration gives the vertical velocity component at the layer interface $k - ½$:-

$$w_{k-\frac{1}{2}} = -\sum_{l=k}^{NL} \left\{ \frac{\partial (hu)}{\partial x} + \frac{\partial (hv)}{\partial y} \right\} \qquad 5.9$$

Equation 5.9 is the continuity equation in differential form for a layer k. At the water surface (where $k = 1$) the continuity equation reduces to:-

$$\frac{\partial \zeta}{\partial t} + \sum_{l=1}^{NL} \left\{ \frac{\partial (hu)}{\partial x} + \frac{\partial (hv)}{\partial y} \right\} = 0 \qquad 5.10$$

where ζ = water elevation above mean sea level. Integrating momentum equations 5.2 and 5.3 with respect to the vertical direction, for the k^{th} layer yields:-

$$\begin{aligned} \frac{\partial \langle u \rangle}{\partial t} + \frac{\partial \langle uu \rangle}{\partial x} + \frac{\partial \langle uv \rangle}{\partial y} + (uw)_{k-\frac{1}{2}} - (uw)_{k+\frac{1}{2}} &= f \langle v \rangle - \frac{1}{\rho} \left\langle \frac{\partial p}{\partial x} \right\rangle \\ &+ \frac{1}{\rho} \left[\frac{\partial \langle \tau_{xx} \rangle}{\partial x} + \frac{\partial \langle \tau_{xy} \rangle}{\partial y} \right] + \frac{1}{\rho} \left(\tau_{xz}\big|_{k-\frac{1}{2}} - \tau_{xz}\big|_{k+\frac{1}{2}} \right) \end{aligned} \qquad 5.11$$

$$\frac{\partial\langle v\rangle}{\partial t}+\frac{\partial\langle uv\rangle}{\partial x}+\frac{\partial\langle vv\rangle}{\partial y}+\left(vw\right)_{k-\frac{1}{2}}-\left(vw\right)_{k+\frac{1}{2}}=-f\langle u\rangle-\frac{1}{\rho}\left\langle\frac{\partial p}{\partial y}\right\rangle + \frac{1}{\rho}\left[\frac{\partial\langle\tau_{yx}\rangle}{\partial x}+\frac{\partial\langle\tau_{yy}\rangle}{\partial y}\right]+\frac{1}{\rho}\left(\tau_{yz}\Big|_{k-\frac{1}{2}}-\tau_{yz}\Big|_{k+\frac{1}{2}}\right) \qquad 5.12$$

where <*u*> and <*v*> are the layer-integrated velocities in the *x* and *y* directions, respectively. Defining the layer-averaged velocity in the *x*-direction as:-

$$\bar{u}=\frac{1}{\Delta Z}\int_{k+\frac{1}{2}}^{k-\frac{1}{2}}u\left(x,y,z,t\right)dz \qquad 5.13$$

where ΔZ is the layer thickness, with a similar expression derived for the *y*-direction. Furthermore, assuming the Boussinesq approximation, then the stress components in the *x*-direction can be expressed as:-

$$\tau_{xx}=\rho\varepsilon_h\left[\frac{\partial\bar{u}}{\partial x}+\frac{\partial\bar{u}}{\partial x}\right],\tau_{xy}=\rho\varepsilon_h\left[\frac{\partial\bar{u}}{\partial y}+\frac{\partial\bar{v}}{\partial x}\right],\tau_{xz}=\rho\varepsilon_v\left[\frac{\partial\bar{u}}{\partial z}+\frac{\partial\bar{w}}{\partial x}\right] \qquad 5.14$$

where ε_h and ε_v are the horizontal and vertical eddy viscosities, respectively. However it is noted that the vertical plane stresses also depend on the bed and free surface boundary conditions, and are modified accordingly. In estuarine modelling applications the vertical eddy viscosity terms are generally much larger than the horizontal terms, and therefore precedence was given to the vertical eddy viscosity term. A two layer mixing length model was used to represent the vertical eddy viscosity, as given in equation 5.15, and the horizontal eddy viscosity was assumed to be constant with depth, and its value equal to the depth averaged eddy viscosity, as given in equation 5.16:-

$$\varepsilon_v=l^2\left[\left(\frac{\partial u}{\partial z}\right)^2+\left(\frac{\partial v}{\partial z}\right)^2\right]^{\frac{1}{2}},\ where\begin{cases} l=\kappa z & for\quad \kappa z\le 0.1H \\ l=0.1H & for\quad \kappa z>0.1H \end{cases} \qquad 5.15$$

$$\varepsilon_h=C_e\frac{H}{C}\sqrt{g\left(U^2+V^2\right)} \qquad 5.16$$

where κ is von Karmen's constant, *H* is the total water depth, *U* and *V* are the depth-averaged velocities in the *x* and *y* directions respectively, C_e is the eddy viscosity coefficient, and *C* is the Chezy coefficient.

As a hydrostatic pressure distribution has been assumed the pressure gradients can be defined as:-

$$\frac{\partial p}{\partial x} \cong g\rho\frac{\partial \zeta}{\partial x}, \qquad \frac{\partial p}{\partial y} \cong g\rho\frac{\partial \zeta}{\partial y} \tag{5.17}$$

and by defining the layer-integrated velocities as:-

$$q_x = \langle u \rangle = \bar{u}\Delta Z, \qquad q_y = \langle v \rangle = \bar{v}\Delta Z, \tag{5.18}$$

then equations 5.11 and 5.12 can be rewritten as:-

$$\begin{aligned}\left.\frac{\partial q_x}{\partial t}\right|_k + \left[\frac{\partial \bar{u}q_x}{\partial x} + \frac{\partial \bar{v}q_x}{\partial y}\right]_k &= fq_y\big|_k - g\Delta Z\left.\frac{\partial \zeta}{\partial x}\right|_k \\ &+ \left\{\frac{\partial}{\partial x}\varepsilon_h\Delta Z\left[\frac{\partial \bar{u}}{\partial x} + \frac{\partial \bar{u}}{\partial x}\right] + \frac{\partial}{\partial y}\varepsilon_h\Delta Z\left[\frac{\partial \bar{u}}{\partial y} + \frac{\partial \bar{v}}{\partial x}\right]\right\}_k \\ &+ \left(w\bar{u}\right)_{k+½} - \left(w\bar{u}\right)_{k-½} + \frac{1}{\rho}\left(\tau_{xz}\big|_{k-½} - \tau_{xz}\big|_{k+½}\right)\end{aligned} \tag{5.19}$$

$$\begin{aligned}\left.\frac{\partial q_y}{\partial t}\right|_k + \left[\frac{\partial \bar{u}q_y}{\partial x} + \frac{\partial \bar{v}q_y}{\partial y}\right]_k &= -fq_x\big|_k - g\Delta Z\left.\frac{\partial \zeta}{\partial y}\right|_k \\ &+ \left\{\frac{\partial}{\partial x}\varepsilon_h\Delta Z\left[\frac{\partial \bar{v}}{\partial x} + \frac{\partial \bar{u}}{\partial y}\right] + \frac{\partial}{\partial y}\varepsilon_h\Delta Z\left[\frac{\partial \bar{v}}{\partial y} + \frac{\partial \bar{v}}{\partial y}\right]\right\}_k \\ &+ \left(w\bar{v}\right)_{k+½} - \left(w\bar{v}\right)_{k-½} + \frac{1}{\rho}\left(\tau_{yz}\big|_{k-½} - \tau_{yz}\big|_{k+½}\right)\end{aligned} \tag{5.20}$$

At the free surface ($k = 1$), the terms $\left(w\bar{u}\right)_{k-½}$ and $\left(w\bar{v}\right)_{k-½}$ can be eliminated using the kinematic free surface condition and Leibnitz rule, and at the bed ($k = NL$) the terms $\left(w\bar{u}\right)_{k+½}$ and $\left(w\bar{v}\right)_{k+½}$ are zero, due to the no-slip boundary condition. To recap, equation 5.9 is the layer-integrated continuity equation (where 5.10 represents the continuity equation at the free surface) and is used to calculate the vertical velocities, and equations 5.19 and 5.20 are the layer-integrated momentum equations, which are used to solve the horizontal velocities, and water elevations.

5.2.2 Two-dimensional depth-integrated equations

When the number of layers is reduced to unity the continuity and momentum equations become the depth-integrated two-dimensional equations, i.e. the model reverts to DIVAST. These equations are given as:-

$$\frac{\delta\zeta}{\delta t}+\frac{\delta q_x}{\delta x}+\frac{\delta q_y}{\delta y}=0 \qquad 5.21$$

$$\frac{\partial q_x}{\partial t}+\beta\left[\frac{\partial U q_x}{\partial x}+\frac{\partial V q_y}{\partial y}\right]=fq_y-gH\frac{\partial\zeta}{\partial x} +\left\{\frac{\partial}{\partial x}\varepsilon_h H\left[\frac{\partial U}{\partial x}+\frac{\partial U}{\partial x}\right]+\frac{\partial}{\partial x}\varepsilon_h H\left[\frac{\partial U}{\partial y}+\frac{\partial V}{\partial x}\right]\right\} +\frac{1}{\rho}\left(\tau_{xz}\big|_{\zeta}-\tau_{xz}\big|_{-h}\right) \qquad 5.22$$

$$\frac{\partial q_y}{\partial t}+\beta\left[\frac{\partial U q_y}{\partial x}+\frac{\partial V q_y}{\partial y}\right]=fq_x-gH\frac{\partial\zeta}{\partial y} +\left\{\frac{\partial}{\partial x}\varepsilon_h H\left[\frac{\partial V}{\partial x}+\frac{\partial U}{\partial y}\right]+\frac{\partial}{\partial y}\varepsilon_h H\left[\frac{\partial V}{\partial y}+\frac{\partial V}{\partial y}\right]\right\} +\frac{1}{\rho}\left(\tau_{yz}\big|_{\zeta}-\tau_{yz}\big|_{-h}\right) \qquad 5.23$$

where q_x and q_y are the depth-integrated discharges per unit width (or depth-integrated velocities) in the x and y directions respectively, U and V are the depth-averaged velocities, where $q_x = UH$ and $q_y = VH$ and β is the momentum correction factor to account for a non-uniform velocity profile.

5.3 Numerical model: ANSYS CFX

The following section provides a general overview of CFX, as well as the particular features and capabilities used in this research study. The aim of using this model was to focus on the near-field scale. Furthermore, the model was only applied at a physical model scale: a like-for-like model of the HRC's recirculating flume was created to enable validation with the data obtained in Chapter 4. Therefore common setup parameters between the various flume models are discussed herein, with specific details of the individual model setups used being given in the relevant sections of Chapter 6.

5.3.1 Model overview

CFX is a general purpose CFD program that can be applied to a wide range of fluid flow problems. It is integrated into the ANSYS Workbench platform and can therefore be coupled with a wide range of programs, from CAD creation and modification, to structural analysis software. CFX can solve any mesh topology, which is a particular advantage as complex geometries can be modelled. It is principally a 3D solver, however 2D simulations can be executed by extruding the mesh by one element in the third dimension, with the model using an element based finite volume method to solve the unsteady Navier-Stokes equations (ANSYS, Inc. 2010b). The capabilities within CFX include the potential to model: laminar and turbulent flow, steady-state flow, quasi-steady and transient flow, ideal and real gases, heat transfer, rotating and stationary domains, Lagrangian particle tracking, chemical reactions and combustion, mesh motion and re-meshing, fluid structure interaction, and rigid body dynamics, to name but a few. Of particular interest in this study were the mesh motion and rotating domain capabilities, as these are necessary to model the unsteady behaviour of the blades etc. in vertical axis turbines. The CFX Expression Language (CEL) also enabled a wide range of functions to be created, which could be applied as boundary conditions, or other modelling constraints.

5.3.2 Model setup

As discussed CFX is integrated into the ANSYS Workbench platform, and relies on other software to generate the geometry and mesh files required to run a simulation. CFX itself consists of three main components, namely: CFX-Pre, for model setup, CFX-Solver, which runs the simulation, and CFX-Post, which is used for post-processing.

The model geometries were created using the DesignModeller software within ANSYS Workbench. This software is similar in capability to a number of CAD packages, and therefore a detailed description is not necessary. A flume model including the turbine geometries was created, and this was decomposed into a number of bodies. This enabled stationary and rotating domains to be later defined, as well as allowing the creation of simpler, structured meshes in the applicable flume sections.

The mesh used in a CFD model plays a critical role in the accuracy of the solution. The computational and practical resources available usually limit the size and number of elements in a mesh, and therefore a suitable sizing must be chosen which strikes a balance between solution accuracy, and computational cost. Structured meshes are more efficient in terms of the number of cells created, and were therefore used in the long sections of the flume, whereas an unstructured mesh was used around the irregular geometry of the turbine. Modelling the near-wall region is a complex process that, depending on the modelling strategy, can increase the mesh requirements dramatically. For example, if the Reynolds Stress Model (RSM) is used as a method of turbulence closure then a very fine mesh resolution is required to accurately resolve the boundary layer, whereas the use of wall functions, which provide a near-wall boundary condition, allow a much larger mesh resolution to be used. For this reason wall functions were used in this thesis. Many metrics exist to determine the quality of a mesh, and one which is of high importance is the y^+ number, given in equation 5.24. This is a dimensionless distance from a wall, and its upper limit is a function of the Reynolds number, therefore determining an appropriate mesh sizing is usually an iterative process. The dimensionless wall Reynolds number used in ANSYS can be defined as:

$$y^+ = \frac{U_* \Delta n}{\upsilon} \qquad 5.24$$

where U_* is the friction velocity and Δn is the distance between the first and second grid points from the wall (ANSYS, Inc. 2010b).

CFX-Pre is used to define all of the simulation settings and parameters, from importing a mesh to creating results files. The following outlines the main requirements to setup a simulation:

- ***Analysis type***- steady state (time-independent) or transient (time-dependant), and where applicable the time step size and duration of simulation.
- ***Domain definition***- identifying the fluid flow domains, and applying appropriate materials definition, initialisation, turbulence closure, and domain motion if applicable. If multiple domains are used then interfaces must also be defined.

- ***Boundary conditions***- inflow and outflow conditions, wall properties, and any other functions using CEL language.
- ***Solver control***- selection of specific numerical methods and controls for the CFX-Solver.
- ***Output control***- selection of results and variables to be exported for post-processing.

For further details the reader is referred to the CFX-Pre user guide (ANSYS, Inc. 2010a). Finally, after the simulation has been completed, the CFX-Post software enables visualisation of the results. In addition these results can be exported for use in other spreadsheet software tools, such as MS Excel.

5.3.3 Mesh motion

Modelling the motion of moving objects adds another level of complexity to a CFD model. If the body is rigid and has 1 degree of freedom, which is the case for a typical tidal stream turbine with no pitch control, then this can be achieved in CFX with relative ease: two domains can be defined - one that contains the main flume geometry and is stationary, and a cylindrical domain that contains the turbine geometry, which is then able to rotate inside the stationary domain. These two domains are connected with a rotor-stator interface. In using this method the mesh itself does not deform and therefore the mesh sizing remains the same, which is advantageous for ensuring model accuracy.

Modelling multiple degrees of freedom is more challenging, as usually mesh deformation is required, and contact between bodies is not possible. Depending on the mesh sizing, small deformations such as a change in blade pitch angle are possible. However, as the mesh deforms the solution accuracy can become compromised and if the deformations become too large this can cause the mesh to fold, thereby causing the model to crash. Limits can be set to prevent these problems and re-meshing commands can be executed to maintain solution accuracy. However, this comes at a high computational cost, and is often considered an unstable method of modelling.

Modelling the CarBine turbines proved to be particularly challenging, due to each flap needing to be able to rotate about its local axis, as well as the global axis of the turbine.

Due to the high computational cost re-meshing methods were considered unfeasible in this thesis and therefore it was not possible to fully model the double flap turbine configurations, as the swept areas of the flaps overlapped with each other. However, the single flap configuration was modelled, as there was no mesh interaction between the blades. The solution required a rotating domain for each flap, each of which was nested inside a larger rotating domain containing the entire turbine, as shown in Figure 5.3.

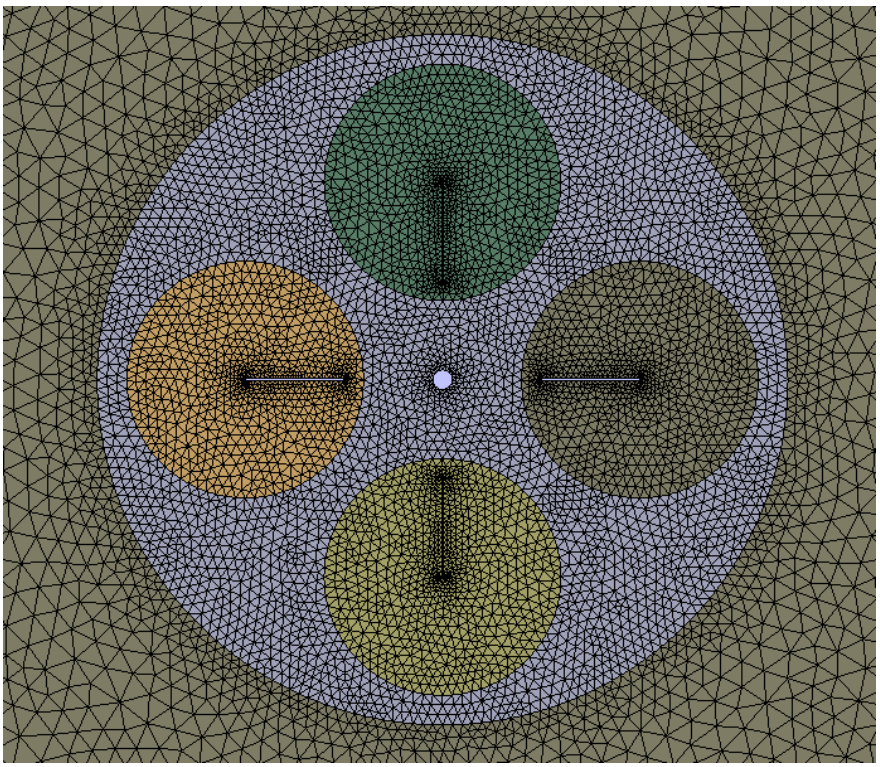

Figure 5.3 Multiple domains and subdomains used to model the CB_4S turbine to enable mesh motion with multiple degrees of freedom

This feature did not exist in CFX, therefore a number of subdomains were defined and using CEL expressions the position of each subdomain could be defined, these expressions and their implementation for a single flap are shown in Figure 5.4 and Figure 5.5, where similar expressions were defined for the remaining flaps. The position of each flap was prescribed using a look-up table, which was defined based on observations from the laboratory tests. Ideally the motion would have been calculated based on the forces acting on each flap, and this is considered as a future development to the model. Due to this prescribed movement of the flaps, as well as the fact that the single flap turbines are very inefficient (as identified in Chapter 4) this model was not considered in performance predictions, but only in the wake characterisation tests. To

the author's knowledge, there has been no prior publication of the use of this mesh motion method to model tidal stream turbines.

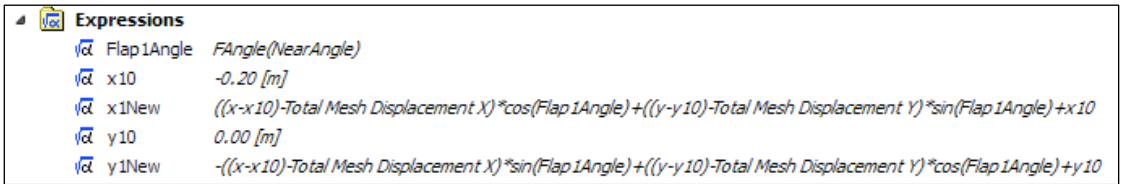

Figure 5.4 Screenshot of CEL expressions used to define mesh motion for a single flap where similar expressions were derived for other flaps

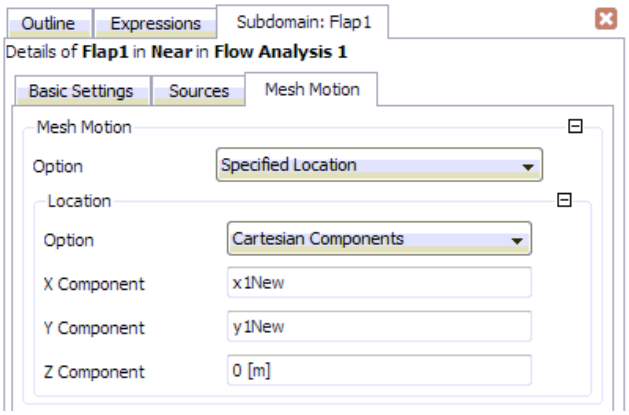

Figure 5.5 Screenshot of the implementation of the new mesh coordinates for a subdomain which contained flap 1, where this process was repeated for all subdomains

5.3.4 Tidal stream turbine analysis

CFX automatically calculates the force on all wall boundaries, and as the turbine geometries were accurately modelled, it was a relatively straightforward process to calculate the power output of the turbine, and record the velocities downstream for the wake characterisation study. CEL expressions were created to monitor the torque acting on the turbine blades, and a second expression was then created to calculate the power, by multiplying this torque by the already defined angular velocity of the turbine. Similarly, time-series data and velocity profiles at the relevant locations were extracted from CFX-Post, with the locations being the same as those used in the physical model tests. Table 5.1 provides a summary of the turbines tested using CFX in this research study, with further details of each model being given in Chapter 6.

Table 5.1 Summary of tests conducted using CFX

Performance tests		
Turbine tested	***Analysis type***	***Test details***
CB_1D	2D Transient	Idealised test taking only positive torque, as it was assumed flaps remove negative torque
SAV_LRG	2D Transient	Model ran for 4 revolutions as torque was repeatable
Wake Characterisation		
Turbine tested	***Analysis type***	***Test details***
CB_4S	3D Transient	Mesh motion applied. Model ran for 100 revolutions, to ensure downstream velocities had stabilised
SAV_SML	3D Transient	Model ran for 100 revolutions, to ensure downstream velocities had stabilised
SAV_LRG	3D Transient	Model ran for 100 revolutions, to ensure downstream velocities had stabilised

5.4 Numerical model: TRIVAST

5.4.1 Model overview

The numerical model TRIVAST (ThRee dimensional layer Integrated Velocities And Solute Transport) solves the layer-integrated RANS equations, previously derived in section 5.2.1, as well as the solute transport equation. It is therefore capable of simulating a wide range of water quality parameters, however, in this thesis only the hydrodynamic aspects of the model are discussed. The model was originally developed by Lin and Falconer (1997), and was originally written in the FORTRAN 77 programming language. However, it has since been rewritten in the FORTRAN 90 programming language, and continues to be developed by academic researchers in the Hydro-environmental Research Centre. Whilst CFX can be applied to almost any type of fluid flow problem, TRIVAST is better suited to modelling large water bodies, such as lakes, estuaries and coastal basins. The model comprises of three main components, namely: the source code, and global common block file, which defines all data arrays and constants, and a model input file, which is used to define an individual model setup.

5.4.2 Implementation of governing equations

The governing equations were solved using a combined implicit and explicit finite difference method. An Alternating Direction Implicit (ADI) scheme was used to solve the depth-integrated equations (i.e. equations 5.21, 5.22 and 5.23), as used in DIVAST. For the layer-integrated equations (i.e. equations 5.9, 5.19 and 5.20), the vertical

diffusion terms were treated implicitly using the Crank-Nicholson scheme, whilst the remaining terms were treated explicitly. In the horizontal plane, the equations were solved using a space staggered regular grid system, with the water elevations, ζ, calculated at the centre of each cell, whereas the velocities and bathymetric data are specified at the centre of each grid side, as shown in Figure 5.6.

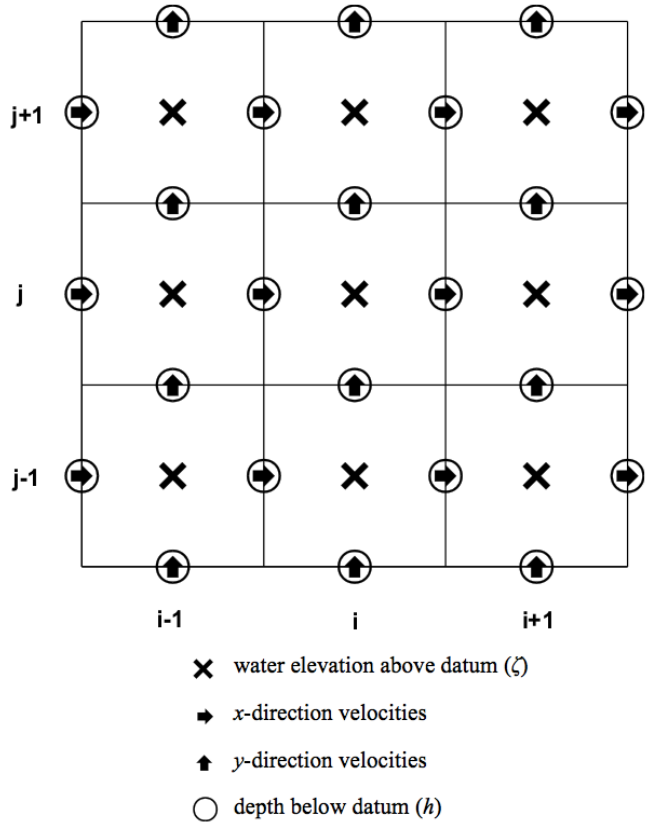

Figure 5.6 Computational space staggered grid system used in horizontal plane

The ADI scheme involves the sub-division of each time step into two half time steps, therefore in the first half time step (n to $n+½$) the water elevations and x-direction velocities were resolved, and similarly for the second half time step ($n+½$ to $n+1$) the water elevations were recalculated, and the y-direction velocities resolved. The following outlines the main solution for the first half time step:

1. The depth-integrated equations are solved to obtain the water elevations, and therefore the pressure gradient term.
2. The layer-integrated equations are then solved using the pressure gradient term from (1) to obtain the layer-averaged velocity $\bar{u}$.

3. The momentum correction factor, β, and the relevant stresses are calculated using the layer-averaged velocity from (2), to refine the depth-averaged solutions.
4. Steps (1) to (3) are iterated over a specified number of times (usually two), then the procedure continues to step (5).
5. The vertical velocity component can then be calculated.
6. Checks for flooding and drying are then made.

This process is then repeated for the *y*-direction equations.

In writing the layer-integrated equations in finite-difference form, equations 5.19 and 5.20 were rearranged in such a way that the LHS represents the terms to be solved implicitly, with the remaining terms on the RHS, to be solved explicitly. This was written in the form (for the *x*-direction only):

$$\underbrace{S_{x0}}_{\textit{implicit terms}} = \underbrace{S_x}_{\textit{explicit terms}}, \textit{where } S_x = ADV + COR + PRE + DIF + VTC \qquad 5.25$$

where S_{x0} represents the local acceleration and vertical diffusion terms, *ADV* are the advective accelerations, *COR* is the Coriolis term, *PRE* is the pressure gradient, *DIF* are the horizontal diffusion terms and *VTC* is the vertical convection term. These terms are written in their respective finite difference forms as:-

$$\begin{aligned} S_{x0} = \left((\overline{u}\Delta Z)_k^{n+½} - (\overline{u}\Delta Z)_k^{n-½}\right) - \frac{\Delta t}{2}\left(\frac{\varepsilon_v}{\Delta Z}\right)_{k-½}\left[\left(\overline{u}_{k-1}^{n+½} - \overline{u}_k^{n+½}\right) + \left(\overline{u}_{k-1}^{n-½} - \overline{u}_k^{n-½}\right)\right] \\ + \frac{\Delta t}{2}\left(\frac{\varepsilon_v}{\Delta Z}\right)_{k+½}\left[\left(\overline{u}_k^{n+½} - \overline{u}_{k+1}^{n+½}\right) + \left(\overline{u}_k^{n-½} - \overline{u}_{k+1}^{n-½}\right)\right] \end{aligned} \qquad 5.26$$

$$ADV = -\frac{\Delta t}{\Delta x}\left[\overline{u}' q_x'\Big|_{i+1,j,k}^n - \overline{u}' q_x'\Big|_{i,j,k}^n + \overline{u}' q_x\Big|_{i+½,j+½,k}^n - \overline{u}' q_x\Big|_{i+½,j-½,k}^n\right] \qquad 5.27$$

$$COR = \Delta t \cdot f \cdot q_y\Big|_{i+½,j,k}^n \qquad 5.28$$

$$PRE = -\frac{g\Delta t}{2\Delta x}\Delta Z_{i+½,j,k}^n\left[\zeta_{i+1,j}^{n+½} + \zeta_{i+1,j}^{n-½} - \zeta_{i,j}^{n+½} - \zeta_{i,j}^{n-½}\right] \qquad 5.29$$

$$DIF = \frac{\Delta t}{(\Delta x)^2}\left\{2\left[\varepsilon_h \Delta Z^n_{i+1,j,k}\left(\overline{u}'_{i+3/2,j,k} - \overline{u}'_{i+1/2,j,k}\right) - \varepsilon_h \Delta Z^n_{i,j,k}\left(\overline{u}'_{i+1/2,j,k} - \overline{u}'_{i-1/2,j,k}\right)\right]\right.$$
$$+\left[\varepsilon_h \Delta Z^n_{i+1/2,j+1/2,k}\left(\overline{u}'_{i+1/2,j+1,k} - \overline{u}'_{i+1/2,j,k}\right) - \varepsilon_h \Delta Z^n_{i+1/2,j-1/2,k}\left(\overline{u}'_{i+1/2,j,k} - \overline{u}'_{i-1/2,j-1,k}\right)\right] \quad 5.30$$
$$\left.+\left[\varepsilon_h \Delta Z^n_{i+1,j,k}\left(\overline{v}'_{i+3/2,j,k} - \overline{v}'_{i+1/2,j,k}\right) - \varepsilon_h \Delta Z^n_{i,j,k}\left(\overline{v}'_{i+1/2,j,k} - \overline{v}'_{i-1/2,j,k}\right)\right]\right\}$$

$$VTC = \Delta t\left[\left(w\overline{u}'\right)_{1+1/2,j,k+1/2} - \left(w\overline{u}'\right)_{1+1/2,j,k-1/2}\right] \quad 5.31$$

where similar expressions can be obtained for the *y*-direction. Further rearrangement of equation 5.25 gives:-

$$p \cdot \overline{u}^{n+1/2}_{k-1} + q \cdot \overline{u}^{n+1/2}_{k} + r \cdot \overline{u}^{n+1/2}_{k+1} = s + S_x \quad 5.32$$

where:

$$p = -\frac{\Delta t}{2}\left(\frac{\varepsilon_v}{\Delta Z}\right)_{k-1/2} \quad 5.33$$

$$q = \Delta Z_k + \frac{\Delta t}{2}\left[\left(\frac{\varepsilon_v}{\Delta Z}\right)_{k-1/2} + \left(\frac{\varepsilon_v}{\Delta Z}\right)_{k+1/2}\right] \quad 5.34$$

$$r = -\frac{\Delta t}{2}\left(\frac{\varepsilon_v}{\Delta Z}\right)_{k+1/2} \quad 5.35$$

$$s = \Delta Z_k \overline{u}^{n-1/2}_k + \frac{\Delta t}{2}\left\{\left(\frac{\varepsilon_v}{\Delta Z}\right)_{k-1/2} \overline{u}^{n-1/2}_{k-1}\right.$$
$$\left.-\left[\left(\frac{\varepsilon_v}{\Delta Z}\right)_{k-1/2} + \left(\frac{\varepsilon_v}{\Delta Z}\right)_{k+1/2}\right]\overline{u}^{n-1/2}_k + \left(\frac{\varepsilon_v}{\Delta Z}\right)_{k+1/2} \overline{u}^{n-1/2}_{k+1}\right\} \quad 5.36$$

The arrangement shown in equation 5.32 creates a tri-diagonal system of equations, the size of which is equal to the number of layers, given in equation 5.37:

$$\begin{pmatrix} q_1 & r_1 & \cdots & & 0 \\ p_2 & q_2 & r_2 & & \\ \vdots & & \ddots & & \\ & & p_{k-1} & q_{k-1} & r_{k-1} \\ 0 & & & p_k & q_k \end{pmatrix} \cdot \begin{pmatrix} \overline{u}_1^{n+½} \\ \overline{u}_2^{n+½} \\ \vdots \\ \overline{u}_{k-1}^{n+½} \\ \overline{u}_k^{n+½} \end{pmatrix} = \begin{pmatrix} (s+S_x)_1 \\ (s+S_x)_2 \\ \vdots \\ (s+S_x)_{k-1} \\ (s+S_x)_k \end{pmatrix} \qquad 5.37$$

The tri-diagonal matrix is then solved using the Thomas algorithm, therefore returning the unknown layer-averaged velocity in the *x*-direction at the end of the first half time step, i.e. $\overline{u}_k^{n+½}$. This process is then repeated in the *y*-direction, returning values for $\overline{v}_k^{n+1}$ across the domain.

5.4.3 Model setup

Once any development to the source code has been made, the model is compiled and built into an executable file. The input file must then be established, in which the relevant input data must be supplied, and model constants set to appropriate values. A brief outline of the structure and required data of the input file is as follows:

- Define IMAX, JMAX and KMAX, i.e. the maximum arrays dimensions.
- Specify the length of the simulation, and the time step size.
- Specify the grid size, bed roughness, eddy viscosity coefficient, and other hydrodynamic parameters.
- If relevant, specify constants relevant to solute transport.
- Supply the location and data of boundary conditions.
- Specify the domain description block (IWET array), which defines cells to be included in calculations (i.e. 0=dry, 1= wet cell).
- Specify bathymetric data for all grid cells (with dry cells having a depth of -99.9 m).

Once the input file has been established the model can be executed through the command line. Results files are created through custom subroutines, and therefore can be used in any post-processing software. In this thesis, the software package Tecplot was used for data visualisation, as too was MS Excel.

5.4.4 Implementation of marine renewable energy technologies

As the governing equations are based on the principles of continuity of mass and conservation of momentum, any energy extracted through marine renewable energy technologies must be conserved. The governing equations therefore had to be modified to represent this energy loss, and this was achieved through the use of momentum source and sink terms.

5.4.4.1 Tidal stream turbine representation

To model the effects of a tidal stream turbine, the thrust force from the turbine blades, as well as the drag force from the supporting structure, were accounted for in the momentum sinks. These terms were treated explicitly in TRIVAST, and added to equation 5.25 as follows:

$$S_x = ADV + COR + PRE + DIF + VTC + TST_{thrust,x} + TST_{drag,x} \quad 5.38$$

where $TST_{thrust,x}$ and $TST_{drag,x}$ are the thrust and drag forces respectively, per unit volume of flow, given as:

$$TST_{thrust,x} = \frac{\pm 1}{\Delta x \Delta y \Delta z} \times \frac{C_T}{2} A \left(\overline{u}_k^n \right)^2 \quad 5.39$$

$$TST_{drag,x} = \frac{\pm 1}{\Delta x \Delta y \Delta z} \times \frac{C_D}{2} A \left(\overline{u}_k^n \right)^2 \quad 5.40$$

where C_T and C_D are the thrust and drag coefficients respectively, which depend on the individual characteristics of the turbines modelled, and A is the turbine area normal to the incoming flow.

5.4.4.2 Barrage representation

To model the effects of a tidal barrage, the structure was treated as a standard no-slip wall boundary, and cells either side were selected to transfer the necessary fluid volume and momentum across the barrage, as shown in Figure 5.7 Cell description for barrage layoutFigure 5.7.

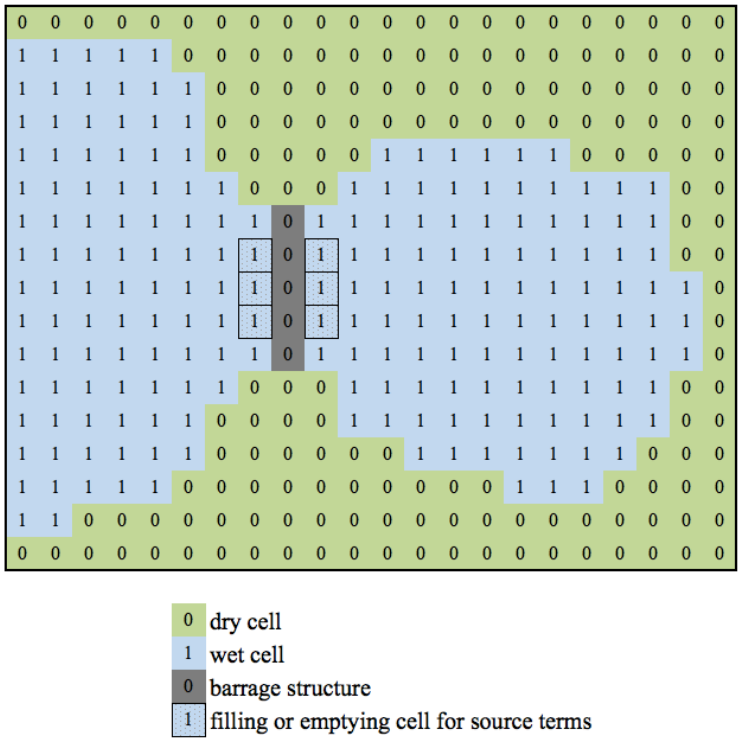

Figure 5.7 Cell description for barrage layout

The source terms added to the continuity and momentum equations are given as follows, which were based on modelling the flow through an orifice (Baker 1991):-

$$w_{k-\frac{1}{2}} = -\sum_{l=k}^{NL}\left\{\frac{\partial(hu)}{\partial x}+\frac{\partial(hv)}{\partial y}\right\} \pm BARR_{cont,x} \qquad 5.41$$

$$S_x = ADV + COR + PRE + DIF + VTC \pm BARR_{mom,x} \qquad 5.42$$

where the sign of each term depends on whether the respective cell is filling or emptying, and each term can be defined as:

$$BARR_{cont,x} = \frac{1}{\Delta x \Delta y} \times q_{orifice} \qquad 5.43$$

$$BARR_{mom,x} = \frac{1}{\Delta x \Delta y \Delta z} \times \rho q_{orifice} u_{orifice} (1-\eta), \quad \textit{if cell is filling} \qquad 5.44$$

or

$$BARR_{mom,x} = 0, \qquad \textit{if cell is emptying (velocity assumed zero)} \qquad 5.45$$

where

$$q_{orifice} = C_{orifice} A_{orifice} \sqrt{2g\Delta H}, \qquad and\ u_{orifice} = {q_{orifice}}/{A_{orifice}} \qquad 5.46$$

The power extracted from the barrage is therefore defined as:

$$BARR_{power} = \eta \rho g q_{orifice} \Delta H \qquad 5.46$$

where $C_{orifice}$ is a discharge coefficient, $A_{orifice}$ is the turbine area, ΔH is the difference in water levels on either side of the barrage, and η is the turbine efficiency. Therefore the orifice can also be operated as a sluice gate, by setting $\eta=0$, and using the appropriate discharge coefficient.

To summarise, this chapter provides details of the computational fluid dynamic models used in this thesis. A RANS modelling approach was adopted, with two different models being used in this study. Firstly, the commercial code ANSYS CFX was used to model the near-field aspects of tidal stream turbines, and then the hydro-environmental model TRIVAST was applied to the Severn Estuary, to investigate the impact of marine energy technologies at a far-field scale. Detailed derivations of the governing equations were made using the notation used in the TRIVAST model. Finally, details have also been given of the methods and source code modifications implemented to model both tidal stream and tidal range devices.

Chapter 6 CFX model application

6.1 Recirculating flume model

Before any turbine geometries could be modelled, a reference model of the flume was established in 2 and 3 dimensions, to obtain a suitable mesh sizing for the free-stream flow conditions. Whilst the recirculating flume has a working length of 17m, this length was shortened in the CFX model to reduce the number of mesh elements. For performance tests, a total length of 6m (3m upstream and 3m downstream) was modelled to ensure the near wake region was captured, whilst for the wake characterisation tests a total length of 13m (3m upstream and 10m downstream) was used. A swept rectangular mesh was used as shown in Figure 6.1, with a maximum grid sizing of 0.025m applied to the cells, with a smaller grid spacing applied in the proximity of the wall boundaries. These boundaries were treated with a no-slip wall condition.

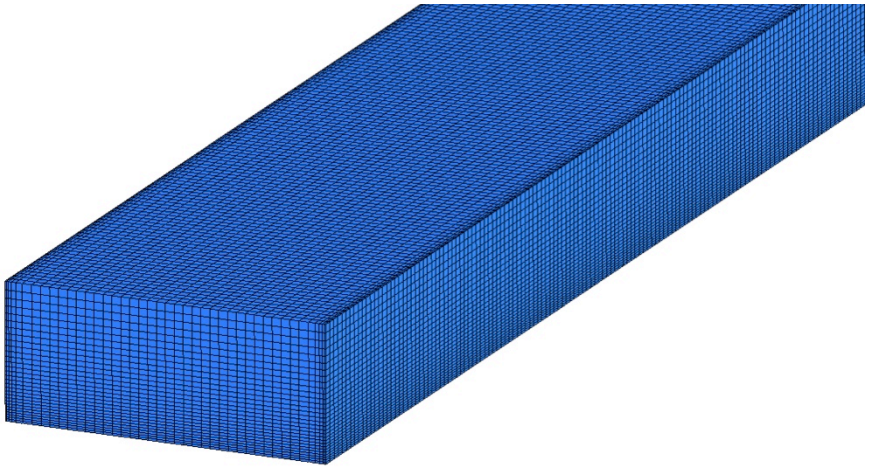

Figure 6.1 Structured mesh used in 3D model of the recirculating flume

As free surface effects were observed to be small in the laboratory, it was decided to model the surface as a free slip wall as opposed to a two-phase solution, as this would have dramatically increased the computational cost. The inlet boundary was defined using the following flow profiles, which were based on data collected in the physical model tests. A parabolic velocity profile was then fitted in the horizontal plane, and a logarithmic profile in the vertical. A static pressure boundary was defined at the outlet. The model was run as a steady-state simulation using automatic timescales, and finally, the k-ε turbulence model was used to close the governing equations.

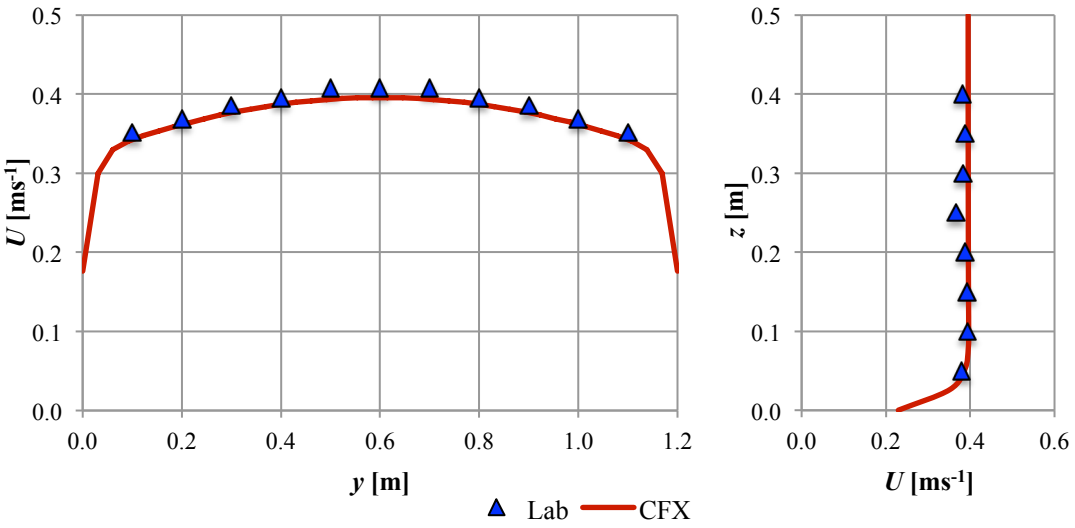

Figure 6.2 Velocity profiles in the recirculating flume, comparing CFX predictions and laboratory measurements (Left: horizontal profile at x/D = 0, Right: vertical profile at x/D = 0)

The validation of the CFX predictions with the previously obtained laboratory data is given in Figure 6.2. This was for flow condition [A], as defined in Chapter 3, in which the average streamwise velocity was 0.38 ms^{-1}. Good agreement was shown between the two datasets, which confirmed the applicability of using this mesh sizing for the far-wake and upstream regions of the flow. Figure 6.3 shows further visualisation of the flow field in the recirculating flume. The development of the boundary layers at the bed and side walls due to the boundary shear stresses can be seen with increasing distance downstream.

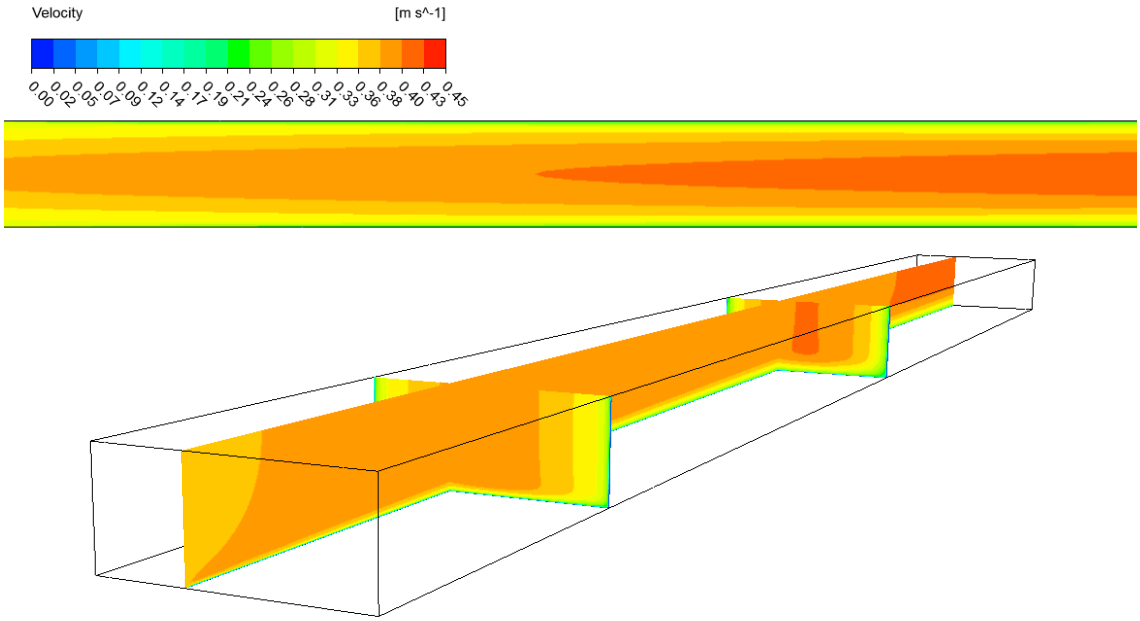

Figure 6.3 Velocity magnitude contours of recirculating flume

6.2 Performance predictions

With a reference model of the recirculating flume established, an initial performance assessment of two tidal stream turbines was conducted, namely: the CarBine and Savonius turbines. To assess the performance of each turbine a process similar to that previously conducted in the experimental tests was undertaken: the *TSR* of the turbines was varied over a number of simulations, and for each corresponding point the turbine power and efficiency were calculated, thereby obtaining the power and torque curves of the device. The performance tests were conducted using a 2D model, and using an average flow velocity of 0.78 ms^{-1}, which corresponded to flow condition [B], to provide a comparison with previously obtained laboratory data.

The accuracy of performance predictions depends on the mesh sizing around the turbine geometry, and as a result for both turbines three separate meshes were modelled: a low, medium and high resolution mesh, details of which are given in Table 6.1. For the main geometry of the flume the mesh in the recirculating flume model was used. To reduce the total simulation time for this study, a reduced number of points were re-run with the medium and high resolution meshes, with the points focused around the peak efficiency as identified by the initial curve obtained with the low resolution mesh.

Table 6.1 Approximate mesh sizing for different mesh files used

Mesh resolution	*Average mesh sizing on turbine blade*	*Approx. number of elements*	*Time taken per operating point (hr)*
LQ	10 mm	10,000	1
MQ	2 mm	50,000	5
HQ	0.5 mm	100,000	10

The time step of the model was varied depending on the chosen *TSR*, and for all simulations an equal number of time steps were solved per revolution. Therefore, for faster turbine speeds the time step decreased, in order to capture the transient effects of the flow. In this study 360 time steps were solved in a single revolution, i.e. the turbine was rotated 1 degree every time step. The accuracy of each solution was quantified by not only comparing the predicted values of power, but also through monitoring the solution residuals during runtime, and other parameters such as the y^+ number. For the low, medium and high meshes the average y^+ numbers were 90, 30 and 15, respectively,

an example of which is given in Figure 6.4. For the k-ε turbulence model the CFX documentation recommends that the y^+ values should be between 11 and 100.

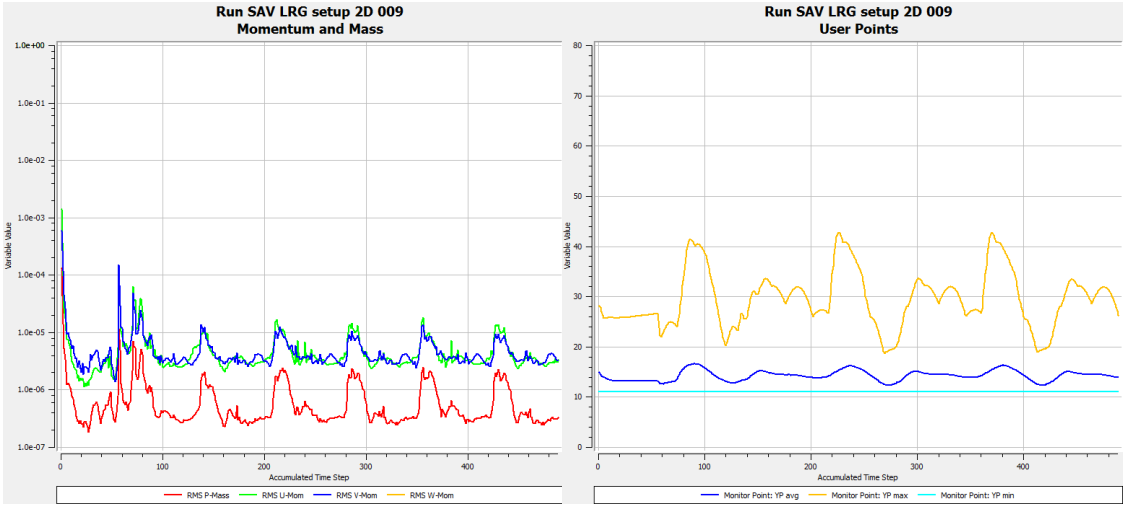

Figure 6.4 Example of solution residuals

6.2.1 CarBine performance

Modelling the CarBine turbines was a complex task due to the multiple degrees of freedom that govern the behaviour of the turbine. As identified in the previous experimental work conducted in Chapter 4, the single flap configurations of the CarBine turbine were poor in terms of efficiency, and therefore there was little value in assessing the performance using CFD techniques. Furthermore, the mesh motion techniques developed in this study were only suitable for single flap turbines, as the double flaps would result in mesh interaction and would require computationally expensive re-meshing techniques. Therefore, to assess the performance of this turbine, an idealised model of CarBine was created, consisting of one rigid arm with closed double flaps, (which will be referred to from this point as the CB_1D configuration) as shown in Figure 6.5. This figure also highlights the varying mesh densities used in the low and high resolution models, respectively. Whilst the flaps did not open at any point during a revolution, predictions of performance were made under the assumption that all negative drag forces can be neglected, as in practise the flaps would be open thereby minimizing negative drag. This method will therefore be optimistic in predicting power output, and it is further limited by the fact that it does not simulate the action of the flaps opening and closing, and that the flow field will not be ideally representative of those for the CarBine turbine. Despite these limitations, it was deemed that this method

was suitable as an initial means of assessing the turbine performance, given the complex rotational behaviour of the device.

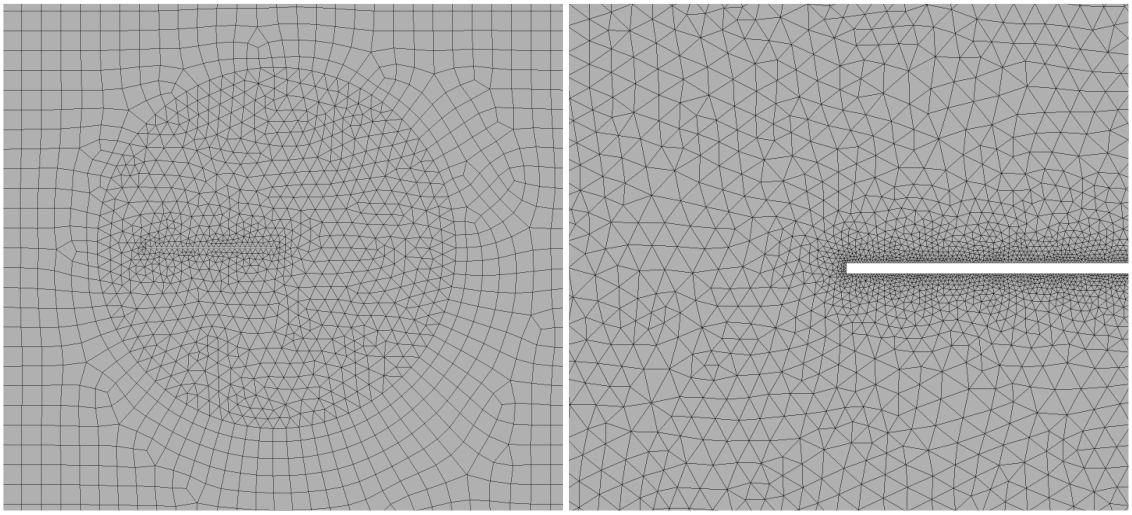

Figure 6.5 Low and high resolution meshes used for CB_1D configuration

The normalised performance values of power and torque for each mesh are given in Figure 6.6. The runtime of each point varied from 1 hour for the LQ mesh, to 10 hours for the HQ mesh. The results showed that despite this wide range in mesh density, the performance predictions were almost identical for each of the three cases. This is due to the relatively simple hydrodynamic behaviour of a flat plate (or closed flaps); the flap is only subjected to drag forces throughout a revolution. The curve shows two peaks in the power coefficient: one at a *TSR* of 0.4, for which the C_P value was equal to 0.15, and another at a *TSR* of 0.7, where the C_P was equal to 0.19. This second peak and the behaviour above a *TSR* of 0.4 were unexpected, as one would expect the performance to decrease until the turbine reached the point of freewheeling (i.e. maximum *TSR*). This increase in performance highlights the limitations of the method used. At higher turbine speeds the negative drag increases with the square of the relative speed between the flap and the fluid flow, and this is ignored using this method. In addition, as the flaps were permanently closed, the resulting flow and pressure fields would be different to those experienced by a turbine, which therefore would result in different forces acting on the flaps. Finally, in this model the turbine was rotated at a constant angular velocity, whereas in practise the flap would pulse as it rotated - a behaviour that has been identified in Chapter 4. This would significantly affect the forces acting on the flap as it completes a revolution.

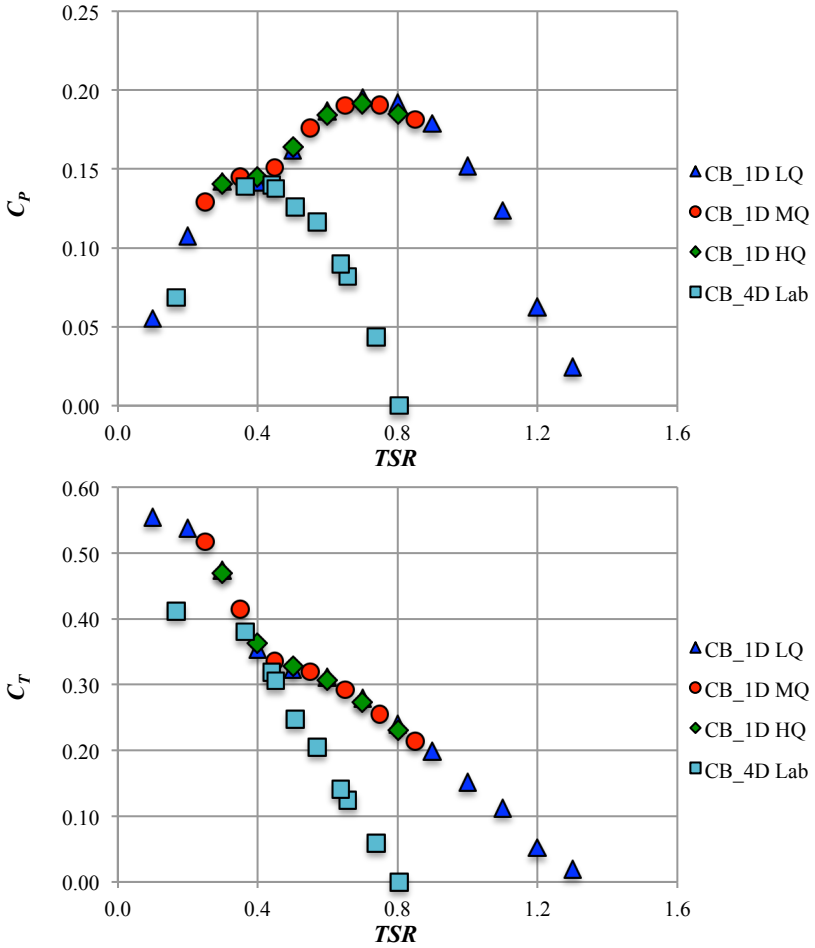

Figure 6.6 Normalised performance predictions for CB_1D configuration, comparing CFX predictions with laboratory data of the CB_4D turbine (Top: Power coefficient, Bottom: Torque coefficient)

In comparison with the laboratory data the model showed good agreement up until a *TSR* of 0.4 was reached, with a peak efficiency of 0.15 being predicted, as compared to a measured value of 0.14 in the laboratory. However, due to the reasons already discussed, when a *TSR* of 0.4 or above is used, then the predictions are greater than the laboratory data, with the maximum *TSR* being 1.3, compared to 0.8. Another factor to consider in this comparison is that in the four-arm configuration the flaps were closed for two arms during certain phases of a revolution, and there will therefore be interaction between the different arms. As the CB_1D model only used one closed arm, this interaction was not modelled.

6.2.2 Savonius performance

As the Savonius turbine has a solid geometry with no moving parts, it was much simpler to model its dynamic behaviour in comparison with the CarBine turbine. The exact geometry of the SAV_LRG configuration was used, as shown in Figure 6.7,

which also depicts the low and high-resolution meshes used in this study. Similar runtimes to the CB_1D model were observed, and again the monitored residuals and y^+ values were of a similar magnitude.

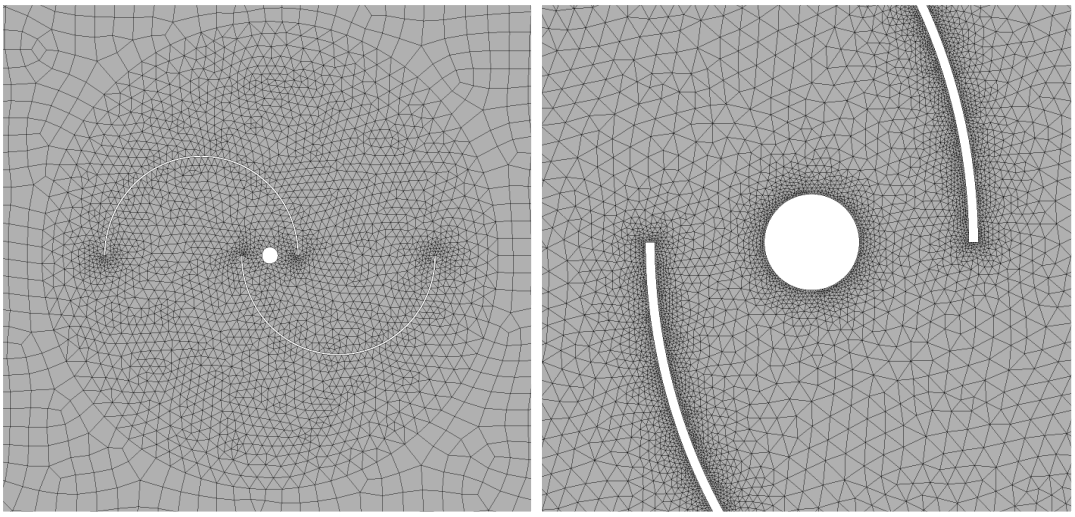

Figure 6.7 Low and high resolution meshes used for SAV_LRG configuration

The results, as shown in Figure 6.8, showed that unlike the CarBine model, the mesh sizing had a significant effect on the predictions of turbine performance. In the low resolution mesh a peak efficiency of 0.36 was predicted, at a *TSR* of 1.2, whereas with the high resolution mesh the peak efficiency predicted was lower, at 0.32 at a *TSR* of 1.0. This highlights the complex hydrodynamic behaviour of the flow field around the Savonius turbine, as lift forces as well as drag forces act on the turbine, which are highly sensitive to the flow over the buckets. A more suitable turbulence model may also have provided more consistent predictions, as it is widely accepted that the k-ε turbulence model does not perform as well as other models in cases of adverse pressure gradients and flow separation. Despite this the model performed well and showed good agreement with the laboratory data, in which the peak efficiency measured was 0.27 at a *TSR* of 1.0. Furthermore, the general shape of the curves is the same as the laboratory data, and similar values were predicted for the freewheeling *TSR*. Finally, it is anticipated that the accuracy of the predictions could be improved in two key ways: (i) improving the angular velocity representation of the turbine, as a constant value was used for each *TSR*, yet in reality the turbine pulses in phase with the number of buckets, and (ii) through running a 3D simulation, as 2D simulations are generally regarded to over-predict performance as the flow is constrained in the vertical dimension. This will,

however, significantly increase the computational cost and was not feasible in this study due to the large number of points being modelled.

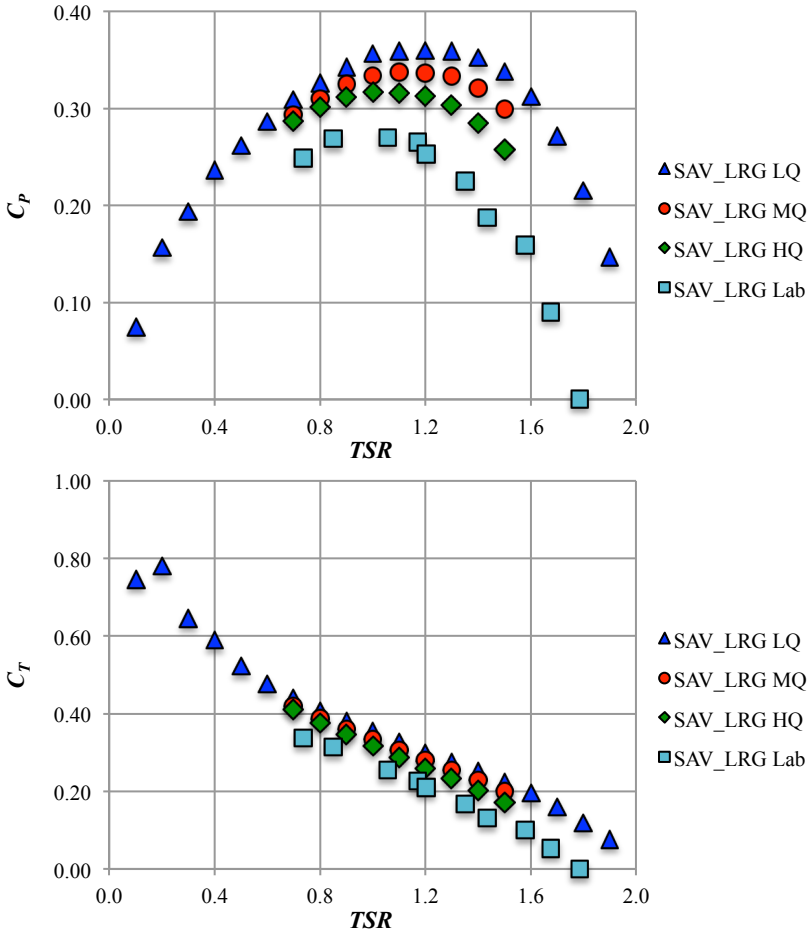

Figure 6.8 Normalised performance predictions for SAV_LRG configuration, comparing CFX predictions with laboratory data (Top: Power coefficient, Bottom: Torque coefficient)

6.3 Wake characterisation

The following section describes the application of CFX to predict the wake characteristics of three vertical axis turbine configurations, namely: the CB_4S CarBine configuration, and two different sizes of the Savonius turbine, the SAV_SML and SAV_LRG configurations respectively. Further details of the design of these turbines can be found in Chapter 3. Like-for-like models of these tests were developed using CFX to provide a comparison with the obtained data, therefore in considering the wake behaviour itself the reader is referred to the recirculating flume results in Chapter 4, with the aim of this section therefore focusing on the suitability of the CFD methods used.

As 3D flow effects were apparent in the flume a full 3D domain was used, as 2D predictions would bear little resemblance with the data due to the additional constraints to the flow. The number of mesh elements in the 3D domain increased dramatically, with approximately 2 million elements being used for each model, with this resolution reaching the memory limits of the computer. Despite this high number of elements, it was not possible to implement a mesh sizing of 0.5 mm around the buckets as used in the section 6.2, and in practise the mesh sizing around the buckets was of the order of 5 mm. Flow condition [A] was used, in which the average velocity was 0.38 ms^{-1}, and whilst a CFD simulation returns the velocities at each grid cell, specific monitoring points were created at identical locations to those used in the physical modelling tests to provide both unsteady and time-averaged point measurements. The length of the simulations was based on the turbine completing 100 revolutions, with this being enough time until the downstream velocities had shown repeatable behaviour, i.e. the unsteady solution had converged. Based on performance tests the turbines were rotated at their respective optimum *TSR*s, which was 0.45 for the CarBine turbine, and 1.0 for the Savonius. This unsteady solution procedure, combined with a 3D mesh, resulted in a long simulation time for each model, i.e. in excess of 3 weeks for a single turbine.

6.3.1 CB_4S turbine

Whilst from a performance perspective the single arm CarBine turbines were not considered due to their low efficiencies, a four arm, single flap CarBine configuration was modelled to investigate the wake characteristics of the device. This is because, to the author's knowledge, the mesh motion techniques developed to model this configuration have not been implemented in this way before, and if shown to provide good predictions this method could be applied to a number of related applications, for example to model dynamic pitching of turbine blades without the need of re-meshing.

The time-averaged vertical and horizontal velocity profiles of the CFX predictions compared with the obtained laboratory data are given in Figure 6.9 and Figure 6.10, respectively. Good agreement was observed with the laboratory data, with CFX accurately predicting the difference in velocities behind the open and closed flaps. The biggest difference between the two datasets was found at $x/D = 1$, $y/D = 0$ (see the left hand graph in Figure 6.9). This was due to the fact that the base and the other

supporting structure necessary to hold the turbine in the flume was not modelled, and the turbine shaft only extended between the two disks, whereas in the flume it protruded through the free surface to connect to the power take-off system. This was done to simplify the domain and reduce the number of mesh elements required; therefore the drag forces that these components would have imposed on the flow were not modelled.

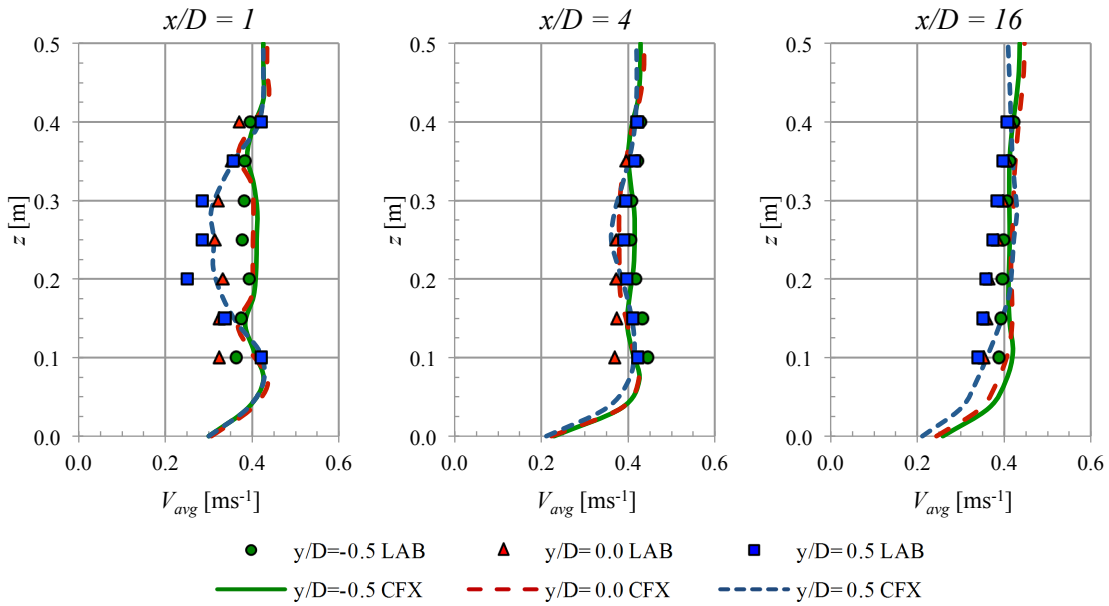

Figure 6.9 Comparison of time-averaged laboratory data and CFX predictions of vertical velocity profiles downstream of CB_4S turbine

The differences between the unsteady and time-averaged flow fields are shown in Figure 6.11. These contour plots highlight the necessity of using the transient methods implemented, as whilst the general shape of the wake is the same, the vortex shedding behaviour is not predicted, particularly in the near wake region of a device, and this flow behaviour is not obtainable using steady methods. Comparison of the unsteady velocities is given in Figure 6.12, and as with the time-averaged data, the model showed very good agreement at predicting the vortex shedding. Overall this method of mesh motion has been demonstrated to provide good predictions of the wake of a turbine, and also has the potential for further refinement through improving the motion of the sub-domain.

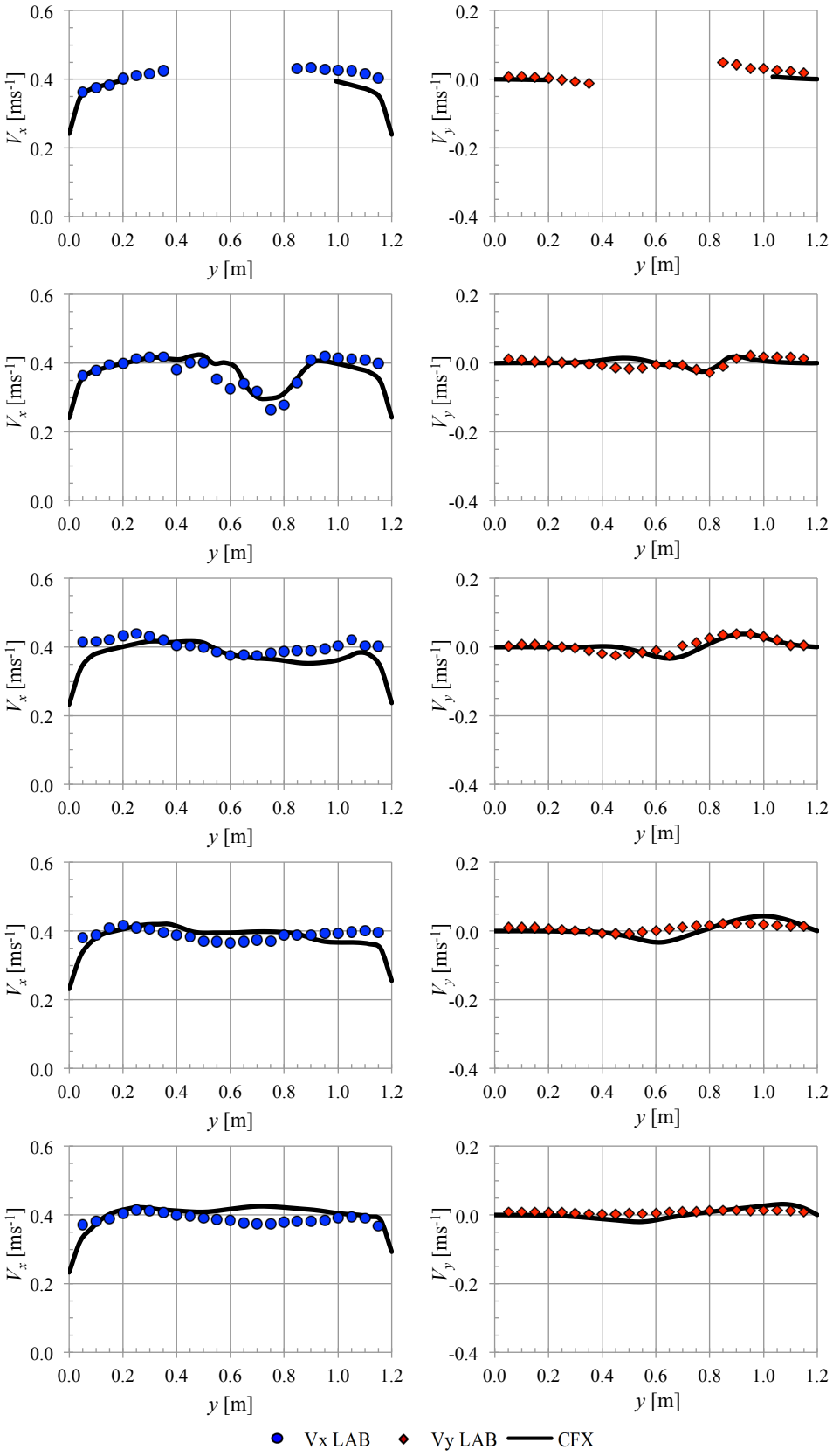

Figure 6.10 Comparison of time-averaged laboratory data and CFX predictions of horizontal velocity profiles downstream of CB_4S turbine (from top to bottom: x/D=0, 1, 4, 8, 16)

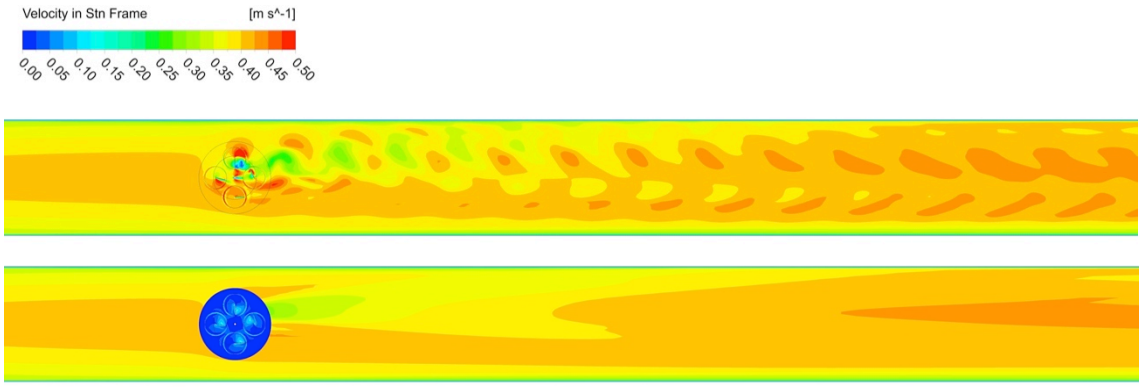

Figure 6.11 Unsteady (top) and time-averaged (bottom) velocity contours for CB_4S configuration at mid depth

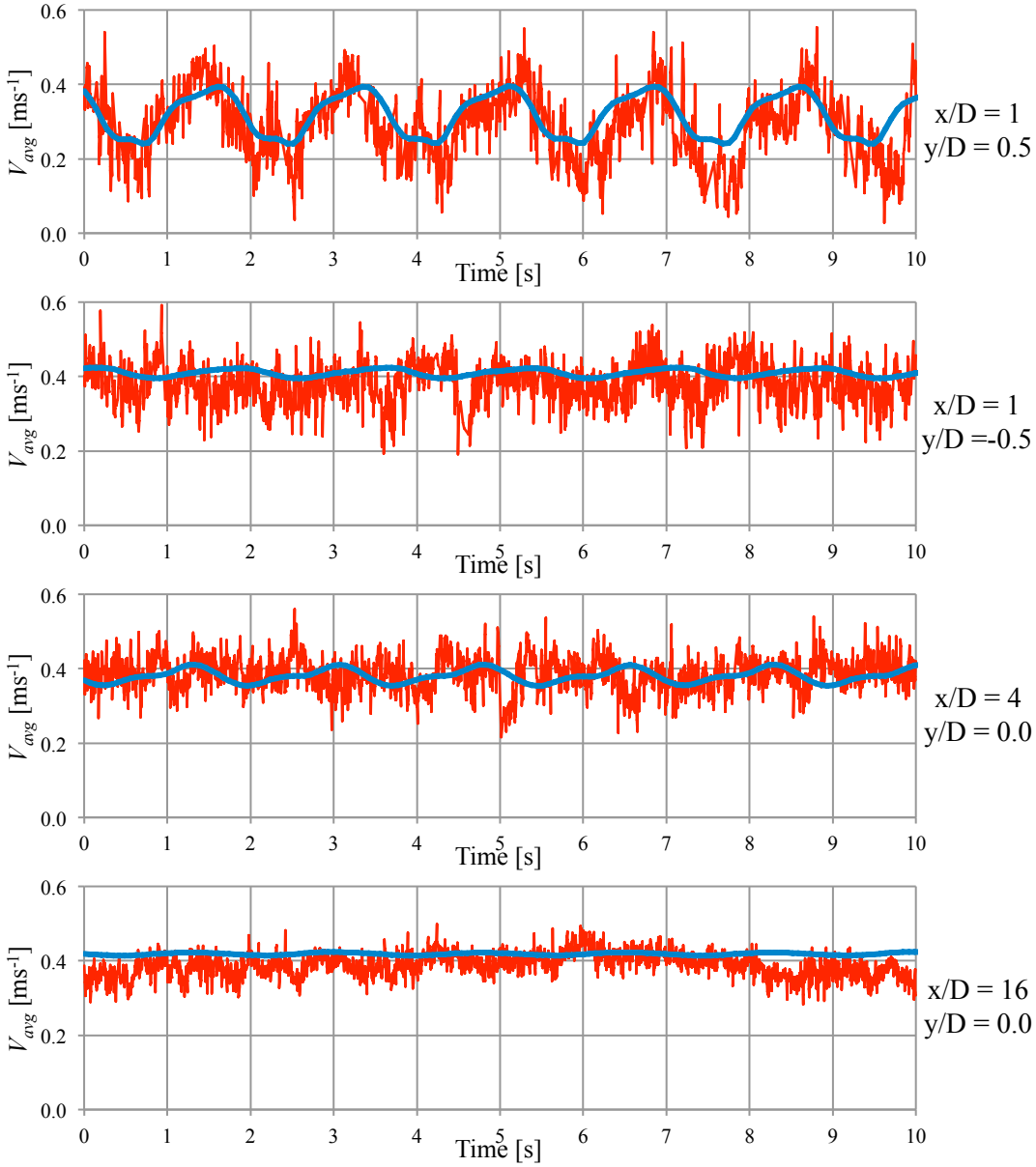

Figure 6.12 Time series data comparison between CFX and laboratory measurements, downstream of CB_4S turbine

6.3.2 SAV_SML turbine

The time-averaged vertical velocity profiles for the SAV_SML configuration are given in Figure 6.13. Similarly to the CB_4S results, the model showed good agreement with laboratory measurements, particularly behind the advancing bucket, i.e. y/D = 0.5. The largest differences occurred behind the returning bucket (y/D = -0.5) at mid-depth in the flume, as CFX predicted faster velocities than at the depths directly behind the turbine disks (z = 0.1875 and 0.3125). These differences may be a result of the mesh sizing not being small enough in this region. This would affect the returning side of the turbine more than the advancing side, as the relative speed between the water flow and the turbine would be greater, requiring a finer mesh as the y^+ values would be greater.

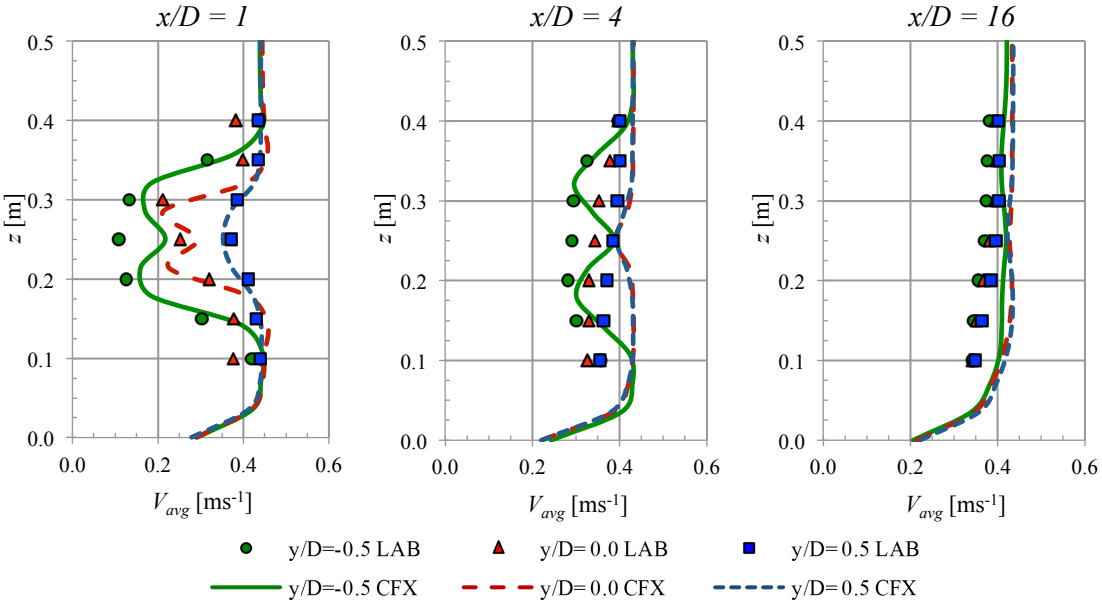

Figure 6.13 Comparison of time-averaged laboratory data and CFX predictions of vertical velocity profiles downstream of SAV_SML turbine

The differences in the velocities at mid-depth are also shown in the horizontal velocity profiles, given in Figure 6.14, and are broken down into their respective x and y direction components. In general, the x direction velocities are predicted with a high degree of accuracy, whereas the y direction velocities showed greater differences in the wake region between 4 and 8 diameters downstream. This resulted in the location of the wake being laterally spaced further away from the turbine axis, i.e. at y = 0.3 m as opposed to y = 0.4 m.

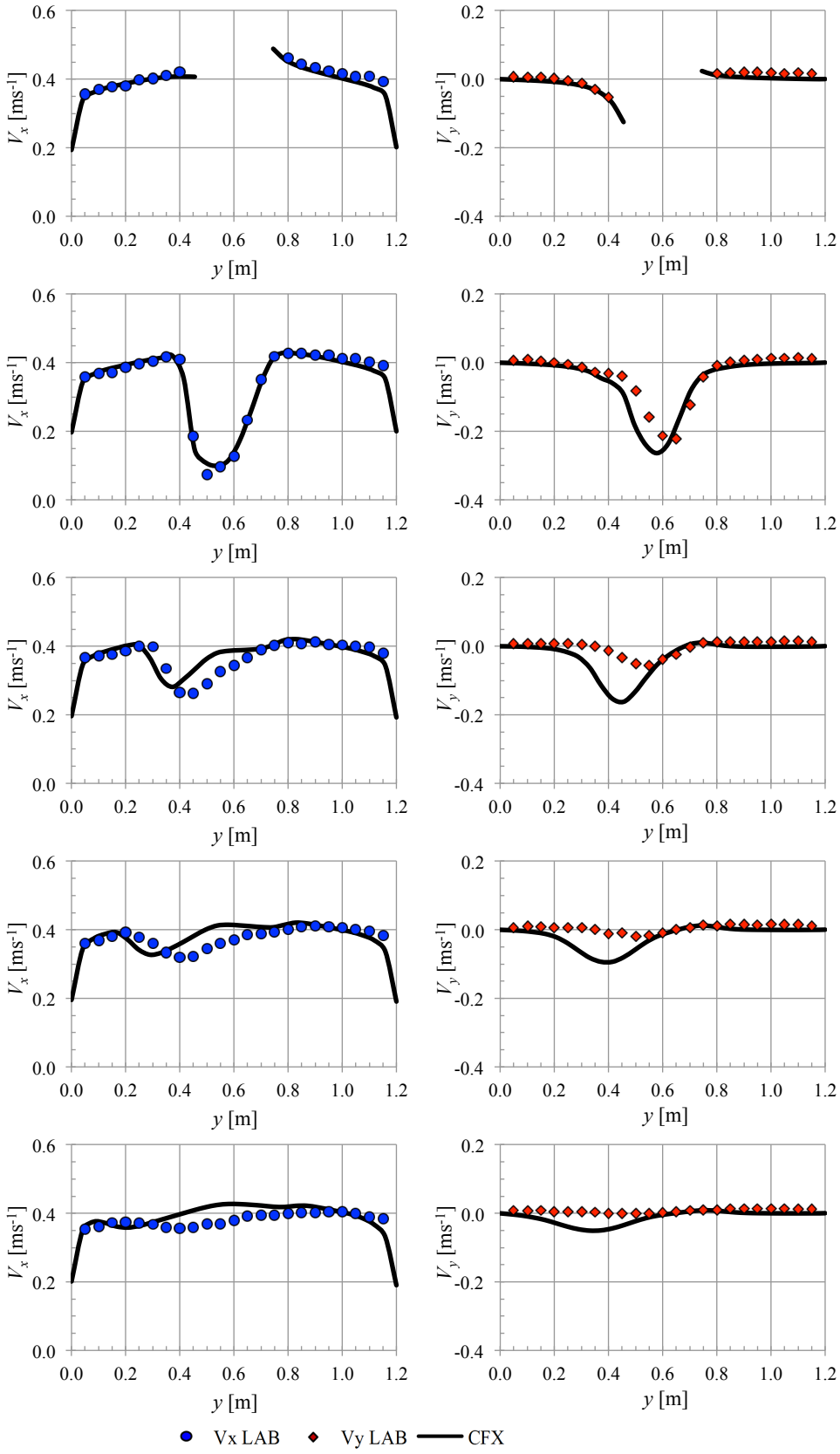

Figure 6.14 Comparison of time-averaged laboratory data and CFX predictions of horizontal velocity profiles downstream of SAV_SML turbine (from top to bottom: x/D=0, 1, 4, 8, 16)

Figure 6.15 shows the difference between the unsteady and time-averaged CFX predictions, at mid-depth. The reduction in flow blockage due to the smaller size of the turbine is apparent, as the velocities near the side walls of the flume remain unaffected by the presence of the turbine. This contour plot is particularly good at highlighting the asymmetrical nature of the wake, which is biased to one side. It is clear therefore that the wake behaviour is different from that for horizontal axis turbines, and downstream turbines could potentially be spaced closer together.

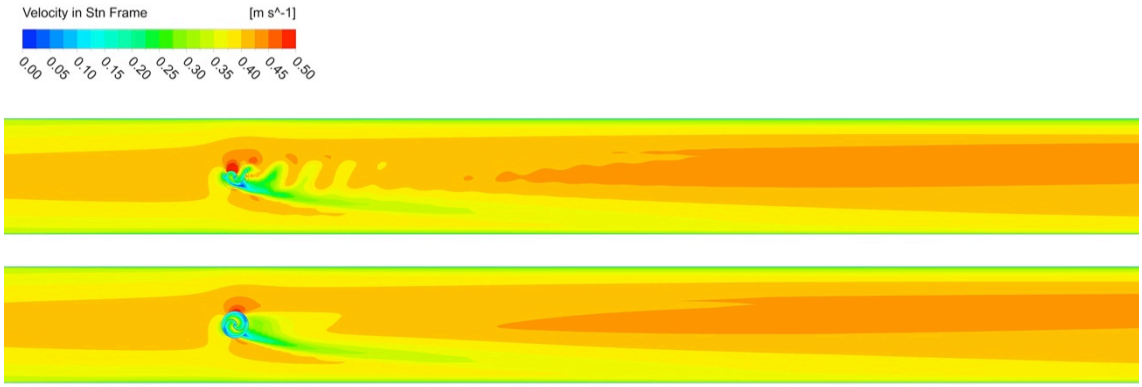

Figure 6.15 Unsteady (top) and time-averaged (bottom) velocity contours for SAV_SML configuration at mid depth

Figure 6.16 gives a comparison between the CFX predictions and laboratory data, for the unsteady velocity measurements at specific points in the flume. Once again, the model showed good agreement in predicting the vortex shedding behaviour as the turbine rotated. However, in general the predicted flow field was not so turbulent, and the fluctuations in velocity were smaller in magnitude. This is partly due to the steady flow conditions prescribed at the inlet boundary. In practise, as well as the turbulent fluctuations, the instantaneous velocity deviated from the mean. Finally, as already discussed, a constant angular velocity of the turbine was prescribed, whereas a 'pulsing' rotation would be more suitable and result in different vortex shedding characteristics.

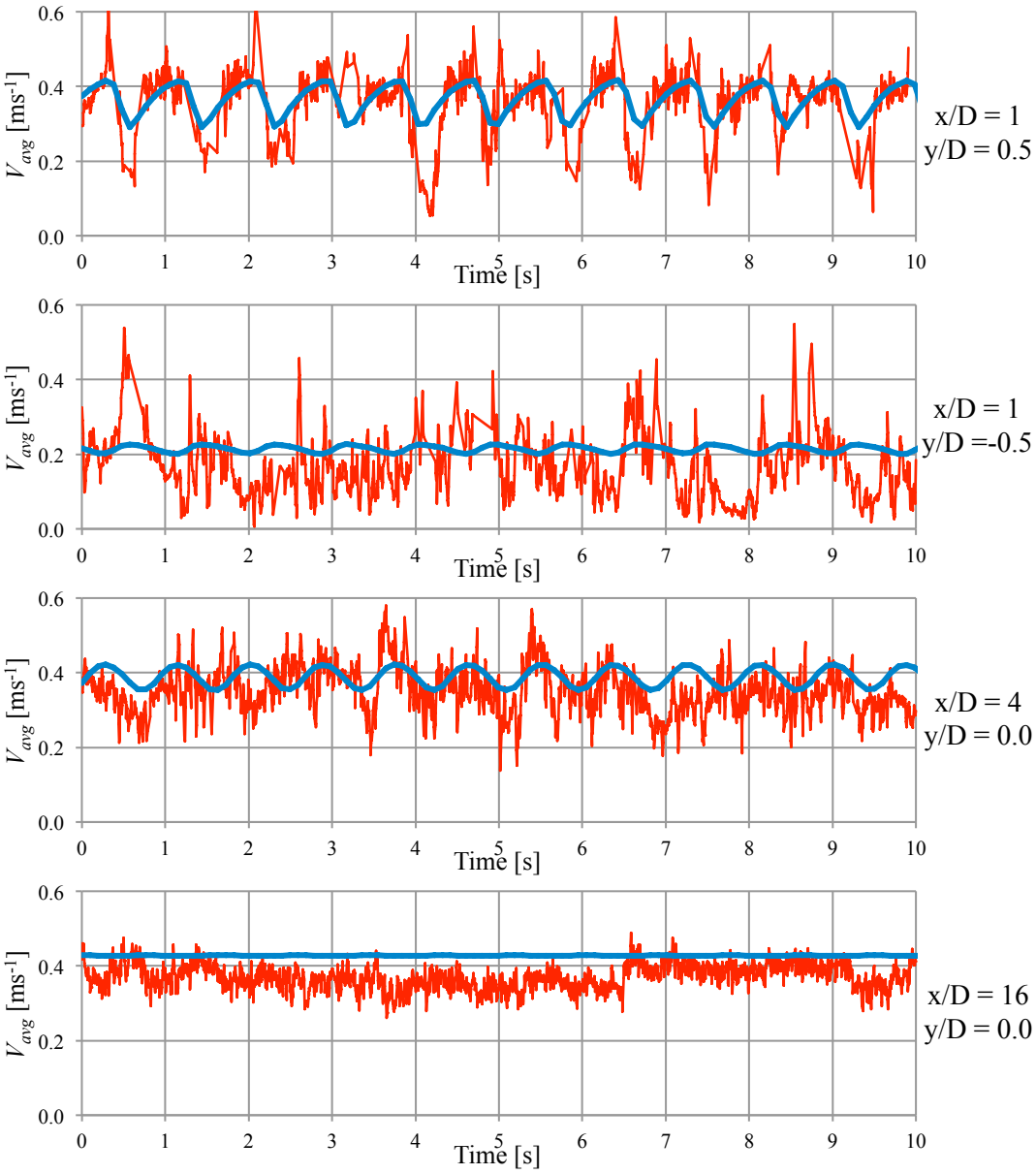

Figure 6.16 Time series data comparison between CFX and laboratory measurements, downstream of SAV_SML turbine

6.3.3 SAV_LRG turbine

The time-averaged velocity profiles in the vertical and horizontal directions for the SAV_LRG turbine configuration are given in Figure 6.17 and Figure 6.18, respectively. In general, the CFX predictions are similar to those obtained for the SAV_SML configuration, with obvious differences between the two turbines arising due to the increased blockage ratio in the flume, which increased from 4% to 17%. This blockage resulted in significant flow acceleration around the device, both underneath and over the top, as seen in the left hand graph in Figure 6.17, and around the sides of the turbine as seen in the horizontal profiles. These increased velocities were in excess of 0.5 ms^{-1}, compared to the free-stream average velocity of 0.38 ms^{-1}. As was the case with the smaller Savonius turbine, the velocity measurements on the side of the advancing bucket showed better agreement than the side of the returning bucket, the reasons for which have already been discussed. These differences were only apparent in the near-wake region and, at a distance of 16 diameters downstream, the model predictions were within 10% of the laboratory measurements.

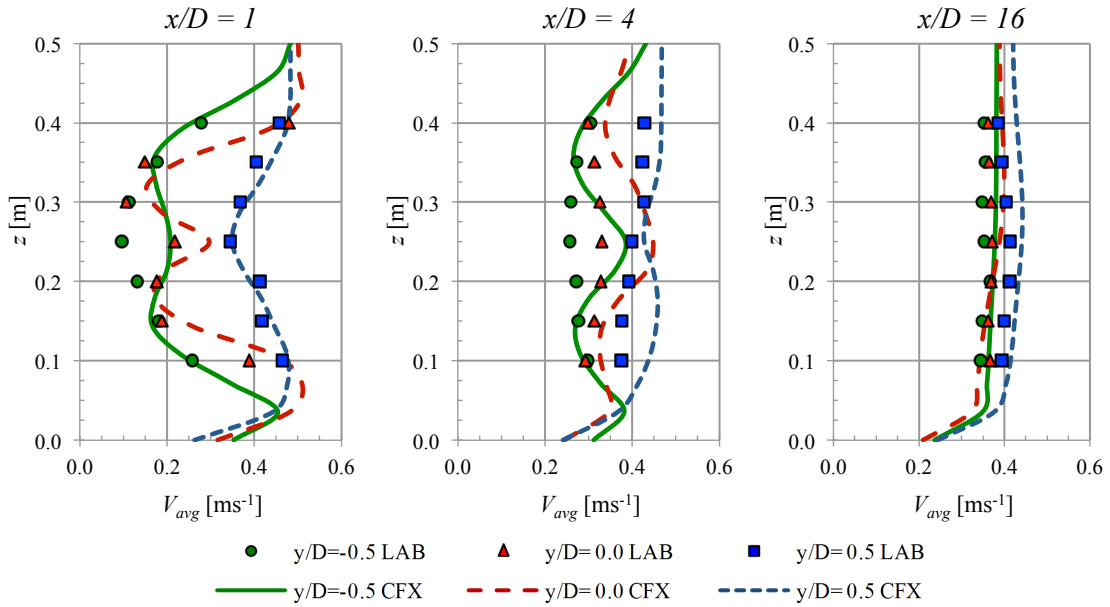

Figure 6.17 Comparison of time-averaged laboratory data and CFX predictions of vertical velocity profiles downstream of SAV_LRG turbine

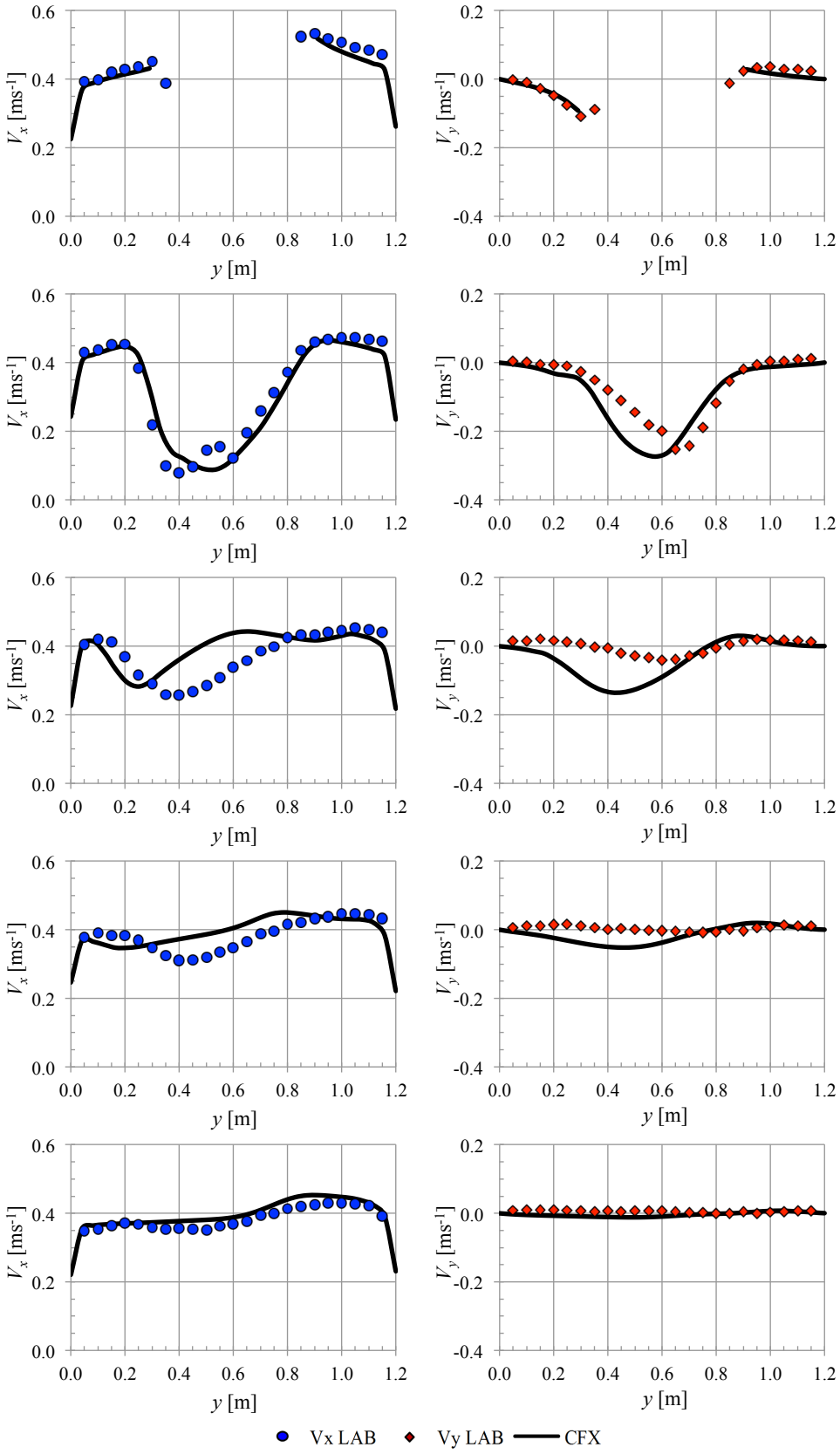

Figure 6.18 Comparison of time-averaged laboratory data and CFX predictions of horizontal velocity profiles downstream of SAV_LRG turbine (from top to bottom: x/D=0, 1, 4, 8, 16)

The effect of the increased blockage in the flume is particularly apparent in Figure 6.19, which shows the contour plots of the unsteady and time-averaged velocities at mid-depth in the flume, as predicted using CFX. The shape and relative size of the wake is the same as for the smaller turbine modelled, but the induced secondary current created on the side of the advancing bucket travels the length of the flume.

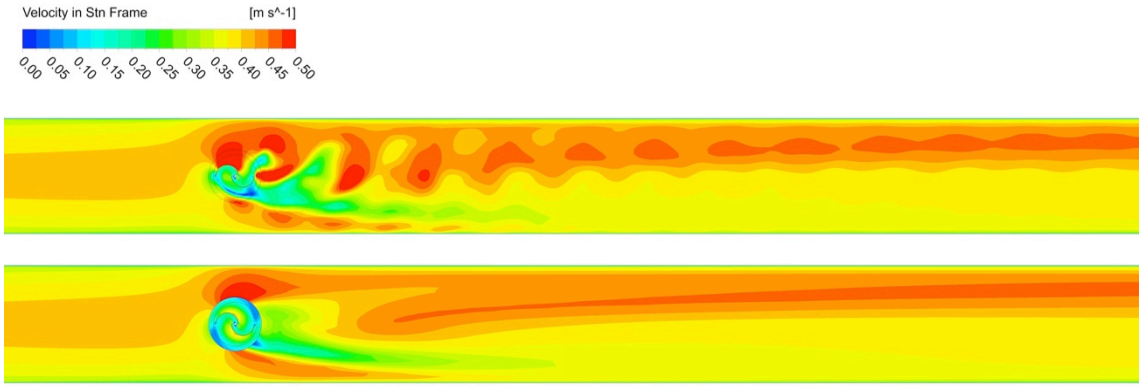

Figure 6.19 Unsteady (top) and time-averaged (bottom) velocity contours for SAV_LRG configuration at mid depth

Finally, the unsteady velocity measurements, and comparisons with the laboratory data are given in Figure 6.20. Once again CFX tended to under-predict the highly turbulent nature of the flow, partly due to the boundary conditions imposed as previously discussed. However, the model still showed good agreement in modelling the vortex shedding behaviour. As discussed these predictions could be further refined by improving the representation of the angular velocity of the turbine. Furthermore if more computational resources were available, alternate turbulence models that are more suited to modelling separation could be implemented.

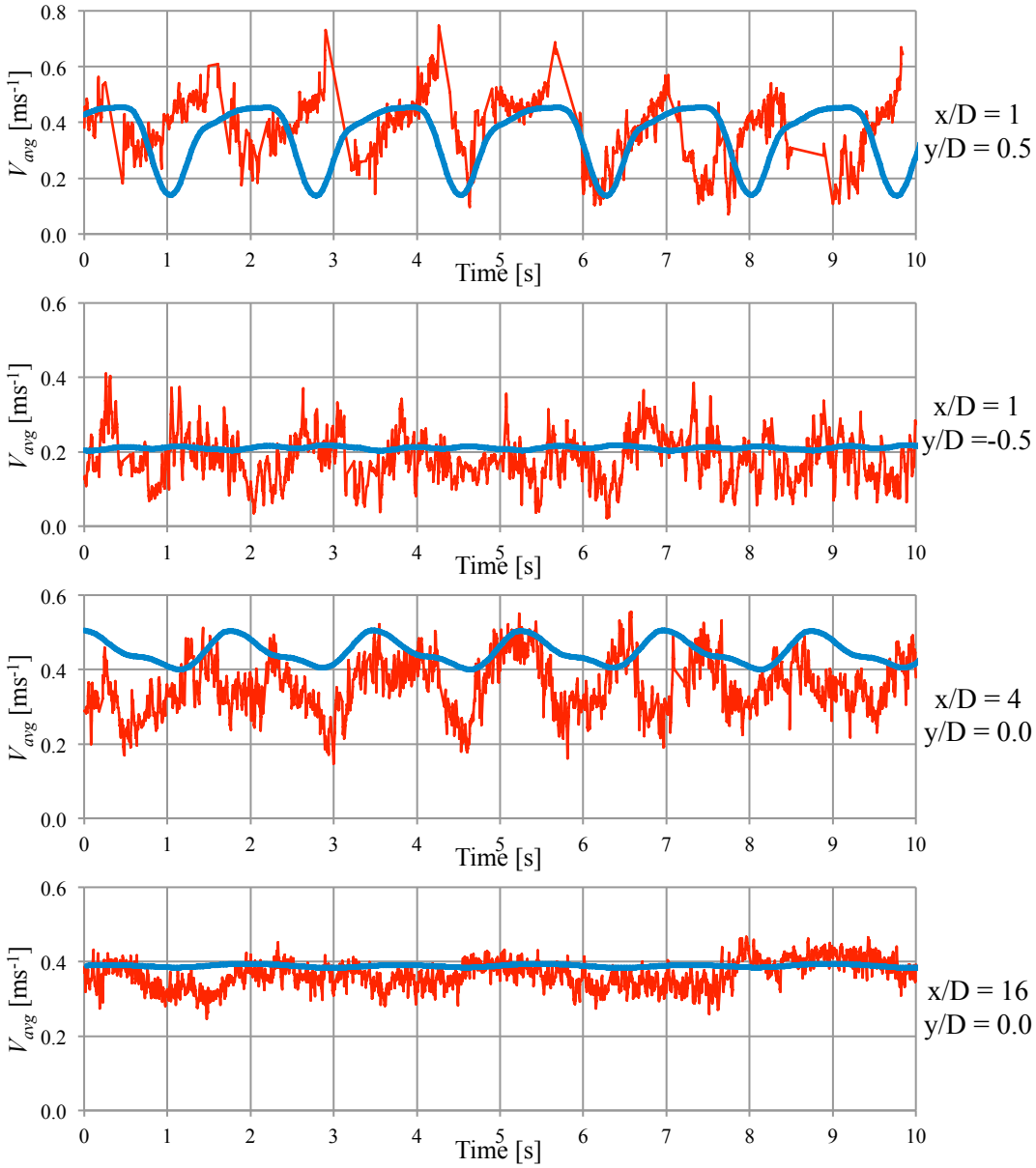

Figure 6.20 Time series data comparison between CFX and laboratory measurements, downstream of SAV_LRG turbine

6.4 Conclusions

This chapter presents and discusses the results from a series of modelling applications using the commercial CFD software, ANSYS CFX. In line with experimental work previously conducted in a recirculating flume, as detailed in Chapter 4, two main studies were undertaken; a performance assessment, and a wake characterisation study of two main vertical axis tidal stream turbine designs, namely: the CarBine and Savonius turbines.

To assess the performance of the CarBine turbine an idealised single arm, double flap configuration (referred to as CB_1D) was modelled. This is because without extensive re-meshing, and given the computational resources available, it was not possible to model moving objects in which their respective mesh would interact with each other. Whilst the CB_1D model showed good agreement with the laboratory data at the optimum operating point, the performance predictions at higher turbine speeds was not as expected, highlighting the limitations of using such an idealised model.

Assessment of the performance of the Savonius turbine showed better agreement with the laboratory data, however, the power coefficient predictions were optimistic. A peak efficiency of 32% was predicted, compared to 27% from the laboratory experiments. It is thought that this optimism was the product of a number of factors, including:

- The simulations were run in 2D, which tends to be optimistic due to the additional flow constraints.
- A constant angular velocity was prescribed for the turbines, whereas a more realistic pulsing angular velocity would lead to different torque predictions.
- The mesh density, as the results were demonstrated to be sensitive to the mesh sizing, unlike for the predictions obtained for the CB_1D model.
- The choice of turbulence model, as whilst the k-ε was used because of the already high demand on computational resources, other turbulence models can be better suited to modelling separated flows.
- The laboratory data will inherently be subjected to experimental error, and other forms of energy losses that cannot be modelled.

Whilst a double flap model of a CarBine turbine could not be modelled due to the mesh interaction discussed previously, a technique was developed in this thesis to rotate an internal subdomain (or multiple subdomains), inside a rotating domain, providing that the subdomains did not interact with each other. This allowed a single flap CarBine turbine to be modelled (i.e. the CB_4S configuration) in a wake characterisation study, as well as two sizes of Savonius turbine (the SAV_SML and SAV_LRG configurations). The modelling results showed good agreement in comparison with the recirculating flume results obtained in Chapter 4, for both unsteady and time-averaged measurements, and the same conclusions with regards to the wake shape, and the

potential for different spacing requirements to those for horizontal axis turbines can be made. This confirms the applicability of the modelling methodology implemented, as previous studies of the wake characteristics of horizontal axis turbines use steady flow techniques. Furthermore, to the author's knowledge, this is the first study in which physical and numerical modelling techniques have been applied to investigate the wake characteristics of vertical axis tidal stream turbines.

In this study for all of the models the computational resources were maximised, to achieve the highest possible solution accuracy within a realistic timeframe. For the performance tests, in which many different operating points were run a 2D domain was used, whereas a full 3D model was implemented for the wake characterisation study. Invariably compromises had to be made with regards to the modelling setup, for example for the 3D mesh a sizing of 5 mm was used on the buckets and flaps of the turbines as the memory limits were reached, whereas the 2D performance results showed that a spacing as small as 0.5 mm would have been more suitable. Furthermore, it is acknowledged that the k-ε turbulence model does not perform as well as others for separated flows, but the computational demand of more sophisticated turbulence models is known to be greater. For example, the k-ω based Shear Stress Transport (SST) model is fast becoming the industry standard choice of turbulence model. Through the use of blending functions, this model combines both the k-ω model at the near-wall region, and the k-ε model in the free stream. This therefore takes advantage of improved modelling of flow separation at boundaries, whilst addressing the issue of omega-based models that is sensitivity to freestream conditions (ANSYS, Inc. 2010b). In addition, a larger range of turbulent length scales can be resolved using Large Eddy Simulation (LES), but at a much higher computational cost. In an effort to balance practicality and the accuracy of the numerical model, techniques such as Scale-Adaptive Simulation (SAS) exist, which switch between classic RANS solutions in steady flow regions and LES-like behaviour in unsteady flow regions. As advancements in computing resources continue to develop the size and sophistication of future CFD models will increase. The capabilities that would be relevant to the development of this work include: improved turbulence modelling, fully transient turbine-to-turbine interactions, array modelling, and coupling with structural and rigid body dynamics models.

Chapter 7 TRIVAST model application

In this chapter results are presented from the modelling studies conducted using the numerical model TRIVAST. This numerical model has been applied to the Severn Estuary, at both a physical and prototype model scale. As previously identified in Chapter 1, in this thesis the Severn Estuary refers to the region encompassing the Inner and Outer Bristol Channels, as well as the Severn Estuary. For all models used in this study the modelling domain extended from Gloucester to an imaginary line between Milford Haven and Hartland Point.

The physical scale modelling study was conducted in conjunction with an MSc project (Ellis 2012), in which water levels and velocities were measured in a physical model of the Severn Estuary, which was located in the Hydro-environmental Research Centre's hydraulics laboratory. The purpose of the study was to investigate the varying impacts of the Severn Barrage proposals on the estuarine hydrodynamics. Scale model barrages were constructed and installed in the physical model, and these were then simulated in TRIVAST, through the implemented modifications to the governing equations, as detailed in Chapter 5.

The TRIVAST model has then been extended to the prototype scale, and the different barrage proposals were re-modelled. Furthermore, the effects of two hypothetical tidal stream arrays were investigated, comparing the varying hydrodynamic impacts of horizontal and vertical axis turbines, using different turbine-to-turbine spacing.

7.1 Scaled modelling of the Severn Estuary

7.1.1 Physical model details

The physical model of the Severn Estuary (referred to herein as the SEPM) extends between Gloucester and an imaginary line between Milford Haven and Hartland Point, as shown in Figure 7.1. In the horizontal direction a scale of 1:25000 was used to scale the geometry, whilst in the vertical direction the scale was 1:125, allowing the model to fit in a 6x4 m basin. Water was delivered to a holding tank via a pump, with the holding tank and basin separated by a mechanically operated weir. This allowed the incoming tidal wave to be specified, and for this study a 4 cm amplitude sinusoidal curve was

used, which corresponded to a typical mean spring tide in the estuary. Based on the principle of keeping the Froude number constant when scaling in the design of the model, a 12.4 hr time period to represent a tide should scale to 20 s. However, due to practical limitations a time period of 40 s was used.

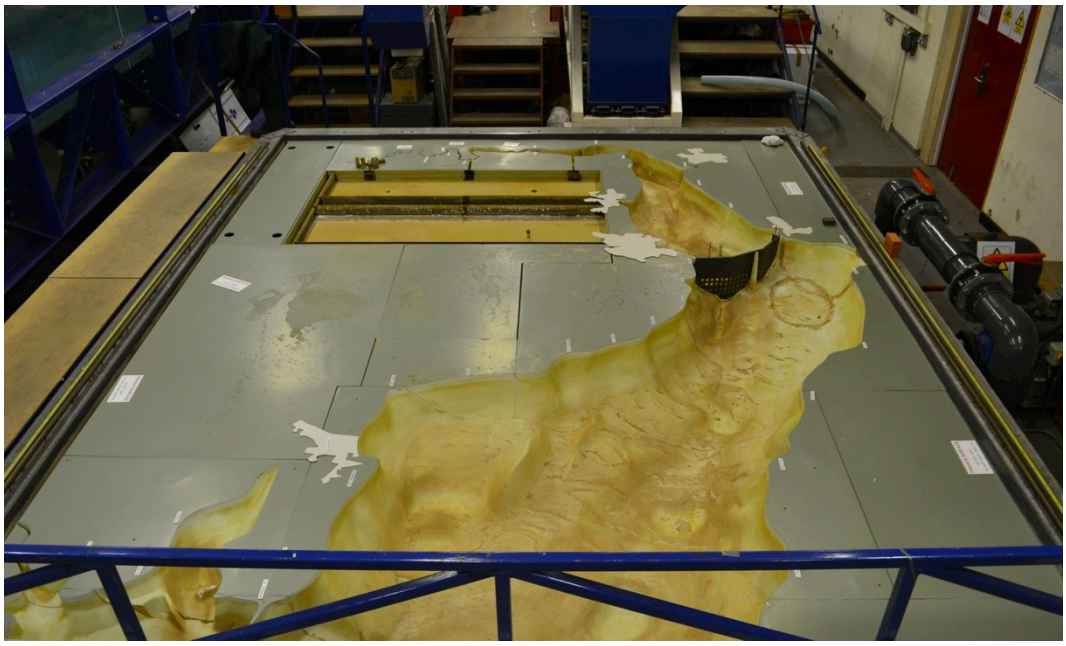

Figure 7.1 The physical model of the Severn Estuary (SEPM)

The original STPG barrage proposal was located between Cardiff and Weston, passing in between the islands of Flat Holm and Steep Holm, and was 16 km in length. Due to the commercial nature of the Hafren Power proposal precise details of the barrage location and technology used have not been released to the public. It is understood that the barrage will be 18 km in length, passing around both islands. However, for the scaled model tests in this study the size and location of the barrages were regarded as being the same for both the STPG and Hafren Power schemes, as shown in Figure 7.2. The barrage models were constructed from PVC plastic, and holes were drilled to represent the turbine ducts. For the STPG scheme, which also used sluicing, two large one-way flaps were used, to allow the basin to fill on the flood tide. The total area of these holes and flaps were derived by geometrically scaling the prototype scale barrages, with details given in Table 7.1. It is noted that due to the limitation of the model using a time period twice as large as that desired- i.e. at 40 s, the barrage models were modified accordingly to take this into account, with the respective areas of the turbines and sluice gates being halved.

Figure 7.2 Model of Hafren Power barrage used in the physical model

To control the holding periods for the Hafren Power scheme a large shutter was constructed, which when fully closed sealed the barrage, and retained the basin volume of water. This shutter was operated by hand, allowing a number of different holding periods to be tested. However, the stop-start nature of opening and closing this shutter over a short time period also induced free surface oscillations, which affected the water level measurements. These measurements were recorded using a calibrated wave probe, whilst the velocities were measured using an ADV, at a frequency of 25 Hz. The depth of these probes was fixed where possible to z=0.4H, to coincide with the location of the mean velocity (assuming an approximate 7th power law velocity distribution). For the case of shallow water measurements (i.e. Points A, C and F) the probes were lowered to ensure that they were submerged at all times. Further details of the experimental setup can be found in Ellis (2012).

Table 7.1 Properties of barrage models tested

	Barrage Scheme	
	STPG	***Hafren Power***
Prototype Details	Ebb-only generation 216 turbines (9m diameter) 166 sluices (22x17.5m) 3hr holding period at high tide	Two-way generation 1026 turbines (9m diameter assumed) Holding period unknown
Physical Model Details	24 holes (15mm diameter) to represent turbines 2 flaps (160mm square) to represent sluices	66 holes (20mm diameter) to represent turbines Shutter to control holding periods

Note: Physical model areas were halved to account for tide period, as previously discussed

7.1.2 Natural condition

Before any barrages were modelled, a like-for-like model of the SEPM was created. After a preliminary test it was found that the model was numerically unstable if the number of layers in the model was above 1. This was thought to be due to the explicit scheme used in solving the layer integrated equations, as well as modelling at such a small scale with a model that is better suited to the prototype scale. Therefore, for the physical model tests the number of layers was reduced to unity; i.e. the depth-averaged equations were solved in the model.

A grid size of 24 mm was used, resulting in a domain with a resolution of 229x167 cells, as shown in Figure 7.3. All water elevation and velocity measurements were sampled at points (A)-(H), which were the same locations as those used in the physical model. The seaward boundary was specified using a water elevation boundary condition.

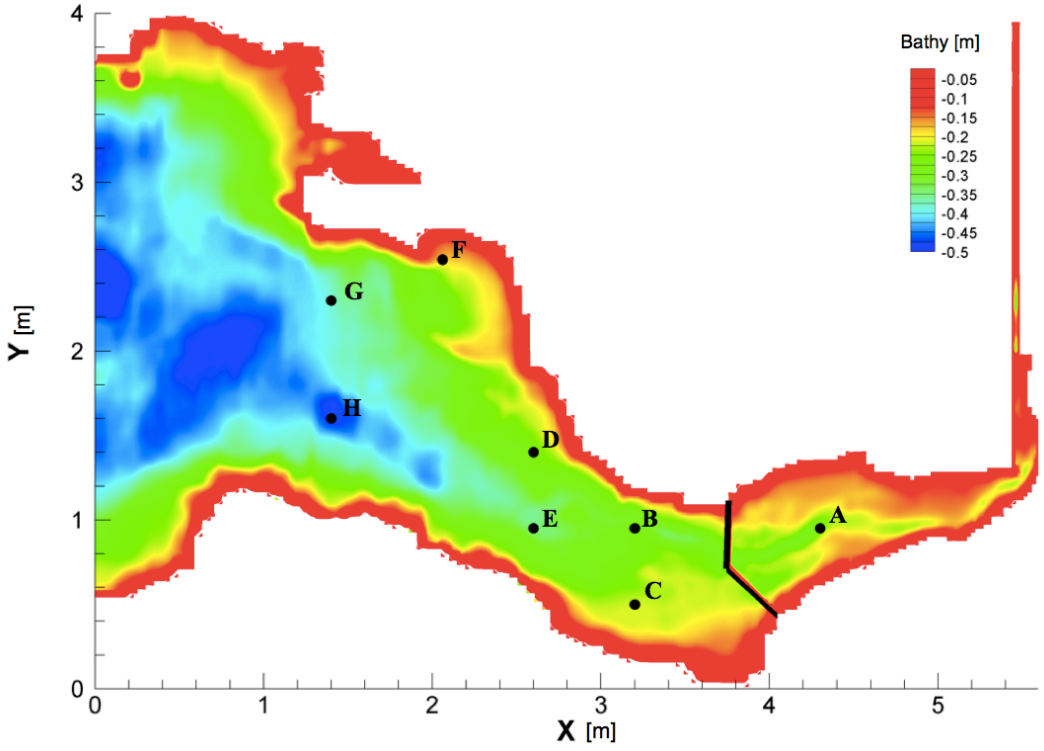

Figure 7.3 Physical model bathymetry, and sampling locations

Other studies have included the discharge from the River Severn, either as a flow boundary or by linking a 1D river model. However, the SEPM does not take this discharge into account. Therefore the upstream extent of the model was treated as a land

boundary, and all land boundaries were defined using a no-slip condition. A time step of 0.02 s was used, based on a Courant number restriction for accuracy, and the model was run for 40 tidal cycles to ensure solution convergence. Other parameters were set based on calibration with laboratory data, and recommendations from the DIVAST user manual (Falconer and Lin 2002b).

Figure 7.4 provides a comparison between the numerical and physical model predictions of water elevations in the SEPM, at two sites; Point H, which was located towards the open boundary, and Point A, which was the highest upstream measuring point.

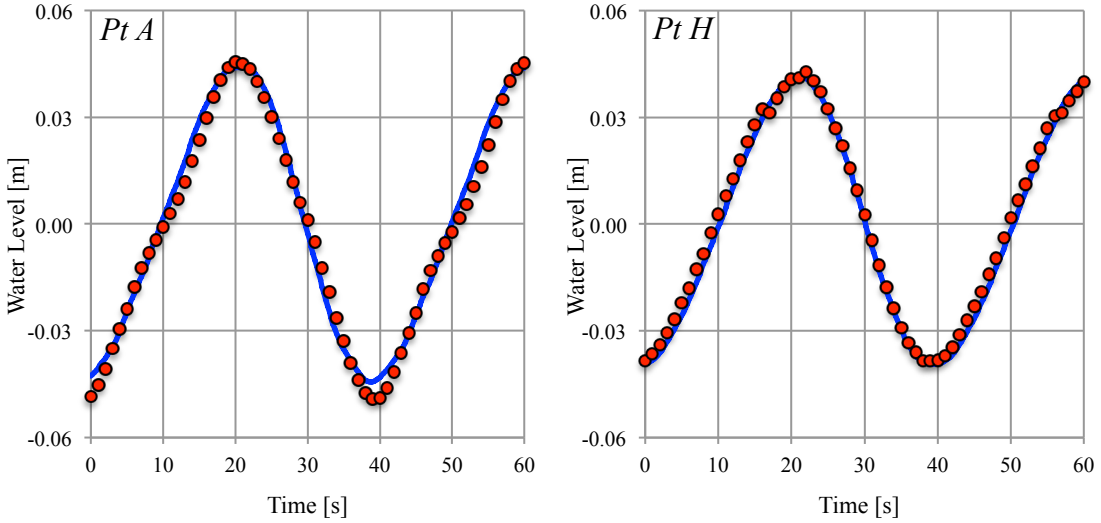

Figure 7.4 TRIVAST (blue line) and laboratory (red dots) predictions of water elevations in the SEPM

The main feature that can be observed in this figure is the tidal range amplification, which occurred due to the natural shape of the estuary. This increased with distance upstream; between Points H and A the amplitude increased by approximately 1.5 cm, which at a prototype scale translates to ≈ 1.9 m. This is lower than expected for the prototype scale, in which values of > 3 m were anticipated. This reduced amplification is a result of doubling the time period to 40 s, as this affected the advective processes in the model. This limitation of the physical model therefore results in an under prediction of the tidal energy resource. In terms of comparing the numerical model predictions with the laboratory measurements, the TRIVAST model showed good agreement with the laboratory data. This is further evidenced in Figure 7.5, in which predictions are given of the tidal velocities in the SEPM. Points A and F showed the least agreement between the physical and numerical model predictions, which was thought to be due to

the lower location of the ADV probe, and the interaction between the probe and the relatively shallow body of water in that area. Both models showed faster currents predicted on the ebb tide, as expected, and this can be clearly seen in Figure 7.6, which gives the velocity predictions across the domain for a flood and ebb tide, respectively.

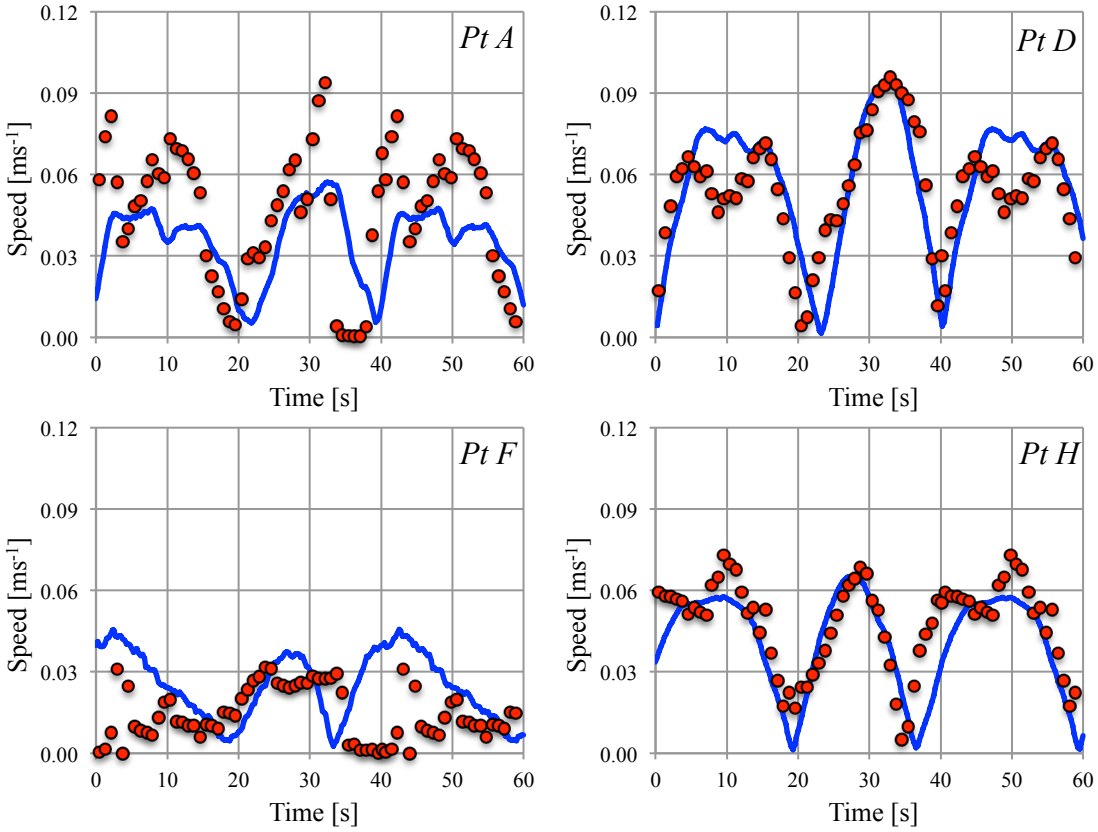

Figure 7.5 TRIVAST (blue line) and laboratory (red dots) predictions of velocities in the SEPM, for the natural condition

The modelling results showed that for a flood tide the peak velocities are in the region of 0.07 ms^{-1}, whereas for an ebb tide the peak velocities exceeded 0.12 ms^{-1}. Using the appropriate scaling factor, which was modified to account for the time period scaling issue (see Ellis (2012)), these velocities correspond to 1.6 and 2.7 ms^{-1}, respectively, at the prototype scale. In general these agree well with estimates of tidal velocities in the Severn Estuary, however, they are lower than expected, which is a result of the scaling issue already discussed.

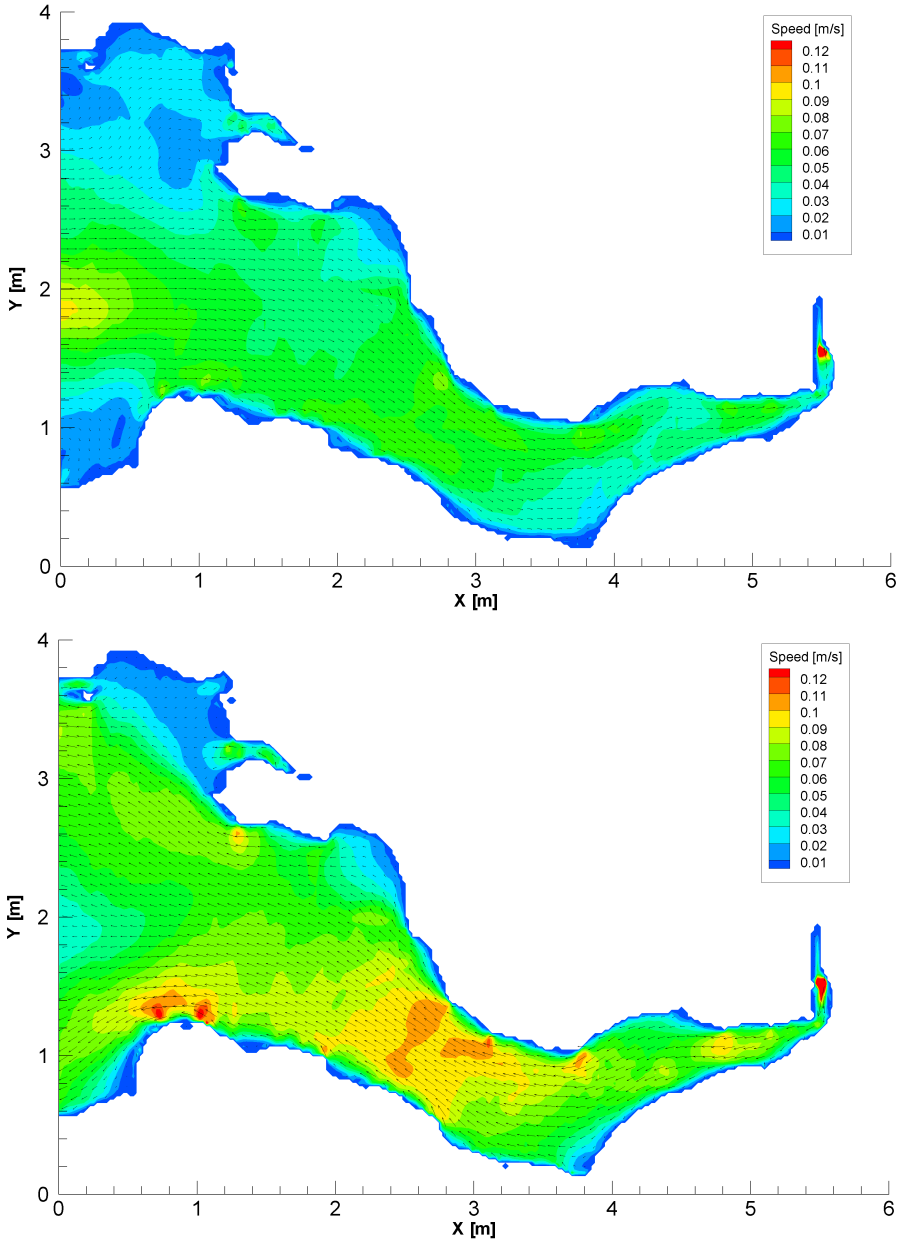

Figure 7.6 TRIVAST predictions of velocities in the SEPM, for the natural condition (top: flood tide, bottom: ebb tide)

7.1.3 STPG barrage

Figure 7.7 shows the physical and numerical model water elevation predictions, both upstream and downstream of the STPG barrage, i.e. for ebb-only generation. The results show a significant increase in the minimum water levels inside the basin, from -4.7 cm to -1.2 cm - an increase of 4.4 m at the prototype scale. Downstream of the barrage and throughout the rest of the estuary the maximum water elevations were observed to have

reduced slightly, as the natural frequency of the estuary is changed due to the presence of a barrage structure.

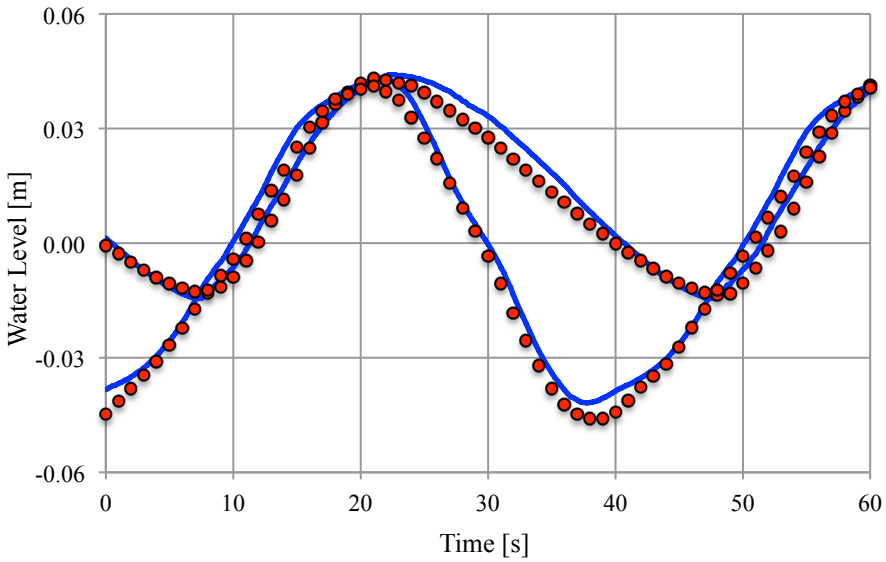

Figure 7.7 TRIVAST (blue line) and laboratory (red dots) predictions of water elevations both upstream and downstream of STPG barrage

These conclusions are the principal findings from previous studies, and the increase in the minimum water levels inside the basin would result in large areas of intertidal habitat being permanently flooded, a finding that has raised many environmental concerns. The predicted tidal velocities for points A, D, F and H are given Figure 7.8, and contour plots of TRIVAST predictions for the mid-flood and ebb tides are given in Figure 7.9. A reduction in the velocities throughout the estuary was observed, except for local increases around the barrage site due to the filling and emptying processes of the barrage. The magnitude of these local increases would not be expected to be transposable to the prototype scale, as they are dependant on the exact geometric details of the barrage structure, and modelling such fine details was not feasible at such a small scale. Furthermore, the TRIVAST model uses a regular grid, and so in order to accurately represent complex geometries a very fine grid resolution would have been required. Despite this, the model showed good agreement with the measured physical model data.

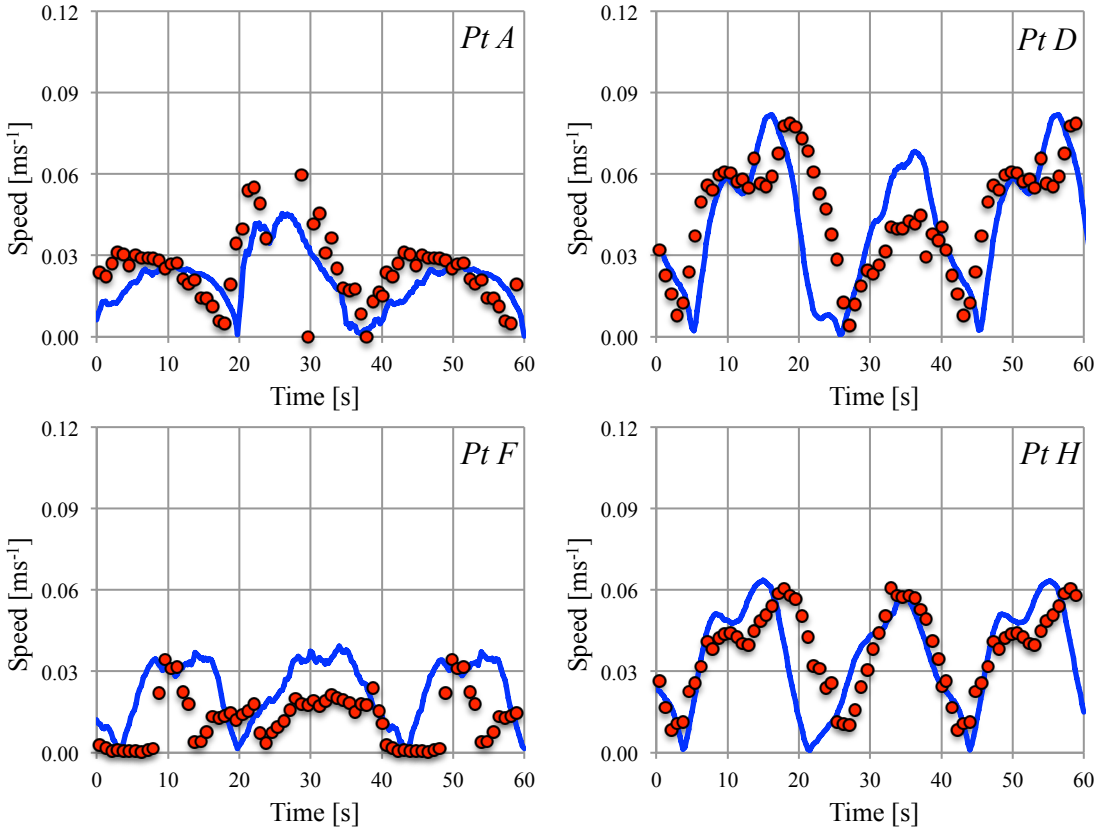

Figure 7.8 TRIVAST (blue line) and laboratory (red dots) predictions of velocities in the SEPM, for the STPG barrage

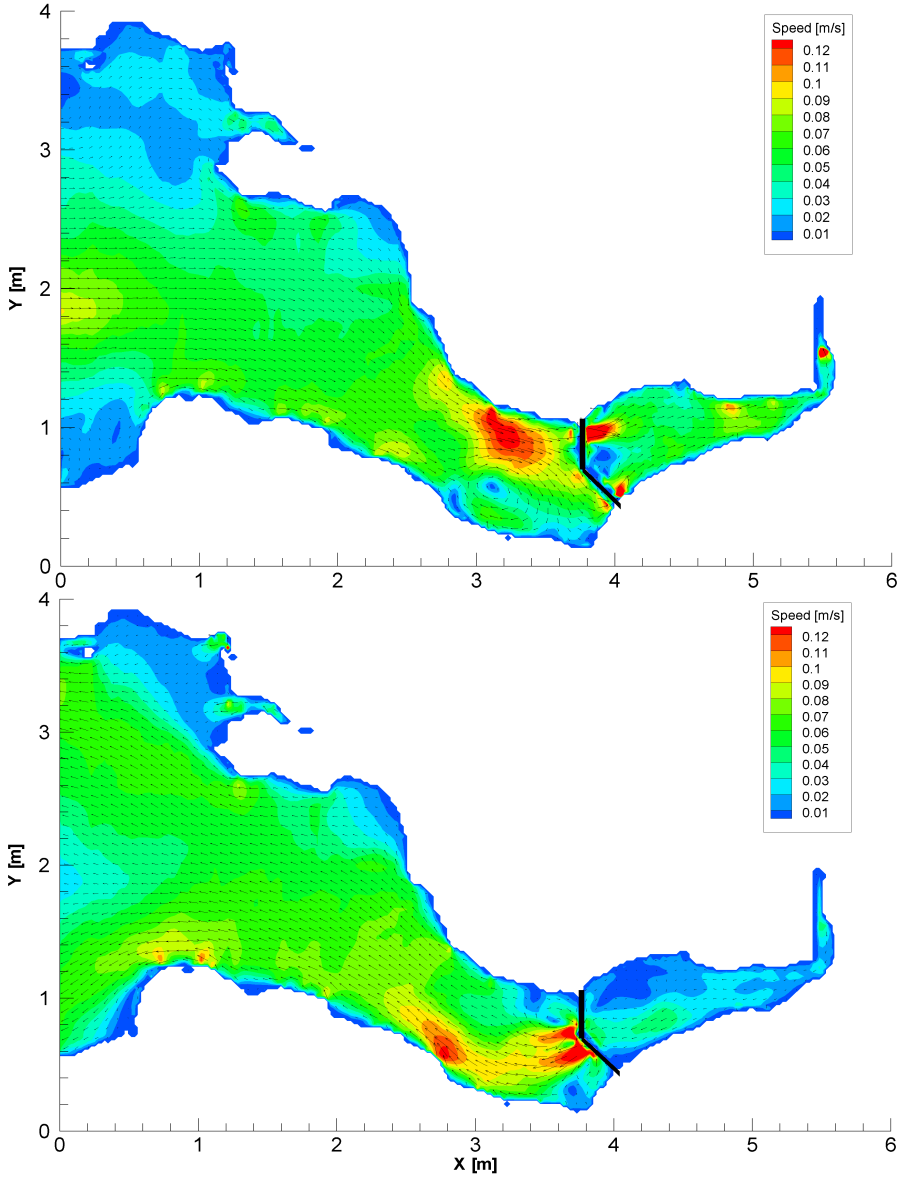

Figure 7.9 TRIVAST predictions of velocities in the SEPM, for the STPG barrage (top: flood tide, bottom: ebb tide)

7.1.4 Hafren Power barrage

With precise details of the Hafren Power scheme being still subject to design clarification, a number of different operating conditions were modelled. Starting heads of 0, 3, 4, 5 cm were tested by manually opening and closing the shutter at different intervals. It was found that with 0 cm head the tidal regime behaved much like the natural conditions, with a small decrease in elevations and velocities throughout the estuary. As the starting head was increased this affected how much both the maximum and minimum water levels would increase and decrease by respectively, upstream of the

barrage, as well as throughout the estuary. A similar behaviour was also observed with respect to the tidal velocities. Practically a head would have to be introduced for feasible power generation, and therefore the following results are presented for a starting head of 3 cm for both the ebb and flood generating phases. The reader is referred to Ellis (2012) for full results of the different starting heads.

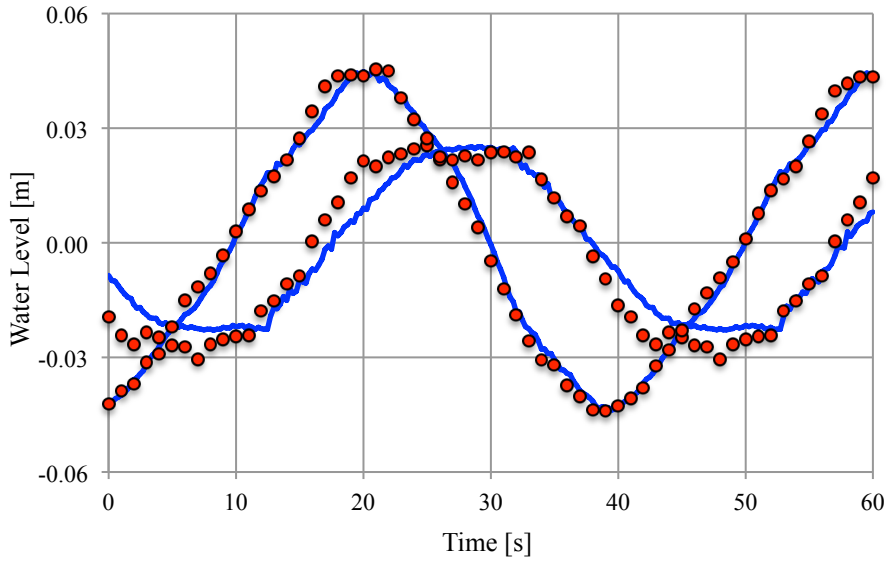

Figure 7.10 TRIVAST (blue line) and laboratory (red dots) predictions of water elevations both upstream and downstream of Hafren Power barrage

The TRIVAST and physical model predictions of water levels both upstream and downstream of the Hafren Power barrage are given in Figure 7.10. A 3 cm starting head led to a 2 cm increase and decrease of the minimum and maximum water levels, respectively. At the prototype scale this corresponded to a 2.5 m increase in the minimum water levels and, as a result, with a two-way scheme there would be less permanent flooding of intertidal habitat areas compared to the STPG barrage. Furthermore, the reduction in maximum water levels has positive implications in terms of increased flood protection for the basin area upstream of the barrage.

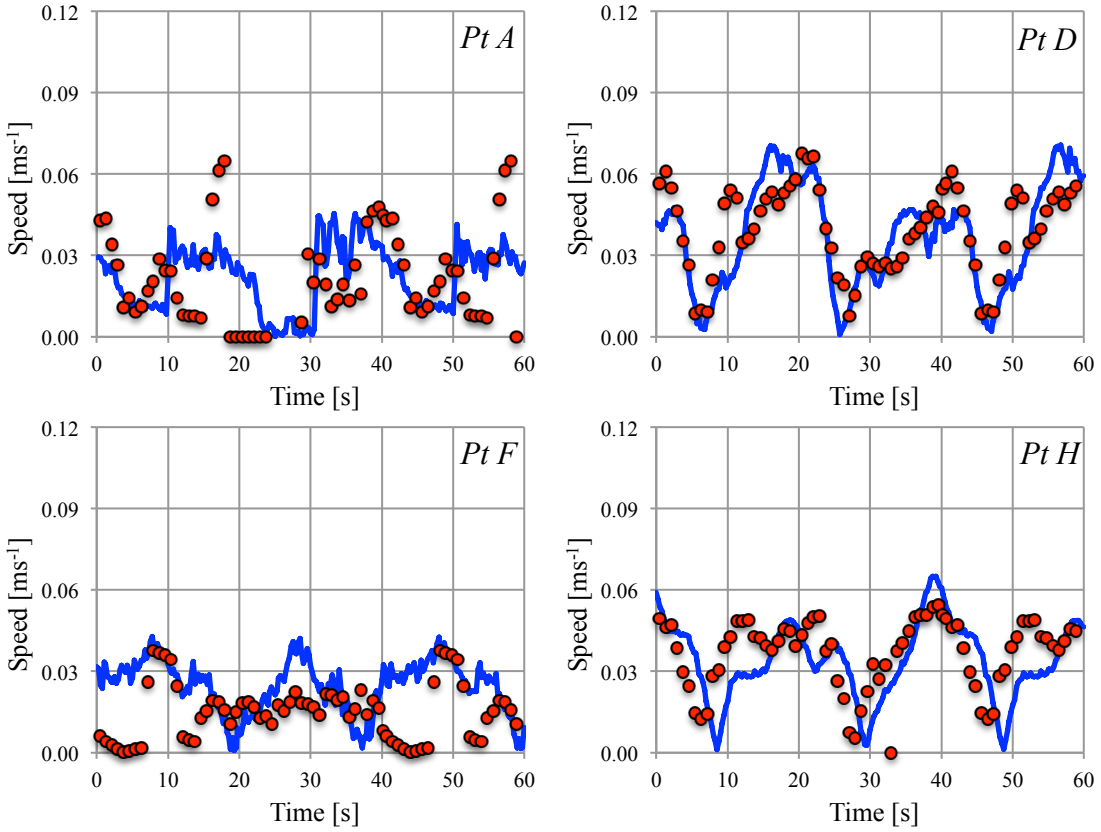

Figure 7.11 TRIVAST (blue line) and laboratory (red dots) predictions of velocities in the SEPM, for the Hafren Power barrage

As with the other conditions modelled, the TRIVAST predictions showed good agreement with the physical model data, and this is also evident in Figure 7.11, which gives the predicted tidal velocities at points A, D, F and H. As with the STPG scheme, the predicted tidal velocities were shown to decrease throughout the estuary with the Hafren Power barrage, the magnitude of which depended on the starting head. However, due to the shutter operation to control the opening and closing of the turbine ducts over a short time period, instabilities in the free surface and velocities were measured, as short-period wave oscillation effects were introduced into the models. This induced numerical instabilities into the TRIVAST model in the region of the barrage, and is particularly evident in Figure 7.11. It can be seen also, however, that further downstream at point H that these oscillations had dissipated. Finally, contour plots of the velocities at mid-flood and ebb tide from TRIVAST model are given in Figure 7.12, which further illustrates the reduction in velocities compared to the natural condition.

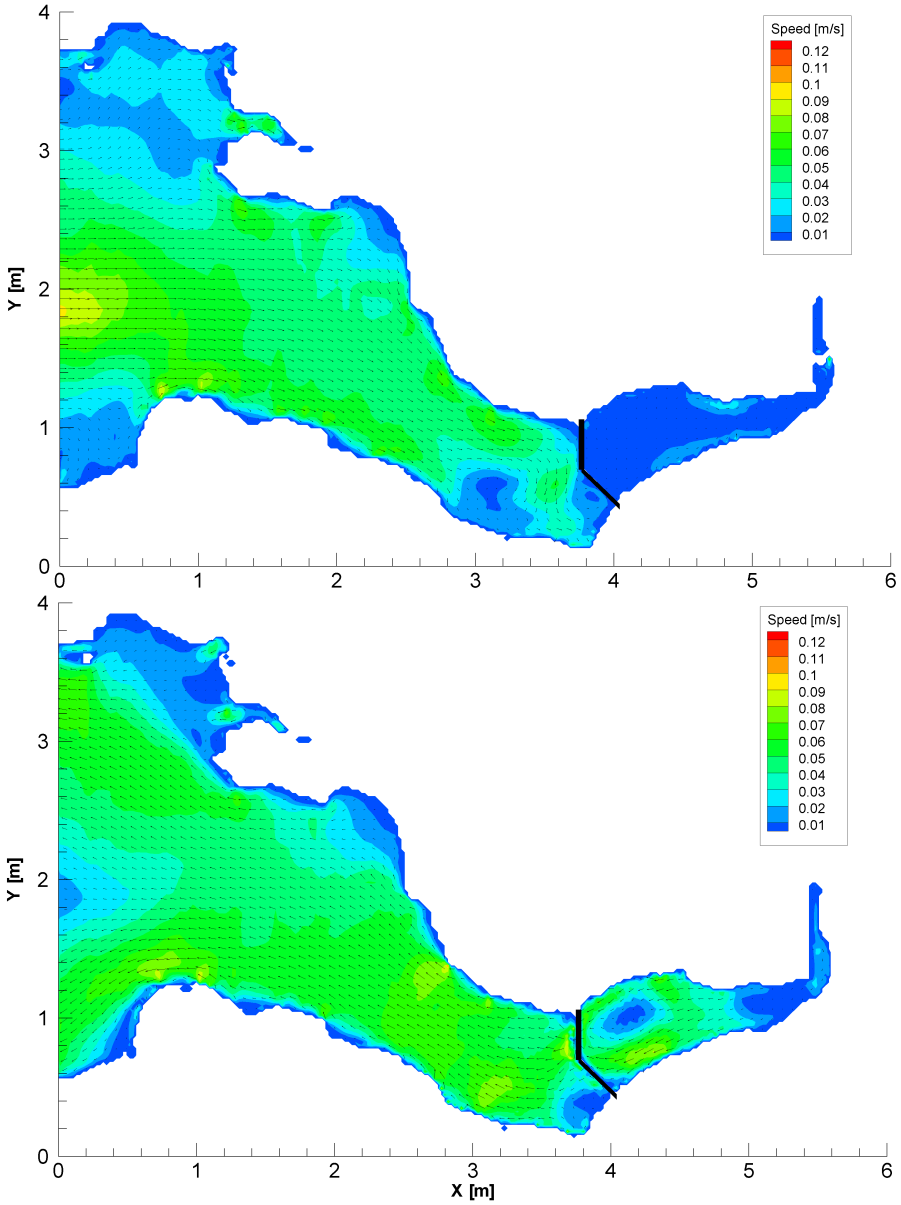

Figure 7.12 TRIVAST predictions of velocities in the SEPM, for the Hafren Power barrage (top: flood tide, bottom: ebb tide)

7.1.5 Energy yield from a barrage

As previously discussed in the physical model setup the turbines and sluice gates were represented by holes drilled through the barrage. Attempting to model power take-off at this scale was impractical due to the small scale used, and specific details of turbine performance and operating conditions would also be required. Hence, whilst it is acknowledged that any calculated energy values bear little resemblance to the prototype scale, comparisons can still be made between different schemes with regards to the total energy yield through the barrage structures. This is given in Table 7.2, and it was found

that both the STPG and Hafren Power schemes could potentially produce a similar amount of energy at the physical model scale; as with a 3 m starting head, a total 38 Ws of energy was transferred through both the STPG and Hafren Power barrages in a single tidal cycle.

Table 7.2 Total energy yield across varying barrage structures at physical model scale for a single tidal cycle

Scheme	*Starting Head [cm]*	*Energy [Ws]*		
		Flood tide	*Ebb tide*	*Total*
STPG	0	0	26.3	26.3
	3	0	37.8	37.8
Hafren Power	0	13.6	20.7	34.3
	3	16.9	20.7	37.6

It remains to be seen if this maximum potential exists at the prototype scale for both schemes, and whether or not the turbines to be used in the Hafren Power barrage can extract this energy efficiently under lower heads throughout a tidal cycle.

7.2 Prototype modelling of the Severn Barrage proposals

As the TRIVAST model showed good agreement with the obtained laboratory data of velocities and elevations, and the operation of tidal barrages at the physical model scale, the model was then extended to the prototype scale. This is one of the main advantages of using CFD models, as they address scaling issues such as the problem of being unable to achieve Reynolds and Froude number similitude in the physical model. Furthermore, in this particular case the prototype model was not limited by an incorrect tidal period. In contrast, the accuracy and reliability of prototype scale predictions are limited by the amount (or rather lack) of data for model calibration. Hence the good agreement achieved at the physical model scale is key in having confidence in the prototype scale predictions.

7.2.1 Natural condition

For the prototype scale predictions, the same model grid was used as in the physical model, with the bathymetry and grid spacing modified using the approximate scale factors. This gave a grid size of 600 m in both the x and y directions. Furthermore, in the physical model the number of layers in the TRIVAST model was reduced to unity, i.e.

the depth-averaged equations were solved. For the prototype scale six layers were used, each with an initial layer thickness of 10 m. Whilst in reality the tidal regime of an estuary is subject to a spring-neap cycle, amongst other tidal harmonics, in this study the model was ran over a typical mean spring tide. This was done not only to simplify the estuary dynamics, but importantly as the mean spring tide is the tidal condition that is commonly used in marine energy assessments.

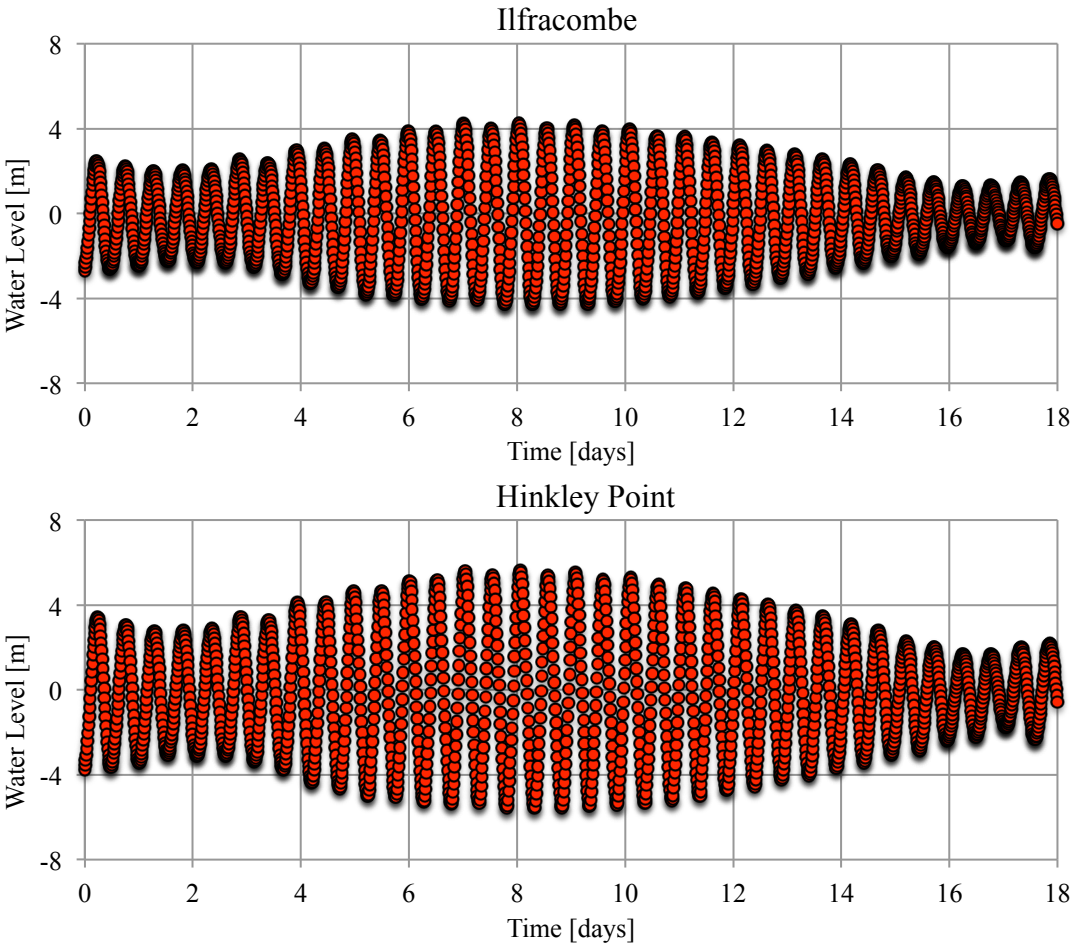

Figure 7.13 Tidal elevations in the Severn Estuary over a spring-neap cycle (top: Ilfracombe, bottom: Hinkley Point)

Figure 7.13 shows tidal gauge data for two stations in the Severn estuary, over a spring-neap cycle. The first point was at Ilfracombe, which is situated at the point where the Irish sea meets the Bristol Channel, and for the purposes of this study can be considered as the start of the Severn estuary modelling domain. The second point, namely Hinkley Point, is located downstream of the Severn Barrage site. The data show that for a spring tide the amplitude of the incoming tidal wave is 4 m, i.e. a tidal range of 8 m, and due to the tidal amplification that occurs then the tidal range is increased to approximately 11

m at Hinkley Point. Therefore, a continuous 4 m amplitude sinusoidal wave, with a 12.4 hr period was imposed at the lower water elevation boundary in the TRIVAST model.

Figure 7.14 shows a comparison of the BODC tidal gauge data, and the TRIVAST predictions of tidal elevations in the Severn Estuary. The model showed excellent agreement in predicting the tidal amplification and, in particular, the distortion of the incoming wave due to the estuary becoming shallower, in that the tide flooded more quickly than it ebbed. The tidal range throughout the estuary, as predicted by TRIVAST, is given in Figure 7.15 and this further highlights the tidal amplification that occurs with increasing distance upstream in the estuary. Furthermore, with the tidal range exceeding 12 m the predictions confirm the high marine energy resource for tidal range technologies.

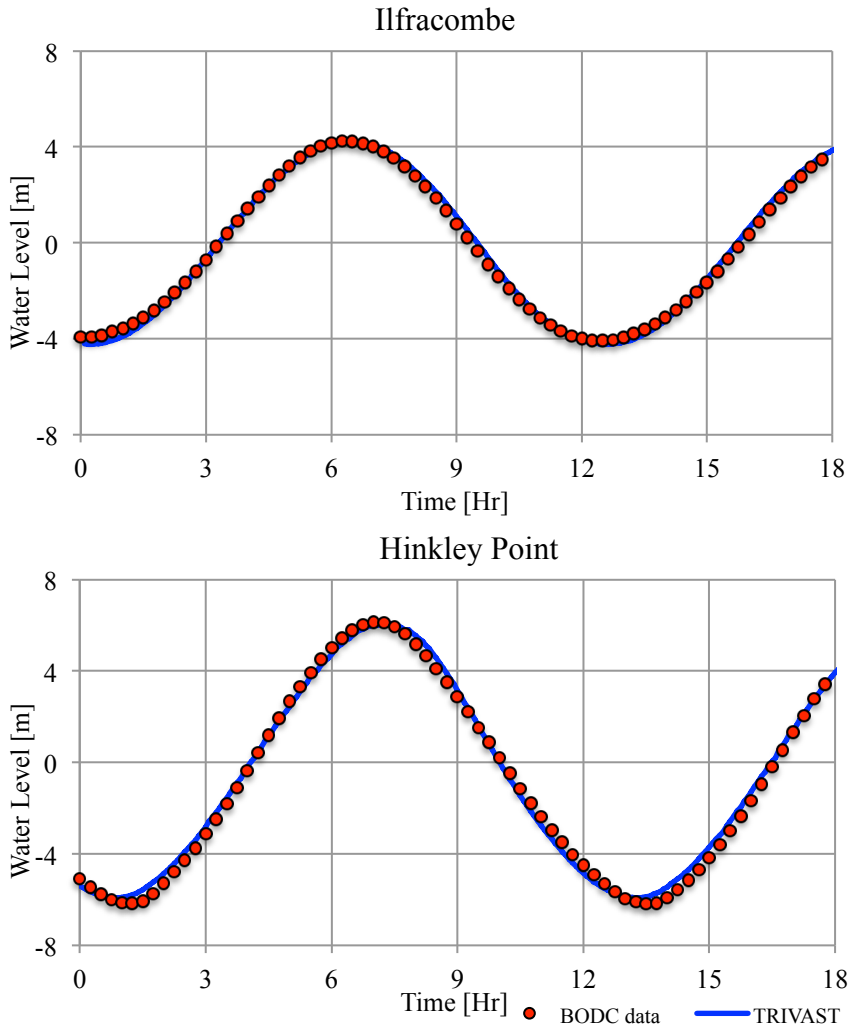

Figure 7.14 Comparison of TRIVAST predictions and BODC data of tidal elevations in the Severn Estuary

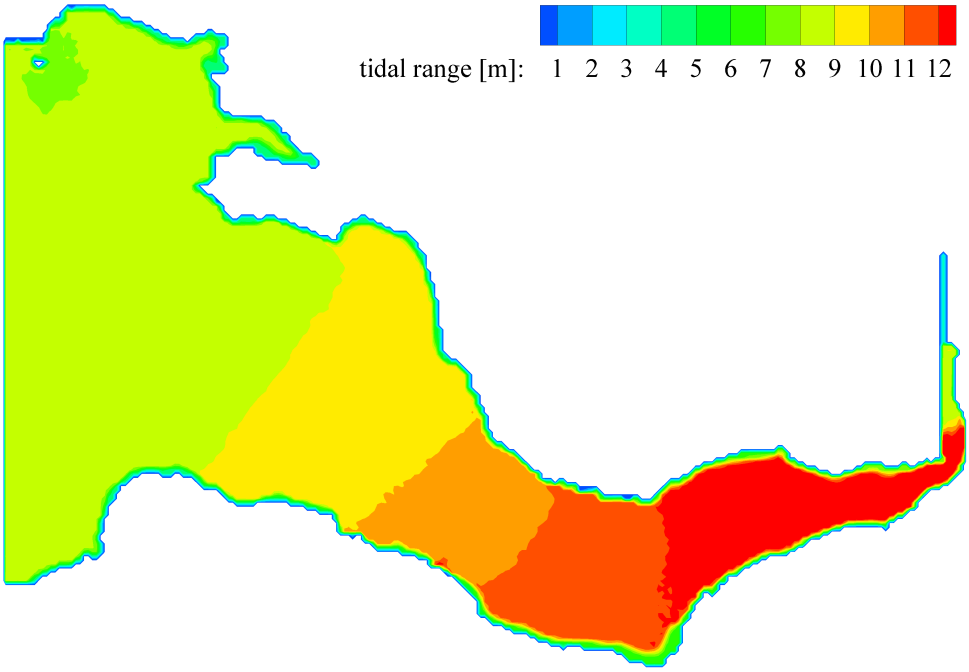

Figure 7.15 TRIVAST model predictions of the tidal range in the Severn Estuary

Hourly velocity measurements over a mean spring tide were available at a number of points located throughout the estuary using Admiralty Chart 1165, the locations of which are given in Figure 7.16. For model calibration six points were chosen, namely: Points E, H, K, L, P and Q respectively.

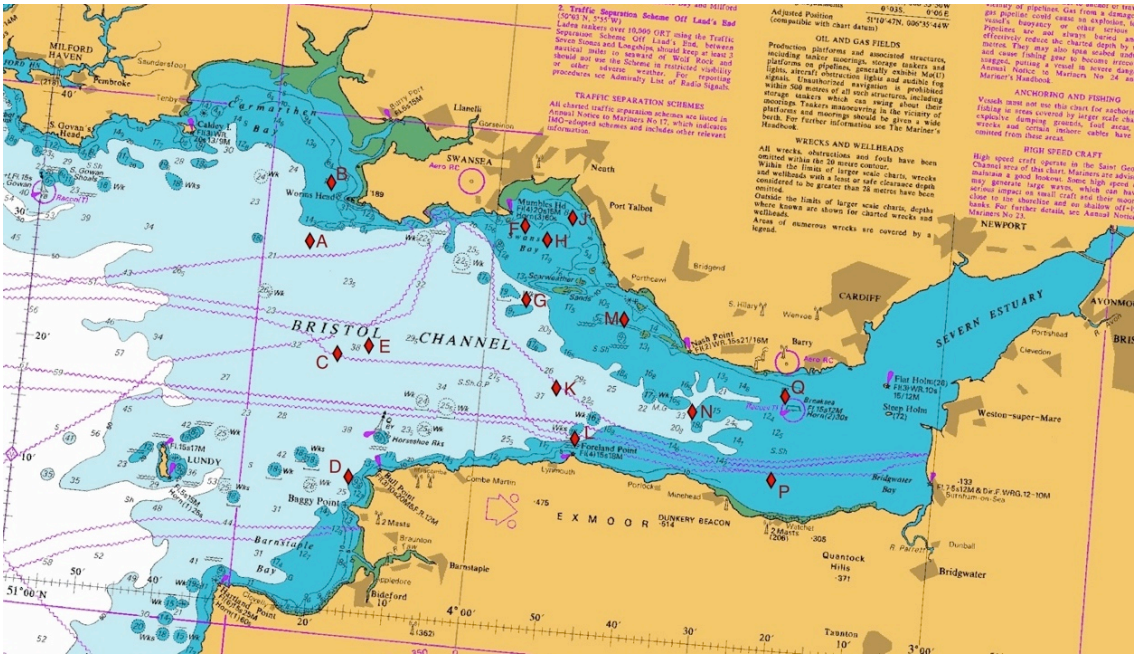

Figure 7.16 Sampling locations of tidal currents, as taken from Admiralty chart 1165

A comparison of the predicted tidal currents from TRIVAST, and the Admiralty chart data is given in Figure 7.17. As well as accurately predicting the tidal elevations, the model demonstrated close agreement with the spring tide currents, , both in terms of the magnitude and direction, throughout the estuary. Peak velocities ranged from 0.7 ms^{-1} at Point H, to 2.4 ms^{-1} at Point L, and in general faster currents were observed on the ebb tide. Lesser agreement, although marginal, was observed on the flood tide where TRIVAST tended to under predict the velocity. With the exception of Point E, the directionality of the measured points was relatively constant over each tidal period - an advantage for tidal stream turbines as this reduces the yawing requirements of the turbines, aiding their performance. However, as the predicted values of velocity have been Reynolds averaged, in practise the velocities would be subject to real time turbulence and changes in direction, and would require further study at a near-field scale to assess the effect on the turbine performance.

Contour plots of the velocity predictions throughout the estuary are given in Figure 7.18, for both the Mean Spring Current (MSC) and the Mean Peak Spring Current (MPSC). The difference between these two variables is important. Whilst the majority of marine energy studies use the value of the MPSC and a load factor to make assessments of the resource, as identified in the literature review, the value of the MSC also gives an indication of how much energy can be extracted throughout a tidal cycle. Figure 7.18 shows that whilst many areas throughout the estuary experience peak currents in excess of 2 ms^{-1}, which is ideal for tidal stream turbines, the mean current value is closer to 1.2 ms^{-1}. Typical tidal stream devices under development have cut-in speeds of 1.5 ms^{-1}, and consequently would not generate any electricity for much of the tidal cycle. Therefore these results highlight that whilst initial resource assessments show that the Severn Estuary possesses a large kinetic energy flux throughout a tidal cycle, the current technology available is not suited to harness this energy. Further discussion of the tidal stream resource is given in section 7.3, whilst the following section discusses the impact of the Severn Barrage proposals.

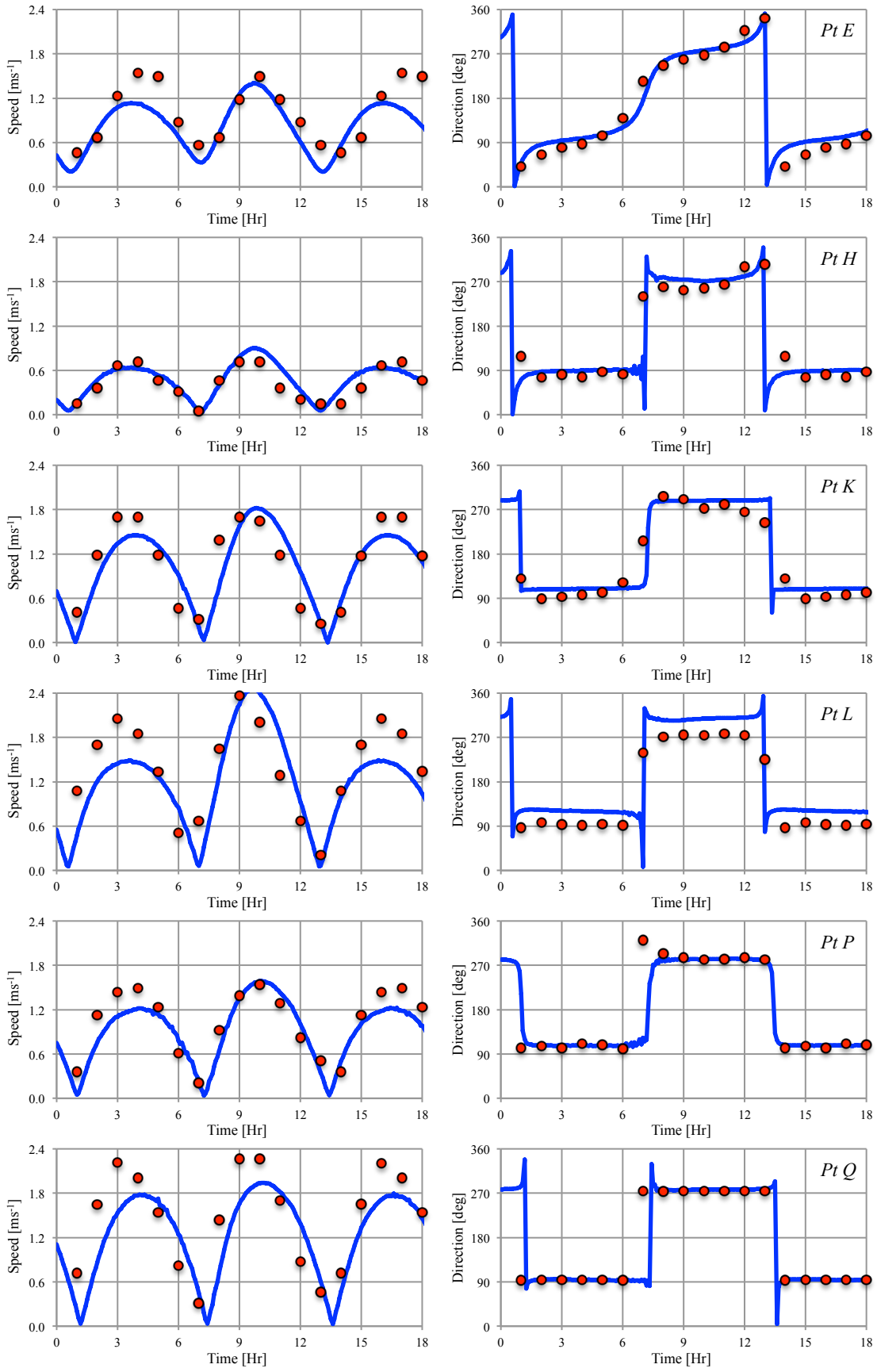

Figure 7.17 Comparison of TRIVAST predictions (Blue line) and Admiralty chart data (Red points) of tidal currents and directionality in the Severn Estuary

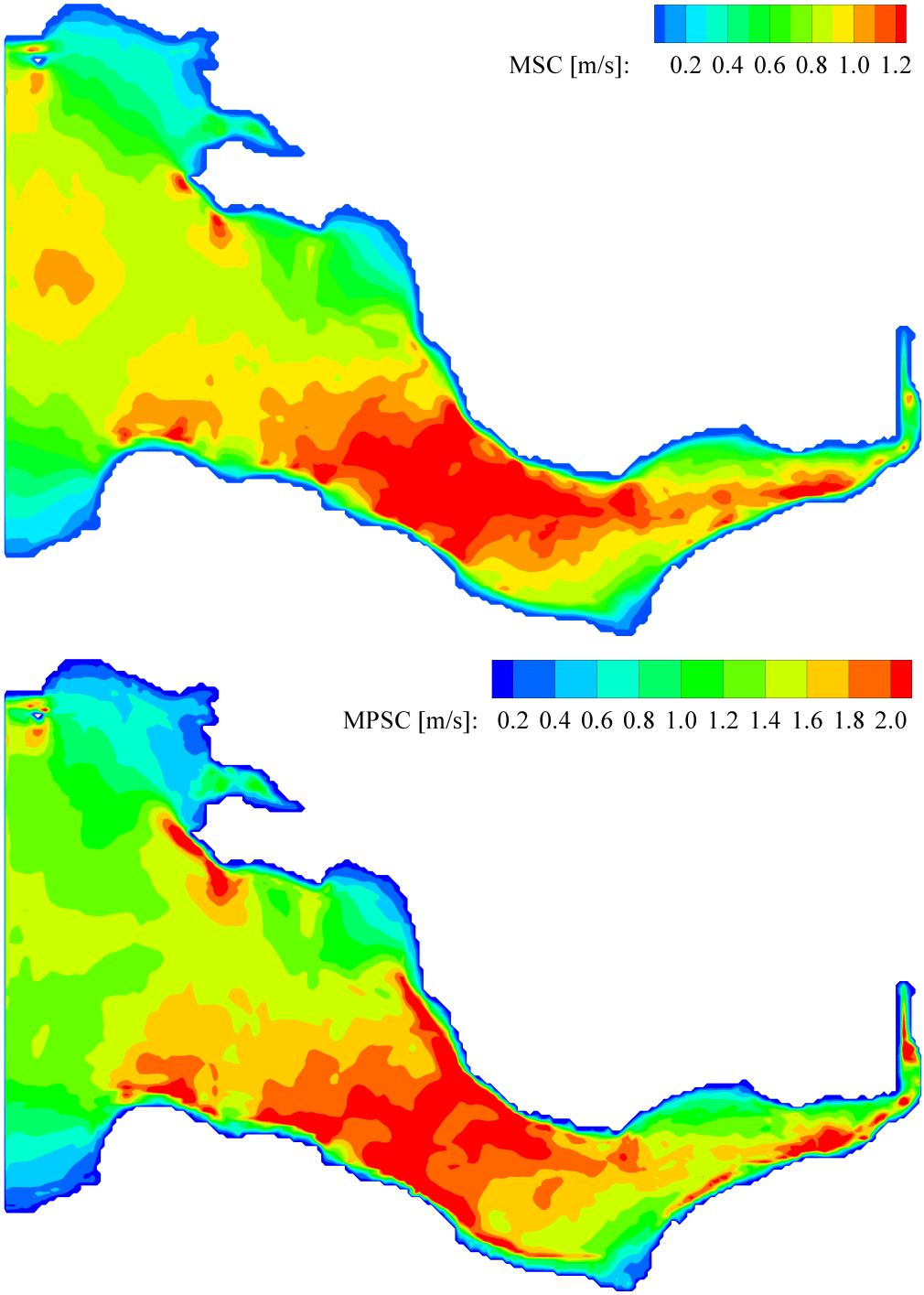

Figure 7.18 TRIVAST predictions tidal velocities in the Severn Estuary (Top: Mean Spring Current, Bottom: Mean Peak Spring Current)

7.2.2 STPG barrage

Figure 7.19 shows the predictions of water levels upstream and downstream of the STPG barrage, and the power generation during a tidal cycle. The results show, as expected, a significant increase of approximately 4 m in the minimum water levels upstream of the barrage. The downstream levels remain relatively unaffected and, once they are above the minimum basin level, the two water levels are similar in magnitude as the basin is filled via the sluice gates. However, on the ebb tide a maximum head difference of 6 m is created, which enables the maximum power output of 8.64 GW to be generated.

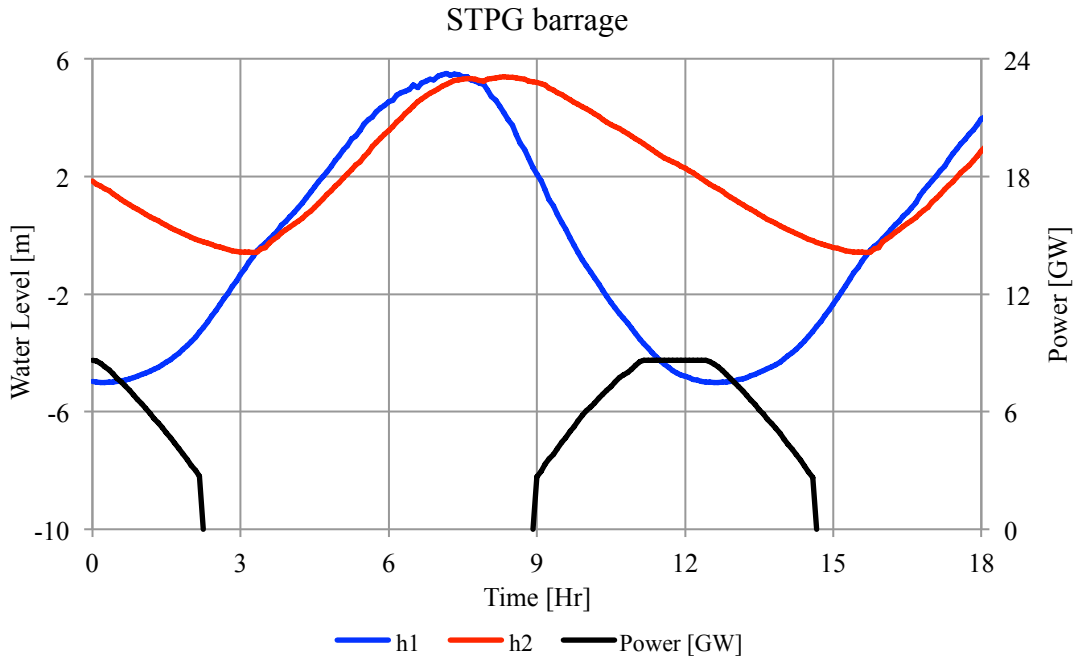

Figure 7.19 TRIVAST predictions of water levels both upstream and downstream of the STPG barrage scheme, and power generated

Over a tidal cycle the TRIVAST model predicted that 37.1 GWhr of energy could be generated. This is larger than estimates from previous numerical model studies, for example Xia et al. (2010a) predicted that 24.4 GWhr could be generated. This is due to the relatively simplistic method used in modelling the barrage operation in this study, in that no turbine hill chart was incorporated, but rather the flow rates were calculated based on the head difference using the orifice equation, as detailed in Chapter 5. Therefore the predicted outputs from the model were anticipated to be optimistic, and can be improved in any further studies if specific details of the turbines and sluice gates are used in the barrage, if available.

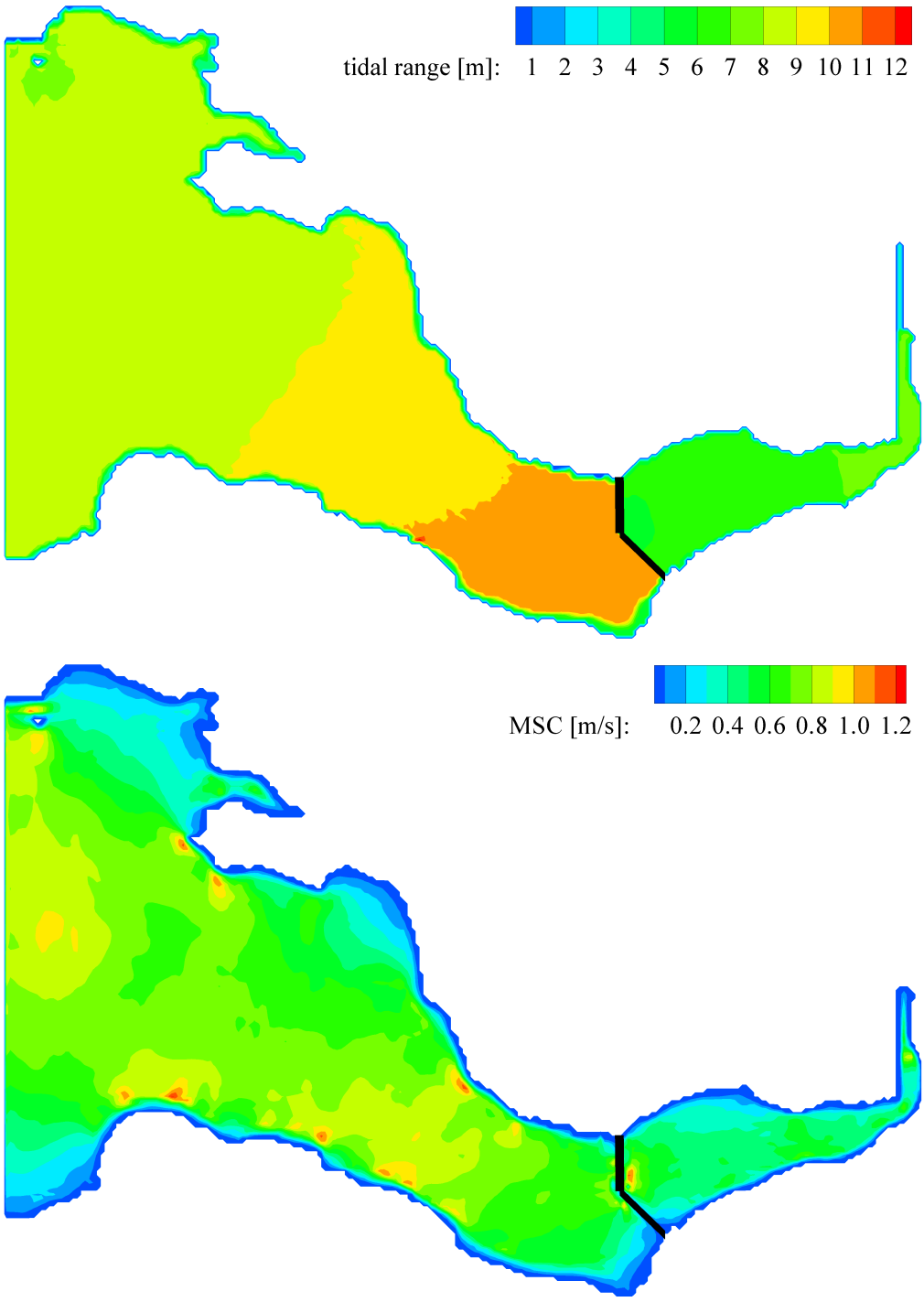

Figure 7.20 TRIVAST predictions of the STPG barrage scheme (Top: tidal range, Bottom: Mean Spring Current)

The affect that the STPG barrage had on the hydrodynamics of the Severn Estuary is given in Figure 7.20. Firstly, the top contour plot shows the effects that the barrage had on the tidal range throughout the estuary. It can be seen that, as already confirmed, the tidal range upstream of the barrage is dramatically reduced to approximately 5 m.

Furthermore, in comparison with the tidal range of the natural condition, given in Figure 7.15, there is also a small reduction in the tidal range downstream of the barrage. The effect of energy extraction, and the significant change in the tidal range, had a large impact on the tidal velocities throughout the estuary, as also shown in Figure 7.20. With the STPG barrage in place, the predicted Mean Spring Current was typically below 0.8 ms^{-1}, whereas for the natural condition the MSP was generally above 1.0 ms^{-1}, and greater in the narrower channel sections. The hydro-environmental consequences of such dramatic changes to the estuary dynamics have already been discussed in previous studies, as identified in the literature review. It is not the intention of this study to re-evaluate these impacts, but rather provide a comparison for the lesser-studied Hafren Power scheme.

7.2.3 Hafren Power barrage

Due to the commercial nature of the Hafren Power scheme, and that at the time of this study the project was at the proposal stage, very few specific details of the barrage design and operation were available. Therefore, a number of assumptions of the barrage design were made, and two operating conditions were modelled. Firstly, it was understood that the barrage would utilise 1026 very-low head turbines (Hafren Power 2013), which would have a much smaller capacity than traditional bulb turbines. Therefore it was assumed that the maximum power output of the barrage was limited to 4.5 GW, and this value was based on similar values obtained in previous research studies (Xia et al. 2010a; Rolls-Royce Plc and Atkins Ltd 2010). For the two operating conditions modelled, both were specified with a 2 m starting head, with the difference between the two conditions being the maximum and minimum water levels upstream of the barrage, before the holding phase began. For the first condition the limit was set to ±4 m relative to mean sea level, whereas the levels were reduced to ±3 m for the second condition.

A comparison between the predicted water levels upstream and downstream of the two operating conditions, and the power generated, is given in Figure 7.21. For the first operating condition, in which the minimum and maximum levels were restricted to ±4 m relative to mean sea level, the results show that the upstream elevations are similar to the downstream levels, i.e. there is relatively little change to the tide, except for a 2 m

reduction in the tidal range. This is significantly different from the STPG scheme, however the predicted power over a tidal cycle was less, at 28.5 GWhr, compared to 37.1 GWhr. In contrast, the second operating condition predicted a similar energy output to the STPG scheme due to the greater head difference, at 36.4 GWhr per tidal cycle. The reduction in the tidal range of 4 m, is the same as the STPG scheme, but the reduction is centred about mean sea level, therefore there was less permanent flooding of intertidal areas, and increased flooding protection due to a decrease in the maximum water levels.

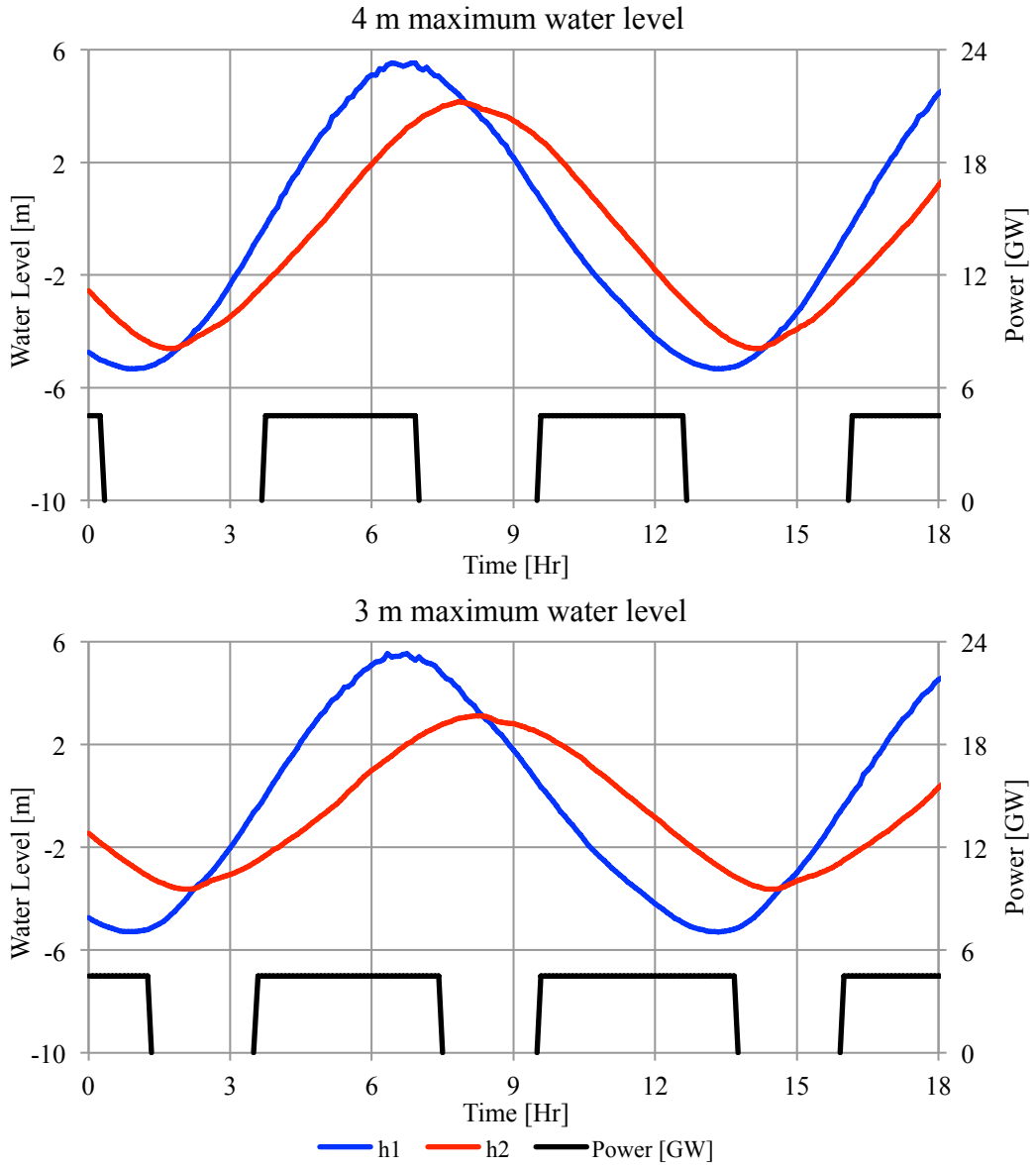

Figure 7.21 TRIVAST predictions of water levels both upstream and downstream of the Hafren Power barrage scheme, and power generated
(Top: 4 m maximum water level constraint applied, Bottom: 3 m maximum water level constraint applied)

The predicted tidal range throughout the estuary, for both operating conditions, is given in Figure 7.22. The results further emphasise the findings from the previous figure, in that depending on the head difference across the barrage, the upstream tidal regime could potentially behave like the natural conditions. For the first operating condition, tidal amplification was still observed upstream of the barrage, with the tidal range reaching 11 m, and for the second case a small amount of tidal amplification was observed, albeit to a much lesser extent. The downstream levels for both operating conditions showed little change when compared with the natural conditions.

The same behaviour was observed with respect to the tidal currents throughout the estuary, as shown in Figure 7.23, whereby, depending on how much resistance the barrage provided to the flow, i.e. how much energy was extracted, the reduction in the velocities varied. Whilst the currents were reduced significantly compared to the natural condition - as one would expect with a barrage in place, the first operating condition showed significantly faster mean currents than the second, with a number of areas experiencing mean spring currents in excess of 1.0 ms^{-1}. For the second operating condition the mean currents were similar in magnitude to the STPG, as both removed equal amounts of energy from the tide.

The results from these two operating points show that a two-way barrage, i.e. the new Hafren Power proposal, offers the potential to limit the hydro-environmental impact significantly, compared to the traditional ebb-only STPG scheme. The main difference is that any changes to the hydrodynamics of the estuary are centred about the mean sea level, thereby reducing any significant changes to the minimum water levels, and additionally providing flood protection due to the reduction of the maximum water levels. The magnitude of these changes depends greatly on the specific operating condition of the barrage, something that is not known at the time. Hydrodynamic conditions similar to the natural conditions can be created, however the trade off is how much energy is generated. The results have shown that similar amounts of energy to the STPG barrage could be generated, although it is noted that at this stage the very-low head turbine technology required operate at this stage will be a new technology, and it remains to be seen if it can efficiently extract the predicted amount of tidal energy.

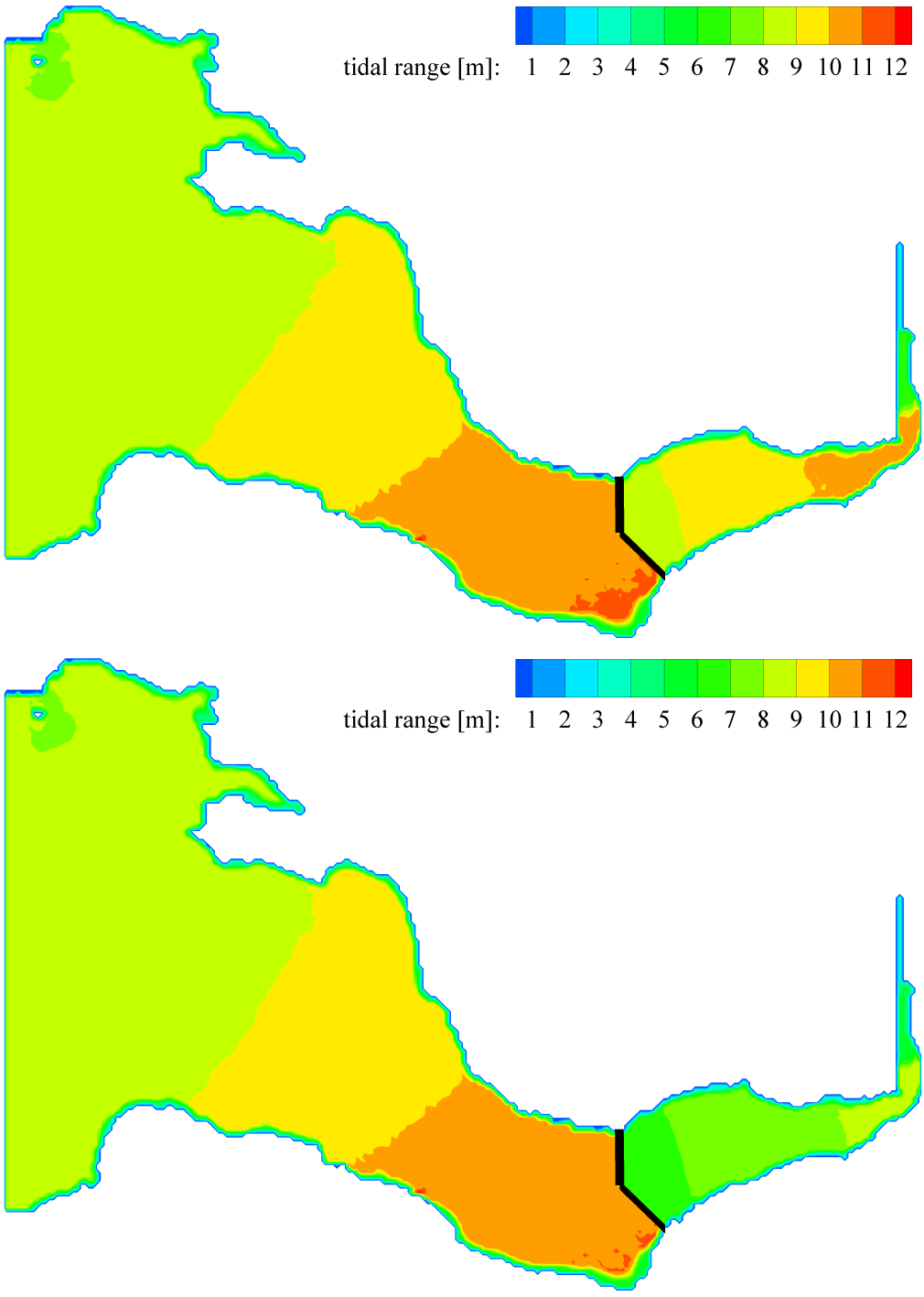

Figure 7.22 Differences in tidal range predictions for the Hafren Power barrage (Top: 1st operating condition, Bottom: 2nd operating condition)

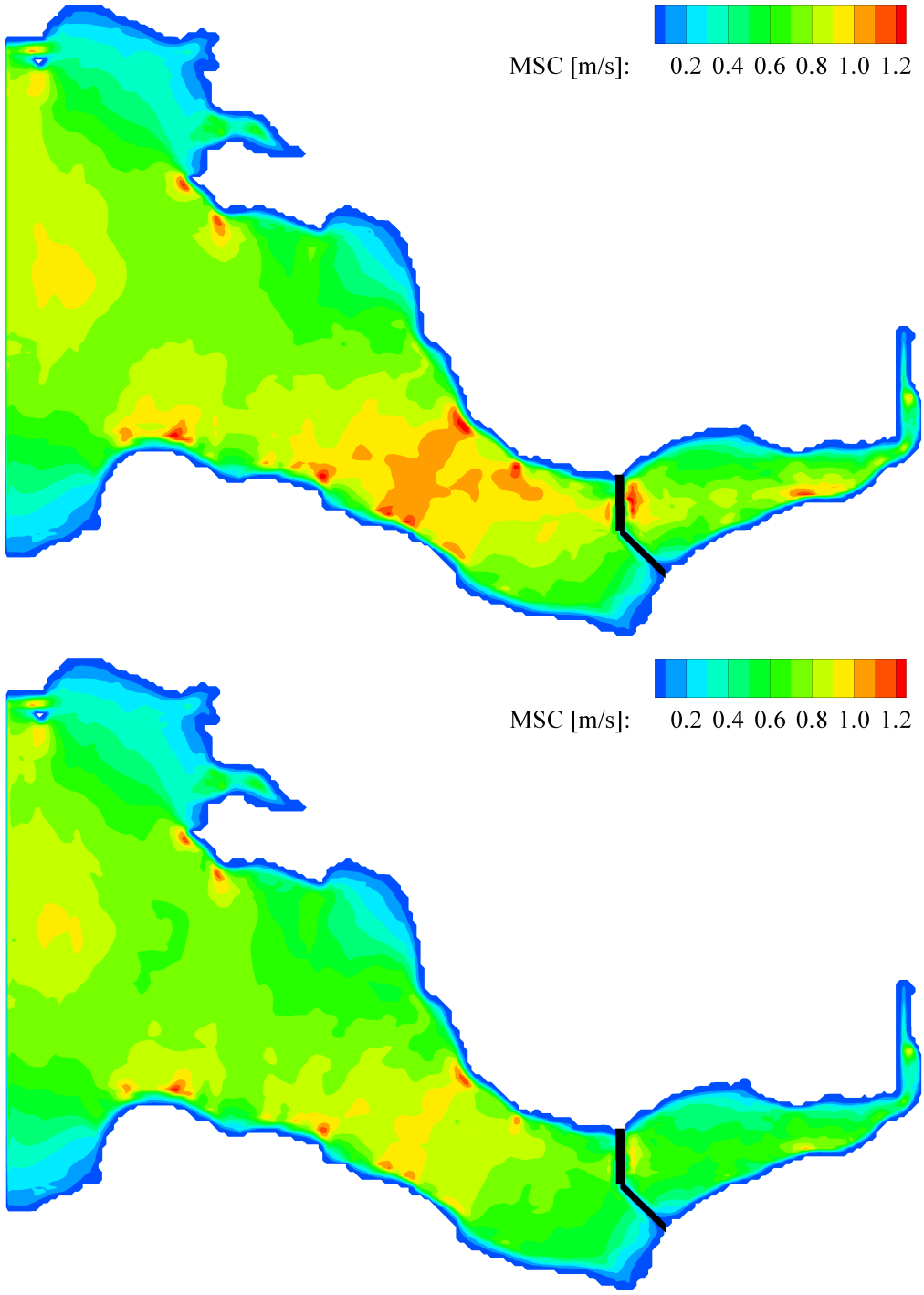

Figure 7.23 Differences in Mean Spring Current predictions for the Hafren Power barrage (Top: 1st operating condition, Bottom: 2nd operating condition

7.3 Tidal stream energy in the Severn Estuary

Due to the significant tidal range energy resource in the Severn Estuary and the scale of the Severn Barrage proposals, the main focus to-date has been on tidal range technology deployment. As a result there has been very little interest in tidal stream energy deployment in the Severn, however, it has already been demonstrated that significant potential for tidal stream energy generation exists. The primary concern is that if a large-scale tidal range project, such as the Severn Barrage, were to be realised, then it could significantly reduce the tidal stream resource. Therefore in Wales, for example, interest in tidal stream deployment has been focused on other sites in Pembrokeshire and Anglesey. Although it is widely accepted that the construction of a Severn Barrage would reduce the tidal stream resource, there has been little research to quantify this reduction and these studies, such as Xia et al. (2010c), have focused on the impact on the tidal stream resource if the STPG barrage were to be built. The results from section 7.2 have demonstrated that the impact of the new Hafren Power proposal has the potential to limit the hydrodynamic changes to the estuary, particularly downstream, and therefore the possibility exists that the two technologies could be deployed together in the estuary. This could particularly be true if shallow water vertical axis turbines were used, as these turbines may potentially be better suited to the Severn Estuary than typical horizontal axis devices, as discussed in Chapter 4. Therefore the following results investigate the potential deployment of a hypothetical array in the estuary, and the effect of the Severn Barrage on the resource.

7.3.1 Site selection

To identify the potential deployment sites suitable for horizontal and vertical axis tidal stream turbines in the Severn Estuary, a routine was added to the TRIVAST model, which, based on a number of simple constraints, returned the grid cells that met the criteria. A site was chosen to be appropriate for horizontal axis turbine (HAT) deployment if the minimum water depth was greater or equal to 20 m, with no upper limit to the depth of deployment applied, as it is anticipated that as the technology develops deeper waters could be exploited by HATs. In addition, a minimum Mean Peak Spring Current (MPSC) of 2.0 ms^{-1} was required. To determine the potential Vertical Axis Turbine (VAT) sites, the depth range was limited between 10 and 30 m,

as otherwise the device could not be considered as operating on shallow waters without becoming unrealistically large in size. The MPSC criterion was lower than that for HATs, with a minimum value of 1.5 ms^{-1} required. No limits to the deployment distance offshore were applied, in an attempt to quantify the maximum potential resource for both turbine types, and it is acknowledged that a number of other factors, such as shipping lanes etc., would also impact the potential resource.

Using the modelling constraints described the areas deemed appropriated for deployment from the TRIVAST model are shown in Figure 7.24, where the orange and blue areas indicate sites identified for HAT and VAT deployment, respectively. It can be clearly seen that there is a significantly larger potential area for vertical axis turbines, with an area of 1151 km^2 predicted by TRIVAST, compared to 255 km^2 of potential deployment area for horizontal axis turbines. These areas show good agreement with the Renewable Atlas data that was used in the introduction of this thesis, and it strongly makes the case that the Severn Estuary is better suited to shallow water technologies, provided that a technology exists that can feasibly extract the energy.

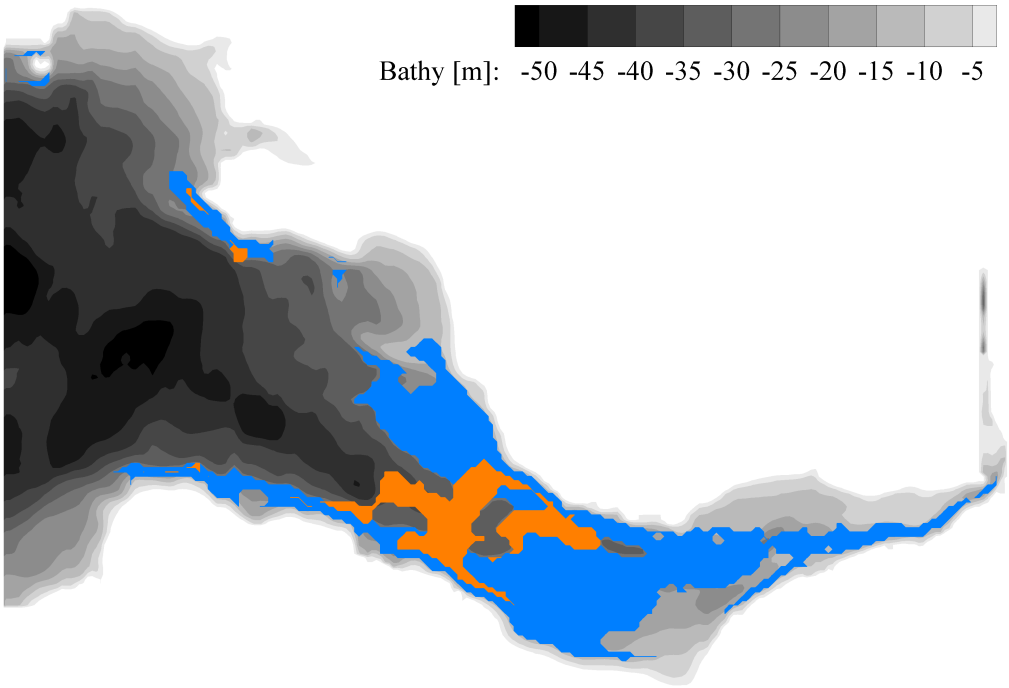

Figure 7.24 Potential tidal stream deployment sites in the Severn Estuary
Orange: horizontal axis turbines, and blue: vertical axis turbines

7.3.2 Hydrodynamic impact of tidal stream arrays

Whilst a significantly greater area of deployment has been identified for vertical axis turbines, the results from Chapter 4 demonstrated that a single VAT is likely to have a lower efficiency than an equivalent HAT, and therefore captures less power. However, the results from Chapters 4 and 6 also highlighted the potential for much closer turbine-to-turbine spacing, thereby increasing the power output per plan area. To investigate these findings a hypothetical array was modelled in TRIVAST. A site was chosen in the Severn Estuary that was suitable for both HATs and VATs, as identified in section 7.3.1. A total of 21 grid cells were selected to contain turbines, giving the total plan area of the array of 7.6 km^2. The details of the different design parameters in the layout of the arrays are given in Table 7.3. It is noted that at this stage the assumptions made are highly subjective, and depend on the specific turbine used.

Table 7.3 HAT and VAT array details

Details	Horizontal axis turbine	Vertical axis turbine
Device size	12m diameter	12x12m (height locally increased to maximise area)
Downstream spacing	15D	7.5D
Lateral spacing	10D	6.5D
Rated flow speed	2.5 ms^{-1}	1.5 ms^{-1}
Device efficiency	45%	30%
Total number of turbines	315	1008
Rated unit power	0.51 MW	0.15 MW
Rated array power	159 MW	147 MW

This is particularly true for the value of the rated flow speed. This parameter is used to design the electrical and mechanical equipment of the turbine, and represents the point at which the turbine is running at its optimal capacity. Due to the excessive loads occurring with the operation of such turbines, these devices do not generate power above their rated capacity, but rather the rated power is maintained and the loads are

minimised. Therefore the rated flow speed represents the upper limit of extractable power. In addition, as the power available is proportional to the cube of the flow speed, the power output calculations are particularly sensitive to this value. A rated flow speed of 2.5 ms^{-1} for a HAT is a typical value, but as no operating vertical axis technology currently exists a value of 1.5 ms^{-1} was assumed for this type of turbine. This value was chosen, as whilst a single VAT will be much smaller in power output than an equivalently sized HAT, a much larger number of turbines can be deployed in an equivalent area. Therefore the total array output was regarded as being approximately the same, with the rated array power of the hypothetical HAT array at 159 MW, compared to 147 MW for a VAT array.

The predicted power output of both arrays over a spring tide is given in Figure 7.25. The results show that due to the larger number of turbines, and favourable flow conditions the vertical axis turbine array produced significantly more power than the horizontal axis array. Considering no rated capacity limit, the VAT array produced flood and ebb tide power peaks of 230 and 325 MW, respectively, which over a full tidal cycle generated 1.6 GWhr of energy. By limiting the output to its rated capacity of 147 MW the energy generated reduces to 1.1 GWhr, but this is still much larger than the 0.75 GWhr generated with the horizontal axis array, which, as the velocities at the chosen site did not reach 2.5 ms^{-1}, never reached its rated capacity.

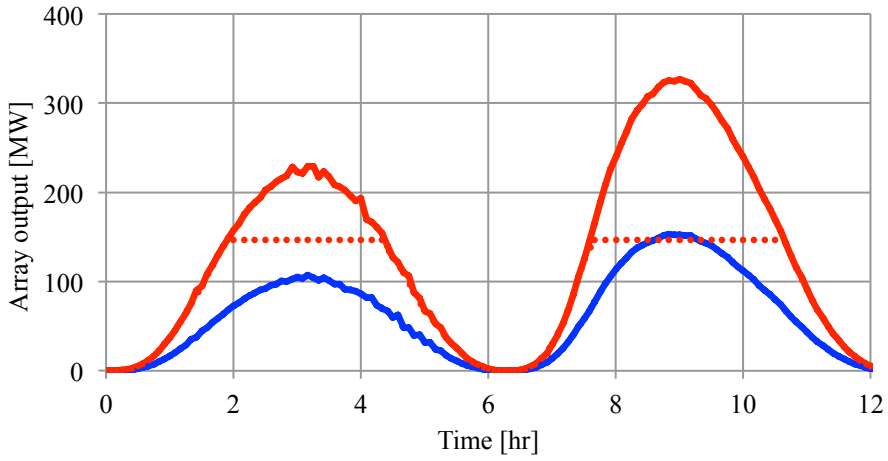

Figure 7.25 Predicted power output of two hypothetical arrays in the Severn Estuary (Blue line: HAT array, Red line: VAT array, where the dotted line represents the rated capacity)

The hydrodynamic impact of the two turbine arrays averaged over a spring flood tide is given in Figure 7.26. As more energy was extracted with the vertical axis turbine array,

a bigger difference in the velocities was observed, both downstream and around the array site, as it represented a bigger resistance to the flow, in comparison to the horizontal axis turbine array. Such changes would affect the tidal stream resource for other array sites, if multiple arrays were to be located in close proximity of each other, and requires further study to assess if this negative interaction would affect the overall resource of the Severn Estuary. Finally, minimal changes to the water levels were observed for both arrays.

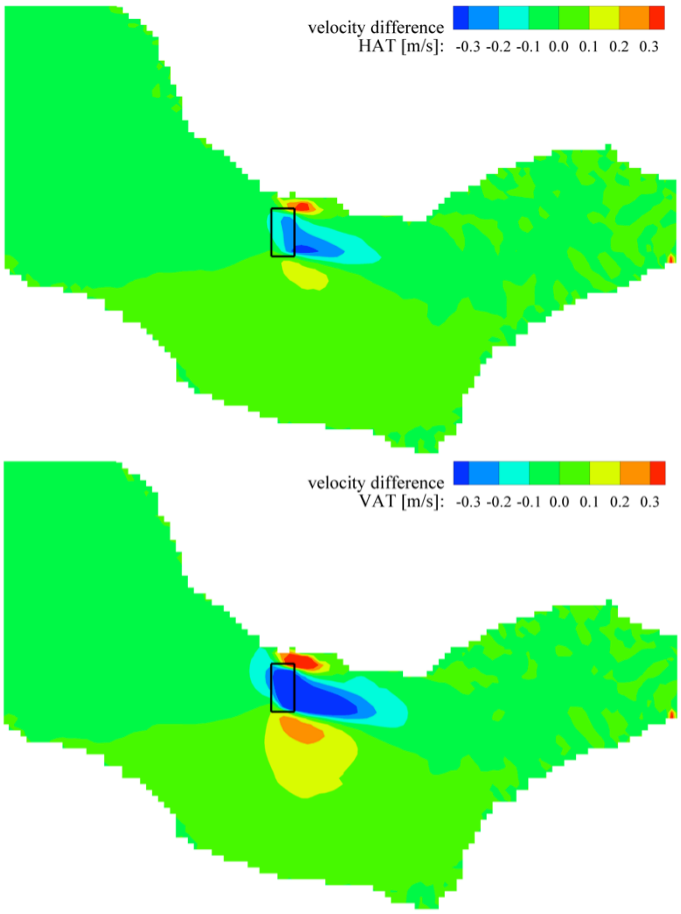

Figure 7.26 Flood tide velocity differences relative to the natural condition due to the presence of a tidal stream array (Top: HAT array, Bottom: VAT array)

Due to the assumptions made it is acknowledged that further study is required in this area in order to determine more specifically what outputs could be feasibly achieved using alternative turbines to typical horizontal axis devices, and what the impacts of their deployment would be. Therefore the results from this study are intended to investigate the potential deployment of vertical axis turbines, as opposed to making energy yield predictions. Based on this analysis it has been demonstrated that when

deployed in shallow water, vertical axis turbines show a significant potential in harnessing marine renewable energy.

7.3.3 The effect of a barrage on the tidal stream resource

The results from section 7.2 have already demonstrated that if a Severn Barrage were to be built, then the tidal currents throughout the estuary would be reduced, the magnitude of which would depend on the exact operation of the barrage and how much energy the barrage extracts from the estuary. To quantify this loss, the site selection routine used in the previous section was applied to each of the three barrage cases already modelled, using the same depth and velocity criteria. Therefore the total area of potential deployment for both HAT and VAT arrays was predicted pre- and post-barrage construction. The results from these model predictions are given in Table 7.4, which clearly depict that if any of the proposed barrage schemes were to be built, then the potential area of deployment for horizontal axis turbines is reduced to practically zero.

Table 7.4 Predicted areas of deployment for tidal stream arrays, with and without a Severn barrage

Case	Total potential area of deployment [km^2]	
	HAT array	VAT array
Natural condition	254.5	1150.6
STPG barrage	0.7	45.7
Hafren Power case 1	3.6	333.4
Hafren Power case 2	1.1	115.9

In contrast, whilst there is a significant reduction in the VAT resource throughout the estuary, an appreciable area for deployment remains. The STPG scheme showed the largest reduction in VAT area, from 1151 km^2 to 46 km^2, whereas the area predicted by the Hafren Power varied from 333 to 116 km^2, depending on the operating condition of the barrage. Significantly, this area is comparable to the potential area for HAT arrays in the natural condition. The locations of these potential sites for the different barrage schemes are given in Figure 7.27. In general, the sites originate from the same locations, with the total areas varying depending on the operation of the barrage. For the first case of the Hafren Power barrage, significant areas were identified in the central channel of the estuary, and a site upstream of the barrage was also established. In contrast, for the second case of the Hafren Power barrage and the STPG scheme the sites were closer to shore, typically near headlands.

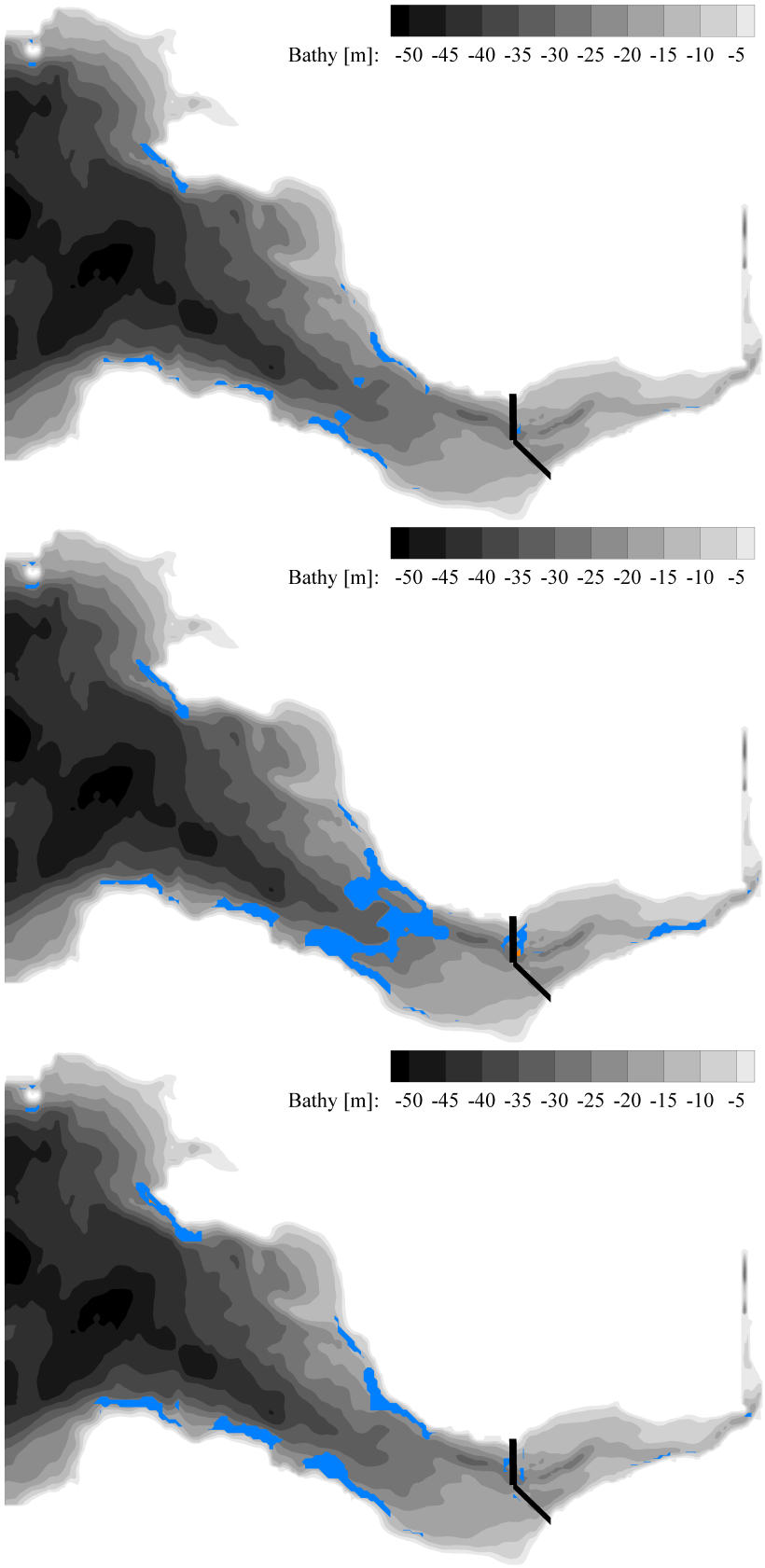

Figure 7.27 Potential areas of deployment for VAT arrays in the Severn Estuary
Top: STPG barrage, Middle: Hafren Power case 1, Bottom: Hafren Power case 2

The results show that whilst the construction of a barrage, if it were to go ahead, would almost entirely eradicate the potential for HAT deployment in the Severn Estuary, in contrast a similar area of deployment would remain that is suitable for shallow water vertical axis turbines. The hypothetical array study demonstrated that similar amounts of energy, and potentially more energy, could be extracted from VAT arrays compared to HAT arrays, albeit with a much larger number of turbines. Therefore the potential exists for both tidal range and tidal stream technologies to be deployed in unison in the Severn Estuary.

7.4 Conclusions

In this chapter the results are presented and discussed from a series of modelling applications using the numerical model TRIVAST. Unlike the previous near-field research conducted using ANSYS CFX in Chapter 6, TRIVAST is better suited to modelling the far-field dynamics of large water bodies, such as lakes, estuaries and coastal basins. In this study the model was applied to the Severn estuary – an area that contains the single largest area of tidal range resource in the UK, as well having a significant tidal stream resource.

Firstly, the Severn Estuary was modelled at a physical model scale, and complimentary laboratory measurements were taken using the physical model of the Severn Estuary, located in the Hydro-environmental Research Centre's hydraulics laboratory, at Cardiff University. This study investigated the impact of the Severn Barrage and, in particular, compared the hydrodynamic effects of the new Hafren Power proposals, with the superseded STPG proposals, as well as the natural condition. Due to the commercial nature of the Hafren Power proposals little was known at the time of the exact operating conditions, and therefore a number of different starting heads were modelled. The results showed that similar amounts of energy as the STPG scheme could be extracted, but more importantly that there was a reduced hydrodynamic impact of the barrage throughout the estuary, as the tide followed the natural state more closely. These impacts included a smaller increase in the minimum water levels upstream of the barrage, compared to the STPG scheme, as well as a reduction in the maximum water levels. This would result in less permanent flooding of the intertidal areas – a major environmental concern, as well as providing additional flood protection benefits. The

model also predicted a lesser reduction in the tidal currents throughout the estuary, the magnitude of which depended on the starting head.

The TRIVAST predictions showed very good agreement with the obtained laboratory data, and the calibrated model was extended to the prototype scale, as this addressed the scaling issues associated with reduced scale physical models. For the natural condition the model agreed well with data obtained from UK Tide Gauge Network, and an Admiralty Chart of the Severn Estuary. The conclusions obtained from modelling the various barrage schemes at the prototype scale agreed with those previously made in the physical modelling study.

The model was then used to identify the potential areas of deployment for tidal stream turbines and, in particular, to make a distinction between the areas suitable for typical horizontal axis turbines and shallow-water vertical axis turbines. The criteria used to determine whether an area in the estuary was suitable for a horizontal axis turbine was based upon the current technology used, as identified in the literature review. For the vertical axis turbines, the criteria were defined by using the outcomes of the physical and numerical modelling tests, as reported in Chapters 4 and 6, respectively. The principal difference between the two types of turbines were the depth at which they could be deployed, as well as the rated flow speed – which was lower for the vertical axis turbines. The numerical model results predicted a much larger area of deployment being available in the Severn Estuary for shallow-water vertical axis turbines. Two hypothetical arrays were considered in the model; the first using typical horizontal axis turbines and the second using vertical axis turbines. The power output and the hydrodynamic impact was compared for both array configurations. The results showed that whilst a much larger number of turbines would be required, a greater energy yield per plan area was achievable with the vertical axis turbines and therefore, given the larger resource area, the Severn Estuary is much better suited to utilising this type of turbine, as opposed to the horizontal axis designs that are currently favoured by developers.

Finally, the interaction of the Severn Barrage and tidal stream turbine deployment were investigated. The TRIVAST predictions showed that for all three of the barrages modelled, practically all of the tidal stream resource for horizontal axis turbines would

be eradicated. In contrast, whilst the vertical axis turbine areas would also be reduced by a significant margin, if the Hafren Power barrage were to be built then the remaining resource area for vertical axis turbines would be of a similar size to the existing area available to horizontal axis turbines. This implies that large-scale deployment of both tidal stream and tidal range technologies could exist in the Severn Estuary. However, whilst this thesis has initially investigated this concept and highlighted the potential advantages of using an alternative turbine design, much more research is required in this area to determine if such a shallow water turbine could be economically developed, and work at the prototype scale.

Chapter 8 Conclusions

8.1 Summary

The main objective of this thesis was to investigate further the hydrodynamic impacts of marine renewable energy (MRE) technologies, with particular focus on their deployment and potential for power generation in the Severn Estuary. Two forms of MRE were considered: tidal stream and tidal range devices, with the Severn Estuary being potentially identified as a substantial resource for both of these technologies. Currently, the tidal stream industry is in its infancy, with development and growth following that of the wind industry, in that single devices are developed with the aim of large-scale arrays being constructed to generate significant amounts of energy. Due to the similarities in how the devices extract the kinetic energy from their respective streams, it is hardly surprising that tidal stream turbines are similar in design to wind turbines, and with developers favouring horizontal axis turbines. Horizontal axis turbines have been demonstrated to have the highest peak efficiencies in unconstrained flows - hence their popularity. However, tidal flows, especially in shallow waters, are constrained by a free surface as well as the proximity of land boundaries that typically characterise a tidal stream site.

This oversight has led a number of researchers to argue that much larger amounts of energy extraction is feasible, if one takes advantage of these flow constraints. In shallow waters in particular, vertical axis (or cross-flow) turbines could potentially be used to maximise the power take-off area, and increase the energy yield compared to a horizontal axis turbine. This is where the Severn Estuary comes into significance, as due to the bathymetry and flow characteristics of the estuary, a much larger area - up to five times greater - of potential deployment exists for vertical axis turbines, by considering shallower waters and a lower flow speed.

How much energy can be extracted from an array of turbines largely depends on: the size of the turbines, the turbine-to-turbine spacing in both the downstream and lateral dimensions, if any interaction exists between them, and whether this interaction has positive or negative effects on the power generated. The wake characteristics of tidal stream turbines have been studied to a much lesser degree compared to performance

tests, and the focus has been on horizontal axis turbines. Practically no research into the wake characteristics of vertical axis turbines existed prior to this thesis. The aforementioned lack of research into vertical axis tidal stream turbines, as well as the potential advantages of shallow water deployment has led to the following two research objectives:

Objective 1: Performance analysis and design of vertical axis tidal stream turbines

Objective 2: Assessment of the wake characteristics of vertical axis devices

As well as tidal stream interest, the Severn Estuary has long been the subject of plans to utilise the large tidal range of the estuary. The Severn Barrage is the largest of these schemes, with the 1989 STPG proposal widely considered as the original Severn Barrage. In 2010 a private consortium, namely Hafren Power, launched fresh proposals for a barrage construction which superseded the STPG scheme. The principle difference between the two is that the Hafren Power barrage would operate under a two-way generation scheme, thus following the natural tide more closely and minimising the hydro-environmental impacts, whilst generating a similar amount of energy. These new proposals have not been tested to the same level of rigour as the STPG scheme and hence little is known about the hydro-environmental impacts of the barrage, as well as its effect on the tidal stream resource in the Severn Estuary, and whether the two differing technologies could be deployed in the estuary together. This has therefore led to an additional final research objective, namely:

Objective 3: Hydrodynamic impact of the Severn Barrage

These research objectives have been achieved using both physical and numerical modelling techniques, at a range of modelling scales. Research objectives 1 and 2 were realised in Chapters 4 and 6, in which a number of scale model vertical axis turbines were tested in the Hydro-environmental Research Centre's (HRC's) recirculating flume, and corresponding CFD models were executed using the commercial code ANSYS CFX. Research objective 3 was accomplished in Chapter 7, where the numerical model TRIVAST was applied to the Severn Estuary, both at a physical and prototype model scale. The conclusions from these studies are given in the following section.

The principle novel aspect of this research is the quantification of the wake behaviour of vertical axis turbines. Previous research studies have focused on horizontal axis turbine wake behaviour and therefore, to the author's knowledge, this is the first research study that has used both physical and numerical modelling techniques to investigate the wake behaviour of vertical axis turbines. Furthermore, whilst the CarBine research builds upon two MSc projects, this is the first research study that quantifies the effects of the number of flaps on the turbine performance. Finally, whilst two-way generation schemes have been considered in the Severn Estuary before, these used the same number of turbines as in the STPG ebb-only scheme (i.e. 216 bulb turbines). This study is the first that has considered a two-way generation scheme according to the recent Hafren Power proposals, i.e. 1000 turbines with no sluice gates. It is also the first study that has used a physical model of the Severn Estuary to investigate the hydro-environmental impacts of marine renewable energies.

8.2 Conclusions

8.2.1 Performance analysis and design of vertical axis tidal stream turbines

Performance tests were conducted in the HRC's large recirculating tidal flume. Scale model turbines were constructed, and three main designs of a vertical axis turbine were used, namely the CarBine, Savonius and Darrieus turbines. A mechanical based power take-off system was designed and implemented by the author and another PhD student, and efforts were made to ensure that the hydraulic conditions in the flume were representative of full-scale conditions. The main conclusions from the tests can be summarised as follows:

CarBine conclusions

- Previous MSc studies of the CarBine turbine were overly optimistic in predicting device performance, with the measured efficiency varying between 14% and 20%, depending on the flow conditions.
- Whilst this is a relatively uncompetitive value of performance, the turbine is still far from a final design and performance could potentially be improved by considering device interaction, as well as the implementation of lift forces to increase rotor speed.

- One design modification was attempted to improve the performance, but this attempt was unsuccessful.

Savonius conclusions

- The Savonius turbine was the best performing turbine in all of the tests, with the peak efficiency ranging from 27% to 38%. This value is competitive with other turbine designs considering the simple design of the turbine.

Darrieus conclusions

- The performance of the Darrieus turbines tested was not as high as expected, as this design typically outperforms the Savonius turbine. The peak efficiency varied between 12% and 27%. However, the configurations tested were not final designs, and research into the performance of this model is on-going within the HRC, at Cardiff University.
- As the Darrieus turbine is typically a high-speed-low-torque turbine, compared to the CarBine and Savonius models, it was more susceptible to friction losses in the power take-off system, which was believed to have affected its performance.

Whilst the Froude numbers in the flume were higher than field conditions, the Reynolds numbers were typically two orders of magnitude lower. With higher Reynolds numbers the negative drag of the turbine blades would reduce, therefore the performance values can be considered conservative. However, further research is required to confirm this assumption with lower Froude numbers. In addition, the disks used to mount the turbine blades would have provided a source of negative drag, although how much effect the disks would have had was not quantified in the tests.

The CFD code ANSYS CFX was used to model two turbine configurations, following the performance tests. An idealised model of CarBine, using one arm, referred to as CB_1D, was modelled, as was the Savonius turbine. For the CB_1D configuration the CFX model predicted the performance values well up until the peak operating point. However, due to the idealised methodology used, the model gave unrealistic values of the performance for higher turbine speeds. On the other hand, the Savonius performance predictions showed good agreement with the laboratory data. These predictions were

generally optimistic compared with the laboratory values, and the following factors were thought to attribute to this finding:

- The simulations were run in 2D, which tends to be optimistic due to the additional flow constraints.
- A constant angular velocity was prescribed for the turbines, whereas a pulsing angular velocity, as observed in the laboratory tests, would lead to different torque predictions.
- The choice of turbulence model, as whilst the k-ε was used because of the already high demand on computational resources, other turbulence models are better suited to modelling flow separation.
- The laboratory data was inherently subjected to experimental error, and other forms of energy losses that cannot be modelled.

In conclusion the modelling studies have demonstrated that utilising a blockage effect can enhance turbine performance. The blockage used in testing was relatively modest at 17%. This suggests that even higher outputs could be achieved, however, the results also show that if no blockage exists, i.e. in deeper waters, then it is unlikely that any of the turbines tested could compete with horizontal axis designs. Therefore, in shallow waters, such as the Severn Estuary, these vertical axis designs could be better suited for energy generation than horizontal axis turbines.

8.2.2 Assessment of the wake characteristics of vertical axis devices

Using the same scale model turbines and experimental setup as was used in the performance tests, the wake characteristics of four turbine configurations were modelled, namely: the CB_4S and CB_4D CarBine configurations, and two sizes of Savonius turbine. Both time-averaged and time-series measurements were recorded at a number of horizontal and vertical profiles in order to establish the length and shape of the wake downstream of each turbine. For each of the configurations tested the general behaviour of the wake was similar, and can be summarised as follows:

- The wake was asymmetrical in shape, as the thrust imparted on the flow varied across the width of the turbine.

- The flow was unsteady, with vortex shedding occurring as the turbine rotated, with the frequency of the vortices depending on the size of the turbine.
- The wake was shorter than that for horizontal axis turbines. Despite the unsteady nature of the flow in the near wake region, by 16 diameters downstream the flow had recovered to a steady state. Furthermore, due to the asymmetrical nature of the wake, some parts of the flow had recovered as close as 4 diameters downstream.
- The turbine was found to induce secondary currents, with the magnitude being dependent upon the blockage and solidity of the turbine.

CFX was again used to model the turbines and their wakes, in a like-for-like model of the recirculating flume. This included using a full 3D domain, and monitoring the velocities at the same locations as recorded by the ADV. Three turbine configurations were modelled: the CarBine CB_4S configuration, and two sizes of Savonius turbine to vary the blockage ratio in the flume.

Firstly, a technique was developed to rotate an internal subdomain in an existing rotating domain, thus allowing the motion of a CarBine flap opening and closing to be modelled. This technique also showed further potential in other applications, for example, by modelling dynamic pitching of Darrieus turbine blades.

The CFD results showed very good agreement with the measured laboratory data, both in predicting the time-averaged and unsteady behaviour. As a result the conclusions with regards to the wake characteristics were the same as those obtained from the laboratory tests. This gave confidence in the modelling methodology used, which could now be applied to scenarios that either address the scaling issues associated with physical model testing, or are not physically possible to achieve in a laboratory. To the author's knowledge, this is the first study in which physical and numerical modelling techniques have been applied to investigate the wake characteristics of vertical axis tidal stream turbines.

The physical and numerical modelling results show that the spacing requirements for vertical axis turbines would be very different to those of horizontal axis turbines. Not only could turbines be spaced closer together, increasing the array output power per unit

area, but the output could potentially be enhanced by exploiting turbine to turbine interactions and the secondary currents created by the blockage effect.

8.2.3 Hydrodynamic impact of the Severn Barrage

Using the numerical model TRIVAST, both the STPG and Hafren Power Severn Barrage proposals were initially modelled at a physical model scale. The developments to the TRIVAST model were demonstrated to be effective in simulating the barrage operation, and the key corresponding conclusions from the modelling results can be summarised as follows:

- The predicted hydrodynamic changes due to the STPG scheme agreed with previous studies, namely that a large increase occurred in the minimum water levels upstream of the barrage, as well as a significant reduction in the tidal currents throughout the estuary.
- The Hafren Power proposal has the potential to produce an equivalent amount of energy as the STPG barrage.
- For the two-way operating mode of the Hafren Power barrage, the resulting tide followed the natural tidal state more closely, depending on the starting head used.
- This starting head increased the minimum water levels upstream of the barrage, as well as reducing the maximum water levels and thereby providing flood protection benefits.
- The tidal currents were reduced throughout the estuary, with the level of reduction again depending on the starting head.

To address the scaling issues that limit the accuracy of model predictions, TRIVAST was extended to the prototype scale and the barrage scenarios were re-run. As well as showing good agreement with available tidal gauge and Admiralty Chart data, the conclusions obtained agreed well with those obtained from the physical model scale.

The modelling focus was then turned to tidal stream deployment in the Severn Estuary, where the following conclusions were made:

- For the natural conditions, the area suitable for shallow water vertical axis turbines is over four times greater than the predicted horizontal axis area, at 1150 km^2 compared to 255 km^2.
- The results from two hypothetical arrays also showed that a vertical axis turbine array has the potential to produce more energy per plan area, than one that uses horizontal axis turbines - albeit with a much larger number of installed turbines. The spacing requirements were based on the results and conclusions from Chapters 4 and 6.
- A tidal stream turbine array has a small hydrodynamic impact compared to a Severn Barrage, however, if deployed on a large scale array interaction could affect the tidal stream resource.
- The power predictions were highly subjective as the technology does not currently exist, and therefore assumptions were made with regards to the rated output of a device.

Finally the interaction of the Severn Barrage proposals and tidal stream deployment were investigated, with the main conclusions being as follows:

- The construction of a Severn Barrage under any operating mode would remove most of the identified horizontal axis turbine resource.
- A significant area - between 100 km^2 and 300 km^2, suitable for vertical axis turbine deployment would remain with the Hafren power scheme. If the STPG scheme were to be built, this area would reduce to approximately 45 km^2. It is acknowledged, however, that the realistic potential resource is subject to a wider range of constraints than those applied in this case.

The research outcomes of this thesis have therefore demonstrated that the potential exists for the deployment of both shallow water vertical axis turbines and a large-scale tidal barrage in the Severn Estuary – provided that the advantages discovered can be transposed to the prototype scale, and that the technology can be feasibly built and deployed.

8.3 Recommendations for further study

1. The experimental setup used to model tidal stream turbines was very effective in allowing for a comparison of the performance and wake characteristics of the different turbines tested, as well as building a reliable dataset that was used for comparison with CFD model predictions. However, the model was limited by the scaling of the hydraulic parameters compared to the prototype scale. Due to the small scale of the turbine, the Reynolds numbers were not only much smaller than at the prototype scale, but the Froude number used was higher, because otherwise for performance tests the flow velocity was too small to provide meaningful performance values. Therefore, in order to gain confidence in the physical modelling results, and transpose these values accurately to the prototype scale, modelling at a larger scale is recommended. This is of course often limited by the facilities available, and an intermediate solution would be to improve the existing power take-off system by minimising frictional losses. This could be achieved, for example, by the use of a servomotor, as used by a number of researchers. However, such a component would also add to the limitation of driving the turbine like a pump and therefore not replicating the pulsing behaviour that has been demonstrated to occur. Nonetheless, it could be argued that the control system used on a prototype device would vary the load in order to minimise the pulses in the velocity, and thus improve the power output quality. In addition, as previously identified, a quantification of the experimental errors should be performed, in order to determine the reliability of the obtained data.

2. Further investigation into the interaction of vertical axis devices is also recommended. In this thesis it has been demonstrated that the blockage effect in the flume increased the turbine performance, but in order for array deployment to be successful the devices would need to positively interact with each other, as well as benefit from blockage effects of the free surface and land boundaries. This applies to the downstream and lateral spacing. With a better understanding of this interaction, improved performance values for array deployment can be better quantified. Due to the modelling domain size required to investigate the impacts of a number of turbines, this study would be better suited to using CFD techniques, and

the unsteady methodology used in this thesis has been shown to give good predictions of both the performance and wake characteristics. As computational resources continue to increase, such unsteady array models are closer to being feasible.

3. Despite showing good agreement with the laboratory data, the use of the k-ε turbulence model in the CFX simulations was considered a necessary limitation, given the already high computational demand and lack of access to high performance computing facilities. If such facilities were available, alternative turbulence models should be used as they better describe the physics of the flow. For example, the k-ω Shear Stress Transport model is widely recognised as having a superior performance compared to that of the k-ε model in predicting flow separation, and should be implemented as an initial improvement to the CFD model. Alternatively, improved turbulence modelling could be achieved through implementing other modelling techniques such as Large Eddy Simulation.

4. The Hafren Power proposals were a new development at the time of this thesis, and therefore no prior research into the proposals existed – although two-way generation using a Severn Barrage has been investigated, using the turbine configuration of the original STPG scheme. Much research is required in order to assess the potential power output and the hydro-environmental impact of this new scheme. An initial improvement to the work conducted in this thesis would be to model more accurately the turbine operation in the TRIVAST model, through incorporating a Hill chart into the model for the specific turbines used in the scheme. However, until specific details of the turbines to be used are released, such a modification would still rely on assumptions of the operating characteristics.

Bibliography

ABPmer 2008. Atlas of UK Marine Renewable Energy Resources [Online]. Available at: http://www.renewables-atlas.info [Accessed: 14 May 2013].

Aggidis, G.A. and Benzon, D.. 2013. Operational optimisation of a tidal barrage across the Mersey estuary using 0-D modelling. *Ocean Engineering* 66, pp. 69–81.

Aggidis, G.A. and Feather, O. 2012. Tidal range turbines and generation on the Solway Firth. *Renewable Energy* 43, pp. 9–17.

Ahmadian, R., Falconer, R. and Bockelmann-Evans, B. 2012. Far-field modelling of the hydro-environmental impact of tidal stream turbines. *Renewable Energy* 38(1), pp. 107–116.

Ahmadian, R., Falconer, R. and Lin, B. 2010. Hydro-environmental modeling of proposed Severn barrage, UK. *Proceedings of the ICE - Energy* 163(3), pp. 107–117.

Ahmadian, R. and Falconer, R.A. 2012. Assessment of array shape of tidal stream turbines on hydro-environmental impacts and power output. *Renewable Energy* 44, pp. 318–327.

Akwa, J.V., Alves da Silva Júnior, G. and Petry, A.P. 2012a. Discussion on the verification of the overlap ratio influence on performance coefficients of a Savonius wind rotor using computational fluid dynamics. *Renewable Energy* 38(1), pp. 141–149.

Akwa, J.V., Vielmo, H.A. and Petry, A.P. 2012b. A review on the performance of Savonius wind turbines. *Renewable and Sustainable Energy Reviews* 16(5), pp. 3054–3064.

ALSTOM Hydro 2009. Bulb Units: The complete solution for low heads.

ANSYS, Inc. 2010a. ANSYS CFX-Pre User's Guide.

ANSYS, Inc. 2010b. ANSYS CFX-Solver Theory Guide.

Antheaume, S., Maître, T. and Achard, J.-L. 2008. Hydraulic Darrieus turbines efficiency for free fluid flow conditions versus power farms conditions. *Renewable Energy* 33(10), pp. 2186–2198.

Bae, Y.H., Kim, K.O. and Choi, B.H. 2010. Lake Sihwa tidal power plant project. *Ocean Engineering* 37(5-6), pp. 454–463.

Bahaj, A.S., Batten, W.M.J. and McCann, G. 2007a. Experimental verifications of numerical predictions for the hydrodynamic performance of horizontal axis marine current turbines. *Renewable Energy* 32(15), pp. 2479–2490.

Bahaj, A.S., Molland, A.F., Chaplin, J.R. and Batten, W.M.J. 2007b. Power and thrust measurements of marine current turbines under various hydrodynamic flow conditions in a cavitation tunnel and a towing tank. *Renewable Energy* 32(3), pp. 407–426.

Bahaj, A.S., Myers, L.E., Thomson, M.D. and Jorge, N. 2007c. Characterising the wake of horizontal axis marine current turbines. In: *Seventh European Wave and Tidal Energy Conference*. Porto, Portugal.

Bai, G., Li, J., Fan, P. and Li, G. 2013. Numerical investigations of the effects of different arrays on power extractions of horizontal axis tidal current turbines. *Renewable Energy* 53, pp. 180–186.

Bai, L., Spence, R.R. and Dudziak, G. 2009. Investigation of the influence of array arrangement and spacing on tidal energy converter (TEC) performance using a 3-dimensional CFD model. In: *Proceedings of the 8th European Wave and Tidal Energy Conference, Uppsala, Sweden*. pp. 654–660.

Baker, A.C. 1991. *Tidal Power*. London: Peter Peregrinus Ltd.

Barltrop, N., Varyani, K.S., Grant, A., Clelland, D. and Pham, X.P. 2007. Investigation into wave—current interactions in marine current turbines. *Proceedings of the Institution of Mechanical Engineers, Part A: Journal of Power and Energy* 221(2), pp. 233–242.

Bates, P.D., Lane, S.N. and Ferguson, R.I. 2005. *Computational Fluid Dynamics: Applications in Environmental Hydraulics*. Wiley.

Batten, W.M.J., Bahaj, A.S., Molland, A.F. and Chaplin, J.R. 2006. Hydrodynamics of marine current turbines. *Renewable energy* 31(2), pp. 249–256.

Batten, W.M.J., Bahaj, A.S., Molland, A.F. and Chaplin, J.R. 2008. The prediction of the hydrodynamic performance of marine current turbines. *Renewable energy* 33(5), pp. 1085–1096.

Batten, W.M.J., Harrison, M.E. and Bahaj, A.S. 2013. Accuracy of the actuator disc-RANS approach for predicting the performance and wake of tidal turbines. *Philosophical Transactions of the Royal Society A: Mathematical, Physical and Engineering Sciences* 371(1985), pp. 20120293–20120293.

Beri, H. 2011. Double Multiple Streamtube Model and Numerical Analysis of Vertical Axis Wind Turbine. *Energy and Power Engineering* 03(03), pp. 262–270.

Biadgo, A.M., Simonovic, A., Komarov, D. and Stupar, S. 2013. Numerical and Analytical Investigation of Vertical Axis Wind Turbine. *FME Transactions* 41, pp. 49–58.

Black & Veatch 2005. *Phase II UK Tidal Stream Energy Resource Assessment*.

Blackwell, B.F., Sheldahl, R.F. and Feltz, L.V. 1977. *Wind tunnel performance data for two-and three-bucket Savonius rotors*. Sandia Laboratories.

Blunden, L.S. and Bahaj, A.S. 2007. Tidal energy resource assessment for tidal stream generators. *Proceedings of the Institution of Mechanical Engineers, Part A: Journal of Power and Energy* 221(2), pp. 137–146.

Bryden, I.G., Couch, S.J., Owen, A. and Melville, G. 2007. Tidal current resource assessment. *Proceedings of the Institution of Mechanical Engineers, Part A: Journal of Power and Energy* 221(2), pp. 125–135.

Buckland, H., Masters, I., Chapman, J.C. and Orme, J.A.C. 2010. Blade Element Momentum Theory in Modelling Tidal Stream Turbines. In: Southampton, UK.

Burrows, R., Walkington, I.A., Yates, N.C., Hedges, T.S., Wolf, J. and Holt, J. 2009a. The tidal range energy potential of the West Coast of the United Kingdom. *Applied Ocean Research* 31(4), pp. 229–238.

Burrows, R., Yates, N.C., Hedges, T.S., Li, M., Zhou, J.G., Chen, D.Y., Walkington, I.A., Wolf, J., Holt, J. and Proctor, R. 2009b. Tidal energy potential in UK waters. *Proceedings of the ICE-Maritime Engineering* 162(4), pp. 155–164.

Carbon Trust 2010. Renewable energy sources: Technology overview.

Challans, P. 2009. Analysis and Modelling of a Tidal Stream Turbine. MSc Thesis. Cardiff University.

Chanson, H. 1999. *The Hydraulics of Open Channel Flow*. Euston Road, London NW1 3BH, UK: Arnold.

Chen, W.-B., Liu, W.-C. and Hsu, M.-H. 2013. Modeling Evaluation of Tidal Stream Energy and the Impacts of Energy Extraction on Hydrodynamics in the Taiwan Strait. *Energies* 6(4), pp. 2191–2203.

Chow, V.T. 1959. *Open-channel hydraulics*. McGraw-Hill.

Chrysafis, N. 2008. Feasibility study of a new turbine concept. MSc Thesis. Cardiff University.

Clarke, J.A., Connor, G., Grant, A.D. and Johnstone, C.M. 2007. Design and testing of a contra-rotating tidal current turbine. *Proceedings of the Institution of Mechanical Engineers, Part A: Journal of Power and Energy* 221(2), pp. 171–179.

Coiro, D.P., De Marco, A., Nicolosi,, F., Melone, S. and Montella, F. 2005. Dynamic Behaviour of the Patented Kobold Tidal Current Turbine: Numerical and Experimental Aspects. *Acta Polytechnika Journal of Advanced Engineering* 45(3).

Cooper, P. and Kennedy, O.C. 2004. Development and analysis of a novel vertical axis wind turbine. . Available at: http://ro.uow.edu.au/engpapers/921/ [Accessed: 5 June 2013].

Couch, S.J. and Bryden, I.G. 2007. Large-scale physical response of the tidal system to energy extraction and its significance for informing environmental and ecological impact assessment. In: *Oceans 2007-Europe*. pp. 1–5.

Crown Estate 2012. *UK Wave and Tidal Key Resource Areas Project Summary Report*. London.

D'Alessandro, V., Montelpare, S., Ricci, R. and Secchiaroli, A. 2010. Unsteady Aerodynamics of a Savonius wind rotor: a new computational approach for the simulation of energy performance. *Energy* 35(8), pp. 3349–3363.

Dai, Y.M., Gardiner, N., Sutton, R. and Dyson, P.K. 2011. Hydrodynamic analysis models for the design of Darrieus-type vertical-axis marine current turbines. *Proceedings of the Institution of Mechanical Engineers, Part M: Journal of Engineering for the Maritime Environment* 225(3), pp. 295–307.

Darrieus, G.J.M. 1931. Turbine Having its Rotating Shaft Transverse to the Flow of the Current.

DECC 2010. *Severn Tidal Power Feasibility Study: Conclusions and Summary Report*. London.

DECC 2009. *Severn Tidal Power: Phase One Consultation*. London.

Defne, Z., Haas, K.A. and Fritz, H.M. 2011. Numerical modeling of tidal currents and the effects of power extraction on estuarine hydrodynamics along the Georgia coast, USA. *Renewable Energy* 36(12), pp. 3461–3471.

Dobrev, I. and Massouh, F. 2011. CFD and PIV investigation of unsteady flow through Savonius wind turbine. *Energy Procedia* 6, pp. 711–720.

Dobrev, I. and Massouh, F. 2012. Exploring the Flow around a Savonius Wind Turbine. In: *16th Int Symp on Applications of Laser Techniques to Fluid Mechanics*. Lisbon, Portugal.

Van Dusen, E.S. 1978. *A Two Dimensional Analysis Of Vertical Axis Windmills*.

Ellis, C. 2012. An Assessment of the Hydro- Environmental Impacts of Various Operating Modes of a Severn Barrage. MSc Thesis. Cardiff University.

EMEC Tidal Devices [Online]. Available at: http://www.emec.org.uk/marine-energy/tidal-devices/ [Accessed: 22 May 2013].

Ettema, R., Arndt, R., Roberts, P. and Wahl, T. 2000. *Hydraulic modeling concepts and practice*. Reston, Va.: ASCE.

EU Climate Change Expert Group 2008. The 2°C target.

Fairley, I., Evans, P., Wooldridge, C., Willis, M. and Masters, I. 2013. Evaluation of tidal stream resource in a potential array area via direct measurements. *Renewable Energy* 57, pp. 70–78.

Falconer, R.A. 2011. Global water security: an introduction. *Science in Parliament, The Journal of the Parliamentary and Scientific Committee* 68(1), pp. 34–36.

Falconer, R.A. and Lin, B.L. 2002a. DIVAST Model Reference Manual.

Falconer, R.A. and Lin, B.L. 2002b. DIVAST User Manual.

Fallon, D. and Nash, S. 2012. The Effects of Array Configuration on the Hydro-environmental Impacts of Tidal Turbines. In: *4th International Conference on Ocean Energy, 17 October, Dublin*. Dublin, Ireland.

Fujisawa, N. 1996. Velocity measurements and numerical calculations of flow fields in and around Savonius rotors. *Journal of Wind Engineering and Industrial Aerodynamics* 59(1), pp. 39–50.

Gant, S. and Stallard, T. 2008. Modelling a tidal turbine in unsteady flow. In: *Proceedings of the International Offshore and Polar Engineering Conference*. pp. 473–479.

Golecha, K., Eldho, T.I. and Prabhu, S.V. 2011. Influence of the deflector plate on the performance of modified Savonius water turbine. *Applied Energy* 88(9), pp. 3207–3217.

Good, A., Hamill, G., Whittaker, T. and Robinson, D. 2011. PIV analysis of the near wake of a tidal turbine. In: *Proceedings of the International Offshore and Polar Engineering Conference*. pp. 770–776.

Gorban', A.N., Gorlov, A.M. and Silantyev, V.M. 2001. Limits of the Turbine Efficiency for Free Fluid Flow. *Journal of Energy Resources Technology* 123(4), p. 311.

Gretton, G., Bruce, T. and Ingram, D. 2009. Hydrodynamic modelling of a vertical axis tidal current turbine using CFD. In: *Proceedings of the 8th European Wave and Tidal Energy Conference*. pp. 468–476.

Hafren Power 2013. Hafren Power 2013 [Online]. Available at: http://www.hafrenpower.com/ [Accessed: 1 May 2013].

Harrison, M.E., Batten, W.M.J., Myers, L.E. and Bahaj, A.S. 2010. Comparison between CFD simulations and experiments for predicting the far wake of horizontal axis tidal turbines. *IET Renewable Power Generation* 4(6), pp. 613 –627.

Houlsby, G.T., Draper, S. and Oldfield, M.L.G. 2008. Application of linear momentum actuator disc theory to open channel flow. *Report no. OUEL* 2296(08).

Hwang, I.S., Lee, Y.H. and Kim, S.J. 2009. Optimization of cycloidal water turbine and the performance improvement by individual blade control. *Applied Energy* 86(9), pp. 1532–1540.

Hyun, B.-S., Choi, D.-H., Han, J.-S. and Jin, J.-Y. 2012. Performance Analysis and Design of Vertical Axis Tidal Stream Turbine. *Journal of Shipping and Ocean Engineering* 2, pp. 191–200.

Ingram, G. 2005. *Wind Turbine Blade Analysis using the Blade Element Momentum Method. Version 1.0*. School of Engineering, Durham University,(13th December 2005).

Islam, M., Ting, D.S.-K. and Fartaj, A. 2008. Aerodynamic models for Darrieus-type straight-bladed vertical axis wind turbines. *Renewable and Sustainable Energy Reviews* 12(4), pp. 1087–1109.

Iyer, A.S., Couch, S.J., Harrison, G.P. and Wallace, A.R. 2013. Variability and phasing of tidal current energy around the United Kingdom. *Renewable Energy* 51, pp. 343–357.

James, S.C., Seetho, E., Jones, C. and Roberts, J. 2010. Simulating environmental changes due to marine hydrokinetic energy installations. In: *OCEANS 2010*. pp. 1–10.

Jeffcoate, P., Stansby, P.K. and Apsley, D. 2011. Near-Field Flow Downstream Of a Barrage: Experiments, 3-D CFD And Depth-averaged Modelling. In: *Proceedings of the 30th International Conference on Ocean, Offshore and Arctic Engineering*. Rotterdam , The Netherlands.

Kadiri, M., Ahmadian, R., Bockelmann-Evans, B., Rauen, W. and Falconer, R. 2012. A review of the potential water quality impacts of tidal renewable energy systems. *Renewable and Sustainable Energy Reviews* 16(1), pp. 329–341.

Kato, S., Doh, D.H. and Suzuki, K. 2010. Power generation characteristics of a novel horizontal tidal current power generation system installed in the Akashi Strait of Japan. In: *Sustainable Energy Technologies (ICSET), 2010 IEEE International Conference on*. pp. 1 –6.

Khalid, S.S., Liang, Z., Qi-hu, S. and Xue-Wei, Z. 2013a. Difference between Fixed and Variable Pitch Vertical Axis Tidal Turbine-Using CFD Analysis in CFX. *Research Journal of Applied Sciences* 5.

Khalid, S.S., Zhiguang, J., Fuding, T., Liang, Z. and Chaudhry, A.Z. 2013b. CFD simulation of vertical axis tidal turbine using two-way fluid structure interaction method. In: *Applied Sciences and Technology (IBCAST), 2013 10th International Bhurban Conference on*. pp. 286–291.

Khan, M.J., Bhuyan, G., Iqbal, M.T. and Quaicoe, J.E. 2009. Hydrokinetic energy conversion systems and assessment of horizontal and vertical axis turbines for river and tidal applications: A technology status review. *Applied Energy* 86(10), pp. 1823–1835.

Khan, M.J., Iqbal, M.T. and Quaicoe, J.E. 2008a. Tow tank testing and performance evaluation of a permanent magnet generator based small vertical axis hydrokinetic turbine. In: *Power Symposium, 2008. NAPS '08. 40th North American*. pp. 1 –7.

Khan, M.N.I., Iqbal, M.T. and Hinchey, M. 2008b. Submerged water current turbines. In: *OCEANS 2008*. pp. 1 –6.

Kiho, S., Shiono, M. and Suzuki, K. 1996. The power generation from tidal currents by darrieus turbine. *Renewable Energy* 9(1–4), pp. 1242–1245.

King, J. and Tryfonas, T. 2009. Tidal stream power technology - state of the art. In: *OCEANS 2009 - EUROPE*. pp. 1 –8.

Kirke, B.K. 2011. Tests on ducted and bare helical and straight blade Darrieus hydrokinetic turbines. *Renewable Energy* 36(11), pp. 3013–3022.

Kyozuka, Y. 2008. An Experimental Study on the Darrieus-Savonius Turbine for the Tidal Current Power Generation. *Journal of Fluid Science and Technology* 3(3), pp. 439–449.

Lain, S. and Osorio, C. 2010. Simulation and evaluation of a straight-bladed Darrieus-type cross flow marine turbine. *Journal of scientific & industrial research* 69(12), pp. 906–912.

Lawson, M.J., Li, Y. and Sale, D.C. 2011. Development and Verification of a Computational Fluid Dynamics Model of a Horizontal-Axis Tidal Current Turbine. In: *30th International Conference on Ocean, Offshore, and Arctic Engineering*. Rotterdam, The Netherlands.

Lee, J.H., Park, S., Kim, D.H., Rhee, S.H. and Kim, M.-C. 2012. Computational methods for performance analysis of horizontal axis tidal stream turbines. *Applied Energy* 98, pp. 512–523.

Li, Y. and Calışal, S.M. 2010. Modeling of twin-turbine systems with vertical axis tidal current turbines: Part I—Power output. *Ocean Engineering* 37(7), pp. 627–637.

Lin, B. and Falconer, R.A. 1997. Three-dimensional Layer-integrated Modelling of Estuarine Flows with Flooding and Drying. *Estuarine, Coastal and Shelf Science* 44(6), pp. 737–751.

Luznik, L., Flack, K.A., Lust, E.E. and Baxter, D.P. 2012. Hydrodynamic performance of a horizontal axis tidal turbine under steady flow conditions. In: *Oceans, 2012*. pp. 1–4.

MacKay, D. 2009. *Sustainable energy: without the hot air*. Cambridge; [Online]: UIT withouthotair.com.

MacKay, D.J. 2007a. Enhancing electrical supply by pumped storage in tidal lagoons. *Cavendish Laboratory, University of Cambridge*. Available at:

http://citeseerx.ist.psu.edu/viewdoc/download?doi=10.1.1.62.8504&rep=rep1&type=pdf [Accessed: 22 May 2013].

MacKay, D.J. 2007b. Under-estimation of the UK tidal resource. *Cambridge:[2006 Dec 7*. Available at: http://www.inference.phy.cam.ac.uk/sustainable/book/tex/TideEstimate.pdf [Accessed: 24 May 2013].

MacLeod, A.J., Barnes, S., Rados, K.G. and Bryden, I.G. 2002. Wake effects in tidal current turbine farms. In: *International Conference on Marine Renewable Energy-Conference Proceedings*. pp. 49–53.

Maganga, F., Germain, G., King, J., Pinon, G. and Rivoalen, E. 2010. Experimental characterisation of flow effects on marine current turbine behaviour and on its wake properties. *IET Renewable Power Generation* 4(6), pp. 498–509.

Maître, T., Amet, E. and Pellone, C. 2012. Modeling of the flow in a Darrieus water turbine: Wall grid refinement analysis and comparison with experiments. *Renewable Energy*.

Malki, R., Masters, I., Williams, A.J. and Croft, T.N. 2012. A numerical investigation into tidal stream turbine wake dynamics and device performance in non-uniform flows. In: *Proceedings of the International Offshore and Polar Engineering Conference*. pp. 745–750.

Malki, R., Williams, A.J., Croft, T.N., Togneri, M. and Masters, I. 2013. A coupled blade element momentum – Computational fluid dynamics model for evaluating tidal stream turbine performance. *Applied Mathematical Modelling* (0).

Marsh, P.J., Ranmuthugala, S.D., Penesis, I. and Thomas, G.A. 2012. Three Dimensional Numerical Simulations of a Straight-Bladed Vertical Axis Tidal Turbine. In: *18th Australasian Fluid Mechanics Conference*. pp. 1–4.

Mason-Jones, A., O'Doherty, D.M., Morris, C.E., O'Doherty, T., Byrne, C.B., Prickett, P.W., Grosvenor, R.I., Owen, I., Tedds, S. and Poole, R.J. 2012. Non-dimensional scaling of tidal stream turbines. *Energy* 44(1), pp. 820–829.

McAdam, R.A. 2011. Studies into the Technical Feasibility of the Transverse Horizontal Axis Water Turbine. PhD Thesis. University of Oxford.

McAdam, R.A., Houlsby, G.T. and Oldfield, M.L.G. 2013. Experimental measurements of the hydrodynamic performance and structural loading of the Transverse Horizontal Axis Water Turbine: Part 1. *Renewable Energy* 59, pp. 105–114.

McCann, G.N. 2007. Tidal current turbine fatigue loading sensitivity to waves and turbulence – a parametric study. In: *Proceedings of the 7th European Wave and Tidal Energy Conference*. Porto, Portugal.

Mccombes, T., Johnstone, C. and Grant, A. 2009. Unsteady wake modelling for tidal current turbines. In: *Proceedings of the 8th European Wave and Tidal Energy Conference, Uppsala, Sweden, 2009*.

McSherry, R., Grimwade, J., Jones, I., Mathias, S., Wells, A. and Mateus, A. 2011. 3D CFD modelling of tidal turbine performance with validation against laboratory experiments. In: *Proc. 9th European Wave and Tidal Energy Conference, University of Southampton, UK*.

MCT Ltd Marine Current Turbines [Online]. Available at: http://www.marineturbines.com [Accessed: 23 May 2013].

Menet, J.-L. 2004. A double-step Savonius rotor for local production of electricity: a design study. *Renewable Energy* 29(11), pp. 1843–1862.

Myers, L. and Bahaj, A.S. 2006. Power output performance characteristics of a horizontal axis marine current turbine. *Renewable energy* 31(2), pp. 197–208.

Myers, L. and Bahaj, A.S. 2007. Wake studies of a 1/30th scale horizontal axis marine current turbine. *Ocean Engineering* 34(5–6), pp. 758–762.

Myers, L.E. and Bahaj, A.S. 2010. Experimental analysis of the flow field around horizontal axis tidal turbines by use of scale mesh disk rotor simulators. *Ocean Engineering* 37(2-3), pp. 218–227.

Myers, L.E., Keogh, B. and Bahaj, A.S. 2011. Experimental investigation of inter-array wake properties in early tidal turbine arrays. In: *OCEANS 2011*. pp. 1–8.

Nakajima, M., Iio, S. and Ikeda, T. 2008. Performance of Savonius Rotor for Environmentally Friendly Hydraulic Turbine. *Journal of Fluid Science and Technology* 3(3), pp. 420–429.

Neary, V.S., Chamorro, L.P., Hill, C., Gunawan, B. and Sotiropoulos, F. 2012. US Department of Energy National Lab Activities in Marine Hydrokinetics: Machine Performance Testing. In: *4th International Conference on Ocean Energy, 17 October, Dublin*. Oak Ridge National Laboratory (ORNL).

Neary, V.S., Gunawan, B., Hill, C. and Chamorro, L.P. 2013. Near and far field flow disturbances induced by model hydrokinetic turbine: ADV and ADP comparison. *Renewable Energy* 60, pp. 1–6.

Neill, S.P., Jordan, J.R. and Couch, S.J. 2012. Impact of tidal energy converter (TEC) arrays on the dynamics of headland sand banks. *Renewable Energy* 37(1), pp. 387–397.

Neptune Renewable Energy 2013. Neptune Renewable Energy goes into liquidation. Company Statement [Online]. Available at: www.neptunerenewableenergy.com [Accessed: 8 February 2013].

Nishino, T. and Willden, R.H.J. 2012. The efficiency of an array of tidal turbines partially blocking a wide channel. *Journal of Fluid Mechanics* 708, pp. 596–606.

NOAA Tide Predictions and Data [Online]. Available at: http://www.co-ops.nos.noaa.gov [Accessed: 22 May 2013].

Novák, P., Guinot, V., Jeffrey, A. and Reeve, D.E. 2010. *Hydraulic modelling: an introduction ; principles, methods and applications*. London; New York: Spon Press.

O'Doherty, T., Mason-Jones, A., O'Doherty, D.M., Byrne, C.B., Owen, I. and Wang, Y.X. 2009. Experimental and Computational Analysis of a Model Horizontal Axis Tidal Turbine. *EWTEC, Uppsala, Sweden*, pp. 833–834.

Park, K., Asim, T., Mishra, R., Shahzad, A. and Marangwanda, G. 2012. Computational Fluid Dynamics based Performance Optimisation of Vertical Axis Marine Current Turbines. In: *2nd International Workshop and Congress on eMaintenance, 13-14 December 2012, Lulea, Sweden.*

Plew, D.R. and Stevens, C.L. 2013. Numerical modelling of the effect of turbines on currents in a tidal channel – Tory Channel, New Zealand. *Renewable Energy* 57, pp. 269–282.

PMSS 2010. *Offshore Renewables Resource Assessment and Development (ORRAD) Project – Technical Report*.

Pope, K. and Naterer, G.F. 2012. Multiple streamtube approximation of flow-induced forces on a Savonius wind turbine. *International Journal of Energy Research*, p. n/a–n/a.

Pugh, D.T. 1987. *Tides, surges, and mean sea-level*. Chichester; New York: J. Wiley.

Regen SW 2012. Bristol Channel Energy: A Balanced Technology Approach.

RenewableUK 2012. *Marine Energy in the UK: State of the Industry Report*.

RenewableUK, BVG associates and GL Garrad Hassan 2012. *Wave and Tidal Energy in the UK Conquering Challenges, Generating Growth*.

Robins, P.E., Neill, S.P. and Davies, A.G. 2012. The impact of tidal energy extraction on the morphodynamics of the Irish Sea. In: *4th International Conference on Ocean Energy*. Dublin, Ireland.

Rolls-Royce Plc and Atkins Ltd 2010. *Concept design of a very-low head dual generation tidal scheme for the Severn Estuary*.

Rose, S., Good, A., Atcheson, M., Hamill, G., Johnstone, C., MacKinnon, P., Robinson, D., Grant, A. and Whittaker, T. 2011. Investigating Experimental Techniques for Measurement of the Downstream Near Wake of a Tidal Turbine. In: *Ninth European Wave and Tidal Energy Conference. Southampton, UK*.

Ross, I. and Altman, A. 2011. Wind tunnel blockage corrections: Review and application to Savonius vertical-axis wind turbines. *Journal of Wind Engineering and Industrial Aerodynamics* 99(5), pp. 523–538.

RPS 2011. *Marine Renewable Energy Strategic Framework: Approach to Sustainable Development*.

Salter, S.H. 2009. Correcting the under-estimate of the tidal-stream resource of the Pentland Firth. In: *Proceedings of the 8th European Wave and Tidal Energy Conference, Uppsala, Sweden*.

Salter, S.H. and Taylor, J.R.M. 2007. Vertical-axis tidal-current generators and the Pentland Firth. *Proceedings of the Institution of Mechanical Engineers, Part A: Journal of Power and Energy* 221(2), pp. 181–199.

Savonius, S.J. 1929. Rotor adapted to be driven by wind or flowing water.

Scheurich, F., Fletcher, T.M. and Brown, R.E. 2011. Simulating the aerodynamic performance and wake dynamics of a vertical-axis wind turbine. *Wind Energy* 14(2), pp. 159–177.

Severn Barrage Committee 1981. *Tidal Power from the Severn Estuary- Volume 1*. Energy Paper 46. UK: Her Majesty's Stationary Office (HMSO).

Shiono, M., Suzuki, K. and Kiho, S. 2000. An experimental study of the characteristics of a Darrieus turbine for tidal power generation. *Electrical Engineering in Japan* 132(3), pp. 38–47.

Sinclair Knight Merz 2008. *Growth scenarios for UK renewables generation and implications for future developments and operation of electricity networks*. Great Britain: BERR.

STPG, S.T.P.G. 1993. *Severn Barrage Project: further environmental and energy capture studies*.

Strickland, J.H. 1975. *The Darrieus Turbine: A Performance Prediction Model Using Multiple Streamtubes*.

Strickland, J.H., Webster, B.T. and Nguyen, T. 1979. A Vortex Model of the Darrieus Turbine: An Analytical and Experimental Study. *Journal of Fluids Engineering* 101.

Sun, X., Bryden, I.G., Jeffrey, H. and Forehand, D. 2008a. An experimental survey in the wake of a simulated tidal current turbine. *Proceedings of IMarEST - Part A - Journal of Marine Engineering and Technology* (12), pp. 13–22.

Sun, X., Chick, J.P. and Bryden, I.G. 2008b. Laboratory-scale simulation of energy extraction from tidal currents. *Renewable Energy* 33(6), pp. 1267–1274.

Sustainable Development Commision 2007. *Turning The Tide, Tidal Power in the UK*. London.

Swift, R. 2009. *Assessment of performance of tidal energy conversion systems: marine renewable energy guides*. Orkney: European Marine Energy Centre : Dept. for Business Enterprise & Regulatory Reform.

Taylor, G.I. 1920. Tidal Friction in the Irish Sea. *Philosophical Transactions of the Royal Society of London. Series A, Containing Papers of a Mathematical or Physical Character* 220(571-581), pp. 1–33.

Taylor, S.J. 2002. The Severn barrage–definition study for a new appraisal of the project. *Energy Technology Support Unit, Report No*. Available at: http://www.dti.gov.uk/energy/renewables/publications/pdfs/t0900212rep.pdf [Accessed: 2 May 2013].

Tedds, S.C., Poole, R.J. and Owen, I. 2012. Wake characteristics of Horizontal Axis Tidal Stream Turbines in uniform and non-uniform steady flows. In: *4th International Conference on Ocean Energy, 17 October, Dublin*.

TGL ltd Product Development [Online]. Available at: http://www.tidalgeneration.co.uk/products/ [Accessed: 22 May 2013].

Tidal Lagoon Power Plc 2012. Tidal Lagoon Swansea Bay Ltd: Project Introduction.

Togneri, M., Masters, I. and Orme, J. 2011. Incorporating Turbulent Inflow Conditions in a Blade Element Momentum Model of Tidal Stream Turbines. In: International Society of Offshore and Polar Engineers.

Tridon, S., Barre, S., Ciocan, G.D., Leroy, P. and Ségoufin, C. 2010. Experimental investigation of draft tube flow instability. *IOP Conference Series: Earth and Environmental Science* 12, p. 012044.

Turnock, S.R., Phillips, A.B., Banks, J. and Nicholls-Lee, R. 2011. Modelling tidal current turbine wakes using a coupled RANS-BEMT approach as a tool for analysing power capture of arrays of turbines. *Ocean Engineering* 38(11–12), pp. 1300–1307.

Urbina, R., Peterson, M.L., Bates, P.M. and Kimball, R.W. 2010. Modeling and validation of a cross flow turbine using free vortex models and an improved 2D lift model. In: *OCEANS 2010*. pp. 1–7.

Voith Tidal Current Power Stations [Online]. Available at: http://www.voith.com/en/products-services/hydro-power/ocean-energies/tidal-current-power-stations--591.html [Accessed: 22 May 2013].

Vu, T.C., Koller, M., Gauthier, M. and Deschênes, C. 2010. Flow simulation and efficiency hill chart prediction for a Propeller turbine. *IOP Conference Series: Earth and Environmental Science* 12, p. 012040.

WAG 2010. *A Low Carbon Revolution – The Welsh Assembly Government Energy Policy Statement*.

Walkington, I. and Burrows, R. 2009. Modelling tidal stream power potential. *Applied Ocean Research* 31(4), pp. 239–245.

Wang, L.B., Zhang, L. and Zeng, N.D. 2007. A potential flow 2-D vortex panel model: Applications to vertical axis straight blade tidal turbine. *Energy Conversion and Management* 48(2), pp. 454–461.

Whelan, J.I., Graham, J.M.R. and Peiró, J. 2009. A free-surface and blockage correction for tidal turbines. *Journal of Fluid Mechanics* 624, pp. 281–291.

Wilson, S., Bourban, S. and Couch, S. 2012. Understanding the interactions of tidal power projects across the UK Continental Shelf. In: *4th International Conference on Ocean Energy*. Dublin, Ireland.

Winchester, J.D. and Quayle, S. 2009. Torque ripple and variable blade force: A comparison of Darrieus and Gorlov-type turbines for tidal stream energy conversion. In: *the 8th European Wave and Tidal Energy Conference, Uppsala, Sweden*. pp. 668–676.

Wolf, J., Walkington, I.A., Holt, J. and Burrows, R. 2009. Environmental impacts of tidal power schemes. In: *Proceedings of the Institution of Civil Engineers-Maritime Engineering*. pp. 165–177.

Wu, H., Chen, L., Yu, M., Li, W. and Chen, B. 2012. On design and performance prediction of the horizontal-axis water turbine. *Ocean Engineering* 50, pp. 23–30.

Xia, J., Falconer, R.A. and Lin, B. 2010a. Impact of different operating modes for a Severn Barrage on the tidal power and flood inundation in the Severn Estuary, UK. *Applied Energy* 87(7), pp. 2374–2391.

Xia, J., Falconer, R.A. and Lin, B. 2010b. Impact of different tidal renewable energy projects on the hydrodynamic processes in the Severn Estuary, UK. *Ocean Modelling* 32(1-2), pp. 86–104.

Xia, J., Falconer, R.A. and Lin, B. 2010c. Numerical model assessment of tidal stream energy resources in the Severn Estuary, UK. *Proceedings of the Institution of Mechanical Engineers, Part A: Journal of Power and Energy* 224(7), pp. 969–983.

Yaakob, O.B. 2013. Experimental Studies on Savonius-type Vertical Axis Turbine for Low Marine Current Velocity. *International Journal of Engineering* 26(1 (A)).

Yaakob, O.B., Ahmed, Y.M. and Ismail, M.A. 2012. Validation Study for Savonius Vertical Axis Marine Current Turbine Using CFD Simulation. In: *Asia-Pasific Workshop on Marine Hydrodynamics*. pp. 327–332.

Yang, Z., Wang, T. and Copping, A.E. 2013. Modeling tidal stream energy extraction and its effects on transport processes in a tidal channel and bay system using a three-dimensional coastal ocean model. *Renewable Energy* 50, pp. 605–613.

Yates, N., Walkington, I., Burrows, R. and Wolf, J. 2013. Appraising the extractable tidal energy resource of the UK's western coastal waters. *Philosophical Transactions of the Royal Society A: Mathematical, Physical and Engineering Sciences* 371(1985), pp. 20120181–20120181.

Zanette, J., Imbault, D. and Tourabi, A. 2010. A design methodology for cross flow water turbines. *Renewable Energy* 35(5), pp. 997–1009.

Zhou, J., Pan, S. and Falconer, R.A. 2014. Effects of open boundary location on the far-field hydrodynamics of a Severn Barrage. *Ocean Modelling* 73(0), pp. 19–29.

Appendix A Physical modelling performance data sets

This appendix contains the performance values for all of the turbine configurations tested, as only selected results were presented in Chapter 4.

Table A.1 Performance data for CB_3S configuration

Flow Condition	*Point no*	*ω* *[rads^{-1}]*	*T_{ave}* *[Nm]*	*RPM*	*TSR*	*P* *[W]*	*C_P*	*C_τ*
[B]	B1	2.28	0.00	21.8	0.64	0.00	0.000	0.00
	B2	1.82	0.52	17.4	0.51	0.96	0.052	0.10
	B3	**1.37**	**0.97**	**13.1**	**0.38**	**1.33**	**0.072**	**0.19**
	B4	1.61	0.76	15.4	0.45	1.22	0.066	0.15
	B5	1.73	0.65	16.5	0.48	1.13	0.061	0.13
	B6	1.80	0.51	17.2	0.50	0.91	0.049	0.10
	B7	1.97	0.37	18.8	0.55	0.72	0.039	0.07
	B8	2.05	0.27	19.6	0.57	0.55	0.030	0.05
	B9	2.13	0.18	20.3	0.59	0.39	0.021	0.04
	B10	2.14	0.12	20.4	0.60	0.26	0.014	0.02
[C]	C1	2.80	0.00	26.7	0.66	0.00	0.000	0.00
	C2	2.46	0.52	23.5	0.58	1.27	0.041	0.07
	C3	2.15	0.89	20.5	0.50	1.91	0.062	0.12
	C4	**1.74**	**1.46**	**16.6**	**0.41**	**2.54**	**0.082**	**0.20**
	C5	1.09	1.66	10.4	0.26	1.80	0.059	0.23
	C6	1.80	1.39	17.2	0.42	2.50	0.081	0.19
	C7	1.98	1.16	18.9	0.47	2.30	0.075	0.16
	C8	2.06	1.05	19.7	0.49	2.16	0.070	0.14
	C9	2.21	0.82	21.1	0.52	1.82	0.059	0.11
	C10	2.38	0.61	22.7	0.56	1.45	0.047	0.08
[D]	D1	3.25	0.00	31.0	0.66	0.00	0.000	0.00
	D2	2.98	0.46	28.5	0.61	1.38	0.029	0.05
	D3	2.62	1.00	25.0	0.53	2.61	0.055	0.10
	D4	2.30	1.54	22.0	0.47	3.55	0.075	0.16
	D5	**1.97**	**2.01**	**18.8**	**0.40**	**3.97**	**0.084**	**0.21**
	D6	1.26	2.26	12.0	0.26	2.84	0.060	0.24
	D7	2.20	1.73	21.0	0.45	3.82	0.081	0.18
	D8	2.45	1.21	23.4	0.50	2.96	0.063	0.13
	D9	2.82	0.77	26.9	0.57	2.17	0.046	0.08
	D10	3.10	0.27	29.6	0.63	0.84	0.018	0.03
[E]	E1	3.65	0.00	34.9	0.67	0.00	0.000	0.00
	E2	3.32	0.54	31.7	0.61	1.81	0.028	0.05
	E3	3.01	0.98	28.7	0.55	2.94	0.046	0.08
	E4	2.76	1.46	26.4	0.51	4.02	0.063	0.12
	E5	2.45	2.02	23.4	0.45	4.96	0.077	0.17
	E6	**2.16**	**2.50**	**20.6**	**0.40**	**5.38**	**0.084**	**0.21**
	E7	1.32	2.77	12.6	0.24	3.66	0.057	0.23
	E8	2.68	1.76	25.6	0.49	4.73	0.073	0.15
	E9	2.79	1.33	26.6	0.51	3.71	0.058	0.11
	E10	3.24	0.77	30.9	0.59	2.50	0.039	0.07

Table A.2 Performance data for CB_4S configuration

Flow Condition	*Point no*	*ω* *[rads^{-1}]*	*T_{ave}* *[Nm]*	*RPM*	*TSR*	*P* *[W]*	*C_P*	*C_τ*
[B]	B1	2.23	0.00	21.3	0.62	0.00	0.000	0.00
	B2	2.04	0.28	19.5	0.57	0.57	0.031	0.05
	B3	1.83	0.54	17.5	0.51	1.00	0.054	0.11
	B4	1.62	0.81	15.5	0.45	1.32	0.071	0.16
	B5	**1.47**	**0.95**	**14.0**	**0.41**	**1.39**	**0.075**	**0.18**
	B6	1.12	1.16	10.7	0.31	1.30	0.070	0.22
	B7	1.26	1.09	12.0	0.35	1.38	0.074	0.21
	B8	1.49	0.89	14.2	0.41	1.32	0.072	0.17
	B9	1.74	0.67	16.6	0.48	1.17	0.063	0.13
	B10	1.83	0.50	17.5	0.51	0.91	0.049	0.10
[C]	C1	2.76	0.00	26.4	0.65	0.00	0.000	0.00
	C2	2.62	0.16	25.0	0.62	0.41	0.013	0.02
	C3	2.43	0.49	23.2	0.57	1.18	0.038	0.07
	C4	2.28	0.71	21.8	0.54	1.62	0.053	0.10
	C5	2.19	0.94	20.9	0.51	2.06	0.067	0.13
	C6	1.92	1.30	18.3	0.45	2.49	0.081	0.18
	C7	**1.54**	**1.63**	**14.7**	**0.36**	**2.50**	**0.081**	**0.22**
	C8	1.32	1.89	12.6	0.31	2.49	0.081	0.26
	C9	2.04	1.11	19.5	0.48	2.27	0.074	0.15
	C10	2.49	0.38	23.8	0.59	0.96	0.031	0.05
[D]	D1	3.20	0.00	30.6	0.65	0.00	0.000	0.00
	D2	3.03	0.37	28.9	0.62	1.13	0.024	0.04
	D3	2.84	0.64	27.1	0.58	1.83	0.039	0.07
	D4	2.67	1.03	25.5	0.54	2.76	0.059	0.11
	D5	2.20	1.70	21.0	0.45	3.74	0.079	0.18
	D6	2.36	1.34	22.5	0.48	3.15	0.067	0.14
	D7	**1.98**	**2.03**	**18.9**	**0.40**	**4.01**	**0.085**	**0.21**
	D8	1.65	2.39	15.8	0.34	3.96	0.084	0.25
	D9	2.24	1.64	21.4	0.46	3.68	0.078	0.17
	D10	2.48	1.24	23.7	0.51	3.07	0.065	0.13
[E]	E1	3.50	0.00	33.4	0.64	0.00	0.000	0.00
	E2	3.14	0.59	30.0	0.58	1.84	0.029	0.05
	E3	2.78	1.07	26.5	0.51	2.98	0.046	0.09
	E4	2.74	1.39	26.2	0.50	3.80	0.059	0.12
	E5	2.62	1.68	25.0	0.48	4.39	0.068	0.14
	E6	2.41	1.99	23.0	0.44	4.79	0.074	0.17
	E7	1.94	2.50	18.5	0.36	4.83	0.075	0.21
	E8	1.85	2.78	17.7	0.34	5.16	0.080	0.24
	E9	1.54	3.17	14.7	0.28	4.87	0.076	0.27
	E10	**2.39**	**2.17**	**22.8**	**0.44**	**5.18**	**0.080**	**0.18**

Table A.3 Performance data for CB_5S configuration

Flow Condition	*Point no*	*ω* *[rads^{-1}]*	*T_{ave}* *[Nm]*	*RPM*	*TSR*	*P* *[W]*	*C_P*	*C_τ*
[B]	B1	2.09	0.39	20.0	0.58	0.82	0.044	0.08
	B2	1.88	0.71	18.0	0.53	1.33	0.072	0.14
	B3	1.68	1.01	16.0	0.47	1.68	0.091	0.20
	B4	**1.36**	**1.52**	**13.0**	**0.38**	**2.08**	**0.112**	**0.30**
	B5	0.84	1.75	8.0	0.23	1.46	0.079	0.34
	B6	1.86	0.77	17.8	0.52	1.42	0.077	0.15
	B7	1.73	1.01	16.5	0.48	1.75	0.095	0.20
	B8	1.65	1.15	15.8	0.46	1.90	0.102	0.22
	B9	1.54	1.28	14.8	0.43	1.97	0.107	0.25
	B10	1.41	1.42	13.5	0.39	2.01	0.109	0.28
[C]	C1	2.67	0.19	25.5	0.63	0.51	0.017	0.03
	C2	2.33	0.72	22.3	0.55	1.68	0.055	0.10
	C3	2.23	1.13	21.3	0.52	2.51	0.081	0.16
	C4	2.04	1.61	19.5	0.48	3.28	0.107	0.22
	C5	1.68	2.09	16.0	0.39	3.50	0.114	0.29
	C6	0.94	2.29	9.0	0.22	2.15	0.070	0.32
	C7	**1.83**	**1.93**	**17.5**	**0.43**	**3.54**	**0.115**	**0.27**
	C8	1.96	1.45	18.8	0.46	2.84	0.092	0.20
	C9	2.17	0.93	20.8	0.51	2.02	0.066	0.13
	C10	2.43	0.49	23.3	0.57	1.19	0.039	0.07
[D]	D1	3.17	0.02	30.3	0.65	0.06	0.001	0.00
	D2	2.83	0.62	27.0	0.58	1.76	0.037	0.06
	D3	2.51	1.21	24.0	0.51	3.04	0.064	0.13
	D4	2.38	1.76	22.8	0.49	4.20	0.089	0.18
	D5	2.09	2.26	20.0	0.43	4.73	0.100	0.24
	D6	1.54	2.84	14.8	0.32	4.38	0.093	0.29
	D7	**1.94**	**2.55**	**18.5**	**0.40**	**4.93**	**0.105**	**0.26**
	D8	2.33	1.96	22.3	0.48	4.58	0.097	0.20
	D9	2.49	1.51	23.8	0.51	3.77	0.080	0.16
	D10	2.91	0.45	27.8	0.59	1.32	0.028	0.05
[E]	E1	3.32	0.70	31.8	0.61	2.31	0.036	0.06
	E2	3.17	0.99	30.3	0.58	3.13	0.049	0.08
	E3	2.91	1.51	27.8	0.53	4.38	0.068	0.13
	E4	2.72	1.90	26.0	0.50	5.17	0.080	0.16
	E5	2.64	2.33	25.3	0.49	6.17	0.096	0.20
	E6	2.51	2.73	24.0	0.46	6.87	0.107	0.23
	E7	**2.25**	**3.12**	**21.5**	**0.41**	**7.01**	**0.109**	**0.26**
	E8	1.73	3.30	16.5	0.32	5.70	0.089	0.28
	E9	2.17	3.18	20.8	0.40	6.91	0.107	0.27
	E10	2.33	2.91	22.3	0.43	6.77	0.105	0.25

Table A.4 Performance data for CB_6S configuration

Flow Condition	*Point no*	*ω* *[rads^{-1}]*	*T_{ave}* *[Nm]*	*RPM*	*TSR*	*P* *[W]*	*C_P*	*C_τ*
[B]	B1	2.30	0.00	22.0	0.64	0.00	0.00	0.00
	B2	1.85	0.63	17.7	0.52	1.16	0.06	0.12
	B3	1.62	1.19	15.5	0.45	1.93	0.10	0.23
	B4	**1.38**	**1.67**	**13.2**	**0.39**	**2.30**	**0.12**	**0.32**
	B5	1.53	1.40	14.6	0.43	2.14	0.12	0.27
	B6	1.52	1.40	14.5	0.42	2.13	0.12	0.27
	B7	1.72	0.91	16.4	0.48	1.56	0.08	0.18
	B8	1.93	0.47	18.4	0.54	0.90	0.05	0.09
	B9	2.12	0.24	20.2	0.59	0.51	0.03	0.05
	B10	1.30	1.78	12.4	0.36	2.32	0.13	0.35
[C]	C1	2.80	0.00	26.7	0.66	0.00	0.00	0.00
	C2	2.51	0.52	24.0	0.59	1.30	0.04	0.07
	C3	2.27	1.00	21.7	0.53	2.26	0.07	0.14
	C4	2.06	1.48	19.7	0.49	3.05	0.10	0.20
	C5	1.94	1.84	18.5	0.46	3.56	0.12	0.25
	C6	1.78	2.23	17.0	0.42	3.97	0.13	0.31
	C7	2.15	1.26	20.5	0.50	2.71	0.09	0.17
	C8	2.37	0.75	22.6	0.56	1.78	0.06	0.10
	C9	2.64	0.27	25.2	0.62	0.72	0.02	0.04
	C10	**1.63**	**2.55**	**15.6**	**0.38**	**4.16**	**0.14**	**0.35**
[D]	D1	3.26	0.00	31.1	0.66	0.00	0.00	0.00
	D2	2.89	0.63	27.6	0.59	1.82	0.04	0.07
	D3	2.69	1.08	25.7	0.55	2.91	0.06	0.11
	D4	2.49	1.52	23.8	0.51	3.79	0.08	0.16
	D5	2.16	2.56	20.6	0.44	5.52	0.12	0.27
	D6	2.04	3.00	19.5	0.42	6.12	0.13	0.31
	D7	1.63	3.45	15.6	0.33	5.64	0.12	0.36
	D8	2.23	2.27	21.3	0.45	5.07	0.11	0.24
	D9	2.42	1.81	23.1	0.49	4.38	0.09	0.19
	D10	**1.80**	**3.56**	**17.2**	**0.37**	**6.42**	**0.14**	**0.37**
[E]	E1	3.69	0.00	35.2	0.68	0.00	0.00	0.00
	E2	3.27	0.57	31.2	0.60	1.87	0.03	0.05
	E3	3.05	1.13	29.1	0.56	3.44	0.05	0.10
	E4	2.89	1.57	27.6	0.53	4.53	0.07	0.13
	E5	2.70	2.14	25.8	0.50	5.78	0.09	0.18
	E6	2.60	2.60	24.8	0.48	6.74	0.10	0.22
	E7	2.38	3.13	22.7	0.44	7.43	0.12	0.26
	E8	**2.23**	**3.76**	**21.3**	**0.41**	**8.38**	**0.13**	**0.32**
	E9	2.10	3.92	20.1	0.39	8.25	0.13	0.33
	E10	1.95	3.96	18.6	0.36	7.72	0.12	0.33

Table A.5 Performance data for CB_3D configuration

Flow Condition	*Point no*	*ω* *[rads^{-1}]*	*T_{ave}* *[Nm]*	*RPM*	*TSR*	*P* *[W]*	*C_P*	*C_τ*
[B]	B1	2.97	0.00	28.4	0.83	0.00	0.00	0.00
	B2	2.51	0.60	24.0	0.70	1.50	0.08	0.12
	B3	2.07	1.15	19.7	0.58	2.37	0.13	0.22
	B4	1.54	1.72	14.7	0.43	2.64	0.14	0.33
	B5	1.27	2.04	12.1	0.35	2.59	0.14	0.40
	B6	1.81	1.39	17.3	0.50	2.52	0.14	0.27
	B7	0.48	1.89	4.6	0.13	0.91	0.05	0.37
	B8	2.51	0.62	24.0	0.70	1.55	0.08	0.12
	B9	1.98	1.23	18.9	0.55	2.42	0.13	0.24
	B10	1.50	1.82	14.3	0.42	2.74	0.15	0.35
[C]	C1	3.70	0.00	35.3	0.87	0.00	0.00	0.00
	C2	3.13	0.76	29.9	0.74	2.37	0.08	0.10
	C3	2.82	1.25	26.9	0.66	3.51	0.11	0.17
	C4	2.42	1.91	23.1	0.57	4.63	0.15	0.26
	C5	2.12	2.35	20.3	0.50	4.99	0.16	0.32
	C6	1.61	3.13	15.4	0.38	5.05	0.16	0.43
	C7	0.66	2.94	6.3	0.16	1.95	0.06	0.41
	C8	0.48	3.00	4.6	0.11	1.45	0.05	0.41
	C9	1.73	2.86	16.5	0.41	4.95	0.16	0.40
	C10	2.53	1.73	24.2	0.60	4.39	0.14	0.24
[D]	D1	4.15	0.00	39.7	0.85	0.00	0.00	0.00
	D2	3.73	0.65	35.7	0.76	2.44	0.05	0.07
	D3	3.39	1.30	32.3	0.69	4.42	0.09	0.14
	D4	3.05	1.84	29.1	0.62	5.61	0.12	0.19
	D5	2.56	2.52	24.4	0.52	6.46	0.14	0.26
	D6	2.14	3.32	20.4	0.44	7.09	0.15	0.34
	D7	1.15	3.75	11.0	0.23	4.31	0.09	0.39
	D8	0.59	3.74	5.7	0.12	2.22	0.05	0.39
	D9	0.43	3.84	4.1	0.09	1.65	0.04	0.40
	D10	2.32	2.98	22.2	0.47	6.93	0.15	0.31
[E]	E1	4.78	0.00	45.6	0.88	0.00	0.00	0.00
	E2	4.32	0.70	41.2	0.79	3.03	0.05	0.06
	E3	4.05	1.30	38.7	0.75	5.28	0.08	0.11
	E4	3.49	2.30	33.4	0.64	8.03	0.12	0.19
	E5	2.94	3.29	28.0	0.54	9.68	0.15	0.28
	E6	2.72	3.83	25.9	0.50	10.41	0.16	0.32
	E7	2.10	5.03	20.0	0.39	10.53	0.16	0.42
	E8	1.19	4.97	11.3	0.22	5.90	0.09	0.42
	E9	3.08	2.91	29.4	0.57	8.98	0.14	0.25
	E10	3.67	1.90	35.1	0.67	6.98	0.11	0.16

Table A.6 Performance data for CB_4D configuration

Flow Condition	*Point no*	*ω* *[rads^{-1}]*	*T_{ave}* *[Nm]*	*RPM*	*TSR*	*P* *[W]*	*C_P*	*C_τ*
[B]	B1	2.89	0.00	28	0.80	0.00	0.00	0.00
	B2	2.36	0.64	23	0.66	1.52	0.08	0.12
	B3	2.04	1.06	20	0.57	2.16	0.12	0.20
	B4	1.58	1.64	15	0.44	2.59	0.14	0.32
	B5	1.31	1.96	13	0.37	2.57	0.14	0.38
	B6	0.60	2.12	6	0.17	1.27	0.07	0.41
	B7	1.62	1.58	15	0.45	2.55	0.14	0.31
	B8	1.82	1.28	17	0.51	2.33	0.13	0.25
	B9	2.29	0.72	22	0.64	1.66	0.09	0.14
	B10	**2.65**	**0.30**	**25**	**0.74**	**0.81**	**0.04**	**0.06**
[C]	C1	3.48	0.00	33	0.82	0.00	0.00	0.00
	C2	3.13	0.55	30	0.74	1.74	0.06	0.08
	C3	2.80	1.04	27	0.66	2.91	0.09	0.14
	C4	2.50	1.54	24	0.59	3.84	0.12	0.21
	C5	2.25	2.05	22	0.53	4.62	0.15	0.28
	C6	1.89	2.56	18	0.44	4.83	0.16	0.35
	C7	2.01	2.38	19	0.47	4.78	0.16	0.33
	C8	2.00	2.29	19	0.47	4.57	0.15	0.32
	C9	2.67	1.30	25	0.63	3.47	0.11	0.18
	C10	**2.97**	**0.81**	**28**	**0.70**	**2.40**	**0.08**	**0.11**
[D]	D1	4.13	0.00	39	0.84	0.00	0.00	0.00
	D2	3.83	0.61	37	0.78	2.35	0.05	0.06
	D3	3.54	1.12	34	0.72	3.95	0.08	0.12
	D4	3.30	1.58	32	0.67	5.23	0.11	0.16
	D5	2.99	2.15	29	0.61	6.42	0.14	0.22
	D6	2.71	2.64	26	0.55	7.14	0.15	0.27
	D7	2.43	3.11	23	0.50	7.56	0.16	0.32
	D8	2.10	3.70	20	0.43	7.78	0.16	0.39
	D9	1.88	4.09	18	0.38	7.68	0.16	0.43
	D10	**1.52**	**4.37**	**15**	**0.31**	**6.64**	**0.14**	**0.45**
[E]	E1	4.71	0.00	45	0.87	0.00	0.00	0.00
	E2	4.41	0.59	42	0.81	2.62	0.04	0.05
	E3	4.22	1.09	40	0.78	4.58	0.07	0.09
	E4	3.99	1.57	38	0.73	6.28	0.10	0.13
	E5	3.68	2.07	35	0.68	7.63	0.12	0.18
	E6	**3.59**	**2.52**	**34**	**0.66**	**9.04**	**0.14**	**0.21**
	E7	3.17	3.08	30	0.58	9.74	0.15	0.26
	E8	2.80	4.00	27	0.52	11.23	0.17	0.34
	E9	2.69	4.47	26	0.49	12.03	0.19	0.38
	E10	1.66	5.82	16	0.31	9.66	0.15	0.49

Table A.7 Performance data for CB_5D configuration

Flow Condition	*Point no*	*ω* *[rads^{-1}]*	*T_{ave}* *[Nm]*	*RPM*	*TSR*	*P* *[W]*	*C_P*	*C_τ*
[B]	B1	2.79	0.00	26.6	0.78	0.00	0.00	0.00
	B2	2.14	0.64	20.4	0.59	1.36	0.07	0.12
	B3	1.28	1.31	12.2	0.36	1.68	0.09	0.25
	B4	1.00	1.61	9.6	0.28	1.61	0.09	0.31
	B5	0.60	2.04	5.7	0.17	1.23	0.07	0.40
	B6	0.72	1.95	6.9	0.20	1.40	0.08	0.38
	B7	1.28	1.32	12.3	0.36	1.70	0.09	0.26
	B8	2.07	0.79	19.8	0.58	1.65	0.09	0.15
	B9	2.57	0.26	24.5	0.72	0.66	0.04	0.05
	B10	1.58	1.13	15.1	0.44	1.80	0.10	0.22
[C]	C1	3.44	0.00	32.9	0.81	0.00	0.000	0.00
	C2	3.10	0.47	29.6	0.73	1.45	0.047	0.06
	C3	2.79	0.89	26.7	0.66	2.49	0.081	0.12
	C4	2.43	1.31	23.2	0.57	3.18	0.103	0.18
	C5	1.83	1.93	17.4	0.43	3.53	0.115	0.27
	C6	1.30	2.43	12.5	0.31	3.17	0.103	0.34
	C7	0.93	2.86	8.9	0.22	2.66	0.087	0.40
	C8	0.58	3.26	5.5	0.14	1.88	0.061	0.45
	C9	1.61	2.12	15.3	0.38	3.40	0.110	0.29
	C10	2.53	1.24	24.1	0.59	3.15	0.102	0.17
[D]	D1	4.06	0.00	38.8	0.83	0.00	0.000	0.00
	D2	3.52	0.80	33.6	0.72	2.82	0.060	0.08
	D3	3.07	1.54	29.3	0.63	4.72	0.100	0.16
	D4	2.56	2.28	24.4	0.52	5.83	0.124	0.24
	D5	1.96	2.91	18.7	0.40	5.70	0.121	0.30
	D6	1.24	3.81	11.8	0.25	4.71	0.100	0.40
	D7	0.82	4.32	7.9	0.17	3.57	0.076	0.45
	D8	2.91	1.82	27.8	0.59	5.30	0.112	0.19
	D9	3.23	1.29	30.8	0.66	4.15	0.088	0.13
	D10	2.68	2.10	25.6	0.55	5.65	0.120	0.22
[E]	E1	4.66	0.00	44.5	0.86	0.00	0.000	0.00
	E2	4.06	1.15	38.7	0.75	4.68	0.073	0.10
	E3	3.51	2.17	33.5	0.64	7.62	0.118	0.18
	E4	2.76	3.19	26.3	0.51	8.80	0.137	0.27
	E5	2.14	4.17	20.5	0.39	8.95	0.139	0.35
	E6	1.31	5.19	12.5	0.24	6.79	0.106	0.44
	E7	0.82	5.87	7.8	0.15	4.79	0.074	0.50
	E8	3.25	2.59	31.0	0.60	8.39	0.130	0.22
	E9	3.76	1.70	35.9	0.69	6.40	0.100	0.14
	E10	1.80	4.63	17.2	0.33	8.33	0.129	0.39

Table A.8 Performance data for CB_3D+3 configuration

Flow Condition	*Point no*	*ω* *[rads^{-1}]*	*T_{ave}* *[Nm]*	*RPM*	*TSR*	*P* *[W]*	*C_P*	*C_τ*
[B]	B1	2.82	0.00	26.9	0.79	0.00	0.000	0.00
	B2	2.19	0.97	20.9	0.61	2.12	0.114	0.19
	B3	2.12	1.11	20.3	0.59	2.35	0.127	0.21
	B4	1.81	1.50	17.3	0.50	2.72	0.147	0.29
	B5	1.39	1.85	13.2	0.39	2.56	0.138	0.36
	B6	1.06	2.15	10.2	0.30	2.29	0.124	0.42
	B7	1.98	1.34	18.9	0.55	2.64	0.143	0.26
	B8	**1.57**	**1.78**	**15.0**	**0.44**	**2.80**	**0.151**	**0.35**
	B9	2.23	0.89	21.3	0.62	2.00	0.108	0.17
	B10	1.30	2.01	12.4	0.36	2.60	0.140	0.39
[C]	C1	3.44	0.00	32.9	0.81	0.00	0.000	0.00
	C2	2.93	0.97	27.9	0.69	2.84	0.092	0.13
	C3	2.68	1.46	25.6	0.63	3.91	0.127	0.20
	C4	2.41	1.91	23.0	0.57	4.58	0.149	0.26
	C5	**1.96**	**2.55**	**18.7**	**0.46**	**4.98**	**0.162**	**0.35**
	C6	1.50	3.01	14.3	0.35	4.50	0.146	0.42
	C7	1.12	3.48	10.7	0.26	3.91	0.127	0.48
	C8	2.77	1.29	26.5	0.65	3.57	0.116	0.18
	C9	2.12	2.32	20.2	0.50	4.92	0.160	0.32
	C10	1.35	3.24	12.9	0.32	4.39	0.143	0.45
[D]	D1	3.97	0.00	38.0	0.81	0.00	0.000	0.00
	D2	3.43	1.26	32.8	0.70	4.32	0.092	0.13
	D3	2.92	2.24	27.9	0.60	6.54	0.139	0.23
	D4	2.65	2.78	25.3	0.54	7.37	0.156	0.29
	D5	**2.21**	**3.61**	**21.1**	**0.45**	**7.97**	**0.169**	**0.38**
	D6	1.82	4.09	17.4	0.37	7.45	0.158	0.43
	D7	1.35	4.53	12.9	0.28	6.11	0.130	0.47
	D8	2.41	3.16	23.0	0.49	7.62	0.162	0.33
	D9	3.28	1.69	31.3	0.67	5.55	0.118	0.18
	D10	1.61	4.30	15.4	0.33	6.92	0.147	0.45
[E]	E1	4.56	0.00	43.5	0.84	0.00	0.000	0.00
	E2	4.07	1.16	38.8	0.75	4.73	0.073	0.10
	E3	3.63	2.22	34.7	0.67	8.08	0.126	0.19
	E4	3.14	3.09	30.0	0.58	9.71	0.151	0.26
	E5	2.64	4.10	25.2	0.49	10.82	0.168	0.35
	E6	**2.11**	**4.93**	**20.2**	**0.39**	**10.40**	**0.162**	**0.42**
	E7	1.95	5.14	18.6	0.36	10.01	0.156	0.43
	E8	3.33	2.69	31.8	0.61	8.95	0.139	0.23
	E9	4.31	0.48	41.2	0.79	2.08	0.032	0.04
	E10	4.31	0.48	41.2	0.79	2.08	0.032	0.04

Table A.9 Performance data for SAV_LRG configuration

Flow Condition	*Point no*	*ω* *[rads^{-1}]*	*T_{ave}* *[Nm]*	*RPM*	*TSR*	*P* *[W]*	*C_P*	*C_τ*
[B]	B1	6.41	0.00	61.2	1.78	0.00	0.000	0.00
	B2	6.01	0.28	57.4	1.68	1.66	0.090	0.05
	B3	5.67	0.52	54.1	1.58	2.94	0.159	0.10
	B4	5.15	0.67	49.2	1.44	3.48	0.188	0.13
	B5	4.85	0.86	46.3	1.35	4.17	0.225	0.17
	B6	4.20	1.17	40.1	1.17	4.91	0.265	0.23
	B7	**3.79**	**1.32**	**36.2**	**1.06**	**5.00**	**0.270**	**0.26**
	B8	3.05	1.63	29.1	0.85	4.97	0.268	0.32
	B9	2.64	1.74	25.2	0.74	4.61	0.249	0.34
	B10	4.31	1.09	41.2	1.20	4.68	0.253	0.21
[C]	C1	7.99	0.00	76.3	1.88	0.00	0.000	0.00
	C2	7.21	0.69	68.8	1.69	4.99	0.162	0.10
	C3	6.21	1.28	59.3	1.46	7.97	0.259	0.18
	C4	5.58	1.57	53.3	1.31	8.77	0.285	0.22
	C5	5.04	1.89	48.1	1.18	9.54	0.310	0.26
	C6	3.88	2.50	37.0	0.91	9.70	0.315	0.35
	C7	3.02	2.75	28.8	0.71	8.31	0.270	0.38
	C8	**4.14**	**2.33**	**39.6**	**0.97**	**9.65**	**0.314**	**0.32**
	C9	4.95	1.91	47.3	1.16	9.46	0.307	0.26
	C10	5.85	1.40	55.8	1.37	8.19	0.266	0.19
[D]	D1	9.47	0.00	90.4	1.93	0.00	0.000	0.00
	D2	3.60	3.96	34.3	0.73	14.24	0.302	0.41
	D3	**4.44**	**3.60**	**42.4**	**0.91**	**16.01**	**0.340**	**0.37**
	D4	5.34	2.99	50.9	1.09	15.96	0.339	0.31
	D5	5.88	2.68	56.1	1.20	15.77	0.335	0.28
	D6	6.69	2.15	63.9	1.36	14.40	0.306	0.22
	D7	7.48	1.58	71.4	1.53	11.83	0.251	0.16
	D8	8.34	0.89	79.7	1.70	7.43	0.158	0.09
	D9	8.68	0.64	82.9	1.77	5.52	0.117	0.07
	D10	7.96	1.31	76.0	1.62	10.41	0.221	0.14
[E]	E1	10.63	0.00	101.5	1.95	0.00	0.000	0.00
	E2	10.17	0.54	97.2	1.87	5.46	0.085	0.05
	E3	9.86	0.99	94.2	1.81	9.80	0.152	0.08
	E4	9.08	1.56	86.7	1.67	14.13	0.220	0.13
	E5	8.64	2.07	82.5	1.59	17.88	0.278	0.17
	E6	8.08	2.54	77.1	1.49	20.51	0.319	0.21
	E7	7.24	3.07	69.2	1.33	22.26	0.346	0.26
	E8	**6.41**	**3.79**	**61.2**	**1.18**	**24.29**	**0.377**	**0.32**
	E9	5.35	4.43	51.1	0.98	23.68	0.368	0.37
	E10	4.08	5.09	38.9	0.75	20.77	0.323	0.43

Table A.10 Performance data for CB_SAVa configuration

Flow Condition	*Point no*	*ω* *[rads^{-1}]*	*T_{ave}* *[Nm]*	*RPM*	*TSR*	*P* *[W]*	*C_P*	*C_τ*
[B]	B1	5.81	0.00	55.5	1.62	0.00	0.000	0.00
	B2	5.47	0.22	52.3	1.52	1.20	0.065	0.04
	B3	4.25	0.73	40.6	1.18	3.11	0.168	0.14
	B4	3.71	0.91	35.4	1.03	3.370	0.182	0.18
	B5	2.79	1.05	26.6	0.78	2.93	0.158	0.20
	B6	2.65	1.12	25.3	0.74	2.96	0.160	0.22
	B7	**3.335**	**1.011**	**31.845**	**0.929**	**3.372**	**0.182**	**0.196**
	B8	4.14	0.74	39.5	1.15	3.06	0.165	0.14
	B9	4.56	0.54	43.5	1.27	2.46	0.133	0.10
	B10	5.54	0.16	52.9	1.54	0.88	0.048	0.03
[C]	C1	7.21	0.00	68.8	1.70	0.00	0.000	0.00
	C2	6.43	0.54	61.4	1.51	3.48	0.113	0.07
	C3	5.49	0.99	52.4	1.29	5.41	0.176	0.14
	C4	4.66	1.28	44.5	1.10	5.95	0.193	0.18
	C5	3.69	1.69	35.3	0.87	6.23	0.202	0.23
	C6	2.70	1.86	25.7	0.63	5.02	0.163	0.26
	C7	2.90	1.88	27.7	0.68	5.45	0.177	0.26
	C8	**4.11**	**1.63**	**39.3**	**0.97**	**6.68**	**0.217**	**0.22**
	C9	5.10	1.27	48.7	1.20	6.46	0.210	0.18
	C10	5.82	0.89	55.6	1.37	5.17	0.168	0.12
[D]	D1	8.21	0.00	78.4	1.68	0.00	0.000	0.00
	D2	7.33	0.78	70.0	1.50	5.69	0.121	0.08
	D3	6.56	1.32	62.7	1.34	8.67	0.184	0.14
	D4	**5.55**	**1.76**	**53.0**	**1.13**	**9.78**	**0.207**	**0.18**
	D5	4.45	2.11	42.5	0.91	9.42	0.200	0.22
	D6	3.54	2.55	33.8	0.72	9.01	0.191	0.27
	D7	2.88	2.64	27.5	0.59	7.61	0.161	0.27
	D8	4.64	2.10	44.3	0.95	9.76	0.207	0.22
	D9	5.96	1.48	56.9	1.22	8.81	0.187	0.15
	D10	6.80	1.07	64.9	1.39	7.27	0.154	0.11
[E]	E1	9.47	0.00	90.4	1.74	0.00	0.000	0.00
	E2	8.06	1.46	77.0	1.48	11.75	0.183	0.12
	E3	7.06	2.14	67.4	1.30	15.11	0.235	0.18
	E4	**6.14**	**2.67**	**58.7**	**1.13**	**16.39**	**0.255**	**0.23**
	E5	5.03	3.14	48.1	0.93	15.79	0.245	0.27
	E6	3.73	3.41	35.6	0.69	12.72	0.198	0.29
	E7	5.32	2.88	50.8	0.98	15.34	0.238	0.24
	E8	6.79	2.27	64.9	1.25	15.46	0.240	0.19
	E9	7.68	1.74	73.4	1.41	13.38	0.208	0.15
	E10	8.84	0.69	84.4	1.63	6.12	0.095	0.06

Table A.11 Performance data for CB_SAVb configuration

Flow Condition	*Point no*	*ω* *[rads^{-1}]*	*T_{ave}* *[Nm]*	*RPM*	*TSR*	*P* *[W]*	*C_P*	*C_τ*
[B]	B1	3.95	0.00	37.8	1.10	0.00	0.000	0.00
	B2	3.57	0.32	34.1	0.99	1.13	0.061	0.06
	B3	3.19	0.57	30.5	0.89	1.81	0.098	0.11
	B4	2.38	0.95	22.7	0.66	2.26	0.122	0.18
	B5	3.43	0.43	32.8	0.96	1.46	0.079	0.08
	B6	**2.75**	**0.85**	**26.3**	**0.77**	**2.34**	**0.126**	**0.16**
	B7	3.16	0.62	30.1	0.88	1.97	0.106	0.12
	B8	3.08	0.70	29.4	0.86	2.17	0.117	0.14
	B9	2.15	0.99	20.5	0.60	2.13	0.115	0.19
	B10	3.64	0.20	34.8	1.01	0.74	0.040	0.04

Table A.12 Performance data for CB_SAVc configuration

Flow Condition	*Point no*	*ω* *[rads^{-1}]*	*T_{ave}* *[Nm]*	*RPM*	*TSR*	*P* *[W]*	*C_P*	*C_τ*
[B]	B1	5.00	0.00	47.8	1.39	0.00	0.000	0.00
	B2	4.22	0.32	40.3	1.18	1.36	0.073	0.06
	B3	3.68	0.53	35.1	1.03	1.95	0.105	0.10
	B4	**2.74**	**0.89**	**26.1**	**0.76**	**2.44**	**0.132**	**0.17**
	B5	2.43	0.95	23.2	0.68	2.30	0.124	0.18
	B6	2.84	0.79	27.1	0.79	2.23	0.121	0.15
	B7	3.20	0.61	30.5	0.89	1.95	0.105	0.12
	B8	3.92	0.42	37.4	1.09	1.63	0.088	0.08
	B9	2.70	0.84	25.8	0.75	2.26	0.122	0.16
	B10	3.39	0.61	32.4	0.94	2.06	0.111	0.12

Table A.13 Performance data for DAR_4b_0.0p configuration

Flow Condition	*Point no*	*ω* *[rads^{-1}]*	*T_{ave}* *[Nm]*	*RPM*	*TSR*	*P* *[W]*	*C_P*	*C_τ*
[B]	B1	4.37	0.00	42	1.22	0.00	0.00	0.00
	B2	4.10	0.10	39	1.14	0.41	0.02	0.02
	B3	4.05	0.12	39	1.13	0.49	0.03	0.02
	B4	3.99	0.15	38	1.11	0.60	0.03	0.03
	B5	3.93	0.15	38	1.10	0.59	0.03	0.03
	B6	3.95	0.16	38	1.10	0.63	0.03	0.03
	B7	3.87	0.18	37	1.08	0.70	0.04	0.03
	B8	3.83	0.19	37	1.07	0.73	0.04	0.04
	B9	3.74	0.18	36	1.04	0.67	0.04	0.03
	B10	**3.67**	**0.21**	**35**	**1.02**	**0.77**	**0.04**	**0.04**
[C]	C1	8.02	0.00	77	1.88	0.00	0.00	0.00
	C2	7.34	0.11	70	1.73	0.81	0.03	0.02
	C3	6.50	0.18	62	1.53	1.17	0.04	0.02
	C4	5.20	0.23	50	1.22	1.20	0.04	0.03
	C5	4.99	0.28	48	1.17	1.40	0.05	0.04
	C6	4.95	0.31	47	1.16	1.53	0.05	0.04
	C7	4.82	0.37	46	1.13	1.79	0.06	0.05
	C8	4.77	0.41	46	1.12	1.96	0.06	0.06
	C9	4.70	0.44	45	1.11	2.07	0.07	0.06
	C10	**4.49**	**0.47**	**43**	**1.06**	**2.11**	**0.07**	**0.06**
[D]	D1	10.13	0.00	97	2.07	0.00	0.00	0.00
	D2	9.29	0.26	89	1.90	2.42	0.05	0.03
	D3	8.53	0.40	81	1.74	3.41	0.07	0.04
	D4	7.57	0.49	72	1.54	3.71	0.08	0.05
	D5	5.81	0.55	55	1.18	3.19	0.07	0.06
	D6	5.67	0.60	54	1.16	3.40	0.07	0.06
	D7	5.54	0.65	53	1.13	3.60	0.08	0.07
	D8	5.51	0.69	53	1.12	3.80	0.08	0.07
	D9	5.42	0.74	52	1.11	4.01	0.09	0.08
	D10	**5.26**	**0.78**	**50**	**1.07**	**4.10**	**0.09**	**0.08**
[E]	E1	11.34	0.00	108	2.08	0.00	0.00	0.00
	E2	10.83	0.27	103	1.99	2.92	0.05	0.02
	E3	10.28	0.48	98	1.89	4.93	0.08	0.04
	E4	9.81	0.60	94	1.80	5.88	0.09	0.05
	E5	8.99	0.71	86	1.65	6.38	0.10	0.06
	E6	**8.56**	**0.75**	**82**	**1.57**	**6.42**	**0.10**	**0.06**
	E7	6.29	0.78	60	1.16	4.91	0.08	0.07
	E8	6.13	0.85	59	1.13	5.21	0.08	0.07
	E9	6.00	0.90	57	1.10	5.40	0.08	0.08
	E10	5.87	0.94	56	1.08	5.52	0.09	0.08

Table A.14 Performance data for DAR_4b_2.5p configuration

Flow Condition	*Point no*	*ω* *[rads^{-1}]*	*T_{ave}* *[Nm]*	*RPM*	*TSR*	*P* *[W]*	*C_P*	*C_τ*
[B]	B1	6.69	0.00	64	1.86	0.00	0.00	0.00
	B2	6.32	0.14	60	1.76	0.88	0.05	0.03
	B3	5.93	0.25	57	1.65	1.48	0.08	0.05
	B4	5.46	0.34	52	1.52	1.86	0.10	0.07
	B5	5.01	0.40	48	1.39	2.00	0.11	0.08
	B6	4.81	0.42	46	1.34	2.02	0.11	0.08
	B7	4.57	0.43	44	1.27	1.96	0.11	0.08
	B8	4.24	0.44	40	1.18	1.86	0.10	0.09
	B9	4.05	0.46	39	1.13	1.86	0.10	0.09
	B10	**3.91**	**0.49**	**37**	**1.09**	**1.92**	**0.10**	**0.10**
[C]	C1	8.70	0.00	83	2.05	0.00	0.00	0.00
	C2	8.25	0.24	79	1.94	1.98	0.06	0.03
	C3	8.02	0.32	77	1.89	2.57	0.08	0.04
	C4	7.72	0.43	74	1.81	3.32	0.11	0.06
	C5	7.31	0.54	70	1.72	3.95	0.13	0.07
	C6	6.91	0.64	66	1.63	4.43	0.14	0.09
	C7	6.56	0.72	63	1.54	4.72	0.15	0.10
	C8	5.80	0.81	55	1.36	4.70	0.15	0.11
	C9	5.41	0.82	52	1.27	4.44	0.14	0.11
	C10	**4.98**	**0.83**	**48**	**1.17**	**4.13**	**0.13**	**0.11**
[D]	D1	10.34	0.00	99	2.11	0.00	0.00	0.00
	D2	9.83	0.23	94	2.01	2.26	0.05	0.02
	D3	9.53	0.45	91	1.94	4.29	0.09	0.05
	D4	9.25	0.55	88	1.89	5.09	0.11	0.06
	D5	8.91	0.68	85	1.82	6.06	0.13	0.07
	D6	8.65	0.77	83	1.76	6.66	0.14	0.08
	D7	8.20	0.93	78	1.67	7.63	0.16	0.10
	D8	7.85	1.04	75	1.60	8.16	0.17	0.11
	D9	7.18	1.15	69	1.46	8.26	0.18	0.12
	D10	**6.18**	**1.22**	**59**	**1.26**	**7.54**	**0.16**	**0.13**
[E]	E1	11.36	0.00	108	2.09	0.00	0.00	0.00
	E2	10.43	1.17	100	1.92	12.21	0.19	0.10
	E3	10.18	1.30	97	1.87	13.23	0.21	0.11
	E4	10.04	1.39	96	1.85	13.96	0.22	0.12
	E5	9.63	1.57	92	1.77	15.12	0.23	0.13
	E6	**9.22**	**1.73**	**88**	**1.70**	**15.96**	**0.25**	**0.15**
	E7	8.98	1.86	86	1.65	16.70	0.26	0.16
	E8	8.54	1.98	82	1.57	16.91	0.26	0.17
	E9	7.86	2.05	75	1.45	16.12	0.25	0.17
	E10	Point not recorded						

Table A.15 Performance data for DAR_4b_5.0p configuration

Flow Condition	*Point no*	*ω* *[rads^{-1}]*	*T_{ave}* *[Nm]*	*RPM*	*TSR*	*P* *[W]*	*C_P*	*C_τ*
[B]	B1	6.76	0.00	65	1.88	0.00	0.00	0.00
	B2	6.29	0.09	60	1.75	0.57	0.03	0.02
	B3	5.94	0.18	57	1.65	1.07	0.06	0.03
	B4	5.82	0.24	56	1.62	1.40	0.08	0.05
	B5	5.66	0.30	54	1.58	1.70	0.09	0.06
	B6	5.52	0.34	53	1.54	1.88	0.10	0.07
	B7	5.35	0.38	51	1.49	2.03	0.11	0.07
	B8	5.17	0.43	49	1.44	2.22	0.12	0.08
	B9	5.05	0.44	48	1.41	2.22	0.12	0.09
	B10	**4.78**	**0.48**	**46**	**1.33**	**2.30**	**0.12**	**0.09**
[C]	C1	8.72	0.00	83	2.05	0.00	0.00	0.00
	C2	8.12	0.35	78	1.91	2.84	0.09	0.05
	C3	7.95	0.47	76	1.87	3.73	0.12	0.06
	C4	7.35	0.76	70	1.73	5.59	0.18	0.11
	C5	7.20	0.84	69	1.69	6.05	0.20	0.12
	C6	6.93	0.91	66	1.63	6.30	0.20	0.13
	C7	6.84	0.95	65	1.61	6.49	0.21	0.13
	C8	6.64	1.03	63	1.56	6.84	0.22	0.14
	C9	6.25	1.14	60	1.47	7.12	0.23	0.16
	C10	**5.94**	**1.18**	**57**	**1.40**	**7.01**	**0.23**	**0.16**
[D]	D1	10.30	0.00	98	2.10	0.00	0.00	0.00
	D2	9.78	0.37	93	1.99	3.62	0.08	0.04
	D3	9.33	0.66	89	1.90	6.16	0.13	0.07
	D4	9.20	0.83	88	1.88	7.64	0.16	0.09
	D5	8.74	1.08	83	1.78	9.44	0.20	0.11
	D6	8.53	1.18	81	1.74	10.07	0.21	0.12
	D7	8.21	1.32	78	1.67	10.83	0.23	0.14
	D8	7.92	1.46	76	1.62	11.57	0.25	0.15
	D9	7.59	1.55	73	1.55	11.77	0.25	0.16
	D10	**6.69**	**1.70**	**64**	**1.36**	**11.38**	**0.24**	**0.18**
[E]	E1	11.43	0.00	109	2.10	0.00	0.00	0.00
	E2	10.93	0.44	104	2.01	4.81	0.07	0.04
	E3	10.46	0.79	100	1.92	8.26	0.13	0.07
	E4	10.12	1.13	97	1.86	11.44	0.18	0.10
	E5	9.58	1.42	91	1.76	13.60	0.21	0.12
	E6	**9.29**	**1.61**	**89**	**1.71**	**14.96**	**0.23**	**0.14**
	E7	9.01	1.75	86	1.66	15.77	0.25	0.15
	E8	8.56	1.94	82	1.57	16.62	0.26	0.16
	E9	8.44	2.03	81	1.55	17.14	0.27	0.17
	E10	8.15	2.14	78	1.50	17.44	0.27	0.18

Table A.16 Performance data for DAR_4b_7.5p configuration

Flow Condition	*Point no*	*ω* *[rads^{-1}]*	*T_{ave}* *[Nm]*	*RPM*	*TSR*	*P* *[W]*	*C_P*	*C_τ*
[B]	B1	6.17	0.00	59	1.72	0.00	0.00	0.00
	B2	6.00	0.07	57	1.67	0.42	0.02	0.01
	B3	5.91	0.16	56	1.65	0.95	0.05	0.03
	B4	5.78	0.22	55	1.61	1.27	0.07	0.04
	B5	5.66	0.25	54	1.58	1.42	0.08	0.05
	B6	5.44	0.34	52	1.52	1.85	0.10	0.07
	B7	5.25	0.42	50	1.46	2.20	0.12	0.08
	B8	5.06	0.50	48	1.41	2.53	0.14	0.10
	B9	4.80	0.50	46	1.34	2.40	0.13	0.10
	B10	**4.70**	**0.54**	**45**	**1.31**	**2.54**	**0.14**	**0.10**
[C]	C1	8.09	0.00	77	1.90	0.00	0.00	0.00
	C2	7.81	0.19	75	1.84	1.48	0.05	0.03
	C3	7.68	0.27	73	1.81	2.07	0.07	0.04
	C4	7.29	0.54	70	1.71	3.93	0.13	0.07
	C5	6.95	0.71	66	1.63	4.93	0.16	0.10
	C6	6.78	0.80	65	1.59	5.43	0.18	0.11
	C7	6.56	0.92	63	1.54	6.04	0.20	0.13
	C8	6.25	1.04	60	1.47	6.50	0.21	0.14
	C9	5.92	1.15	57	1.39	6.81	0.22	0.16
	C10	**5.70**	**1.18**	**54**	**1.34**	**6.72**	**0.22**	**0.16**
[D]	D1	9.45	0.00	90	1.93	0.00	0.00	0.00
	D2	9.14	0.26	87	1.86	2.38	0.05	0.03
	D3	8.90	0.43	85	1.82	3.83	0.08	0.04
	D4	8.56	0.77	82	1.75	6.59	0.14	0.08
	D5	8.27	0.94	79	1.69	7.77	0.16	0.10
	D6	8.04	1.15	77	1.64	9.24	0.20	0.12
	D7	7.78	1.30	74	1.59	10.12	0.21	0.14
	D8	7.45	1.48	71	1.52	11.02	0.23	0.15
	D9	7.11	1.61	68	1.45	11.44	0.24	0.17
	D10	**6.67**	**1.73**	**64**	**1.36**	**11.55**	**0.24**	**0.18**
[E]	E1	10.30	0.00	98	1.89	0.00	0.00	0.00
	E2	9.93	0.24	95	1.83	2.38	0.04	0.02
	E3	9.57	0.50	91	1.76	4.79	0.07	0.04
	E4	9.34	0.67	89	1.72	6.26	0.10	0.06
	E5	9.13	0.87	87	1.68	7.94	0.12	0.07
	E6	**8.89**	**1.14**	**85**	**1.63**	**10.13**	**0.16**	**0.10**
	E7	8.41	1.34	80	1.55	11.26	0.17	0.11
	E8	8.19	1.52	78	1.51	12.45	0.19	0.13
	E9	7.90	1.67	75	1.45	13.20	0.21	0.14
	E10	7.75	1.76	74	1.42	13.63	0.21	0.15

Table A.17 Performance data for DAR_4b_10.0p configuration

Flow Condition	*Point no*	*ω* *[rads^{-1}]*	*T_{ave}* *[Nm]*	*RPM*	*TSR*	*P* *[W]*	*C_P*	*C_τ*
[B]	B1	6.10	0.00	58	1.70	0.00	0.00	0.00
	B2	5.73	0.15	55	1.60	0.86	0.05	0.03
	B3	5.58	0.21	53	1.55	1.17	0.06	0.04
	B4	5.44	0.26	52	1.51	1.41	0.08	0.05
	B5	5.39	0.27	52	1.50	1.46	0.08	0.05
	B6	5.42	0.30	52	1.51	1.63	0.09	0.06
	B7	5.26	0.33	50	1.47	1.74	0.09	0.06
	B8	5.25	0.34	50	1.46	1.78	0.10	0.07
	B9	5.22	0.36	50	1.46	1.88	0.10	0.07
	B10	**5.15**	**0.38**	**49**	**1.43**	**1.96**	**0.11**	**0.07**
[C]	C1	7.57	0.00	72	1.78	0.00	0.00	0.00
	C2	7.12	0.33	68	1.68	2.35	0.08	0.05
	C3	6.99	0.44	67	1.64	3.08	0.10	0.06
	C4	6.76	0.54	65	1.59	3.65	0.12	0.07
	C5	6.65	0.63	63	1.56	4.19	0.14	0.09
	C6	6.48	0.67	62	1.52	4.34	0.14	0.09
	C7	6.44	0.71	61	1.51	4.57	0.15	0.10
	C8	6.34	0.80	61	1.49	5.07	0.16	0.11
	C9	6.27	0.81	60	1.47	5.08	0.16	0.11
	C10	**6.11**	**0.82**	**58**	**1.44**	**5.01**	**0.16**	**0.11**
[D]	D1	8.80	0.00	84	1.79	0.00	0.00	0.00
	D2	8.39	0.32	80	1.71	2.69	0.06	0.03
	D3	8.23	0.46	79	1.68	3.79	0.08	0.05
	D4	8.07	0.62	77	1.65	5.00	0.11	0.06
	D5	7.85	0.75	75	1.60	5.89	0.12	0.08
	D6	7.79	0.84	74	1.59	6.54	0.14	0.09
	D7	7.60	0.93	73	1.55	7.06	0.15	0.10
	D8	7.49	1.01	72	1.53	7.57	0.16	0.11
	D9	7.29	1.08	70	1.49	7.87	0.17	0.11
	D10	**7.11**	**1.18**	**68**	**1.45**	**8.38**	**0.18**	**0.12**
[E]	E1	9.64	0.00	92	1.77	0.00	0.00	0.00
	E2	9.30	0.34	89	1.71	3.16	0.05	0.03
	E3	9.17	0.57	88	1.69	5.23	0.08	0.05
	E4	8.88	0.72	85	1.63	6.39	0.10	0.06
	E5	8.52	0.85	81	1.57	7.24	0.11	0.07
	E6	**8.66**	**0.93**	**83**	**1.59**	**8.05**	**0.13**	**0.08**
	E7	8.34	1.04	80	1.53	8.68	0.13	0.09
	E8	8.14	1.12	78	1.50	9.11	0.14	0.09
	E9	8.10	1.18	77	1.49	9.56	0.15	0.10
	E10	8.03	1.28	77	1.48	10.28	0.16	0.11